POLYURETHANE SCAFFOLDS WITH DELIVERY OF BIOLOGICALLY ACTIVE MOLECULES FOR TISSUE REGENERATION

By

Andrea Elise Hafeman

Dissertation

Submitted to the Faculty of the

Graduate School of Vanderbilt University

in partial fulfillment of the requirements

for the degree of

DOCTOR OF PHILOSOPHY

in

Chemical Engineering

May, 2010

Nashville, Tennessee

Approved:

Professor Scott A. Guelcher

Professor G. Kane Jennings

Professor Paul E. Laibinis

Professor M. Douglas LeVan

Professor Jeffrey M. Davidson

To my wonderful parents, Drs. Dean G. Hafeman and Evelyn L. McGown, with their infinite support, encouragement, and love, have provided me with incredible experiences and educational opportunities.

ACKNOWLEDGEMENTS

I would first like to acknowledge my sources of funding, without which this research would not have been possible: the United States Army Institute for Surgical Research (USAISR), National Institutes of Health (NIH), Vanderbilt Skin Diseases Research Core Center, and the Department of Veterans Affairs.

I would like to express my immense gratitude to all those who have helped me to complete my studies. I am exceptionally grateful to Katarzyna Zienkiewicz for her wisdom and patience, and help with experiments. Thanks to Mark Holmes for all his support with the lab equipment, and Dr. Tiffany Rau and Dr. Anthony Hmelo for teaching me to operate the cell culture and SEM instruments, respectively. Thanks to John Fellenstein in the Physics Machine Shop, Dr. Joseph Wenke at the USAISR for his beneficial collaborations, and Dr. Eugene LeBoeuf for the use of equipment and facilities in the lab, as well as the Vanderbilt Institute of Nanoscale Engineering (VINSE), and the Vanderbilt Cell Imaging Shared Resource Center.

I would like to thank my fellow graduate students in the Guelcher lab for their friendship and insight: Margarita Prieto, Nazanin Ruppender, Elizabeth Adolph, Bing Li, and Jerald Dumas for maintaining my spirits and laughter in the lab. Similarly, thanks to the undergraduates who have contributed to my research: Matthew Mansel, Michelle Brouner, Lance Hochhauser, and Mallory Smyth.

Members of the Vanderbilt University Bone Center have provided invaluable knowledge and expertise. Thank you to Dr. Gregory Mundy, for your guidance both inside and outside of the research setting, and to Dr. Gloria Gutierrez for your

encouragement and warm smile, even during stressful times. Thanks to Dr. James Edwards for teaching me cell culture techniques, Javier Esparza for your proficiency and contributions to numerous *in vivo* studies, and Dr. Toshitaka Yoshii for an excellent collaboration and some elementary Japanese lessons.

Thanks to the "Regeneration Team" for your cooperative resources, insight, and feedback at our weekly meetings: Dr. Jeffrey Davidson, Dr. Lillian Nanney, Dr. Susan Opalenik, Dr. John Wikswo, Dr. Fang Yu, R. Michael Slowey, Nancy Cardwell, Alonda Pollins, and help from Jayasri Dasgupta. Thank you especially to Dr. Davidson, for your tireless explanations of wound healing, invaluable contribution of ideas, and help with interpreting histology.

I especially appreciate all the efforts of the Department of Chemical and Biomolecular Engineering staff, including Rae Uson and Susan Hilderbrand, and especially Mary Gilleran, for all their help and spirited conversations. Thank you to the members of my committee for their insightful criticism and support throughout this process. I cannot begin to express my extreme appreciation and gratitude to my advisor, Dr. Scott Guelcher, for your teaching and research guidance. Thank you for the memorable and positive graduate experience, especially for allowing me to work on projects that I really enjoyed, without having to worry about funding issues. I greatly appreciate all the opportunities to attend and present at national and international conferences, which have been a pivotal aspect of my graduate years.

Finally, thank you to Alex Zider for your feedback and support during these years apart as we pursue our own ambitions.

TABLE OF CONTENTS

Page

LIST OF TABLES

LIST OF FIGURES

LIST OF ABBREVIATIONS

AA	Ascorbic acid
ALP	Alkaline phosphatase
BMP-2	Bone morphogenetic protein-2
CE	Cholesterol esterase
CMC	Carboxymethylcellulose
CXE	Carboxyl esterase
DMA	Dynamic mechanical analysis
DSC	Differential scanning calorimetry
EthAm	Ethanolamine
FTIR	Fourier transform infrared spectroscopy
GPC	Gas permeation chromatography
HA	Hyaluronic acid
HDIt	Hexamethylene diisocyanate trimer
HPLC	High performance liquid chromatography
L	Lipase
LDI	Lysine methyl ester diisocyanate
LTI	Lysine methyl ester triisocyanate
LTI-PEG	Prepolymer of LTI and 200-MW PEG
LV	Lovastatin
M_n	Number-average molecular weight
M_w	Weight-average molecular weight

OH No.	Hydroxyl number
PDGF	Platelet-derived growth factor
PDI	Polydispersity index
PEG	Poly(ethylene glycol)
PPF	Poly(propylene fumarate)
PUR	Polyurethane, specifically poly(ester urea)urethane
ROI	Reactive oxygen intermediates
SEM	Scanning electron microscopy
T_g	Glass transition temperature
TGA	Thermal gravimetric analysis
900	900-MW trifunctional polyol of 60/30/10 ε-caprolactone/glycolide/lactide
1800	1800-MW trifunctional polyol of 60/30/10 ε-caprolactone/glycolide/lactide

CHAPTER I

INTRODUCTION

Limited availability of autograft tissue for wound healing has established the demand for improved synthetic biomaterials. The human wound repair response transitions from fetal regeneration to inflammation and scarring after birth, so recreating this regenerative response is a major goal of biomaterials [1]. Such materials would preferably undergo controlled degradation, at a rate comparable to new tissue formation. Concurrent delivery of biologically active small molecules and growth factors delivered may enhance or accelerate healing. Research is ongoing around the world to achieve regeneration of various tissues, from bone and cartilage to internal organs. Perhaps the future can bring the development of composite scaffolds for simultaneous repair of multiple tissue types. These studies focus specifically on repair of bone defects from trauma, osteoporosis, and osteolytic bone tumors, as well as large dermal burns and chronic wounds.

A successful biomaterial and its degradation products must be biocompatible and non-cytotoxic, generating a minimal immune response. High porosity and inter-connected pores facilitate the permeation of nutrients and cells into the scaffold, as well as ingrowth of new tissue. Scaffolds should undergo degradation to non-cytotoxic decomposition products concurrently with new tissue formation. Materials that exhibit gel times of 5 – 10 minutes and low temperature exotherms are particularly suitable for clinical use as injectable therapies that can be

administered percutaneously using minimally invasive surgical techniques. Additionally, scaffolds should possess sufficient biomechanical strength to withstand physiologically relevant forces. Release of growth factors with fibrogenic, angiogenic, and osteogenic properties, such as platelet-derived growth factor, vascular endothelial growth factor and bone morphogenetic protein-2, may further enhance integration of the device and improved healing.

Bone fracture healing

Due to the high frequency of bone fractures, resulting in over 900,000 hospitalizations and 200,000 bone grafts each year in the United States, there is a compelling clinical need for improved fracture healing therapies [2, 3]. Fractures can result from trauma or pathologic conditions, such as osteoporotic compression fractures and osteolytic bone tumors, which is especially a concern amid the aging population. Autologous bone grafts are an ideal treatment due to their osteogenic, osteoinductive, and osteoconductive properties, but they are available in limited quantities and frequently result in donor site morbidity. Both synthetic and biological biomaterials have been investigated as substitutes for autologous bone grafts, and a number of desirable properties have been identified for biomaterials designed for orthopedic applications [4]. The past decade has seen significant advances in the range of synthetic and biological materials available for bone repair [5]. The materials described here are intended for applications known as bone void fillers. They do not approach the compressive mechanical properties of native bone, which is on the order of hundreds of MPa for the compressive modulus or stiffness.

These target non-load bearing wound sites that can be fixed externally until healing is complete, which allows the use of highly porous materials that facilitate cellular ingrowth. Load-bearing sites benefit from much stronger, but also less porous, bone cements.

Due to their ability to meet many of the above-mentioned performance characteristics, both synthetic and biopolymers have been investigated as scaffolds for tissue engineering. The poly(α-esters), including poly(D,L-lactic acid), poly(glycolic acid), and their copolymers, are thermoplastic polymers incorporated in a variety of FDA-approved biomedical devices, including surgical sutures, orthopedic fixation, and drug and growth factor delivery [6]. Scaffolds prepared from other thermoplastic biomaterials, such as tyrosine-derived polycarbonates and polyphosphazenes, have been shown to exhibit tunable degradation to non-cytotoxic decomposition products, high tensile strength, and bone tissue ingrowth *in vivo* [7-9]. However, thermoplastic biomaterials cannot be injected, and must be melt- or solvent-processed *ex vivo* to yield solid scaffolds prior to implantation. Injectable hydrogels, such as poly(ethylene glycol), collagen, fibrin, chitosan, alginate, and hyaluronan, have been shown to support bone ingrowth *in vivo*, particularly when combined with angiogenic and osteogenic growth factors, but they lack the robust mechanical properties of thermoplastic polymers [10-16].

Two-component reactive polymers are promising because they can be formed *in situ* without the use of solvents. Poly(propylene fumarate) (PPF) can be injected as a liquid and thermally or photo cross-linked with various cross-linking agents for bone void applications [17]. Semi-porous composite scaffolds have been

developed recently by gas foaming *in situ*, with up to 61% porosity, 50-500 μm pores, and a compressive modulus of 20 – 40 MPa [18]. PPF biomaterials have been shown to support osteoblast attachment and proliferation *in vitro*, and ingrowth of new bone tissue *in vivo* [19-22]. Growth factors have been incorporated via PLGA microspheres into PPF materials for controlled release [23].

Dermal wound healing

Skin is the largest organ of the body, yet its complexity and heterogeneity render it challenging to regenerate, especially because of the importance of aesthetics as well as restored function. Burns cause at least 45,000 hospitalizations and 4500 deaths annually in the US. Non-healing, chronic wounds (ulcers) introduce a greater economic impact, affecting more than two million people in the US at over $1 billion health care costs annually [24]. As with bone repair, the gold standard remains autografts, which are split-thickness grafts taken from another part of the patient's body. However, these are clearly limited in supply, especially for patients with large burn wounds, and painful at the harvest site. Allograft skin is also limited in supply, and xenografts (usually porcine) do not engender permanent revascularization. At this time, there are no engineered skin substitutes that can completely duplicate the complexity of human skin, which leaves open the impetus for research to design better skin substitutes for dermal wound healing.

Current dermal substitutes are mostly derived from natural sources, and categorized as cellular or acellular, such as collagen, hyaluronan, fibrin, fibronectin, chitosan, alginate, and glycosaminoglycans [24-26]. Engineered cellular skin

substitutes contain autologous or allogeneic cells combined with scaffolds made from natural extracellular matrix (ECM) components. It can be advantageous to culture autologous keratinocytes or fibroblasts on these scaffolds before implantation, but this procedure requires three weeks or more to complete. Examples of commercially available skin substitutes, both cellular and acellular, are provided in Table 1.1. These naturally derived skin substitutes successfully stabilize damaged skin with protection from dehydration and infection, but nevertheless heal by contraction and scarring. As thin sheets, they lack sufficient mechanical strength to mimic native skin or stand alone as end-point therapies. Thus many are temporary dressings until an epidermal autograft can be applied. The resulting wound healing lacks proper architectural and biomechanical properties, in addition to functional skin appendages such as hair follicles and sebaceous glands [24].

Synthetic biomaterials can also be used for skin and soft tissue repair, although current options produce poor matrix remodeling. Some materials include poly(lactic-co-glycolic acid), polycaprolactone, polyurethanes, and poly(ethylene oxide)-based hydrogels. These are often combined with natural ECM components to facilitate cell ingrowth and granulation tissue formation. A promising wound healing response with these porous polyurethane scaffolds has the capacity to greatly impact the field of dermal repair if successful. A full regenerative response would be ideal, so restoration of proper connective tissue architecture, biomechanical properties, hair follicles, sweat glands, and sebaceous glands is a central goal of recent studies [27, 28].

Table 1.1. Commercially available skin substitutes [24, 25].

Product	Manufacturer	Components
Acellular		
Integra	Integra Life Sciences (Plainsboro, NJ)	Bovine collagen & silicone
Biobrane	Bertek Pharmaceuticals (Morgantown, WV)	Silicone & nylon
Alloderm	LifeCell Corporation (Branchburg, NJ)	Allogeneic dermis with cells removed
Cellular (allogeneic)		
Apligraf	Novartis (Canton, MA)	Bovine collagen & neonatal fibroblasts & keratinocytes
Dermagraft	Smith & Nephew (Largo, FL)	Polyglactin & neonatal fibroblasts
TransCyte	Smith & Nephew (Largo, FL)	Nylon & neonatal fibroblasts
OrCel	Forticell Bioscience (New York, NY)	Bovine collagen sponge with keratinocytes & fibroblasts
Hyalograft	Fidia Advanced Biopolymers (Padua, Italy)	Benzyl hyaluronate & keratinocytes
Cellular (autologous)		
Epicel	Genzyme (Cambridge, MA)	Autologous keratinocytes on petrolatum gauze
Epidex	Modex Therapeutiques (Lausanne, Switzerland)	Autologous keratinocytes on silicone membrane
Bioseed	BioTissue Technologies (Freiburg, Germany)	Autologous keratinocytes in fibrin sealant
Myskin	CellTran Limited (Sheffield, UK)	Autologous keratinocytes on silicone

Biodegradable polyurethanes

Biodegradable polyurethanes present a favorable biomaterial platform because of their wide range of physical, mechanical, and biological properties that can be achieved depending on the specific constituents. Polyurethane (PUR) scaffolds have been investigated for use in several areas in tissue engineering, including skin [29-31], cardiovasculature [32, 33], and bone [34, 35]. These scaffolds supported cellular infiltration and promotion of tissue repair, as well as degradation to non-toxic products [29, 32, 36-38]. Like other biomaterials, polyurethanes have been utilized in the controlled release and localized delivery of small molecule drugs and growth factors to accelerate tissue repair, including basic fibroblast growth factor (bFGF) [39], platelet-derived growth factor (PDGF) [30, 31] and bone morphogenetic protein-2 (BMP-2) [40].

Polyurethanes can range from cast film elastomers to rigid or flexible foams and can be synthesized by reactive liquid molding to allow for injectability [41]. Nucleophilic reaction of isocyanates with hydroxyl groups result in urethane linkages and reaction with amine groups forms urea linkages. Water can also react with isocyanates to form an unstable carbamic acid intermediate, which reacts with another isocyanate to form a urea and carbon dioxide gas. This carbon dioxide byproduct acts as a blowing agent for polyurethane foams. Aromatic or aliphatic polyisocyanates are generally combined with viscous polyester or polyether polyols, which can be combined to control the hydrophobicity or hydrophilicity of the products. These result in segmented elastomers, which can be microphase-separated due to polarity differences between the alternating hard (nonpolar) and

soft (polar) segments. The materials become harder and less elastic with increased hard segment length, while the polyol molecular weight dictates the soft segment length and degradation rate. Degradation is suggested to occur by ester linkage hydrolysis, yielding α-hydroxy acids and urethane or urea fragments.

In this work, poly(ester urea)urethanes (PUR) were synthesized from trifunctional aliphatic isocyanates, which are generally less toxic than their aromatic counterparts, with trifunctional polyester polyols comprised of the α-hydroxy acids glycolide, lactide, and caprolactone. Scaffold synthesis involves a gelling reaction to form the polyurethane network and a foaming reaction to produce carbon dioxide, which creates pores within the foam. Additives, such as catalysts, surfactant stabilizers, and pore openers, control the balance of these simultaneous reactions to achieve the desired scaffold properties and pore morphology.

This study focuses on the novel development of injectable, biodegradable polyurethane scaffolds that provide both delivery vehicles for bioactive small molecules and a template for infiltration of new cells and tissue. Their highly resilient and elastomeric mechanical properties could allow the scaffolds to adapt to irregular defects, promote intimate contact between the material and surrounding tissue, and help keep the material in place when subjected to physiologically relevant strains. Local, sustained delivery of antibiotics and drugs can improve their efficacy over systemic or repeated dosages. The versatility of this system enhances its potential for other uses, either with other stimulatory components, or for other applications such as soft tissue or craniofacial reconstruction.

References

1. Ferguson MW, Whitby DJ, Shah MMB, Armstrong J, Siebert JW, Longaker MT. Scar formation: The spectral nature of fetal and adult wound repair. *Plastic & Reconstructive Surgery* 1996; 97(4): 854-860.

2. Yuan H, Yang Z, Li Y, Zhang X, De Bruijn JD, De Groot K. Osteoinduction by calcium phosphate biomaterials. *Journal of Materials Science: Materials in Medicine* 1998; 9(12): 723-726.

3. American academy of orthopaedic surgeons website (www.aaos.org).

4. Temenoff JS, Mikos AG. Injectable biodegradable materials for orthopedic tissue engineering. *Biomaterials* 2000; 21(23): 2405-2412.

5. Giannoudis PV, Dinopoulos H, Tsiridis E. Bone substitutes: An update. *Injury* 2005; 36 Suppl 3: S20-27.

6. Gunatillake P, Mayadunne R, Adhikari R, El-Gewely MR. Recent developments in biodegradable synthetic polymers. Biotechnology annual review: Elsevier, 2006. p. 301-347.

7. Bourke SL, Kohn J. Polymers derived from the amino acid -tyrosine: Polycarbonates, polyarylates and copolymers with poly(ethylene glycol). *Advanced Drug Delivery Reviews* 2003; 55(4): 447-466.

8. Ertel SI, Kohn J. Evaluation of a series of tyrosine-derived polycarbonates as degradable biomaterials. *Journal of Biomedical Materials Research* 1994; 28(8): 919-930.

9. Yu C, Kohn J. Tyrosine-peg-derived poly(ether carbonate)s as new biomaterials: Part i: Synthesis and evaluation. *Biomaterials* 1999; 20(3): 253-264.

10. Chen RR, Mooney DJ. Polymeric growth factor delivery strategies for tissue engineering. *Pharmaceutical Research* 2003; 20(8): 1103-1112.

11. Augst AD, Kong H-J, Mooney DJ. Alginate hydrogels as biomaterials. *Macromolecular Bioscience* 2006; 6(8): 623-633.

12. Labhasetwar V, Bonadio J, Goldstein S, Chen W, Levy RJ. A DNA controlled-release coating for gene transfer: Transfection in skeletal and cardiac muscle. *Journal of Pharmaceutical Sciences* 1998; 87(11): 1347-1350.

13. Kipshidze N, Chawla P, Keelan MH. Fibrin meshwork as a carrier for delivery of angiogenic growth factors in patients with ischemic limb. *Mayo Clinic Proceedings* 1999; 74(8): 847-848.

14. Mizuno K, Yamamura K, Yano K, Osada T, Saeki S, Takimoto N, et al. Effect of chitosan film containing basic fibroblast growth factor on wound healing in genetically diabetic mice. *Journal of Biomedical Materials Research Part A* 2003; 64A(1): 177-181.

15. Simmons CA, Alsberg E, Hsiong S, Kim WJ, Mooney DJ. Dual growth factor delivery and controlled scaffold degradation enhance in vivo bone formation by transplanted bone marrow stromal cells. *Bone* 2004; 35(2): 562-569.

16. Zawko SA, Truong Q, Schmidt CE. Drug-binding hydrogels of hyaluronic acid functionalized with β-cyclodextrin. *Journal of Biomedical Materials Research Part A* 2008; 87(4): 1044-1052.

17. Timmer MD, Ambrose CG, Mikos AG. Evaluation of thermal- and photo-crosslinked biodegradable poly(propylene fumarate)-based networks. *Journal of Biomedical Materials Research Part A* 2003; 66A(4): 811-818.

18. Kim CW, Talac R, Lu L, Moore MJ, Currier BL, Yaszemski MJ. Characterization of porous injectable poly(propylene fumarate)-based bone graft substitute. *Journal of Biomedical Materials Research Part A* 2008; 85(4): 1114-1119.

19. Fisher JP, Vehof JWM, Dean D, van der Waerden JP, Holland TA, Mikos AG, et al. Soft and hard tissue response to photocrosslinked poly(propylene fumarate) scaffolds in a rabbit model. *Journal of Biomedical Materials Research* 2002; 59(3): 547-556.

20. Peter SJ, Lu L, Kim DJ, Mikos AG. Marrow stromal osteoblast function on a poly(propylene fumarate)/[beta]-tricalcium phosphate biodegradable orthopaedic composite. *Biomaterials* 2000; 21(12): 1207-1213.

21. Peter SJ, Miller ST, Zhu G, Yasko AW, Mikos AG. *In vivo* degradation of a poly(propylene fumarate)/β-tricalcium phosphate injectable composite scaffold. *Journal of Biomedical Materials Research* 1998; 41(1): 1-7.

22. Yaszemski MJ, Payne RG, Hayes WC, Langer RS, Aufdemorte TB, Mikos AG. The ingrowth of new bone tissue and initial mechanical properties of a degrading polymeric composite scaffold. *Tissue Engineering* 1995; 1(1): 41-52.

23. Kempen DHR, Lu L, Kim C, Zhu X, Dhert WJA, Curreir BL, et al. Controlled drug release from a novel injectable biodegradable microsphere/scaffold composite based on poly(propylene fumarate). *Journal of Biomedical Materials Research, Part A* 2006; 77A(1): 103-111.

24. Supp DM, Boyce ST. Engineered skin substitutes: Practices and potentials. *Clinics in Dermatology* 2005; 23(4): 403-412.

25. Boateng JS, Matthews KH, Stevens HNE, Eccleston GM. Wound healing dressings and drug delivery systems: A review. *Journal of Pharmaceutical Sciences* 2008; 97(8): 2892-2923.

26. Metcalfe AD, Ferguson MWJ. Bioengineering skin using mechanisms of regeneration and repair. *Biomaterials* 2007; 28(34): 5100-5113.

27. Adolphe C, Wainwright B. Pathways to improving skin regeneration. *Expert Reviews in Molecular Medicine* 2005; 7(20): 1-14.

28. Metcalfe AD, Ferguson MW. Harnessing wound healing and regeneration for tissue engineering. *Biochemical Society Transactions* 2005; 33(2): 413-317.

29. Zhang JY, Beckman EJ, Hu J, Yang GG, Agarwal S, Hollinger JO. Synthesis, biodegradability, and biocompatibility of lysine diisocyanate-glucose polymers. *Tissue Eng* 2002; 8(5): 771-785.

30. Li B, Davidson JM, Guelcher SA. The effect of the local delivery of platelet-derived growth factor from reactive two-component polyurethane scaffolds on the healing in rat skin excisional wounds. *Biomaterials* 2009; 30(20): 3486-3494.

31. Hafeman AE, Li B, Yoshii T, Zienkiewicz K, Davidson JM, Guelcher SA. Injectable biodegradable polyurethane scaffolds with release of platelet-derived growth factor for tissue repair and regeneration. *Pharm Res* 2008; 25(10): 2387-2399.

32. Guan J, Sacks MS, Beckman EJ, Wagner WR. Synthesis, characterization, and cytocompatibility of elastomeric, biodegradable poly(ester-urethane)ureas based on poly(caprolactone) and putrescine. *J Biomed Mater Res* 2002; 61(3): 493-503.

33. Fujimoto KL, Guan J, Oshima H, Sakai T, Wagner WR. In vivo evaluation of a porous, elastic, biodegradable patch for reconstructive cardiac procedures. *Ann Thorac Surg* 2007; 83(2): 648-654.

34. Gorna K, Gogolewski S. Preparation, degradation, and calcification of biodegradable polyurethane foams for bone graft substitutes. *J Biomed Mater Res A* 2003; 67(3): 813-827.

35. Adhikari R, Gunatillake PA, Griffiths I, Tatai L, Wickramaratna M, Houshyar S, et al. Biodegradable injectable polyurethanes: Synthesis and evaluation for orthopaedic applications. *Biomaterials* 2008; 29(28): 3762-3770.

36. Guelcher SA, Patel V, Gallagher KM, Connolly S, Didier JE, Doctor JS, et al. Synthesis and in vitro biocompatibility of injectable polyurethane foam scaffolds. *Tissue Eng* 2006; 12(5): 1247-1259.

37. Guelcher S, Srinivasan A, Hafeman A, Gallagher K, Doctor J, Khetan S, et al. Synthesis, in vitro degradation, and mechanical properties of two-component poly(ester urethane)urea scaffolds: Effects of water and polyol composition. *Tissue Eng* 2007; 13(9): 2321-2333.

38. Guelcher SA. Biodegradable polyurethanes: Synthesis and applications in regenerative medicine. *Tissue Eng Part B Rev* 2008; 14(1): 3-17.

39. Guan J, Stankus JJ, Wagner WR. Biodegradable elastomeric scaffolds with basic fibroblast growth factor release. *J Control Release* 2007; 120(1-2): 70-78.

40. Goldstrohm GL, Mears DC, Swartz WM. The results of 39 fractures complicated by major segmental bone loss and/or leg length discrepancy. *J Trauma* 1984; 24(1): 50-58.

41. Oertel G. Polyurethane handbook. 2 ed. Berlin: Hanser Gardner Publications, 1994.

CHAPTER II

DESIGN AND DEVELOPMENT OF POLY(ESTER URETHANE)UREA SCAFFOLD IMPLANTS FOR TARGETETED PHYSICAL AND BIOLOGICAL PROPERTIES

Introduction

Two-component biodegradable polyurethane (PUR) networks have also been investigated as scaffolds for tissue engineering. Porous PUR scaffolds prepared from lysine-derived and aliphatic polyisocyanates by reactive liquid molding have been reported to degrade to non-toxic decomposition products, while supporting the migration of cells and ingrowth of new tissue *in vitro* and *in vivo* [1-4]. Crosslinked scaffolds with varying hydrophilicity were synthesized by prepolymer formation and chain extension from hexamethylene diisocyanate (HDI), poly(ε-caprolactone), poly(ethylene oxide) (600 g/mol), and amine-and sucrose-based polyols, followed by gas foaming [5, 6]. These materials exhibited successful osseointegration and formation of new cancellous bone in both healthy and estrogen-deficient sheep. Gas foaming of a glycerol-LDI prepolymer with either glucose or ascorbic acid produced scaffolds that supported proliferation and attachment of bone marrow stromal cells, as well as differentiation of osteoblast precursor cells [4, 7-9]. Chain extension of prepolymers, consisting of poly(ε-caprolactone), poly(ethylene oxide) (600 and 1000 g/mol), and 1,4-diisocyanobutane (BDI), was followed by thermally induced phase separation and solvent evaporation to construct porous scaffolds [5, 6]. These materials supported

adhesion and proliferation of human umbilical vein endothelial cells and smooth muscle cells *in vitro*. In adult rats, fibroblast ingrowth and endocardial endothelialization with minimal inflammation was observed when the materials were implanted into ventricular defects, and smooth muscle tissue formation with proper contractile function and cardiac remodeling when implanted onto a subacute myocardial infarction [7, 8].

The studies preceding this work improved upon the synthesis method of flexible, porous polyurethane scaffolds for tissue engineering. Many polyisocyanates typically used for polyurethane biomaterials are toxic by inhalation because they have high vapor pressures at room temperature, such as toluene diisocyanate (TDI, 0.018 mm Hg) and hexamethylene diisocyanate (HDI, 0.05 mm Hg). This toxicity precludes them from use by injection in a clinical environment, and prepolymers must be synthesized first by capping a polyol with the polyisocyanate.

To overcome this limitation, injectable poly(ester urea urethane) (PUR) biomaterials were formulated using lysine diisocyanate (LDI), a lysine-derived polyisocyanate with a vapor pressure substantially less than that of HDI [3, 4, 9]. These scaffolds could be synthesized without the prepolymer step by one-shot, reactive liquid mixing of the LDI with a resin that contained the polyester triol, water, triethylene diamine catalyst, sulfated castor oil stabilizer, and calcium stearate pore opener. Because of the incompatibility of the polyisocyanate and polyester polyol phases, stabilizers and pore openers must be added to promote the miscibility of the two phases and stabilize the rising bubbles in the foam [10, 11].

The one-shot foam synthesis becomes a balance between the gelling reaction to establish the polyurethane networks, and the foaming reaction to create the porous structure.

The one-shot LDI scaffolds were shown to support cell migration and proliferation *in vitro*, as well as biodegrade to non-cytotoxic decomposition products [3, 10]. However, they had very poor resilience when pressure was applied in any way. The absence of hydrogen-bonded urethane carbonyl peaks in the IR spectra implies that LDI scaffolds lack the physical crosslinks reported for commercial PUR foams manufactured from aromatic polyisocyanates [3, 11]. The two-component polyurethanes prepared from LDI exhibit microphase-mixed behavior, which inhibits the formation of hydrogen bonds between hard segments in adjacent chains and may adversely affect mechanical properties [3]. Therefore, by increasing the chemical crosslink density, trifunctional isocyanates are anticipated to yield microphase-mixed PUR scaffolds with improved mechanical properties and resilience.

Lysine triisocyanate (LTI) is a lysine-derived polyisocyanate with a vapor pressure of 7.5×10^{-4} mm Hg at 25 °C, while Desmodur N3300A is a hexamethylene diisocyanate trimer (HDIt) with a vapor pressure of 5.2×10^{-9} mm Hg at 20 °C [12]. Porous scaffolds were synthesized by a one-shot foaming process, allowing for time to manipulate and inject the polymer, followed by rapid foaming and setting. In this study, the effects of the triisocyanate on biocompatibility, degradation, and mechanical properties were investigated.

Methods

Materials. Glycolide and D,L-lactide were obtained from Polysciences (Warrington, PA), tertiary amine catalyst (TEGOAMIN33) from Goldschmidt (Hopewell, VA), polyethylene glycol (PEG, MW 600 Da) from Alfa Aesar (Ward Hill, MA), and glucose from Acros Organics (Morris Plains, NJ). Lysine triisocyanate (LTI) was purchased from Kyowa Hakko USA (New York), and hexamethylene diisocyanate trimer (HDIt, Desmodur N3300A) was received as a gift from Bayer Material Science (Pittsburgh, PA). Reagents for cell culture were all purchased from HyClone (Logan, UT). All other reagents were purchased from Sigma-Aldrich (St. Louis, MO). Prior to use, glycerol and PEG were dried at 10 mm Hg for 3 hours at 80 °C, and ε-caprolactone was dried over anhydrous magnesium sulfate, while all other materials were used as received [9].

Polyurethane (PUR) scaffold synthesis. Trifunctional polyester polyols of 900-Da and 1800-Da molecular weight (abbreviated as 900 and 1800) were synthesized by ring-opening polymerization of cyclic hydroxy acid (mono- and di-) esters. The reaction schematic is displayed in Figure 2.1. They were prepared from a mixture of glycerol starter (MW 92) at 10 wt-% of the total polyol mass, and ε-caprolactone, glycolide, and D,L-lactide monomers at ratios of 60/30/10 (6C3G1L) or 70/20/10 (7C2G1L) [3, 10, 13]. These components were mixed with stannous octoate catalyst in a 100-mL three-neck reaction flask with mechanical stirring under argon for 36 hours at 140 °C. The polyols were then dried under vacuum at 80 °C for 14 hours.

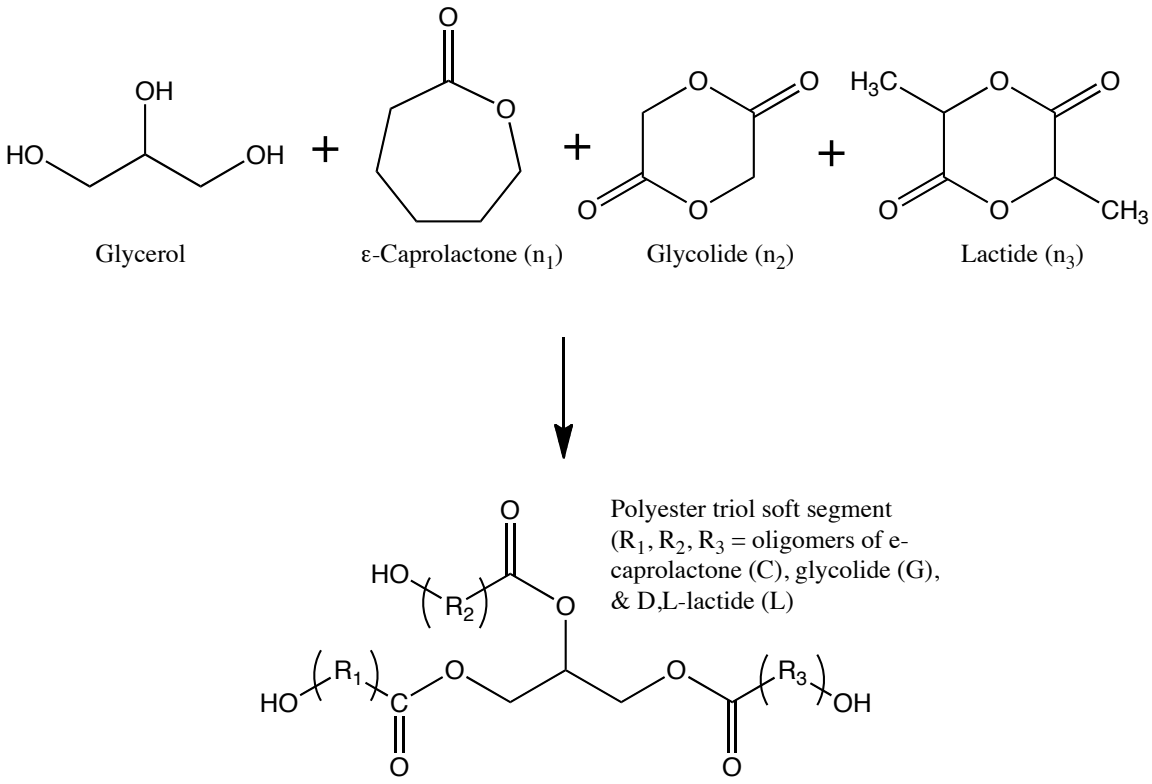

Figure 2.1. Polyester polyol synthesis from cyclic hydroxy acid esters by ring opening polymerization.

The polyester triol molecular weights were assessed by gel permeation chromatography (GPC) equipped with a 1525 binary LC pump, 2414 Refractive Index Detector, and a column temperature stabilizer, all part of a Water's Breeze® System (Milford, MA). The triols (0.5 g) were dissolved to 2 mL 0.5% in tetrahydrofuran (THF) and separated in two sequential 30 cm x 7.5 mm Mesopore columns (Polymer Laboratories, Amherst, MA) at 1.0 mL/min and 35 °C. Stabilized THF was used as an eluent and a trace of toluene was added to the sample as an internal standard. Triol molecular weights were calibrated to polystyrene standards. Triols were dissolved in deuterated chloroform and analyzed by solution-phase nuclear magnetic resonance (NMR), using a Bruker 300 MHz DPX-

300 FT-NMR Spectrometer (Billerica, MA), to verify the extent of reaction and chemical structure of the polyols. The spectra were analyzed using TOPSPIN software.

The theoretical hydroxyl (OH) numbers, calculated from the number-average molecular weight (M_n) and functionality (f) of the triols (f = 3), were used to formulate the PUR foams assuming complete conversion of the triol monomers.

$$\text{OH No.} = \frac{\left(56.1 \times 10^3\right) f}{M_n} \tag{2.1}$$

The actual hydroxyl numbers of the triols were measured according to an ASTM NCO titration method; the corresponding OH titration method was inaccurate due to side reactions [14]. The titrations and calculations for %NCO and OH numbers were performed as described previously [3].

The PUR scaffolds were synthesized by one-shot reactive liquid molding of an aliphatic triisocyanate, either hexamethylene diisocyanate trimer (HDIt; Desmodur N3300A) or lysine triisocyanate (LTI), with a hardener [3, 10]. The polyurethane gelling and blowing reactions are illustrated in Figure 2.2.

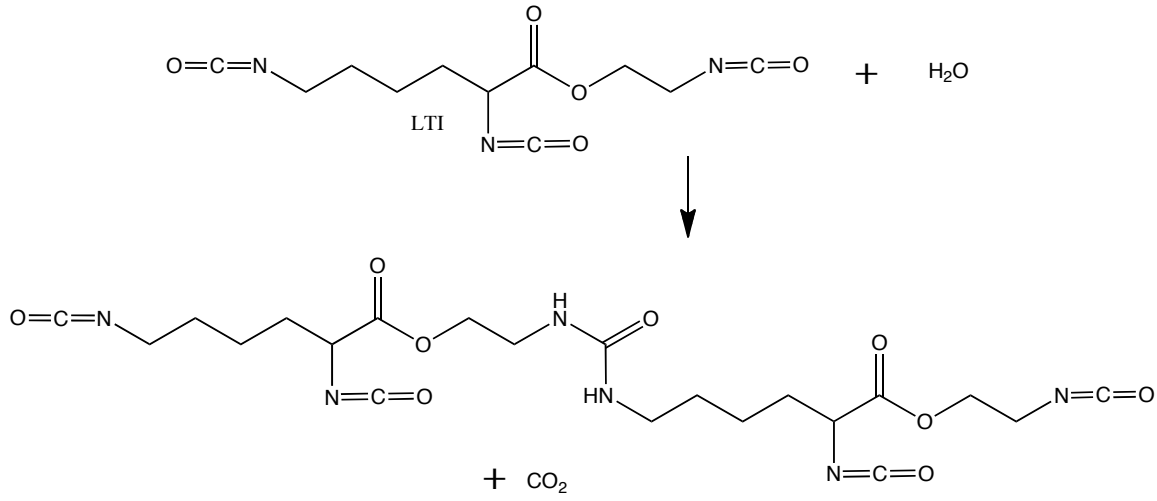

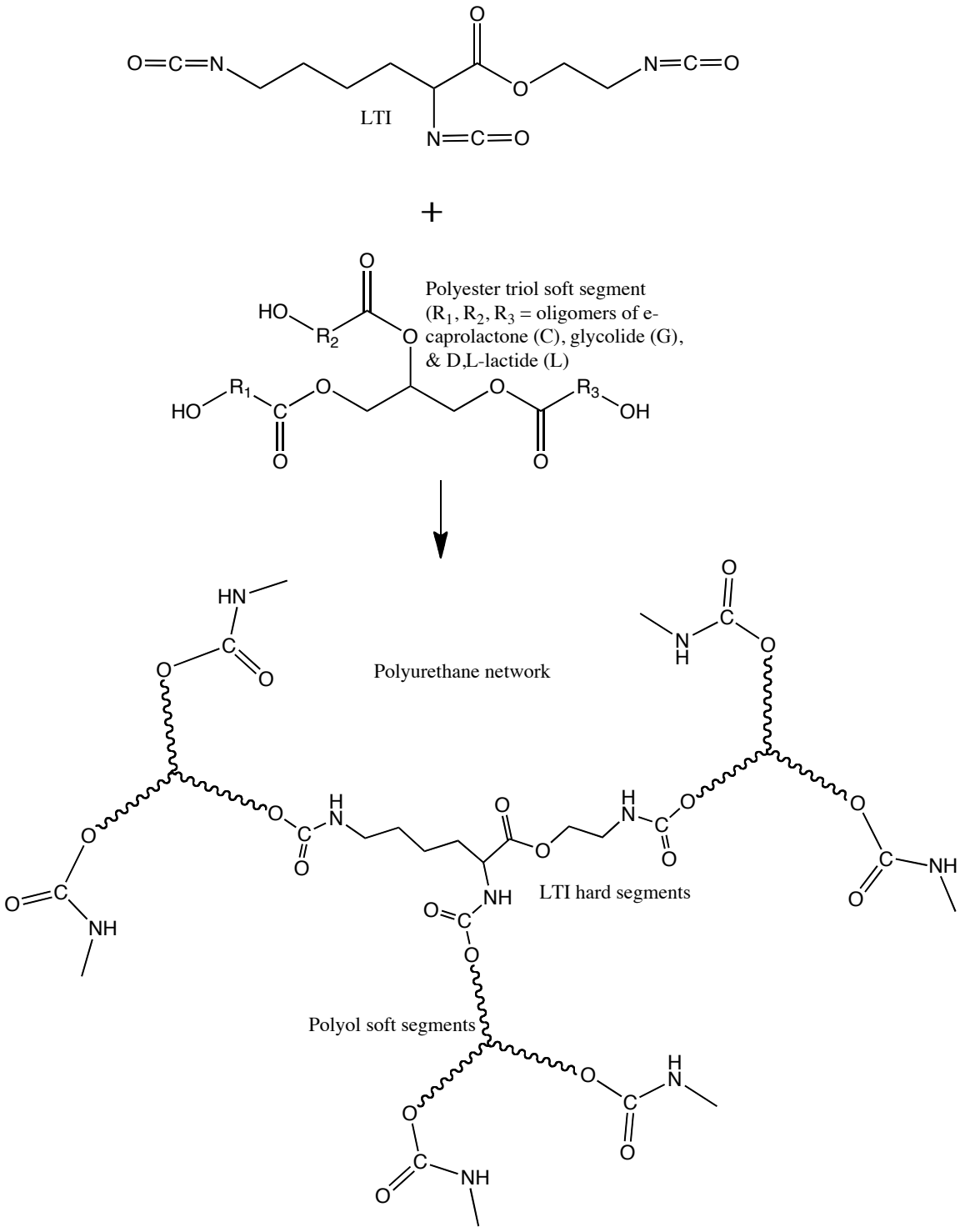

Figure 2.2. Blowing (top) and gelling (bottom) reactions involved in one-shot porous polyurethane scaffold synthesis.

Scaffolds were initially made with lysine diisocyanate (LDI), but subsequently with the triisocyanates for improved resilience and mechanical properties, as described below. The hardener contained the polyol, 1.5 parts per hundred parts polyol (pphp) water, 4.5 pphp TEGOAMIN33 tertiary amine catalyst (1.5 pphp for LTI foams), 1.5 pphp sulfated castor oil stabilizer, 4.0 pphp calcium stearate pore opener. The isocyanate was added to the hardener and mixed for 15 seconds in a Hauschild SpeedMixer™ DAC 150 FVZ-K vortex mixer (FlackTek, Inc., Landrum, SC). The targeted index was 115, as calculated below (Equations 2.2 and 2.3), where I and P represent the isocyanate and polyol components, q is the number of equivalents, m and w are the mass and equivalent weight of each component.

$$\text{NCO}:\text{OH ratio} = \frac{q_{NCO,I}}{q_{OH,P}} = \frac{m_I / w_I}{m_P / w_P} \tag{2.2}$$

$$\text{Index} = \left(\frac{q_{NCO,I}}{q_{OH,P}} \right) \times 100 \tag{2.3}$$

The resulting reactive liquid mixture then rose freely for 10 – 20 minutes [3, 10]. To examine the effects of a hydrophilic polyether segment on the material properties, some materials were synthesized with poly(ethylene glycol) (PEG, 600 Da) in the hardener, such that the total polyol content consisted of 30 or 50 mol-% PEG and 70 or 50 mol-% of the polyester polyol. Temperature profiles of the reactive mixture during foaming were assessed in triplicate with a digital thermocouple at the centers of the rising foams. Batch sizes (3-g) were large enough to diminish the effects of heat loss from the exterior surfaces of the foam.

PUR scaffold characterization. Core densities were determined from mass and volume measurements of triplicate cylindrical foam cores, of 7 mm diameter x 10 mm height samples, at least 24 hours after foam synthesis to ensure full curing and drying [15]. The core porosities (ε_C) were calculated in Equation 2.4 from the density values (ρ_C), where ρ_P = 1200 kg/m^3 is the polyurethane specific gravity and ρ_A = 1.29 kg/m^3 is the specific gravity of air [3].

$$\varepsilon_C = 1 - \frac{\rho_C - \rho_A}{\rho_P - \rho_A} \tag{2.4}$$

The pore size and distribution were also assessed by scanning electron microscopy (Hitachi S-4200 SEM, Finchampstead, UK).

The water uptake in a polymer is indicative of its hydrophobicity or hydrophilicity. This water absorbance, or % swelling, of the PUR scaffolds was measured after incubation of samples in water for 24 hours. The samples were weighed before incubation, and dabbed briefly with a tissue to remove excess water before weighing after incubation. The % swelling was calculated by the change in change in scaffold weight when dry (w_{dry}) vs. wet (w_{wet}).

$$\%\ \text{swelling} = \frac{\left(w_{wet} - w_{dry}\right)}{w_{dry}} \times 100 \tag{2.5}$$

Compression set, or permanent deformation, of the scaffolds was determined using a TA Instruments Q800 Dynamic Mechanical Analyzer (DMA, New Castle, DE) in static compression mode. After measuring their initial heights, triplicate 7 mm diameter cylindrical foam cores were compressed to 50% strain (i.e., 50% of their initial height) for 24 hours at room temperature according to ASTM standards [15].

The samples were allowed to recover for 30 minutes, and then their final heights were measured. Compression set was calculated as the permanent deformation after the period of compressive stress, expressed as a percentage of the original height.

Scaffold degradation rates *in vitro* were evaluated by measuring the mass loss at various time points up to 36 weeks of incubation of triplicate 10-mg samples in 1 mL phosphate buffered saline (PBS) (pH 7.4) at 37 °C. At each time point, the samples were rinsed in deionized water, dried under vacuum for 48 hours at room temperature, and weighed. The degradation media from 4 and 8 weeks were reserved for *in vitro* cell viability experiments.

Thermal analysis. Thermal decomposition of the materials was ascertained by thermal gravimetric analysis (TGA). Samples (3 to 6 mg) were heated from 25 °C to 600 °C at 20 °C/min in an Instrument Specialist TGA 1000.

Thermal transitions of the materials were evaluated by differential scanning calorimetry (DSC) using a Thermal Analysis Q1000 Differential Scanning Calorimeter. 10-mg samples underwent two cycles of cooling (20 °C/min) and heating (10 °C/min), between -80 °C and 100 °C.

Dynamic mechanical properties: Compression. Cylindrical 7 x 6 mm samples were compressed along the axis of foam rise. The temperature-dependent storage modulus and glass transition temperature (T_g) of each material was evaluated with a temperature sweep of -80 °C to 100 °C, at a compression frequency of 1 Hz, 20-μm amplitude, 0.3-% strain, and 0.2-N static force. The relaxation modulus was evaluated as a function of time with stress relaxation under 2-% strain and 0.2-N

static force. The frequency-dependent storage modulus (energy stored elastically) and loss modulus (energy lost due to viscous dissipation) were also evaluated with a 0.1 to 10 Hz frequency sweep at 37 °C, with 0.3-% strain and 0.2-N static force. Stress-strain curves were generated by controlled-force compression of the cylindrical foam cores at 37 °C. With an initial force of 0.1 N, each sample was deformed at 0.1 N/min until it reached 50% strain (i.e., 50% of its initial height). The Young's (elastic) modulus was determined from the slope of the initial linear region of each stress-strain curve [16]. Due to their highly elastic properties, the scaffolds could not be compressed to failure. Therefore, as a measure of compressive strength, the compressive stress of triplicate cylindrical samples after one minute at 50% strain was measured using the DMA stress relaxation mode at 37 °C [15]. Calculated from the measured force and cross-sectional sample area, the compressive stress indicates material compliance such that more compliant materials require lower stress to induce a particular strain.

Dynamic mechanical properties: Tension. Tensile testing was performed on thin, rectangular scaffold samples (10 mm long x 5 mm wide x 1.7 mm thick). Stress-strain curves were generated by elongating the samples at 1% strain per minute at 37 °C until failure, and show the long elongations at sample break. The Young's modulus was calculated as described above, and the tensile strength was determined as the stress (kPa) at failure.

In vitro biocompatibility. MC3T3-E1 embryonic mouse osteoblast precursor cells were statically seeded onto thin foam discs (25 x 1 mm) at 5 x 10^4 cells per well in 24-well tissue-culture polystyrene plates. The cells were cultured with 1 mL α-

minimum essential medium (α-MEM) per well, containing 10% fetal bovine serum, 1% penicillin (100 units/mL) and streptomycin (100 μg/mL). The plates were maintained in a humidified incubator with 5% CO_2 for 5 days, with the medium refreshed after 2 days. The cell-seeded scaffolds were then removed from culture, washed with PBS, and transferred to a new 24-well plate to verify cell adherence to the materials. 4 μM Calcein AM from the Live/Dead Viability/Cytotoxicity Kit for mammalian cells (Invitrogen, Eugene, OR) was added to the samples. Live cells retain Calcein AM dye, imparting green fluorescence (excitation/emission: 485/515 nm). Ethidium homodimer-1 enters dead cells through their damaged membranes and produces red fluorescence (excitation/emission: 525/590 nm) upon binding to nucleic acids. Cell viability was assessed qualitatively by fluorescent images acquired with an Olympus DP71 camera attached to a fluorescent microscope (Olympus CKX41, U-RFLT50, Center Valley, PA).

In addition, PUR degradation products from 4 and 8 weeks were analyzed for cell viability and cytotoxicity. The same MC3T3-E1 cells were seeded at 5 x 10^3 cells per well in a 96-well plate with 90 μL cell culture medium (described above) and 10 μL degradation media or PBS control. After the cells were cultured for 72 hours, the media was removed, the wells were rinsed with fresh PBS, and 2 μM Calcein AM was added to the wells. The percentage of viable cells was quantified by the fluorescence intensity of the samples in comparison to wells that were cultured in media only, with a Biotek (Winooski, VT) fluorescence microplate reader.

In vivo biocompatibility in full-thickness dermal wounds. Biocompatibility of the PUR scaffolds was evaluated in both excisional and subcutaneous dermal

wounds. After polymerization, the materials were cut into 8 x 2 mm discs for *in vivo* implantation to assess biocompatibility and degradation properties. The discs were sterilized for 5 minutes in ethanol prior to dorsal implantation in adult male Sprague-Dawley rats. The excisional wounds were splinted with stainless steel washers and stay sutures for 7 days to prevent wound contraction and thereby allow the normal wound filling and granulation tissue infiltration typical in humans. Semi-occlusive Tegaderm dressing (3M, St. Paul, MN) held the scaffolds in place and protected the wound. Implants were retrieved from euthanized animals at 5, 14, and 21 days post-implantation, fixed in formalin for 24 hours, embedded in paraffin, and processed for histological evaluation with Gomori's trichrome as well as hematoxylin and eosin staining.

In vivo biocompatibility in bone defects. The biocompatibility and osteoconductivity of the PUR scaffolds were evaluated in a rat tibial plug defect model. Cylindrical scaffold cores (6 x 3 mm) were implanted into bilateral tibial defects of athymic Sprague-Dawley rats. After 3 weeks, the samples were harvested and fixed in 10% phosphate-buffered formalin. Undecalicified sections were then stained with toluidine blue. This experiment was conducted as part of a collaborative project at the US Army Institute of Surgical Research.

Statistical Analysis. Statistical analysis of the results was performed using single factor analysis of variance (ANOVA). In cases where statistical significance is cited, the sample size is greater than or equal to three replicates per material.

Results

PUR scaffold characterization. The polyol number-average and weight-average molecular weights, as determined by GPC, are given in Table 2.1. These molecular weights are consistently greater than the target values of 900 and 1800 g/mol, most likely because they are measured relative to the GPC weight standards. A similar trend has been reported previously [17-19]. The NMR spectra of each polyol showed that synthesis had proceeded to completion, with no detectible peaks representing free monomer. Table 2.1 provides the polyol %NCO and OH numbers, as measured by NCO titration, which were used to determine the foam indexes. These measured OH numbers are within 10% (900-MW polyols) and 30% (1800-MW polyol) of the theoretical OH numbers, which were calculated based on the polyol compositions.

Table 2.2. Polyester polyol properties, including number-average molecular weight (M_n), weight-average molecular weight (M_w), and the polydispersity index (PDI).

Polyol	M_n	M_w	PDI	OH # (theor.)	OH # (act.)	T_g (°C)
T6C3G1L900	1422	2031	1.9	186.8	210.4	- 41.7
T6C3G1L1800	3176	4105	1.3	94.4	125.4	- 44.7
T7C2G1L900	1432	2086	1.5	187.1	202.5	- 38.2

The core densities and porosities of the scaffolds were assessed at least 24 hours after foam synthesis to ensure full curing and drying. The scaffold densities ranged from 86 – 98 kg/m^3 and porosities from 92 – 93 vol-% (Table 2.2). The differences between the densities and porosities measured for the materials were not statistically significant ($p > 0.05$). SEM images illustrated that the pores were

almost uniformly spherical, 200 – 500 μm in diameter, and inter-connected by openings in the pore walls (Figure 2.3). Previous studies with LDI scaffolds have shown that MC3T3 cells penetrated up to 5 mm into the interior of the scaffolds after 21 days, suggesting that the pores were inter-connected [3]. Addition of PEG (at 30 and 50 wt-%) had an insignificant effect on the scaffold density and porosity, but SEM showed that the pores were more irregularly shaped and variable in size, reaching 600 μm in diameter. The irregular pore shape and rough surface are thought to result from microphase-separation of the PEG and polyester polyol components [11].

Table 2.3. PUR scaffold physical and thermal properties.

Polyol	Isocyanate	Density (kg/m^3)	Porosity (vol-%)	T_g - DSC (°C)	T_g - DMA (°C)
T6C3G1L900	LTI	88 ± 5	93 ± 0.4	6.4	57
T6C3G1L1800	LTI	86 ± 1	93 ± 0.1	- 16	24
T7C2G1L900	LTI	85 ± 14	93 ± 1	- 5	38
T6C3G1L900	HDIt	98 ± 13	92 ± 1	0.2	40
T6C3G1L1800	HDIt	93 ± 8	92 ± 0.6	- 21	28
T6C3G1L900 + 30% PEG	HDIt	90 ± 3	93 ± 0.2	- 10	24
T6C3G1L900 + 50% PEG	HDIt	94 ± 11	92 ± 1	- 31	19

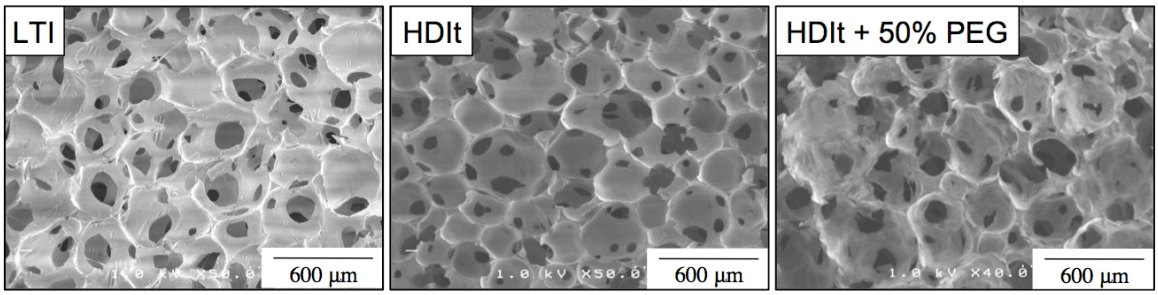

Figure 2.3. SEM images of foams made with the 6C3G1L900 triol suggest interconnected pore structures with mostly uniform pore sizes of 200-500 µm.

The LTI (4.7 ± 0.3%), HDIt (2.2 ± 0.5%), and HDIt + 50% PEG (2.5 ± 0.5%) materials exhibited minimal permanent deformation after being subjected to a 50% compressive strain for 24 hours (Figure 2.4). In contrast, materials synthesized from lysine methyl diisocyanate (LDI) displayed a substantially higher compression set, with statistically significant differences ($p < 0.005$) [3]. Thus the PUR scaffolds synthesized from triisocyanates were more resilient than those prepared from diisocyanates. The favorable mechanical properties of segmented polyurethane elastomers and foams traditionally have been attributed to microphase-separation of hard and soft segments and subsequent hydrogen bonding between hard segments [11]. However, previous studies showed that PUR scaffolds prepared from LDI were microphase-mixed and exhibited negligible hydrogen bonding between urethane and urea groups in adjacent hard segments due to the asymmetric structure of LDI [3].

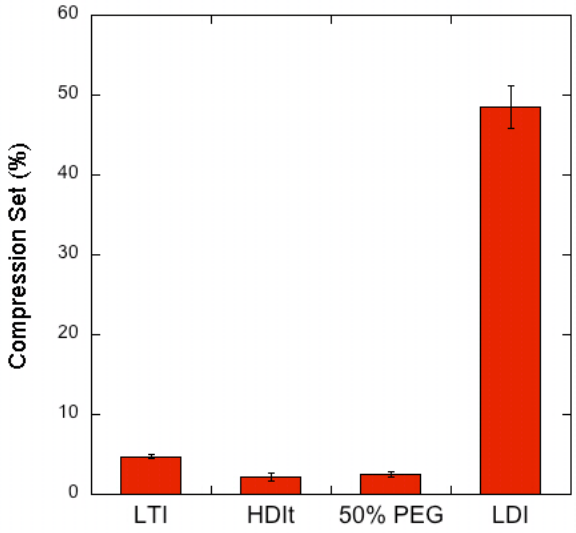

Figure 2.4. Compression set of LTI, HDIt, HDIt + 50% PEG, and LDI scaffolds made with the 900-Da triol. LDI materials had larger permanent deformations than did materials with either of the triisocyanates (n = 3).

Tissue necrosis can occur when exposed to temperatures greater than 50 °C for longer than one minute, so it is important to address the reaction temperatures of potentially injectable systems [20]. The urethane synthesis reaction of polyester polyol and isocyanate is exothermic, although the aliphatic polyisocyanates used in this study are less reactive than aromatic polyisocyanates [11]. The maximum temperature in the center of the foam was 30.5 °C for HDIt materials and 40.0 °C for LTI materials (Figure 2.5). Both are significantly lower than the maximum exotherm temperature of up to 110 °C for poly(methyl methacrylate) (PMMA), which were also measured at the internal core of the material and starting at room temperature [21]. The gel times of the mixtures, estimated by observing the change in viscosity from a viscous liquid to a non-flowable gel, were approximately 3 minutes (LTI) and 5 minutes (HDIt). Despite the higher catalyst concentration used in the HDIt formulations, these polymers exhibited lower reaction exotherms and

longer gel times, suggesting that HDIt is less reactive than LTI.

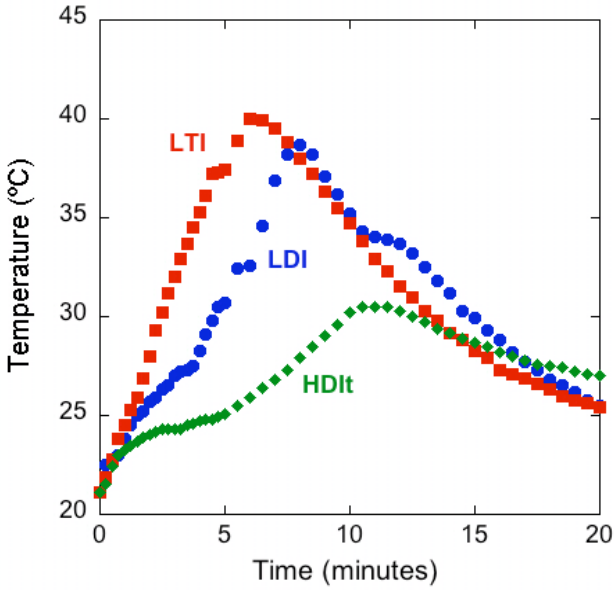

Figure 2.5. Temperature profile for reacting PUR foams.

FT-IR analysis produced characteristic vibration peaks for the ester (1765, 1303, & 1114 cm^{-1}), urethane (3422 & 1765 cm^{-1}), and urea (1469 cm^{-1}) groups. There was no evident NCO peak at 2285-2250 cm^{-1}, which implies negligible free NCO in the cured materials [22, 23]. The absence of a peak near 1710 cm^{-1} suggests negligible hydrogen bonding of the urethane and urea groups [24]. Thus the substantially higher resilience observed with the triisocyanate-based PUR scaffolds may result from the higher chemical crosslink density relative to that with diisocyanates, compensating for the lack of physical crosslinks.

The degradation rates are shown in Figure 2.6. All of the materials retained 85 – 90% of their original mass after 8 weeks. The LTI scaffolds degraded rather quickly thereafter, with only 22% (900/LTI) and 48% (1800/LTI) mass remaining

after 14 and 18 weeks, respectively, and no intact mass remaining by 36 weeks. On the other hand, the HDIt materials degraded steadily, with 52 – 81% mass remaining at 36 weeks. LTI scaffolds thus degraded faster than the HDIt materials, which has been attributed to the degradable ester linkage present in the backbone of lysine derived polyisocyanates. The 7C2G1L polyol has a longer half-life (225 days) than 6C3G1L (20 days), causing the corresponding polyurethane scaffold to degrade more slowly [3, 13]. Hydrolysis of this ester group yields a carboxylic acid group in the polymer, which has been suggested to catalyze further degradation [25]. Higher soft segment content may also explain the faster degradation of the LTI materials, due to the higher %NCO (lower equivalent weight) of LTI relative to that of HDIt. The addition of PEG 600 to HDIt foams increased the initial degradation rate (1 – 8 weeks), which is attributed to increased bulk hydrophilicity resulting from higher PEG content. This increases water absorption into the material, which results in enhanced diffusion of water to hydrolyze the ester linkages, and faster diffusion of degradation products out of the scaffold [6, 11]. However, PEG caused long-term degradation rates (10 – 36 weeks) to slow, perhaps because ethers, as in PEG, are less susceptible than esters to hydrolysis.

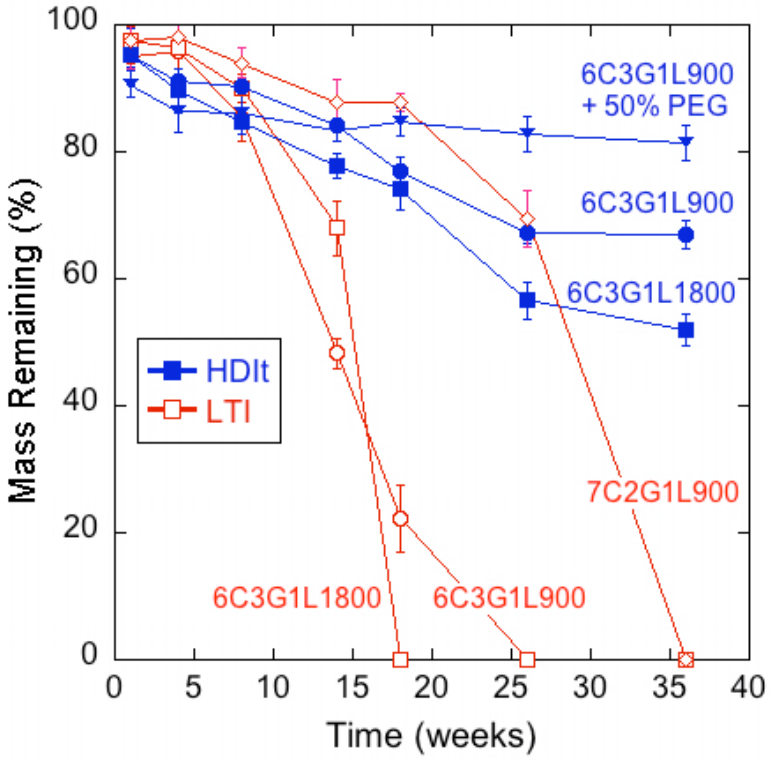

Figure 2.6. ***In vitro*** **degradation of PUR scaffolds in PBS at 37 °C (n = 3).**

Thermal analysis. The materials all had similar TGA thermal decomposition profiles: they began to decompose at 200 °C and completely disintegrated by 600 °C. The DSC thermal profiles demonstrated single second-order glass transitions (Figure 2.7). The glass transition temperatures (T_g), extrapolated from the steepest point of the heat flow (mW/mg) vs. temperature (°C) curve during the second heating cycle, ranged from -30.7 °C (HDIt + 50% PEG) to 6.4 °C (900/LTI) (Table 2.2). The T_g's of the pure polyols were significantly lower than those of the PUR networks: -38.2 (7C2G1L900), -41.7 °C (6C3G1L900) and -44.7 °C (6C3G1L1800). The substantial increase in T_g of the PUR networks relative to those of the pure polyols suggests that microphase-mixing of hard (isocyanate) and soft (polyol) segments has occurred. This trend is consistent with the Fox equation for

predicting glass transition temperatures of polymer blends based on the weight fraction (w_i) and glass transition temperature ($T_{g,i}$) of each component [26].

$$\frac{1}{T_{g,blend}} = \sum_i \frac{w_i}{T_{g,i}} \tag{2.6}$$

The polyol composition had a significant effect on the T_g of the PUR scaffolds. PUR scaffolds prepared from the 1800 g/mol (600 g/eq) polyol had T_g values ~20 °C lower than those prepared from 900 g/mol (300 g/eq) polyol, perhaps due to enhanced microphase-separation of the larger soft segments. Addition of PEG proportionally depressed the glass transition temperatures, which is attributed to the lower T_g of PEG relative to the polyester polyols. As anticipated, the PUR networks did not display any melting transitions because of the amorphous polyols.

Dynamic mechanical properties: Compression. While each of the materials had a similar profile for the temperature-dependent storage modulus, the glass transition temperatures, determined at the inflection point of each curve, ranged from 18.5 to 56.6 °C (Figure 2.8). The T_g values determined by DMA were 34 – 50 °C higher than values determined by DSC, likely due to the different mechanisms of analysis. The DSC glass transition is determined by the change in heat capacity of the sample, while the DMA glass transition is a function of amorphous polymer relaxation (Figure 2.9).

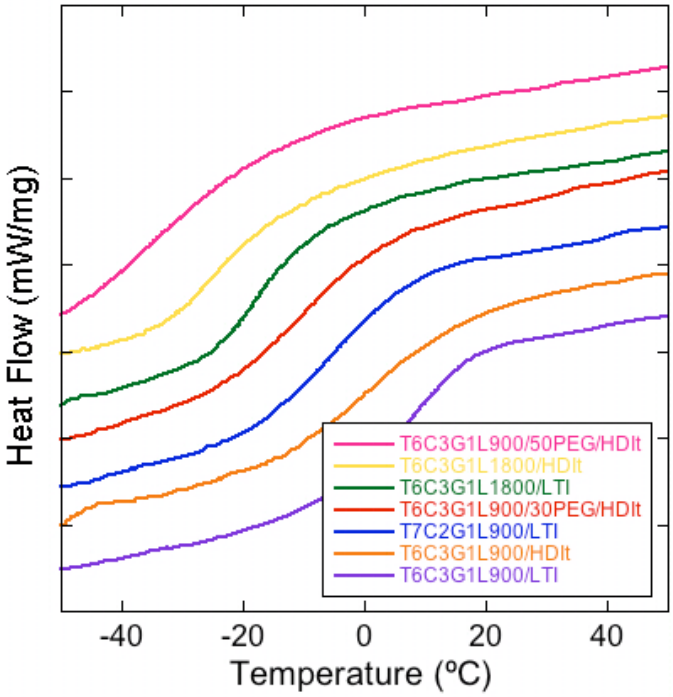

Figure 2.7. Thermal glass transition temperatures of foams are determined at the inflection point in DSC thermograms during the second heating cycle.

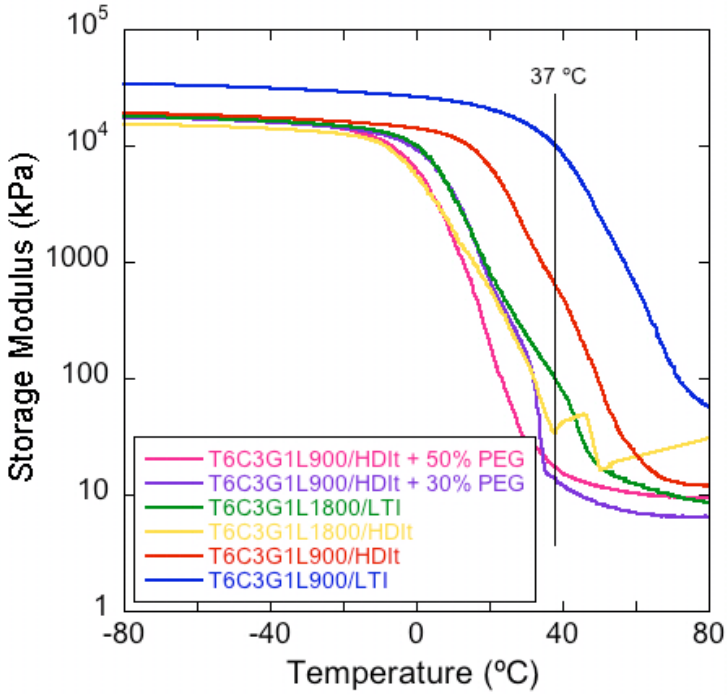

Figure 2.8. Temperature-dependent storage modulus profile of foams in a DMA temperature sweep. T_g is determined at the inflection point of each curve.

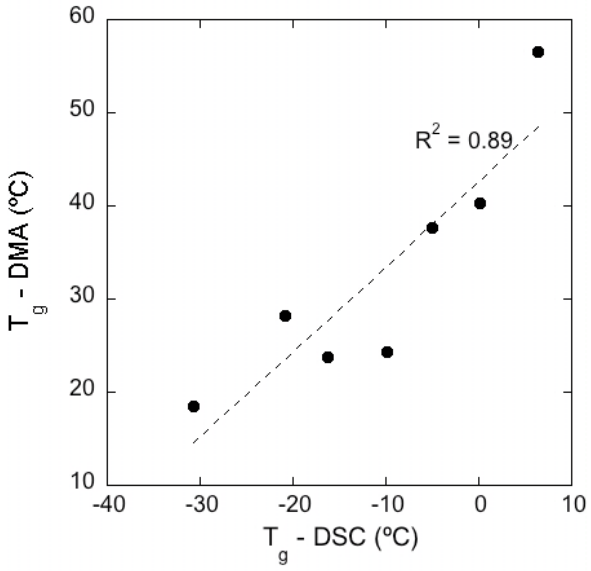

Figure 2.9. Glass transitions as measured by DMA occur approximately 40 °C higher than those by DSC presumably due to the different mechanisms of analysis (changes in mechanical relaxation vs. heat capacity).

The PUR scaffolds exhibited elastomeric dynamic mechanical properties, ranging from ideal elastomers, where the deformation energy is primarily stored elastically, to high-damping elastomers, where the energy is both stored elastically and thermally dissipated. Figure 2.10 shows the materials, organized in order of increasing T_g, analyzed using stress relaxation and frequency sweep tests to evaluate their viscoelastic properties, which were shown to depend on the glass transition temperature. The 900/HDIt + PEG materials, which had DMA glass transition temperatures of 18.5 °C (50% PEG) and 24.3 °C (30% PEG), exhibited dynamic mechanical behavior similar to that of an ideal elastomer in the rubbery plateau zone [27]. The storage modulus E', which represents the energy stored elastically, was nearly constant over the entire frequency range (0.1 – 10 Hz), while

the loss modulus E'', which represents the energy lost due to viscous dissipation, was very low at low frequencies and approaches E' at higher frequencies (e.g., > 5 Hz). Similarly, the stress relaxation data showed a negligible (50% PEG) or slight (30% PEG) decrease in relaxation modulus over the 20 minutes of strain due to relaxation of the polymer network. The frequency sweep and stress relaxation data together suggest that the PUR scaffolds with PEG are rubbery elastomers.

The T_g's of the 1800/LTI (T_g 23.8 °C) and 1800/HDIt (T_g 28.2 °C) materials are closer to the experimental temperature (37 °C), and therefore exhibited viscoelastic properties representative of a material approaching the transition zone, where (a) the values of E' and E'' increase with increasing frequency, and (b) the value of E" approaches E' [28]. As E" approaches E', an increasing fraction of the energy of deformation is dissipated as heat due to increased friction between polymer chains [28]. The vibration damping properties of the material increase with increasing loss modulus E". The frequency sweep data for the 1800/HDIt material show that E' increased with increasing frequency and the value of E" was close to that of E', thereby suggesting that a substantial portion of the energy of deformation was dissipated as heat. The stress relaxation data are in qualitative agreement with the frequency sweep data, as the relaxation modulus decreased with time. At short times (corresponding to high frequencies), the period is too short to enable an active segment of the network to exhibit all possible conformations. Therefore, the strain resulting from a given stress is less than that at longer times (i.e., lower frequencies); thus the relaxation modulus is expected to decrease with increasing time (i.e., decreasing frequency) [28].

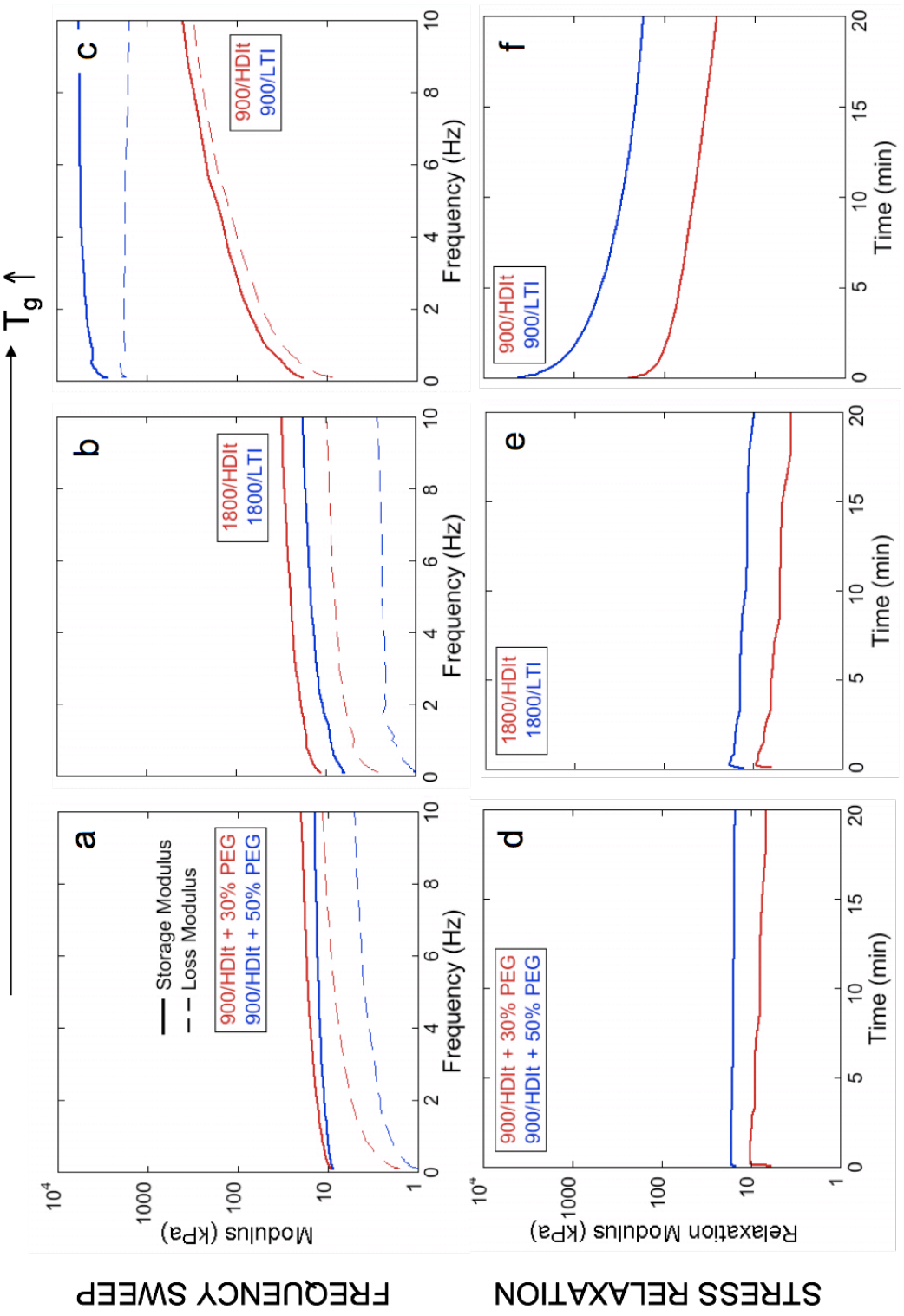

Figure 2.10. Storage and loss moduli as a function of shear rate during DMA frequency sweeps from 0.1 to 10 Hz, and stress relaxation response to 2% strain over 20 minutes. Panels are shown in order of increasing T_g (left to right): materials with PEG (a & d), with 1800-Da polyol (b & e), and 900-Da polyol (c & f).

The 900/HDIt material (T_g 40.3 °C) exhibited properties typical of the transition zone, with a T_g slightly greater than 37 °C. The moduli E' and E" increased with increasing frequency, and the values of E" were close to E'. In the stress relaxation experiments, the relaxation modulus initially reached a high value when the strain was applied and then decayed over 20 minutes by an order of magnitude. In contrast, the T_g of the 900/LTI material (T_g 56.6 °C) is substantially greater than 37 °C, and therefore exhibited properties typical of the glassy zone, characterized by storage modulus 2 – 3 orders of magnitude greater than that in the rubbery plateau. Furthermore, the values of E' and E" did not change substantially with increasing frequency.

Stress-strain plots show elastomeric behavior of the PUR scaffolds even up to 50% compressive strain (Figure 2.11). The Young's moduli, calculated from the slope of the initial linear region of the stress-strain curves, are listed in Table 2.3. 900/LTI scaffolds exhibited the highest modulus values, followed by the 900/HDIt materials, while the 1800-Da polyol or additional PEG appeared to reduce the modulus and compressive strength of the scaffolds. The modulus differences among the materials were statistically significant ($p < 0.005$).

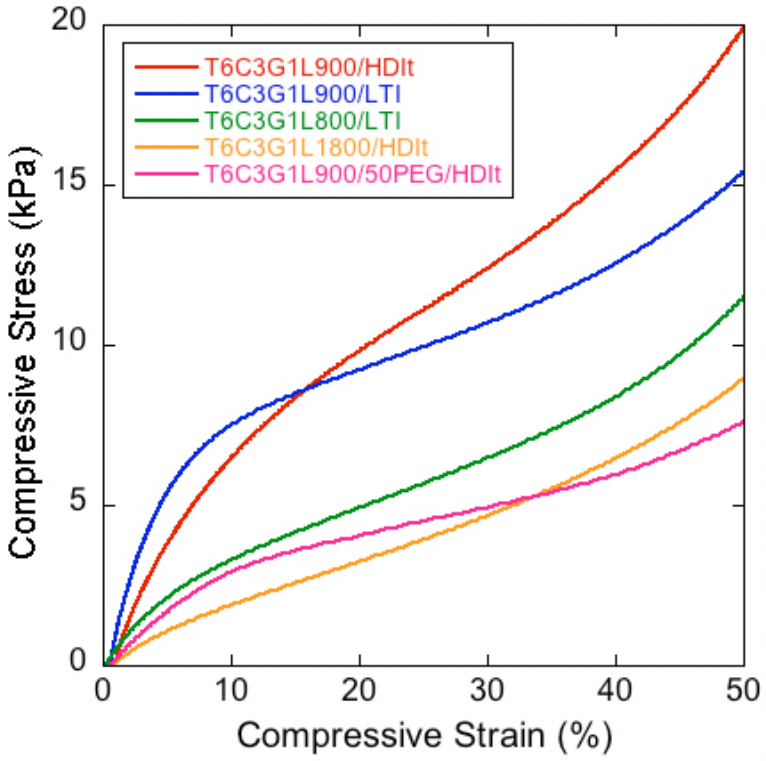

Figure 2.11. Stress-strain curves measured in compression mode. Young's Modulus values were calculated from the initial linear slopes.

Table 2.4. PUR scaffold mechanical properties as measured by DMA in compression (n=3).

Polyol	Isocyanate	Young's Modulus (kPa)	Compressive Stress (kPa)
T6C3G1L900	LTI	177 ± 27	9 ± 0.8
T6C3G1L1800	LTI	42 ± 13	5 ± 0.9
T7C2G1L900	LTI	86 ± 15	15 ± 0.2
T6C3G1L900	HDIt	115 ± 30	11 ± 1
T6C3G1L1800	HDIt	26 ± 2	5. ± 0.4
T6C3G1L900 + 30% PEG	HDIt	58 ± 15	7 ± 0.5
T6C3G1L900 + 50% PEG	HDIt	15 ± 3	7 ± 0.6

The compressive stress at 50% strain ranged from 5 to 11 kPa for the different scaffold formulations (Table 2.3), and the addition of PEG reduced the compressive stress relative to the equivalent scaffold without PEG. The two materials with PEG had nearly equivalent compressive stress values, but all other differences were statistically significant ($p < 0.005$).

Dynamic mechanical properties: Tension. Stress-strain curves for three representative materials are shown in Figure 2.12. The tensile strength and Young's modulus of the thin scaffold samples are given in Table 2.4, both determined from stress-strain curves performed until sample failure. The trend is similar to the compressive strengths, where the 900/LTI materials had the highest tensile strength (267 ± 34 kPa), followed by the 900/HDIt materials (34 ± 9 kPa). Use of the 1800-Da polyol or PEG decreased the modulus and strength. The Young's moduli of 1800/LTI, 1800/HDIt, and 900/HDIt + 30% PEG were statistically similar ($p > 0.05$), but all other tensile strength differences were statistically significant ($p < 0.005$). These PUR scaffolds exhibited elastomeric dynamic mechanical properties, as evidenced by their high elongation at break and low compression set.

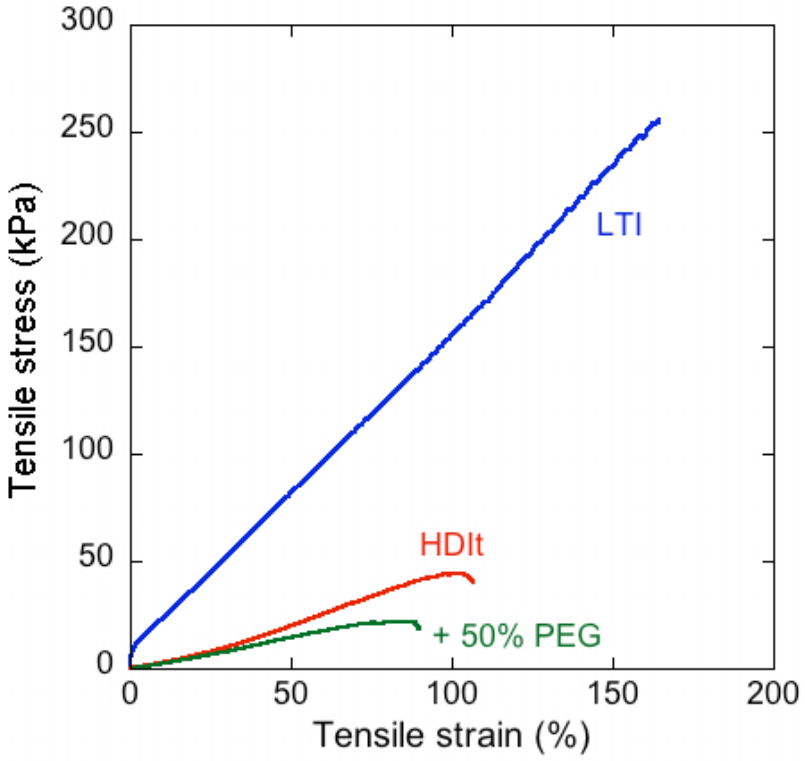

Figure 2.12. Tensile stress-strain curves show the stress and elongation at break. Young's Modulus values were calculated from the initial linear slopes.

Table 2.5. PUR scaffold mechanical properties as measured by DMA in tension mode (n = 3).

Polyol	Isocyanate	Young's Modulus (kPa)	Tensile Strength (kPa)	Strain at Failure (%)
T6C3G1L900	LTI	122 ± 4	267 ± 34	216 ± 75
T6C3G1L1800	LTI	12 ± 3	19 ± 8	170 ± 49
T6C3G1L900	HDIt	389 ± 8	34 ± 9	104 ± 35
T6C3G1L1800	HDIt	9 ± 2	13 ± 2	156 ± 39
T6C3G1L900 + 30% PEG	HDIt	11 ± 5	9 ± 0.2	105 ± 51
T6C3G1L900 + 50% PEG	HDIt	44 ± 17	20 ± 5	59 ± 23

In vitro biocompatibility. The MC3T3 cells permeated and adhered to the scaffold interstices, as shown by fluorescent microscope images (Figure 2.13). Live cells, as indicated by Calcein dye uptake, remained attached to the scaffold during

transfer procedures. The cells were easily distinguished from the autofluorescent scaffold. The percent viability (Table 2.5) was determined as the proportion of live cells, or fluorescence intensity, in the wells cultured with the 4-week and 8-week degradation products, in comparison to that of cells cultured in media only. Cells cultured with 10 μL PBS exhibited 95% viability, while the 4-week and 8-week degradation samples yielded 88 – 95% and 88 – 90% viability, respectively. All differences, including the PBS control, were not statistically significant ($p > 0.5$).

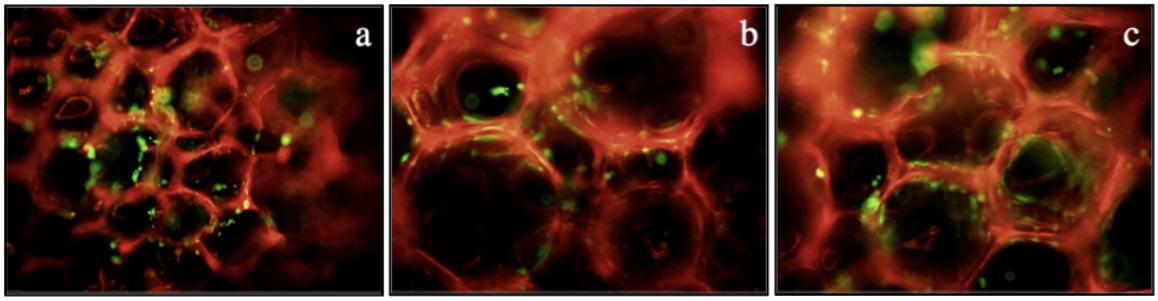

Figure 2.13. Calcein AM staining of live cells (green) seeded on PUR scaffolds, which autofluoresce red (excitation/emission 495/515 nm). a) LTI, b) HDIt, c) HDIt + 50% PEG.

Table 2.5. Percentage of viable cells cultured for 72 hours with 4- and 8-week PUR degradation products. Scaffolds here were synthesized with the T6C3G1L900 polyol (n = 4).

	LTI	HDIt	HDIt + 50% PEG	Control (PBS)
4 weeks	94 ± 8%	95 ± 9%	88 ± 12%	95 ± 11%
8 weeks	89 ± 8%	88 ± 6%	90 ± 10%	95 ± 11%

In vivo biocompatibility in full-thickness dermal wounds. Tissue response was evaluated by subcutaneous implantation of 2 x 8 mm discs of each formulation in rats for up to 21 days (Figure 2.14). During this time, initial infiltration of plasma progressed to the formation of dense granulation tissue. Extracellular matrix with

dense collagen fibers progressively replaced the characteristic, early cellular response, with little evidence of an overt inflammatory response or cytotoxicity. Fibroplasia and angiogenesis appeared to be equivalent among the different formulations. Excisional wounds showed almost complete reepithelialization. With time, each of the materials showed signs of fragmentation and engulfment by a transient, giant cell, foreign body response, with extensive material degradation by 21 days. After the remnant material was resorbed, giant cells were no longer evident. Degradation rates were much higher *in vivo* than *in vitro*. The LTI scaffolds exhibited a greater extent of degradation at 21 days, although the incorporation of PEG into the HDIt scaffold accelerated its degradation significantly.

In some excisional wound studies, the PUR scaffolds were copolymerized with small amounts of the fluorescent dye rhodamine isothiocyanate (TRITC, MW 479; excitation/emission 544/572 nm). 10 mg TRITC was dissolved in 20 μL DMSO and added to a 1-g reaction mixture of polyol and isocyanate. The isothiocyanate (N=C=S) group of TRITC (see Appendix) reacted with the polyol hydroxyl groups to become covalently bound to the polymer. It was added in a small enough quantity to avoid interfering with the urethane reaction and foam index. The TRITC-labeled scaffolds fragments were visible in histological sections with a fluorescent microscope, after 28 days *in vivo* (Figure 2.15).

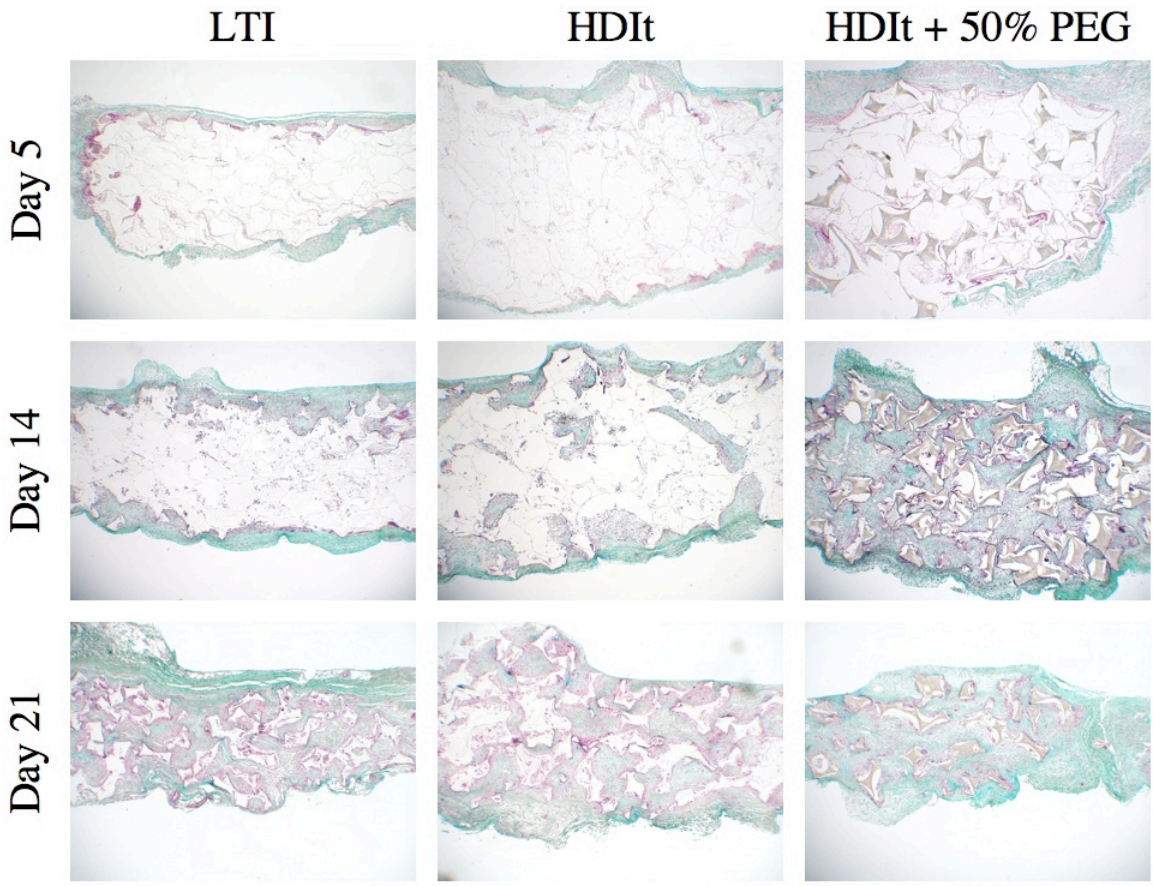

Figure 2.14. Trichrome stain of subcutaneous in vivo implants after 5, 14, and 21 days. All scaffolds shown were made with the 900-Da triol. Material remnants are shown as white segments. Granulation tissue, collagen deposition, and giant cell response are visible.

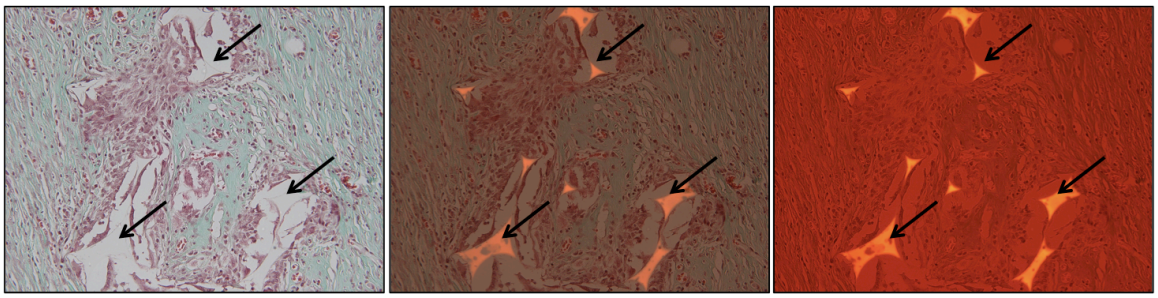

Figure 2.15. Copolymerization of PUR scaffolds with TRITC induces scaffold fluorescence under polarized light. The same histological section from day 28 of an excisional wound study is compared under normal light conditions (left), and two different fluorescent wavelength polarizations (middle & right).

In vivo biocompatibility in bone defects. Undecalcified histological sections stained with toluidine blue showed evidence of cellular ingrowth, formation of new bone, and mineralization after 3 weeks (Figure 2.16). The implants exhibited osteoconductivity and no visible inflammatory response. Scaffold biodegradation was also apparent by 3 weeks.

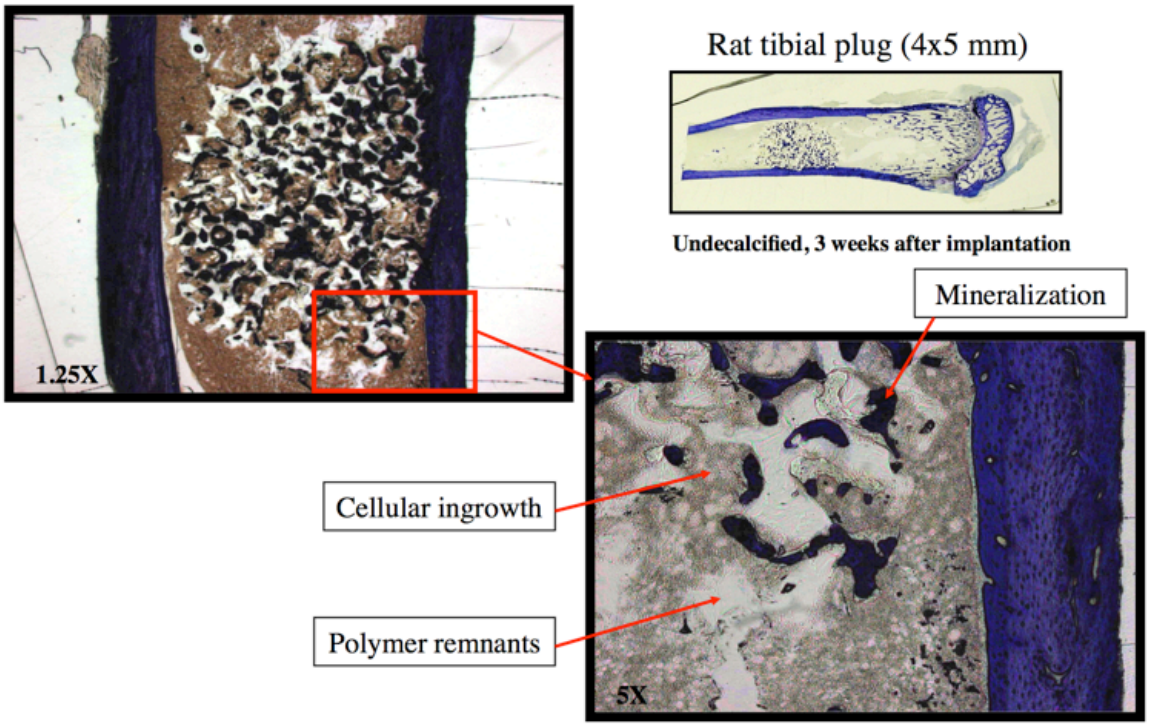

Figure 2.16. Toluidine blue stain of bone histological section of rat tibial defect. Scaffold exhibits cellular ingrowth, new bone, and polymer degradation.

Effects of Mechanical Properties on Wound Healing

As described in the Results section above, the structure-property relationships of the polyurethane scaffolds were investigated. Variations in the polymer backbone – that is, the polyol composition and molecular weight, or the isocyanate used – alter the thermal and mechanical properties of the resultant

scaffolds. However, the effect of these differences in mechanical properties on wound healing is unclear. Experiments were therefore conducted to evaluate the difference in wound healing response to materials of similar composition but with different moduli. In open cell foams such as these polyurethane scaffolds, the Young's modulus of the bulk foam (E^*) and cell struts (E_s), or pore walls, is proportional to the relative density of the cell (ρ^*/ρ_s) [29].

$$\frac{E^*}{E_s} \approx \left(\frac{\rho^*}{\rho_s}\right)^2 \tag{2.7}$$

According to this relationship, the mechanical properties of polyurethane material at the level of the pore wall should change with the bulk scaffold mechanical properties. Cells *in vivo* can sense these mechanical differences at the level of the material surface via mechanotransduction [30]. The hypothesis thus follows that altering the scaffold modulus might affect the pheontypes of cells within the scaffold, as well as cell migration, proliferation, and new matrix production inside the scaffolds.

The goal in selecting the materials for this experiment was to vary only the mechanical properties, specifically modulus, keeping the degradation rates relatively consistent. The chosen approach involved varying the polyol molecular weights, but all other compositional variables stayed constant. The scaffolds were synthesized with HDIt, which degrades more slowly than LTI, such that degradation would not be significant within the experimental timescale (7 to 21 days).

Two polyester polyols were synthesized as described in the Methods section above. The monomeric composition consisted of glycolide/lactide/caprolactone

(60/30/10), with target molecular weights of 600 and 1800. The experiments above illustrate that scaffolds with a higher soft segment molecular weight exhibited lower moduli, largely due to a higher glass transition temperature and soft segment length. The T_g measured by DSC was -23 °C for the T6C3G1L1800/HDIt scaffold (28.2 °C by DMA), and -6 °C for the T6C3G1L600/HDIt material.

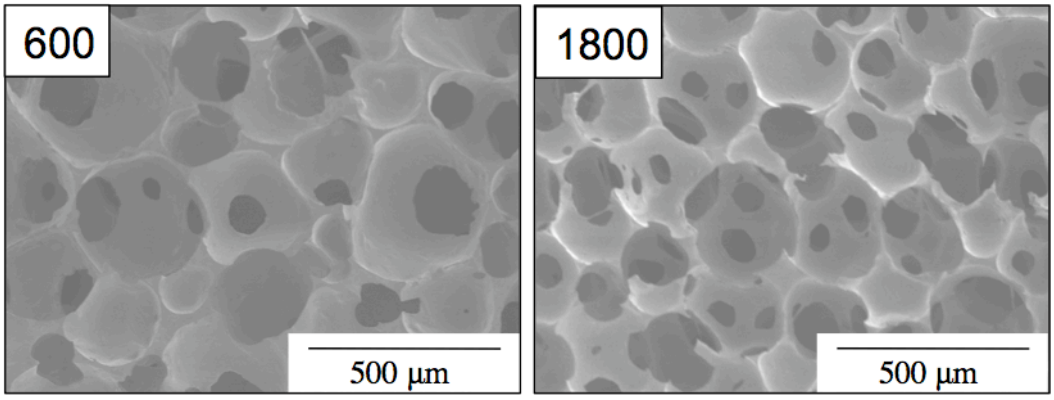

Figure 2.17. SEM images of scaffolds for mechanical properties of healing study show interconnected pores.

The materials were first characterized to verify physical similarities but differences in mechanical properties. Density and porosity measurements were conducted with triplicate samples, and the glass transition temperature was assessed by DSC. The mechanical properties were evaluated by DMA in compression and tension modes. Each of these experiments followed the procedures outlined in the Methods section above. Table 2.5 lists the physical, thermal, and mechanical properties of the PUR scaffolds. As a point of comparison, normal human skin has an ultimate tensile strength of 2873 ± 743.6 kPa, ultimate strain of 70.0 ± 3.4%, and Young's modulus of 2325 ± 300 kPa [31]. SEM images of

the materials were also acquired to verify similar pore sizes, structures and interconnectedness (Figure 2.17).

Table 2.6. Physical and mechanical properties of HDIt scaffolds and PVA (control) used to study effects of mechanical properties on wound healing.

Property	MW 600	MW 1800	PVA
Polyol OH# (theor.)	280	93	-
Polyol OH# (act.)	280	105	-
Density (kg/m^3)	99 ± 4	101 ± 2	55 ± 5
Porosity (vol-%)	92 ± 0.3	92 ± 0.2	96 ± 0.5
Swelling (%)	52 ± 2	88 ± 3	232 ± 7
Polyol T_g (°C) - DSC	-50	-38	-
Scaffold T_g (°C) - DSC	-6	-23	85 °C [32]
Compression			
Young's modulus (kPa)	183 ± 52	25 ± 5	702 ± 367
Compressive stress (kPa)	51 ± 8	9 ± 2	-
Tension			
Young's modulus (kPa)	402 ± 192	36 ± 8	-
Ultimate strength (kPa)	195 ± 15	23 ± 6	-
Ultimate strain (%)	88 ± 13	72 ± 15	-

To evaluate the comparative behaviors of these scaffolds *in vivo*, 10 x 2 mm discs were implanted in a subcutaneous pocket in male Sprague-Dawley rats. A nondegradable polyvinyl alcohol (PVA) sponge was used as a control in the pocket model; the relevant physical and mechanical properties are listed in Table 2.5, and representative stress-strain curves in compression mode are shown in Figure 2.18. These were harvested at 7, 14, 21, and 28 days, and processed for histological evaluation with Gomori's trichrome staining (Figure 2.19).

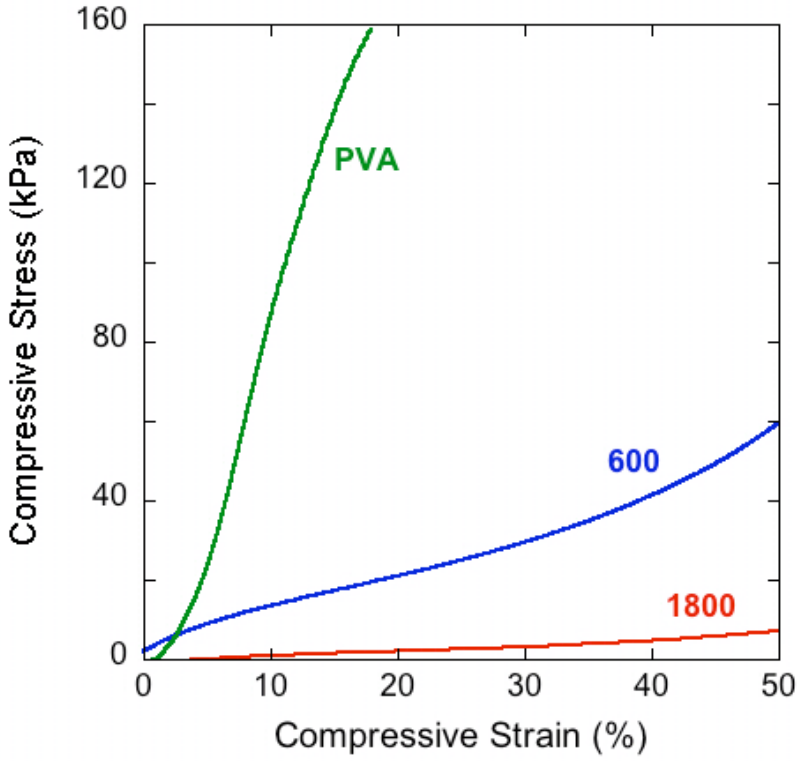

Figure 2.18. Representative stress-strain curves in compressive mode illustrate the relative thickness of each material.

The PUR degradation was generally consistent between samples for each given material. Some samples varied slightly at later time points, depending on the extent of cellular infiltration, as the rate of material degradation directly corresponds with cellular content. Overall, the scaffolds with MW 1800 polyol seemed to exhibit greater cellular infiltration and granulation tissue than those with the MW 600 polyol. However, the amount of new collagen deposition within both scaffolds seemed to lag behind the levels seen in the earlier *in vivo* dermal studies (Figure 2.14). The PVA sponges surprisingly facilitated faster cellular infiltration, by 7 days, and new collagen deposition than either of the PUR scaffolds. Predictably, no PVA had degraded by 28 days.

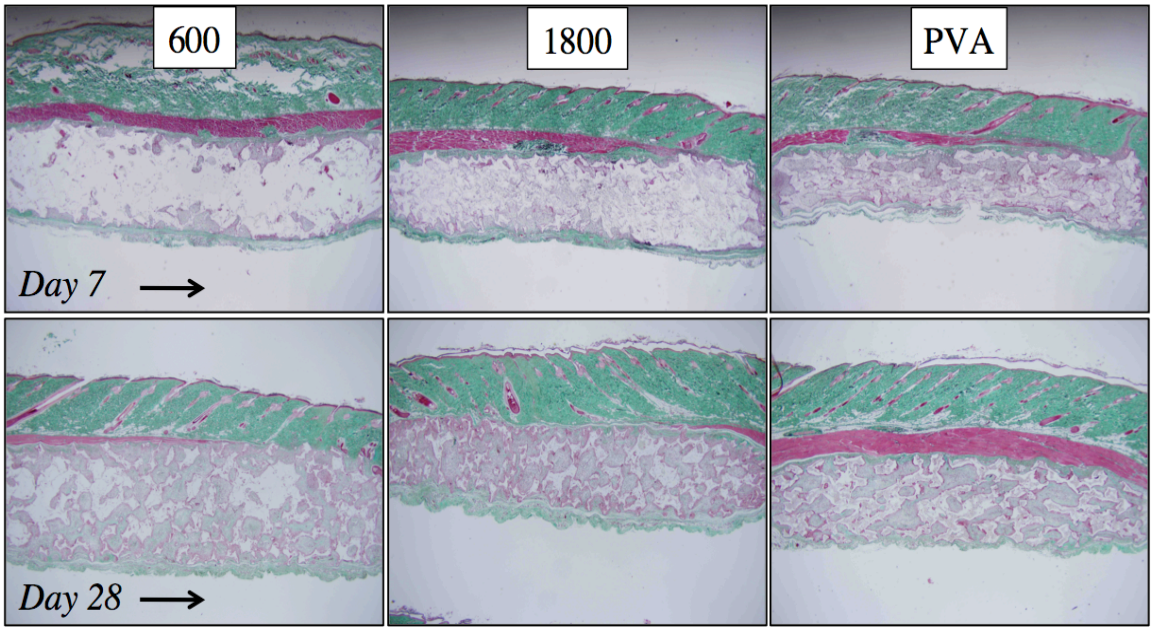

Figure 2.19. Effect of mechanical properties on wound healing. The softer scaffold (MW 1800) allowed more infiltration by day 7 and collagen at later time points. PVA allowed more new tissue ingrowth, which suggested other factors at play.

The study was thus inconclusive. The reason for this was conjectured to be an unexpected consequence during the experiment. Standard practice for implantation of the PVA sponges includes dipping them in saline before placement in the wound. However, this is not typically carried out for the PUR scaffolds. Thus an unintended variable was introduced to the experiment, as the PVA sponges were moist when implanted, but the PUR scaffolds were completely dry. Optimal wound healing occurs with a fine balance between too much fluid (i.e. blood and serum) and too little moisture, and so it seems that the wounds containing PUR scaffolds demonstrated delayed wound healing. The wounds did not show evidence of infection or elevated presence of neutrophils, which could otherwise hinder

formation of granulation tissue and new matrix. Similarly, histology displayed normal levels of macrophages surround the material edges.

This inadvertent issue of moisture level within the wound bed presented a new angle to the evaluation of the PUR scaffolds with 600- vs. 1800-MW polyols. The 1800 scaffolds seemed to allow more cellular infiltration and granulation tissue, albeit not much new collagen, at any given time point. This difference could be mainly due to the greater degree of swelling in a higher molecular weight polyol, resulting from its larger soft segments within the polyurethane. Fibroblasts, keratinocytes, and macrophages might therefore be more inclined to migrate into the 1800 scaffolds, which would absorb more water and therefore be slightly more hydrophilic, than the 600 scaffolds.

Discussion

Polyurethane scaffolds synthesized from aliphatic and lysine-derived polyisocyanates have been reported to support cell attachment and proliferation *in vitro*, as well as ingrowth of new tissue and degradation to non-cytotoxic decomposition products *in vivo* [3, 5, 33, 34]. While the low vapor pressure of LDI renders it potentially useful for injectable biomaterials, LDI-based PUR scaffolds synthesized by the gas foaming process displayed poor resiliency, with up to 50% permanent deformation when subjected to compressive loads. The high compression set of LDI-based PUR scaffolds is conjectured to result from the absence of physical crosslinks in the polymer network, as evidenced by the lack of hydrogen-bonded urethane and urea groups in the hard segment [11]. For

segmented PUR elastomers synthesized from LDI, the microphase morphology depends on the molecular weight of the soft segment [35, 36]. For LDI elastomers incorporating a 2000 g/mol poly(e-caprolactone) (PCL) diol soft segment, the value of T_g was -52 °C, which is close to that of pure PCL diol. However, for soft segments with molecular weights of 1250 or 530 g/mol, the value of T_g increased 20 – 45 °C, suggesting the presence of significant microphase-mixing that has been attributed to the asymmetric ethyl branch in LDI. Considering that microphase-mixing of LDI segmented elastomers becomes significant at soft segment equivalent weights of 625 g/eq, it is not surprising that LDI-based PUR networks exhibited microphase-mixing at soft segment equivalent weights of 300 g/eq. We reasoned that triisocyanates would yield PUR networks with higher chemical crosslink density, thus compensating for the lack of physical crosslinks and improving mechanical properties such as compression set. In this study, PUR scaffolds were prepared from LTI and Desmodur N3300A HDI trimer using the one-shot gas foaming process as described previously for LDI [3, 10]. Both HDIt and LTI have low vapor pressure at ambient temperature, thus minimizing the risk of exposure by inhalation when the materials are injected. Furthermore, it was of interest to compare the biocompatibility and degradation of PUR scaffolds synthesized from aliphatic and lysine-derived triisocyanates. While LTI and HDIt have been used to synthesize cast elastomers with improved properties, such as optical clarity and thermal stability [37], their use in biodegradable PUR scaffolds has not been previously reported. The effects of triisocyanate composition on biocompatibility, biodegradation, and

mechanical properties were investigated, as well as the potential of the PUR scaffolds for release of growth factors.

The data in Figure 2.4 demonstrate that the PUR networks synthesized from LTI and HDIt exhibited significantly lower permanent deformation than those synthesized from LDI. Materials in wound healing applications could benefit from greater resilience, allowing them to better conform to the wound site and maintain contact with the host tissue when subjected to compressive or tensile forces.

Polyether and polyester polyols have been mixed in previous studies to produce foams via prepolymers and chain extension, but not for one-shot foams prepared directly from polyisocyanates without the prepolymer step [5, 6, 10, 11, 37, 41]. Polyethers are generally immiscible with polyesters and are typically stabilized with water-soluble polyethersiloxanes [11]. However, foams with polyethersiloxane stabilizers have been reported not to support cell attachment or proliferation [10]. Instead, we have shown that stable scaffolds can be synthesized with polyether-polyester mixtures using turkey red oil as a stabilizer and surfactant as previously used to stabilize polyester foams [11]. These materials were stable with up to 70% PEG.

As shown in Table 2.2, the composition of the polyol component substantially affected the glass transition temperatures of the PUR scaffolds. PUR scaffolds prepared from the 1800 g/mol (600 g/eq) polyol had T_g values ~20 °C higher than those prepared from 900 g/mol (300 g/eq) polyol, which is consistent with the effects of soft segment equivalent weight on T_g observed previously for segmented PUR elastomers prepared from LDI [35, 36]. The addition of PEG also reduced the

T_g of the PUR networks, which is attributed to the lower T_g of PEG relative to the polyester polyols. As anticipated, the PUR networks did not display any melting transitions because amorphous polyols were used. In a previous study, PUR scaffolds synthesized from HDIt with PEG and poly(e-caprolactone) polyols exhibited melting transitions (associated with the semi-crystalline soft segments) ranging from 39 – 58 °C [38]. However, no glass transitions were reported within the range of -20 – 200 °C, so the extent of microphase separation of the materials is not known.

While previous studies showed that *in vitro* degradation is controlled by the polyol composition [3], the data in Figure 2.6 demonstrate that the polyisocyanate composition also has a dramatic effect on the degradation of the PUR scaffolds. LTI scaffolds degraded faster than the HDIt materials, which has been attributed to the degradable ester linkage present in the backbone of lysine derived polyisocyanates (see Appendix). Hydrolysis of this ester group yields a carboxylic acid group in the polymer, which has been suggested to catalyze further degradation [25]. For lysine-derived polyisocyanates, hydrolysis of urethane linkages to lysine has been reported, while others have reported that urethane and urea linkages are only enzymatically degraded [4, 7, 42]. Higher soft segment content may also explain the faster degradation of the LTI materials, due to the higher %NCO (lower equivalent weight) of LTI relative to that of HDIt. *In vivo*, the materials degraded significantly faster than *in vitro*, an observation that has been documented previously for porous poly(D-lactic-*co*-glycolic acid) scaffolds and most likely due to an enzymatic mechanism [39]. Furthermore, enzymatic cleavage of the lysine residues likely

contributes to accelerated degradation of the LTI scaffolds *in vivo* [40]. Previous studies have shown that the addition of PEG increases the hydrolytic degradation rate, presumably due to the increased hydrophilicity with PEG [5, 6, 10, 11]. The addition of PEG 600 to HDIt foams increased the initial degradation rate (1 – 8 weeks), which is attributed to increased bulk hydrophilicity resulting from higher PEG content. This increases water absorption into the material, which results in enhanced diffusion of water to hydrolyze the ester linkages, and faster diffusion of degradation products out of the scaffold [6, 11]. However, at later time points (10 – 36 weeks), the degradation rate decreased, which is inconsistent with previous studies. Furthermore, addition of PEG was observed to increase the polymer degradation *in vivo* in the subcutaneous implant model. The cause of the discrepancy between the *in vitro* and *in vivo* degradation data is not known, although it is most likely due to cell-mediated effects.

The PUR scaffolds exhibited elastomeric dynamic mechanical properties, as evidenced by their high elongation at break and low compression set; they ranged from ideal elastomers, where the deformation energy is primarily stored elastically, to high-damping elastomers, where the energy is both stored elastically and thermally dissipated. By varying the composition of the triisocyanate and polyol components, it is possible to prepare elastomeric PUR scaffolds with tunable damping properties. Application of rubbery elastomers (i.e., low-damping) as scaffolds for bone defects has been suggested to promote intimate contact between the implant and the host bone [33]. The elastomer can be compressed prior to implantation, where it then expands in the wound to maintain intimate contact with

the local tissue. Maintaining good contact between the bone and implant may promote the migration of local osteoprogenitor cells from the bone into the implant, thereby enhancing bone regeneration. It has also been suggested that elastomeric properties can protect the implant from shear forces at the bone-implant interface. However, the effects of the damping properties of the scaffold on tissue regeneration are not known. If the damping is excessive, then, upon exposure to physiological strains, the relaxation modulus may drop to values too low to provide significant support.

Materials prepared from triisocyanates in the present study displayed slightly higher densities but comparable porosities to one-shot polyurethanes made from LDI in a previous study [10]. However, the compressive strength (i.e., the compressive stress measured at 50% strain) of the HDIt and LTI materials (5 – 15 kPa) was higher than that of the LDI materials (2 – 4 kPa). HDI-prepolymer foams of comparable density (80 – 107 kg/m^3) from a previous study [5, 6] were generally stronger than the one-shot HDIt and LTI foams of the present study, with compressive strengths of 30 – 85 kPa (at 40% strain) versus 5 – 15 kPa (at 50% strain) for the HDIt and LTI foams. However, the Young's moduli of the HDI-prepolymer foams are lower, at 9 – 21 kPa, compared to 26 – 202 kPa for the one-shot foams. While the HDI-prepolymer foams exhibit elastomeric mechanical properties and good biocompatibility *in vivo*, they are not injectable due to the high temperature (60 °C) cure step.

In a previous study, endothelial cell adhesion *in vitro* to a poly(ether ester urethane)urea scaffold was inversely proportional to the hydrophilicity, although

smooth muscle cells grew faster in the more hydrophilic scaffold [5, 6]. Bone regeneration occurred in polyurethane scaffolds implanted into defects of sheep iliac crests, with more calcium phosphate salts mineralized in defects with hydrophilic scaffolds, which also had the highest porosities [41]. Original ilium thickness was reestablished only in defects with the most hydrophobic scaffolds, perhaps because their slow degradation rates allowed more time for bone ingrowth [33]. In the PUR scaffolds of the present study, greater collagen accumulation appeared in the implants with PEG scaffolds. However, it cannot be determined conclusively whether this is a direct result of the increased hydrophilicity, the faster degradation rate, or lower damping properties of the PEG scaffolds.

A biodegradable, elastomeric polyurethane scaffold that released basic fibroblast growth factor (bFGF) has been reported for soft tissue engineering applications [42]. Segmented PUR elastomers were synthesized from butane diisocyanate (BDI), putrescine, and poly(e-caprolactone) diol. Scaffolds incorporating bFGF were processed using a thermally induced phase separation method. The scaffolds showed a two-stage release behavior characterized by an initial period of fast release (19 – 37% on day 1) followed by a second period of slow release over 4 weeks. The released bFGF was shown to induce proliferation of rat smooth muscle cells. However, in this study, the bFGF was released from a pre-formed polymer scaffold, not from a reactive polymer. PUR scaffolds prepared by reactive liquid molding of LDI, glycerol, water, and ascorbic acid (AA) have been shown to support controlled release of AA over 60 days [43]. By dissolving the AA in the glycerol prior to adding the LDI, the AA was covalently bound to the polymer

through reaction of the primary hydroxyl group in the AA with LDI to form urethane linkages. In the HDIt material of the present study, PDGF-BB was added as a lyophilized powder to minimize its reaction with the PUR. While the covalent binding approach was successful with a small molecule such as ascorbic acid, proteins were expected to lose their three-dimensional structure and denature upon reaction with the polymer. The faster release of PDGF-BB from the HDIt scaffolds compared to release of ascorbic acid from the LDI scaffolds is attributed to the absence of covalent bonds. As the scaffold swells with water, the PDGF dissolves and diffuses out of the scaffold, and the release is not dependent on the hydrolysis of covalent bonds.

Conclusions

Biodegradable PUR scaffolds prepared from triisocyanates using a one-shot process exhibited elastomeric mechanical properties and substantially lower compression set relative to scaffolds prepared from LDI. Their elastic behavior is thought to promote intimate contact between the material and surrounding tissue, which may facilitate ingrowth of new tissue and help keep the material in place when subjected to physiologically relevant strains. Both low- and high-damping elastomers can be synthesized by varying the glass transition temperature of the materials. Processing by two-component reactive liquid molding allows them to be injected and conform to the wound boundaries. The gel time of 3 – 5 minutes and moderate exotherm (e.g., < 15 °C increase) suggests their potential utility for injectable wound healing applications. The materials supported cellular infiltration

and generation of new tissue and facilitate neodermis formation with minimal inflammation. Signaling molecules were incorporated as labile powders upon synthesis, further enhancing their regenerative capabilities.

References

1. Bonzani IC, Adhikari R, Houshyar S, Mayadunne R, Gunatillake P, Stevens MM. Synthesis of two-component injectable polyurethanes for bone tissue engineering. *Biomaterials* 2007; 28(3): 423-433.

2. Gorna K, Gogolewski S. Preparation, degradation, and calcification of biodegradable polyurethane foams for bone graft substitutes. *Journal of Biomedical Materials Research, Part A* 2003; 67A(3): 813-827.

3. Guelcher S, Srinivasan A, Hafeman A, Gallagher K, Doctor J, Khetan S, et al. Synthesis, in vitro degradation, and mechanical properties of two-component poly(ester urethane)urea scaffolds: Effects of water and polyol composition. *Tissue Engineering* 2007; 13(9): 2321-2333.

4. Zhang J-Y, Beckman EJ, Hu J, Yang G-g, Agarwal S, Hollinger JO. Synthesis, biodegradability, and biocompatibility of lysine diisocyanate-glucose polymers. *Tissue Engineering* 2002; 8(5): 771-785.

5. Guan J, Fujimoto KL, Sacks MS, Wagner WR. Preparation and characterization of highly porous, biodegradable polyurethane scaffolds for soft tissue applications. *Biomaterials* 2005; 26(18): 3961-3971.

6. Guan J, Sacks MS, Beckman EJ, Wagner WR. Biodegradable poly(ether ester urethane)urea elastomers based on poly(ether ester) triblock copolymers and putrescine: Synthesis, characterization and cytocompatibility. *Biomaterials* 2004; 25(1): 85-96.

7. Fujimoto KL, Guan J, Oshima H, Sakai T, Wagner WR. In vivo evaluation of a porous, elastic, biodegradable patch for reconstructive cardiac procedures. *The Annals of Thoracic Surgery* 2007; 83(2): 648-654.

8. Fujimoto KL, Tobita K, Merryman WD, Guan J, Momoi N, Stolz DB, et al. An elastic, biodegradable cardiac patch induces contractile smooth muscle and improves cardiac remodeling and function in subacute myocardial infarction. *Journal of the American College of Cardiology* 2007; 49(23): 2292-2300.

9. Adhikari R, Gunatillake PA, inventors. Biodegradable polyurethane/urea compositions Patent No. WO 2004/009227 A2, 2004.

10. Guelcher SA, Patel V, Gallagher KM, Connolly S, Didier JE, Doctor JS, et al. Synthesis and in vitro biocompatibility of injectable polyurethane foam scaffolds. *Tissue Engineering* 2006; 12(5): 1247-1259.

11. Oertel G. Polyurethane handbook. 2 ed. Berlin: Hanser Gardner Publications, 1994.

12. Kitai M, Ryuutou H, Yahata T, Hara Y, Iwane H, Soejima Y, inventors. Aliphatic triisocyanate compound, process for producing the same, and polyurethane resin made from the compound, 2002.

13. Sawhney AS, Hubbell JA. Rapidly degraded terpolymers of d,l-lactide, glycolide, and ε-caprolactone with increased hydrophilicity by copolymerization with polyethers. *Journal of Biomedical Materials Research* 1990; 24: 1397-1411.

14. ASTM-International. D4662-03. Standard test methods for polyurethane raw materials. Determination of acid and alkalinity numbers of polyols. 2007.

15. ASTM-International. D3574-05. Standard test methods for flexible cellular materials - slab, bonded, and molded urethane foams. 2007; p. 360-368.

16. ASTM-International. D695-02a. Standard test method for compressive properties of rigid plastics. 2007.

17. Storey RF, Wiggins JS, Mauritz KA, Puckett AD. Bioabsorbable composites. Ii: Nontoxic, l-lysine-based poly(ester-urethane) matrix composites. *Polymer Composites* 1993; 14(1): 17-25.

18. Storey RF, Wiggins JS, Puckett AD. Hydrolyzable poly(ester-urethane) networks from l-lysine diisocyanate and d,l-lactide/ε-capralactone homo- and copolyester triols. *Journal of Polymer Science, Part A: Polymer Chemistry* 1994; 32: 2345-2363.

19. Wiggins JS, Storey RF. Synthesis and characterization of l-lysine-based poly(ester urethane) networks. *Polymer Preprints* 1992; 33(2): 516-517.

20. Eriksson R, Albrektsson T, Magnusson B. Assessment of bone viability after heat trauma. A histological, histochemical and vital microscopic study in the rabbit. *Scandinavian Journal of Plastic and Reconstructive Surgery* 1984; 18(3): 261-268.

21. Meyer PJ, Lautenschlager E, Moore B. On the setting properties of acrylic bone cement. *Journal of Bone & Joint Surgery American volume* 1973; 55(1): 149-156.

22. Kothandaraman H, Nasar AS, Lakshmi RK. Synthesis and thermal dissociation of phenol- and naphthol-blocked diisocyanates. *Journal of Applied Polymer Science* 1994; 53(1): 31-38.

23. Socrates G. Infrared characteristic group frequencies: Tables and charts. 2 ed. New York: John Wiley & Sons, 1994.

24. Stuart BH. Infrared spectroscopy: Fundamentals and applications New York: Wiley, 2004.

25. Bruin P, Veenstra GJ, Nijenhuis AJ, Pennings AJ. Design and synthesis of biodegradable poly(ester-urethane) elastomer networks composed of non-toxic building blocks. *Die Makromolekulare Chemie, Rapid Communications* 1988; 9(8): 589-594.

26. Sperling LH. Introduction to physical polymer science. 4th ed. Hoboken, NJ: John Wiley & Sons, Inc., 2005.

27. Mark JE, Erman E, Eirich FR, editors. Science and technology of rubber. 2nd ed. San Diego, CA: Academic Press, Inc., 1994.

28. Kramer O, Hvidt S, Ferry JD. Dynamic mechanical properties. In: Mark JE, Erman E, Eirich FR, editors. Science and technology of rubber. 2nd ed. San Diego, CA: Academic Press, Inc., 1994.

29. Gibson LJ, Ashby MF. Cellular solids: Structure and properties. 2nd ed. Cambridge, UK: Cambridge University Press, 1997.

30. Discher DE, Janmey P, Wang Y-l. Tissue cells feel and respond to the stiffness of their substrate. *Science* 2005; 310(5751): 1139(1135).

31. Powell HM, McFarland KL, Butler DL, Supp DM, Boyce ST. Uniaxial strain regulates morphogenesis, gene expression, and tissue strength in engineered skin. *Tissue Engineering Part A* 2010; 16(3): 1083-1092.

32. Carraher CE. Introduction to polymer chemistry. 1st ed: CRC Press, 2006.

33. Gogolewski S, Gorna K, Turner AS. Regeneration of bicortical defects in the iliac crest of estrogen-deficient sheep, using new biodegradable polyurethane bone graft substitutes. *Journal of Biomedical Materials Research, Part A* 2006; 77A(4): 802-810.

34. Zhang J-Y, Beckman EJ, Piesco NP, Agarwal S. A new peptide-based urethane polymer: Synthesis, biodegradation, and potential to support cell growth in vitro. *Biomaterials* 2000; 21: 1247-1258.

35. de Groot JH, de Vrijer R, Wildeboer BS, Spaans CS, Pennings AJ. New biomedical polyurethane ureas with high tear strengths. *Polymer Bulletin* 1997; 38(2): 211-218.

36. Skarja GA, Woodhouse KA. Structure-property relationships of degradable polyurethane elastomers containing an amino acid-based chain extender. *Journal of Applied Polymer Science* 2000; 75(12): 1522-1534.

37. Tsutsumi N, Yoshizaki S, Sakai W, Kiyotsukuri T. Nonlinear optical polymers. 1. Novel network polyurethane with azobenzene dye in the main frame. *Macromolecules* 1995; 28(19): 6437-6442.

38. Gorna K, Gogolewski S. Molecular stability, mechanical properties, surface characteristics and sterility of biodegradable polyurethanes treated with low-temperature plasma. *Polymer Degradation and Stability* 2003; 79: 475-485.

39. Lu L, Peter SJ, D. Lyman M, Lai H-L, Leite SM, Tamada JA, et al. In vitro and in vivo degradation of porous poly(d-lactic-co-glycolic acid) foams. *Biomaterials* 2000; 21(18): 1837-1845.

40. Elliott SL, Fromstein JD, Santerre JP, Woodhouse KA. Identification of biodegradation products formed by l-phenylalanine based segmented polyurethaneureas. *Journal of Biomaterials Science Polymer Edition* 2002; 13(6): 691-711.

41. Gogolewski S, Gorna K. Biodegradable polyurethane cancellous bone graft substitutes in the treatment of iliac crest defects. *Journal of Biomedical Materials Research Part A* 2007; 80A(1): 94-101.

42. Guan J, Stankus JJ, Wagner WR. Biodegradable elastomeric scaffolds with basic fibroblast growth factor release. *Journal of Controlled Release* 2007; 120(1-2): 70-78.

43. Zhang J-Y, Doll BA, Beckman EJ, Hollinger JO. A biodegradable polyurethane-ascorbic acid scaffold for bone tissue engineering. *Journal of Biomedical Materials Research, Part A* 2003; 67(2): 389-400.

CHAPTER III

DEVELOPMENT OF AN INJECTABLE SCAFFOLD FORMULATION

Introduction

Increasing clinical demand for minimally invasive surgical procedures elicits the necessary development of injectable biomaterials. Such materials facilitate operational ease in both orthopaedic and dermal indications with possible percutaneous administration and allow surgery-specific customization [1]. Furthermore, a biomaterial that is applied as a liquid and cured *in situ* can flow to fill the contours of irregularly shaped wounds, which otherwise might present difficulties in trimming an implant to the appropriate size. Maximizing the contact surface area between the material and surrounding tissue could encourage cellular infiltration and integration of the scaffold.

Several requirements govern the success of an injectable application. First and foremost, the therapy must be easy to use. The biomaterial should cure quickly, and the reaction must be minimally exothermic and not leach any toxic monomers or other components, either by contact or inhalation. The material reactants must be stable for an adequate shelf life until use. One of the biggest challenges might be ensuring reproducible properties, such as porosity, degradation, and setting time, even in uncontrolled (i.e. non-laboratory) environments. Khan, et al. assert that injectable biomaterials tend to lack a pore structure, sufficient to allow cell migration, nutrient exchange, and new tissue ingrowth [2].

Injectable hydrogels, such as poly(ethylene glycol) (PEG), collagen, fibrin, chitosan, alginate, and hyaluronan, have been shown to support bone ingrowth *in vivo*, particularly when combined with angio-osteogenic growth factors [3-9]. However, hydrogels lack the robust mechanical properties of thermoplastic polymers. As another example, poly(propylene fumarate) can be injected into orthopaedic or cranial defects as a liquid and thermally or photo cross-linked *in situ* with various cross-linking agents, which affect the final mechanical and degradation properties [3]. Recently developed porous composite scaffolds have been formed by gas foaming, with up to 61% porosity, 50-500 μm pores, and a compressive modulus of 20 – 40 MPa [4].

The polyurethane scaffolds developed in this work are prime candidates for injectable biomaterials. The one-shot mixing of two reactive components, the resin and isocyanate, without the need of solvents allows the materials to be injectable and cure *in situ*. The reaction exotherms reach only 30.5 and 40 °C, with 8 and 10-minute rise times for the HDIt and LTI scaffolds, respectively (Figure 2.5). Preliminary injectability experiments in dermal excisional and subcutaneous wounds showed no evidence of an immune response or rejection to the polyurethane reaction. However, several aspects of the reactive system required improvements. Although the rise time was suitable, the scaffolds cured and dried completely in 30 minutes or longer, which is impractical for a normal surgical setting. This was addressed by increasing the catalyst added to the resin component.

Traditionally, the resin and hardener components have been mixed together in a Hauschild mixer in the lab, which is a heavy, biaxial mixer that would be improbable to have in a surgical field. Therefore the materials need to be mixed by an alternative method, preferably by hand without any other equipment, in order to be injectable. Fortunately, and somewhat surprisingly, the reactive mixture foamed and cured properly when mixed by hand, either with a spatula and mixing cup, or passed back-and-forth between two syringes coupled by a luer-lok connector. Because the shear force generated when mixing by hand is less than in the Hauschild mixer, the optimal mixing time was approximately one minute, instead of 30 seconds.

Another challenging issue with *in situ* application of the polyurethane scaffolds is the concern of the free terminal NCO groups in unreacted polyisocyanates, which can be toxic by inhalation or prolonged skin contact. The vapor pressures of lysine-derived polyisocyanates are lower than that of hexamethylene diisocyanate trimer (HDIt), which in turn is much lower than the more toxic toluene diisocyanate (TDI, 0.018 mm Hg) and hexamethylene diisocyanate (HDI, 0.05 mm Hg) [5, 6]. Even so, concern could arise for surgeons who might use this reactive system repeatedly. The terminal NCO groups of LTI were capped with a 200-MW poly(ethylene glycol) to form an LTI-PEG prepolymer. This reaction scheme is shown in Figure 3.1. These primary NCO groups are more reactive than the secondary NCO from the lysine backbone, which is then free to participate in the polyurethane network. The lower reactivity of this secondary NCO allows the free isocyanate to be less toxic, but also necessitates a more reactive

catalyst. The reaction outcome is a polydisperse molecular weight distribution of products, ranging from 16.8% monomeric LTI (n = 0 in Figure 3.1) to 31.7% as an oligomer (n = 4) [7]. This approach was eventually successful, with adjustment of the various component ratios and catalyst type used for this particular reactive system. Commercial interest in these polyurethane scaffolds has secured a source of LTI, which previously had been a concern.

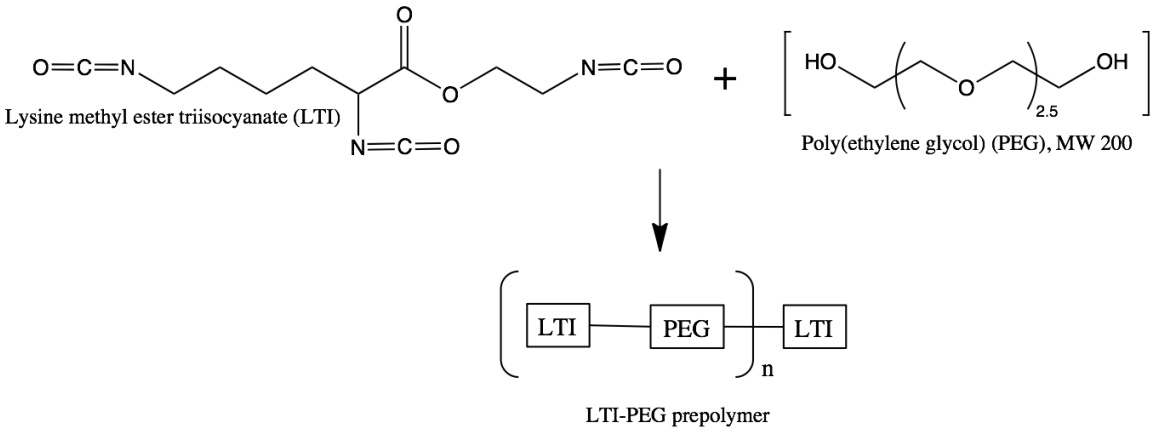

Figure 3.20. LTI-PEG prepolymer synthesis from LTI and MW 200 PEG. LTI-PEG prepolymer schematic shown representative of the polydisperse reaction products. The most common products range from LTI monomer (n = 0) to oligomers (n = 4) [7].

An unexpected phenomenon arose during the first attempt at applying the injectable polyurethane scaffold to a large excisional dermal rat wound. The wound bed and surroundings exude a good deal of blood and serum initially and whenever debrided. Since the polyurethane foam formation depends in large part on water to stimulate the foaming reaction, excess moisture clearly affects the foaming outcome because the ratio of reactive –NCO to –OH functional groups is unbalanced. The materials over-expanded and formed coarse voids, which cause poor adherence to wound boundaries. While this was discovered in the dermal wound, this same

situation of excess fluid at the wound site occurred in the bone defect models as well, to an even greater extent. Meticulous swabbing of the wound did not address this problem adequately, so a different approach was attempted.

Other, unrelated scaffold formulations with highly hygroscopic fillers (such as demineralized bone matrix) were observed to require additional water to compensate for the water in the resin absorbed by the filler. This concept was applied to these injectable materials. Hyaluronic acid (HA) is a high-molecular weight (MW ~ 3,000 kDa) polysaccharide naturally found in the extracellular matrix, especially important in skin and cartilage, and swells to a gel when added to water. It has been shown to promote local wound healing through inflammation [8]. Carboxymethylcellulose (CMC), also a plant-derived high-MW polysaccharide (MW ~ 90,000), was tested in tandem as a less expensive alternative to hyaluronic acid. As demonstrated in the Results and Discussion sections, this approach was successful in overcoming the effects of excess moisture upon foaming.

Methods

Materials. All materials are consistent with those described in Chapter II. Additionally, polyethylene glycol (PEG, MW 200 Da) was purchased from Alfa Aesar (Ward Hill, MA) and bis(2-dimethylaminoethyl)ether (BDAE) from Sigma-Aldrich (St. Louis, MO). Sodium hyaluronate (HA) and carboxymethylcellulose (CMC) were purchased from Acros Organics (Morris Plains, NJ).

LTI-PEG prepolymer synthesis. The terminal NCO groups of LTI were capped with 200-MW poly(ethylene glycol) (PEG) to form an LTI-PEG prepolymer, leaving

the secondary NCO groups free for formation of the polyurethane network with the polyol. PEG was added dropwise at a stoichiometric ratio to the LTI in a 100-mL reaction flask with mechanical stirring under argon for 24 hours at 45 °C. The prepolymer was then dried under vacuum at 80 °C for 14 hours.

Injectable scaffold synthesis. Capping of the LTI isocyanate end groups results in slightly decreased LTI reactivity, so a more reactive catalyst is needed for the polyurethane synthesis. More specifically, the blowing reaction, between isocyanate and water, needed a blowing catalyst for a proper balance between the blowing and gelling reactions. The catalyst bis(2-dimethylaminoethyl)ether (BDAEE), diluted (30: 70) in poly(propylene glycol), was applied to the system in combination with TEGOAMIN33 tertiary amine catalyst. After several trial attempts, the optimal level of each of component was determined for balanced gelling and blowing reactions, as well as a ≤ 10-minute rise time. The soft segment resin thus comprised the polyester polyol (900-MW, either T6C3G1L or T7C2G1L), 2.0 pphp water, 0.375 pphp BDAE:PPG, 0.625 pphp TEGOAMIN33, and 4.0 pphp calcium stearate. It was observed that materials mixed in the Hauschild mixer rose in approximately 25% faster than those hand-mixed in syringes. If needed, this discrepancy can be addressed by increasing the catalyst in the syringe-mixed formulations.

To synthesize the PUR scaffolds, the soft segment hardener and LTI-PEG prepolymer were combined in a one-shot manner with 0 to 35-wt% CMC or HA. These were mixed either in syringes linked by a luer-lok connector, or with a spatula in a mixing cup (as described in the following section), and injected into the particular mold or wound site. The targeted index (the ratio of NCO to OH

equivalents times 100) remained 115. This reactive liquid mixture then rose freely for 10 minutes and cured within 20 minutes to form the porous foams.

Development of mixing procedure. The polyol-based hardener and isocyanate-based resin were each loaded into separate syringes, which were then linked by a luer-lok connector. The experimental batch sizes could be mixed in 1, 3, and 10-mL luer-lok syringes. It was observed that additional air within the syringes resulted in more turbulent mixing and over-blown foams with coarse voids instead of a homogenous pore structure. The minimum mixing time for full emulsion was observed to be 2 minutes, with irregular foams resulting from shorter mixing times. The longer time limit for mixing, approximately 5 minutes, was governed by the increased viscosity of the polyurethane during the reaction and insurance of sufficient time for surgical manipulation. Interestingly, the smaller syringes required longer mixing times, perhaps because the larger syringes impart greater shear stress on the liquid when forced from the large syringe body to the narrow luer-lok connector. Figure 3.2 illustrates the material foaming after syringe mixing.

Alternatively, and especially when the material formulation contained a high percentage of solid filler, the two reactive components were combined in a small plastic mixing cup and stirred by hand with a spatula. This may be the most surgically relevant mixing procedure.

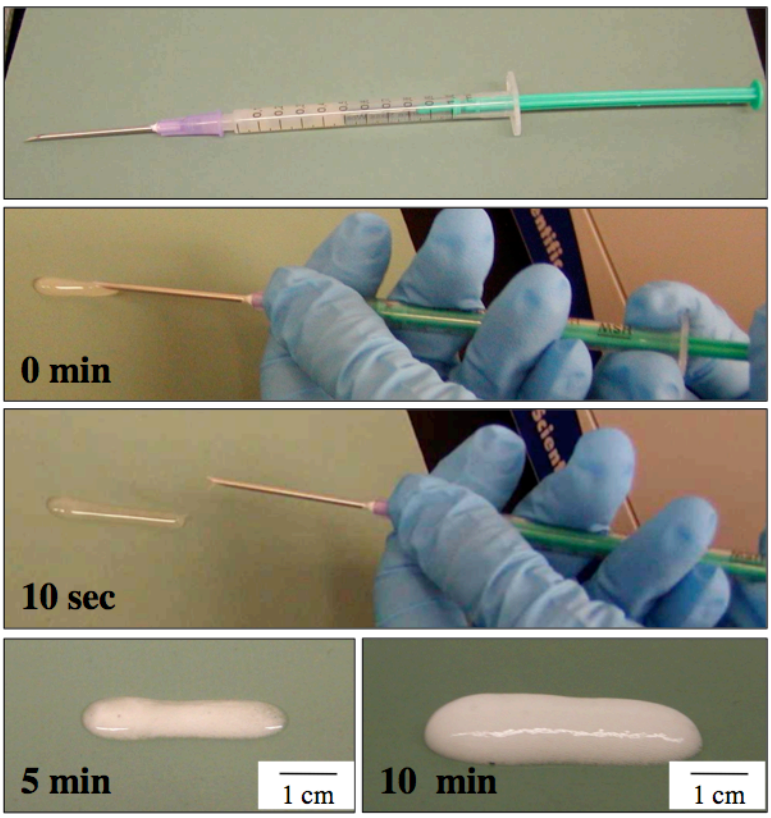

Figure 3.21. Injectability of PUR scaffolds: time-lapse photographs showing injection of the reactive liquid system.

Scaffold characterization. Core densities and porosities were determined from mass and volume measurements of triplicate cylindrical foam cores [9, 10]. The scaffold pore size and distribution were also assessed by scanning electron microscopy (Hitachi S-4200 SEM, Finchampstead, UK), after gold sputter coating with a Cressington Sputter Coater. Temperature profiles of the reactive mixture during foaming were assessed with a digital thermocouple at the centers of the rising foams. Scaffold degradation rates *in vitro* were evaluated by measuring the mass loss at various time points up to 24 weeks of incubation of triplicate 20-mg samples in 1 ml phosphate buffered saline (PBS) (pH 7.4) at 37 °C. At each time point, the samples were rinsed in deionized water, dried under vacuum for 48 hours

at room temperature, and weighed. For all characterization experiments of scaffolds containing solid fillers, CMC was used due to the lower cost.

Thermal analysis. Thermal transitions of the materials were evaluated by differential scanning calorimetry (DSC) using a Thermal Analysis Q1000 Differential Scanning Calorimeter. 10-mg samples underwent two cycles of cooling (20 °C/min) and heating (10 °C/min), between -80 °C and 100 °C.

Dynamic mechanical properties. Dynamic mechanical properties were measured using a TA Instruments Q800 Dynamic Mechanical Analyzer (DMA) in compression and tension modes (New Castle, DE). The protocols followed those outline in the Methods section of Chapter II. In compression mode, the compressive modulus was measured by the relaxation modulus after one minute at 50% compression (as a stress relaxation test). The compressive Young's modulus and compressive stress were determined from stress-strain tests form 0 to 50% strain. The glass transition temperature was also determined by cyclic heating and cooling between -80 and 100 °C. In tension mode, stress-strain tests were conducted until sample failure to determine the Young's modulus, ultimate strain, and ultimate stress.

In vivo dermal wound healing. The capacity of the scaffolds to facilitate dermal wound healing was evaluated in an excisional wound model (10-mm diameter) in adult male Sprague-Dawley rats, an example of which is shown in Figure 3.3. The materials were applied as a reactive liquid and expanded by gas foaming to fill the defects and cure *in situ*. The scaffolds were trimmed to be flush with the skin surface when they expanded beyond the wound outline. All materials

were sterilized by gamma irradiation at 5 kGy prior to surgery. The wounds were harvested at 4, 14, 21, and 28 days, and histological sections were stained with Gomori's trichrome or hematoxylin and eosin. The scaffolds were assessed for biocompatibility, biodegradation, cellular infiltration, and tissue regeneration. Other variables investigated included the performance of injectable scaffolds in comparison to the implants, and the possible benefit of HA over CMC. The study design is outlined in Table 3.1.

Figure 3.22. The PUR scaffold is applied as a reactive liquid mixture (left) and foamed *in situ* in a dermal excisional rat wound. The material expanded beyond the wound boundaries (middle), but was trimmed to size after it had completely dried (right).

Table 3.7. Study design to evaluate injectable scaffolds in an excisional dermal wound healing model.

Treatment groups		4 days	14 days	21 days	28 days
Injectable	25 wt-% HA	3	3	3	3
Injectable	25 wt-% CMC	3	3	3	3
Implant	15 wt-% HA	3	3	3	3
Implant	15 wt-% CMC	3	3	3	3

A second, larger dermal wound model was also evaluated, as it might be more realistic of a human dermal wound, with a larger surface available for tissue-material adherence. The treatment groups and time points are outlined in Table 3.2. The injectable materials were applied as above to an unstented, 1 in^2 square wound on the dorsum of each rat. Each wound and scaffold was covered with a non-stick absorbent Release gauze (Johnson & Johnson) and Tegaderm. The wounds were harvested at four time points evenly spaced between 7 and 35 days (days 7, 17, 26, and 35). The wounds were processed an evaluated as described above.

Table 3.8. Study design to evaluate injectable scaffolds with HA in a large excisional wound.

Treatment groups		7 days	17 days	26 days	35 days
Injectable	25 wt-% HA	4	4	4	4
Control	Blank	4	4	4	4

In vivo bone formation within scaffolds. Osteoconductivity of the injected scaffolds was evaluated in bilateral femoral plug defects in male Sprague-Dawley rats (Figure 3.4). The study design and treatment groups are outlined in Table 3.3. A monocortical plug bone defect (3 mm) was created in the distal region of the femur diaphysis, and hemostasis achieved as best as possible. The resin and hardener components were added to a mixing cup containing 25 wt-% hyaluronic acid and mixed with a spatula for 1 minute. The reactive mixture was then applied to the femoral defect(s). Depending on the batch size, several femoral plug defects could be filled with a single batch. All PUR materials were gamma-irradiated at 5 kGy before the surgeries. The femurs were harvested after 2 and 4 weeks and fixed in 10% phosphate-buffered formalin.

Table 3.9. Study design to evaluate the performance of the injectable scaffolds vs. implants in femoral plug defects.

Treatment groups		2 weeks	4 weeks
Injectable	35 wt-% HA	3	3
Implant	25 wt-% HA	3	3

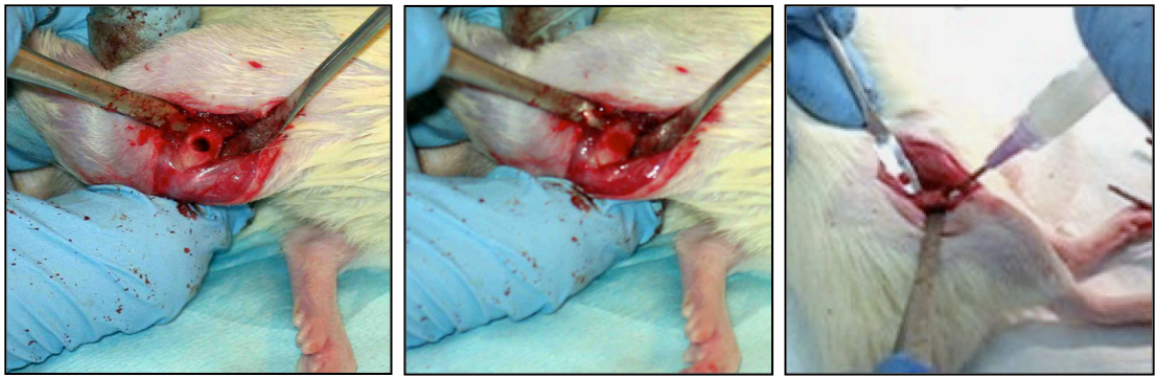

Figure 3.23. Femoral plug defect (left), filled with a PUR implant (middle) and injectable PUR (right).

Qualitative 3D analysis of mineralized bone formation in the scaffolds was performed using a μCT40 (SCANCO Medical, Bassersdorf, Switzerland) at a voxel size of 24 μm (isotropic). The PUR scaffold itself is not radio-opaque, so it does not appear in the μCT images.

The rat femur samples were then decalcified with 10% ethylenediaminetetraacetic acid (EDTA, Invitrogen), dehydrated, embedded in paraffin, and sectioned into 5-μm thick slices. The coronal slice sections were stained with hematoxylin and eosin (H & E). Specimens were examined under light microscopy. For histomorphometric examination, the amount of new bone formation in the scaffolds and the residual scaffolds were quantified at the center

sections of the samples [11]. The newly formed bone and polymer scaffold remnants at the defect site were highlighted using image-editing software (Photoshop, Adobe Systems Incorporated) and measured using image-analysis software (Scion Image, Scion Corporation), and the ratio of new bone formation and implant per whole scaffold area was evaluated.

Statistical Analysis. Statistical analysis of the results was performed using single factor analysis of variance (ANOVA). In cases where statistical significance is cited, the sample size is greater than or equal to three replicates per material.

Results

Incorporation of solid hygroscopic fillers. The hyaluronic acid and carboxymethylcellulose fillers could be added at up to 35 wt-%, above which the scaffolds could not properly cure. The reactive mixture could be mixed in syringes with up to 15 wt-% HA or CMC. The amount of filler chosen for a particular application was determined based on the amount of fluid (blood and serum) predicted to be present during the surgery. This generally concluded with 35 wt-% for bone defect, and 20 – 25 wt-% for dermal excisional wounds.

Scaffold characterization. The core densities and porosities of the injectable PUR scaffolds synthesized using the LTI-PEG prepolymer are given in Table 3.4. With no filler, they are slightly less porous than the equivalent LTI or HDIt foams. As expected, the densities increase and porosities decrease with a greater wt-% additive.

Table 3.10. PUR scaffold physical and thermal properties.

Sample (% CMC)	Density (kg/m^3)	Porosity (vol-%)	T_g – DSC (ºC)
6C3G1L (0)	110 ± 2	91 ± 0.1	19
7C2G1L (0)	150 ± 6	88 ± 0.5	-8
6C3G1L (15)	161 ± 8	87 ± 0.6	5
7C2G1L (15)	139 ± 14	89 ± 1	-2
6C3G1L (30)	269 ± 8	78 ± 0.6	-2
7C2G1L (30)	271 ± 20	79 ± 0.1	1

SEM images of foam cross-sections show interconnected pores in the range of 200 – 400 μm in diameter without any filler (Figure 3.5). When the materials are foamed with granular HA or CMC, the granules rise with the foam to become well dispersed through the scaffold and embedded in the pore walls. However, when the materials are foamed in a high-moisture environment, much of the hygroscopic filler absorbs moisture and dissolves, leaving behind evidence of the granules. Thus the final wt-% additive in the scaffold when foamed with excess moisture may be less than the amount initially added. The resulting physical and mechanical properties would be expected to fall between dry scaffolds at the initial loading and a scaffold with no filler.

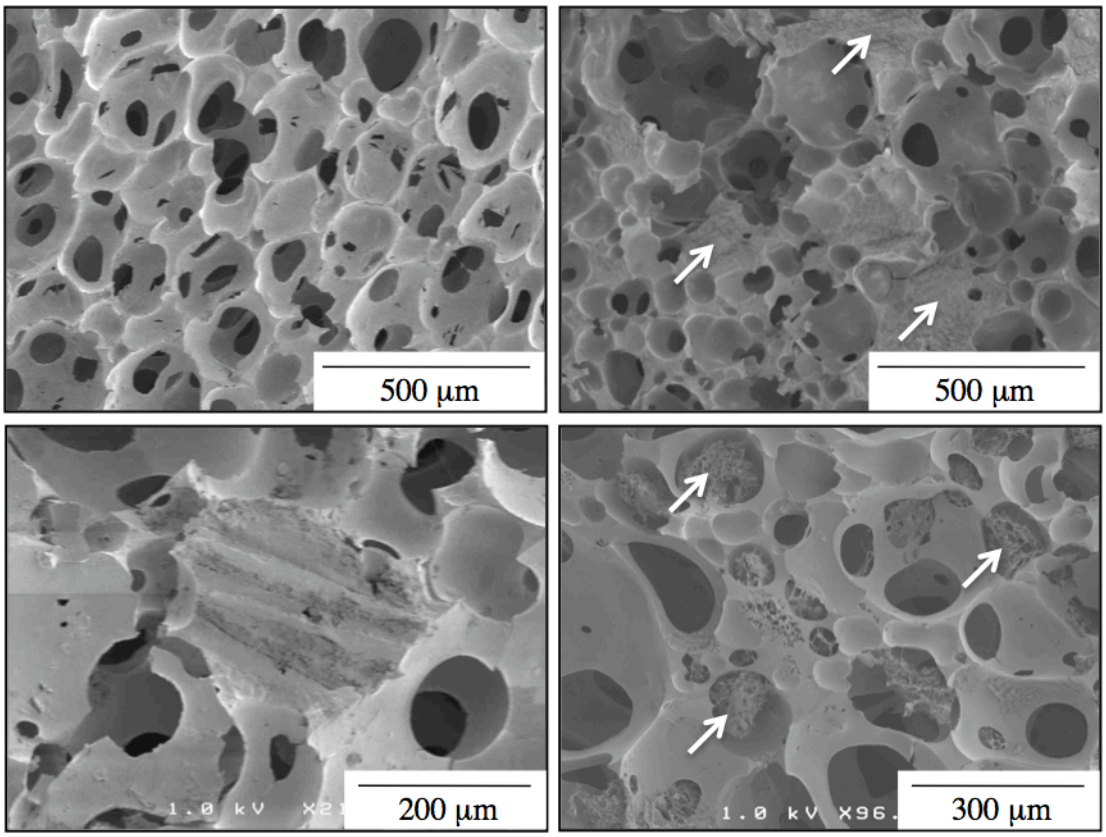

Figure 3.24. SEM images of injectable LTI-PEG PUR scaffolds with no additive (top left) and 35 wt-% HA (top right). The HA (or CMC) granules rise with the foam and become bridged in the pore walls, as indicated by the arrows, and magnified at bottom left. Some of the HA dissolved (arrows) when the PUR is foamed in a high-moisture environment, as would occur *in vivo* (bottom right).

The internal temperature within the polyurethane mixture was recorded with a digital thermocouple at the center of the rising foams in triplicate during the exothermic foaming reaction. Batch sizes (3-g) were large enough to diminish the effects of heat loss from the exterior surfaces of the foam. Starting at room temperature (21.2 °C), the maximum increase in temperature was 10.2 °C (Figure 3.6). *In vivo*, the maximum temperature and the exotherm would expectedly be higher, since the starting temperature would be elevated, at 37 °C.

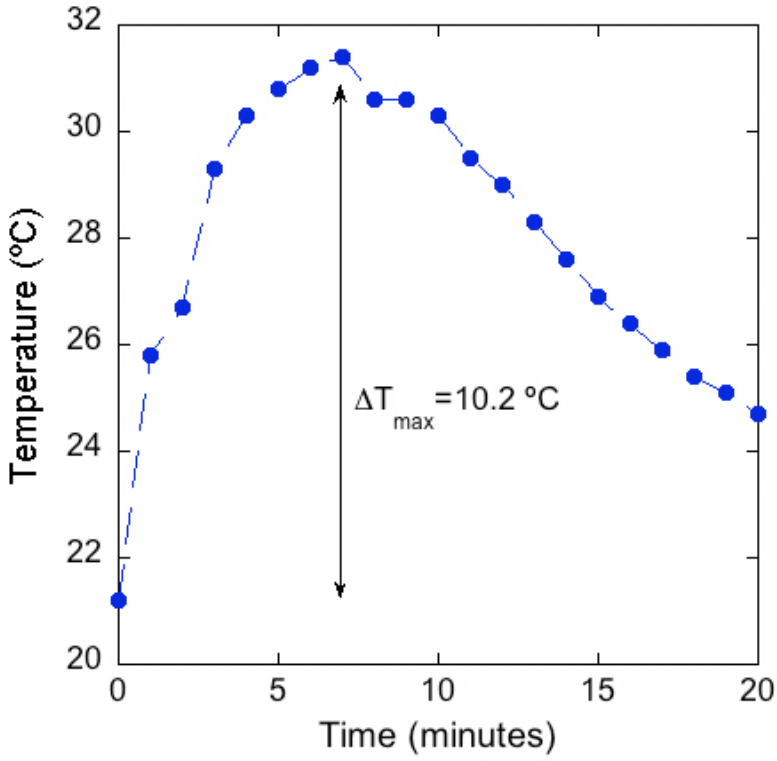

Figure 3.25. Temperature profile for rising PUR foam with LTI-PEG.

The degradation rates of the T6C3G1L/LTI-PEG and T7C2G1L/LTI-PEG materials in buffer at 37 °C, with 0, 15, and 35 wt-% CMC, were recorded for up to 24 weeks (Figure 3.7). The primary mechanism of degradation is hydrolysis of the ester bonds within the polyester soft segment. Interestingly, the hydrolysis rates for these LTI-PEG scaffolds are much slower than the corresponding LTI scaffolds, although these formulations all swell with water to a similar degree. By 24 weeks, the T6C3G1L900/LTI scaffolds had completely degraded to soluble fragments, and the T7C2G1L900/LTI materials had about 70% mass remaining (Figure 2.6). The slower degradation of the LTI-PEG materials most likely results from the reduced susceptibility of ether linkages to hydrolysis in comparison to ester linkages. PEG similarly slowed degradation of the T6C3G1L900/HDIt materials (Figure 2.6). The

fillers caused the materials to initially lose more mass within the first few days, which presumably corresponds to the CMC dissolution, after which the rates of polymer degradation are parallel.

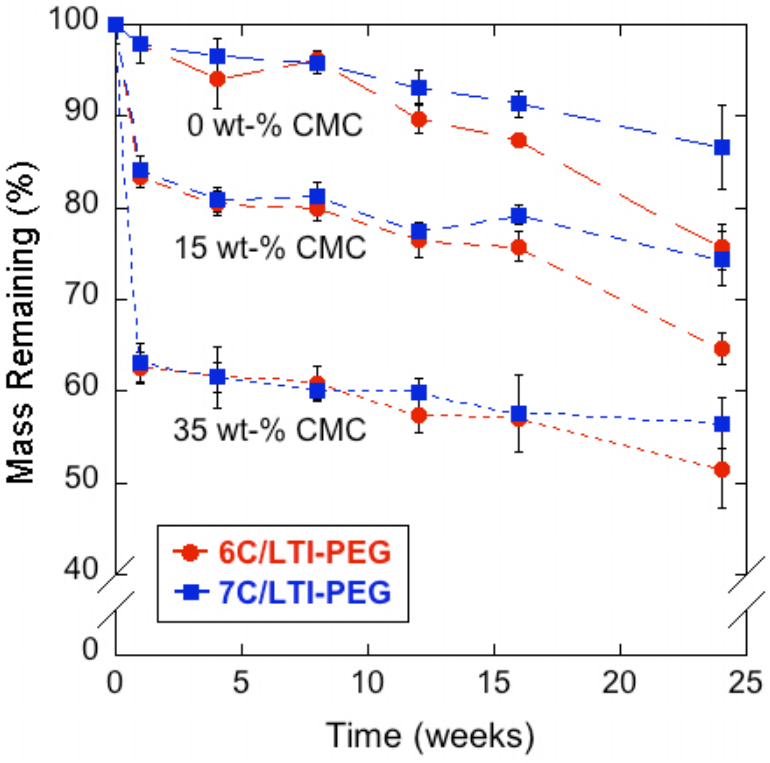

Figure 3.26. Degradation of injectable LTI-PEG scaffolds in PBS at 37 °C. The wt-% filler affects overall extent of degradation due to CMC dissolution, but at parallel rates (n = 3).

Thermal analysis. The glass transition temperatures by DSC of the LTI-PEG scaffolds ranged from -8.3 to 19.1 °C, but did not follow distinct trends with the increasing additive amounts.

Dynamic mechanical properties. When compressed for extended periods of time, these materials exhibit less than 5% permanent deformation. This elastomeric quality means that the materials do not fail under compression. Therefore

compressive stress-strain tests were carried out to 50% strain, instead of to failure. The Young's modulus values ranged from 69.8 kPa for scaffolds with no filler, to 140.9 kPa for those with 30 wt-% CMC. The differences were statistically significant ($p < 0.05$) only for the 30 wt-% scaffolds when compared to the 0 wt-%. The compressive stress, or stress measured at 50% strain, ranged from 16.9 to 95.3 kPa, with statistically significant differences between each of the 15 wt-% and 30 wt-% materials with respect to the 0 wt-% material. Representative stress-strain curves show how the fillers contribute greater strength and stiffness to the composite materials (Figure 3.8). These values are lower, for scaffolds with no filler, than those of the corresponding LTI & HDIt scaffolds (reference Table 2.3). Again, PEG seems to be the principal reason for the mechanical property difference, since the same trend occurs when PEG is added to the HDIt scaffolds. PEG depresses the glass transition temperature and causes the material to be within the rubbery plateau region at 37 °C instead of in the glassy or glass transition regions.

Table 3.11. PUR scaffold compressive mechanical properties as measured by DMA (n=3).

Sample	T_g – DMA (°C)	Young's Modulus (kPa)	Compressive Stress (kPa)
6C3G1L (0)	27	80 ± 9	18 ± 1
6C3G1L (15)	28	86 ± 11	81 ± 3
6C3G1L (30)	-	124 ± 15	92 ± 5

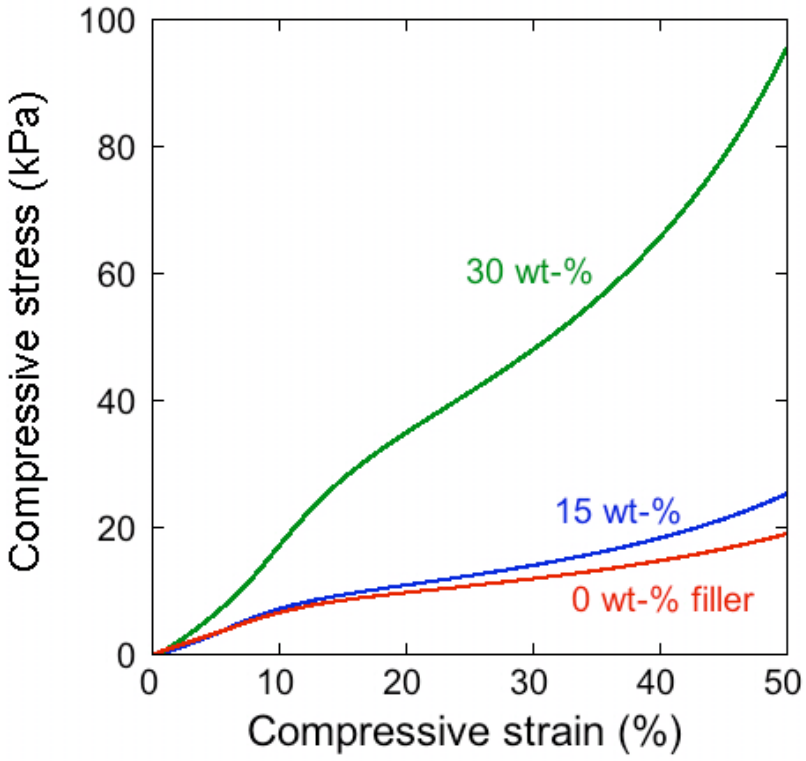

Figure 3.27. Representative compressive stress-strain profiles of LTI-PEG scaffolds until 50% strain.

Tensile stress-strain tests were conducted at a strain rate of 1% per minute until sample failure. The results are outlined in Table 3.6, and representative tensile stress-strain curves are shown in Figure 3.9. The Young's modulus values ranged from 60 to 280 kPa. The PEG in the LTI-PEG prepolymer lowered these values compared to the equivalent LTI scaffolds (reference Table 2.4) for scaffolds with no filler, while adding CMC reasonably increased the Young's modulus. The elongation (% strain) values at break were also less for these LTI-PEG materials, at 45 to 145 %, than for the LTI and HDIt scaffolds. The added fillers proportionately and significantly ($p < 0.05$) lowered the ultimate strain values, essentially acting as points of stress cracking in a nonhomogeneous composite material. The tensile

strength, or tensile stress at sample failure, ranged from 95 to 200 kPa, and the wt-% filler did not seem to have a significant effect.

Table 3.12. PUR scaffold mechanical properties as measured by DMA in tension mode (n=3).

	Tension		
Sample	**Young's Modulus (kPa)**	**Tensile Strength (kPa)**	**Strain at Failure (%)**
6C3G1L (0)	62.6 ± 4.0	121.5 ± 1.7	115.4 ± 7.6
6C3G1L (15)	135.2 ± 44.0	178.0 ± 32.2	114.6 ± 43.6
6C3G1L (30)	277.0 ± 9.7	90.6 ± 6.3	43.3 ± 1.8

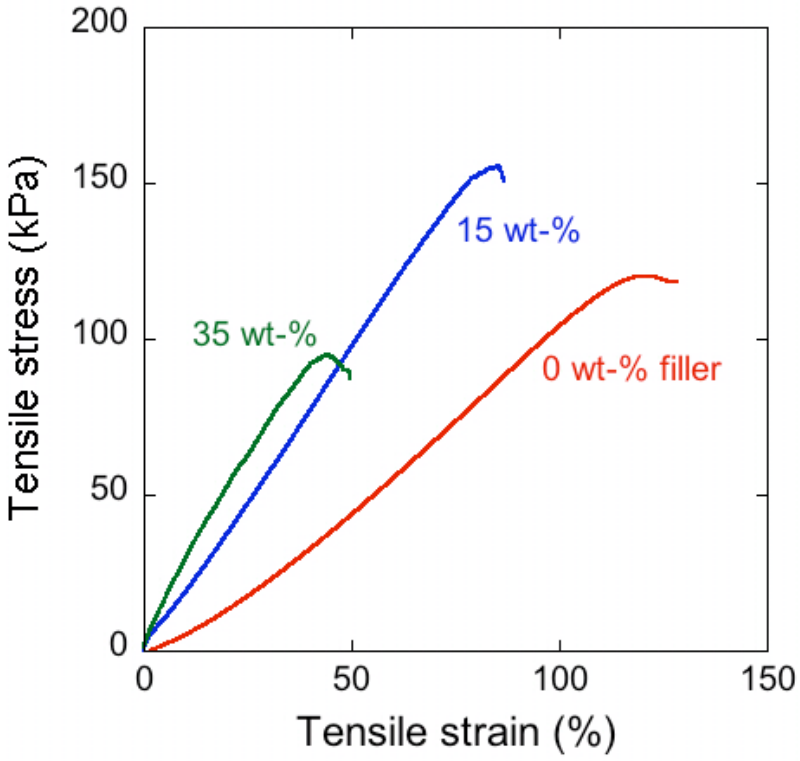

Figure 3.28. Representative stress-strain profiles of LTI-PEG scaffolds in DMA tension mode until failure.

In vivo dermal wound healing. The purpose of these experiments was to verify that the polyurethane reaction *in situ* does not elicit a substantial

inflammatory response, and that the cellular infiltration and material biodegradation is similar to that of the corresponding implants. Trichrome histology indicated mononuclear cell infiltration and early granulation tissue by day 4 (Figure 3.10). Collagen deposition and new tissue organization proceeded at 14 days and material remnants were transiently engulfed by macrophages with extensive angiogenesis. Mature granulation tissue and almost complete repithelialization were present by day 21, followed by evidence of folliculogenesis in the neoepidermis by day 28. Inclusion of the solid hygroscopic fillers HA and CMC in the scaffolds improved adhesion between the material and wound bed by absorbing excess moisture, and its presence may have augmented the local healing response. Qualitatively, hyaluronic acid may have promoted more accelerated angiogenesis and material degradation than CMC.

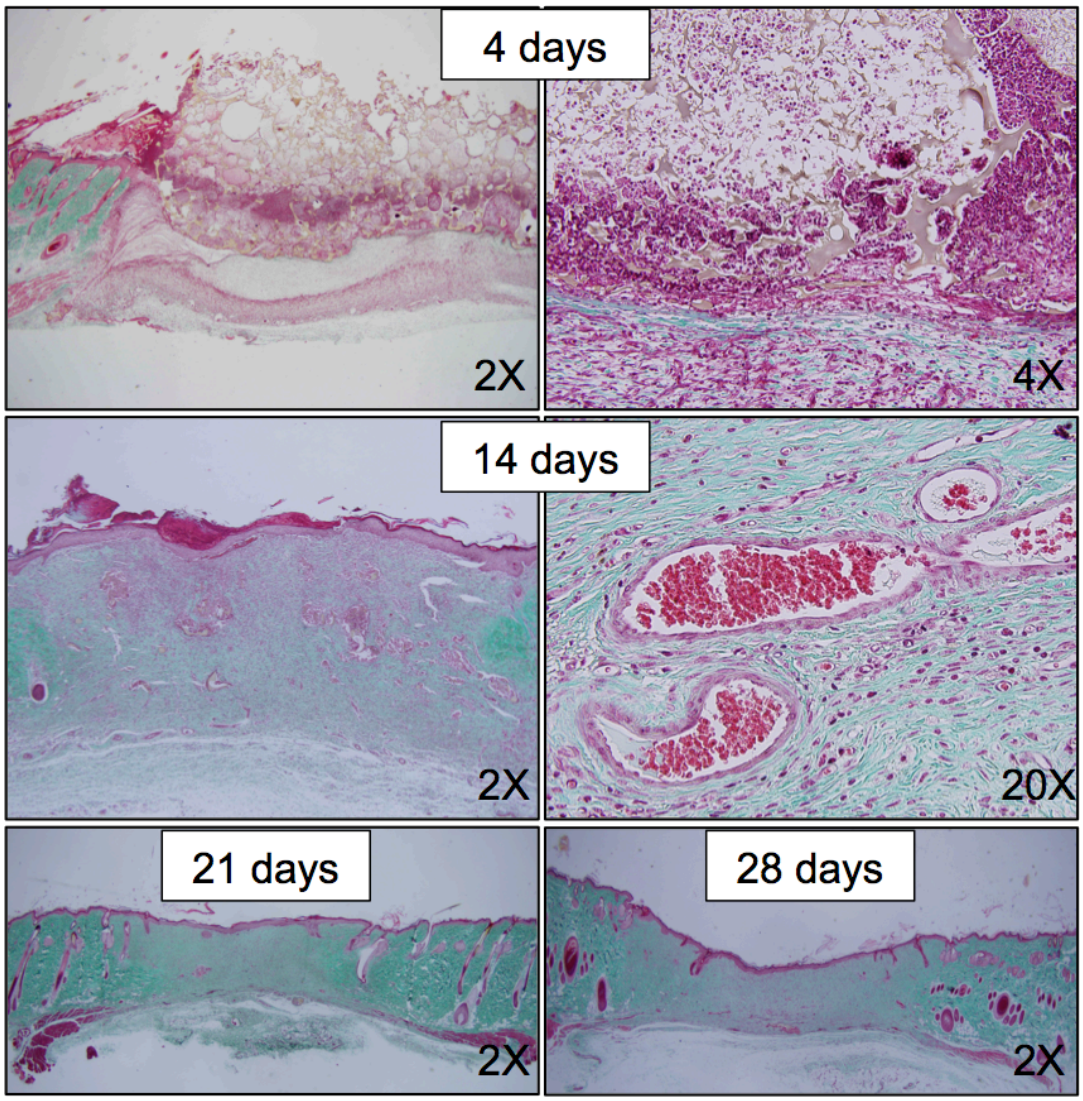

Figure 3.29. Trichrome-stained histological sections show the progression of dermal wound healing with the injectable PUR scaffold (35 wt-% HA). Cells migrate into scaffold edges by day 4 (top), with PUR degradation, granulation tissue and angiogenesis by day 14 (middle). Extensive collagen deposition and epidermal closure appear by days 21 and 28 (bottom).

Several healed wounds demonstrated evidence of appendage formation, specifically possible hair follicles and sebaceous glands, from the epidermis (Figure 3.11). Viewing dermal histological sections through a polarizing lens helps to distinguish mature collagen from newly deposited collagen. Specifically mature collagen fluoresces brightly, as in the unwounded tissue, while new collagen does

not fluoresce. These possible appendages are positioned within areas of new collagen, suggesting that they have developed de novo instead of being a product of epidermal contraction from the wound boundaries. The appearance of these appendages is particularly noteworthy because hair follicles and sebaceous glands do not typically emerge in scar formation. Complete regeneration of dermal wounds of this size as yet has not been successful.

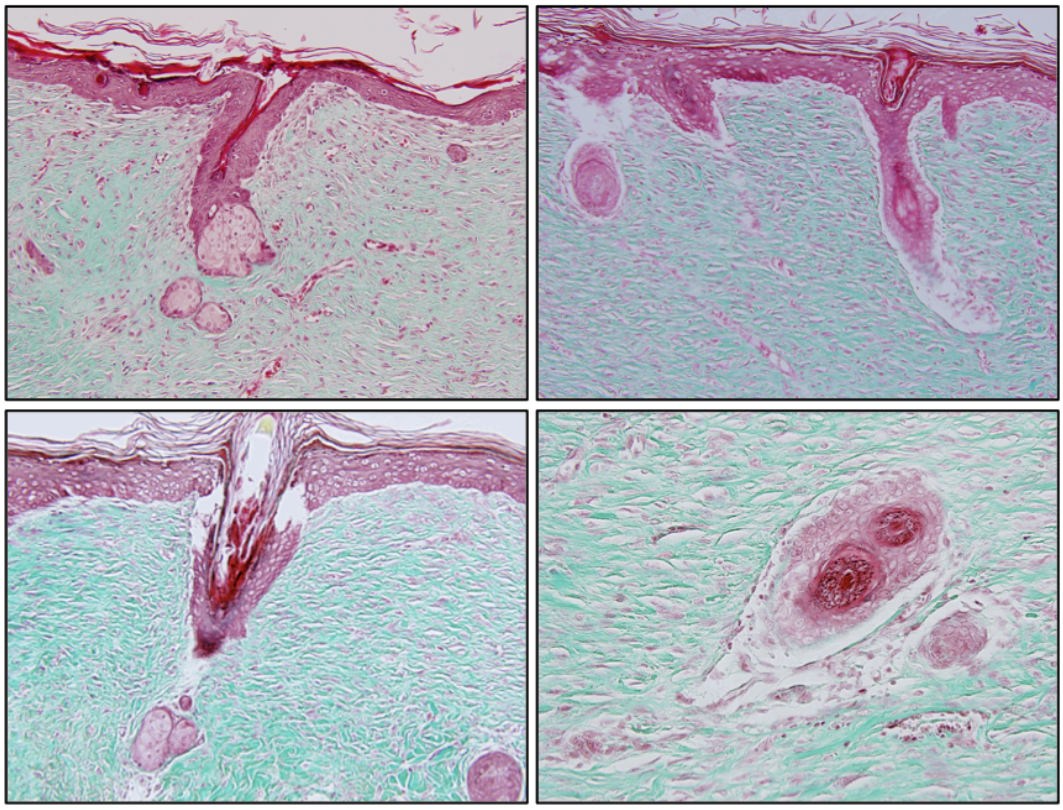

Figure 3.30. Appendages seen extending from the neoepidermis within the repaired wound area. These images were selected from different studies, with different additives, suggesting reproducible results. Probable folliculogenesis in upper left (30 wt-% HA, 28 days), upper right (25 wt-% CMC, 18 days), and bottom left (15 wt-% HA, 18 days). A possible sebaceous gland has begun to appear in the bottom right image (15 wt-% HA, 18 days).

The large excisional dermal wounds (1 x 1 in) were intended to be a more accurate model of a typical human wound. They demonstrated that the PUR

scaffolds adhere sufficiently to the underlying wound bed, provided that the scaffolds are covered with Tegaderm dressing. Due to their size, these wounds healed at a slightly slower rate than the smaller 10-mm excisional wounds. Figure 3.12 shows representative trichrome-stained histological sections of PUR scaffolds with 25 wt-% CMC. At day 7, much of the scaffold remained, with cellular infiltration visible at the bottom and sides of the section. By 17 days, the material had degraded significantly and the wound bed was filled with granulation tissue and some collagen deposition. Extensive angiogenesis was apparent with small blood vessels permeating of the wound bed. An eschar covered most of the wound surface, as the epithelium began to migrate from the wound edges toward the center. At 26 days, PUR degradation had proceeded, with mature granulation tissue and increased collagen throughout the wound bed. The epithelium had nearly covered the wound, although it appeared to still be in its hypertrophic phase characteristic of initial healing. No scaffold remnants were visible at day 35, and the reepithelialization was complete. These results confirmed that the PUR scaffolds could be successful in various wound sizes, although the healing time corresponded to the wound size.

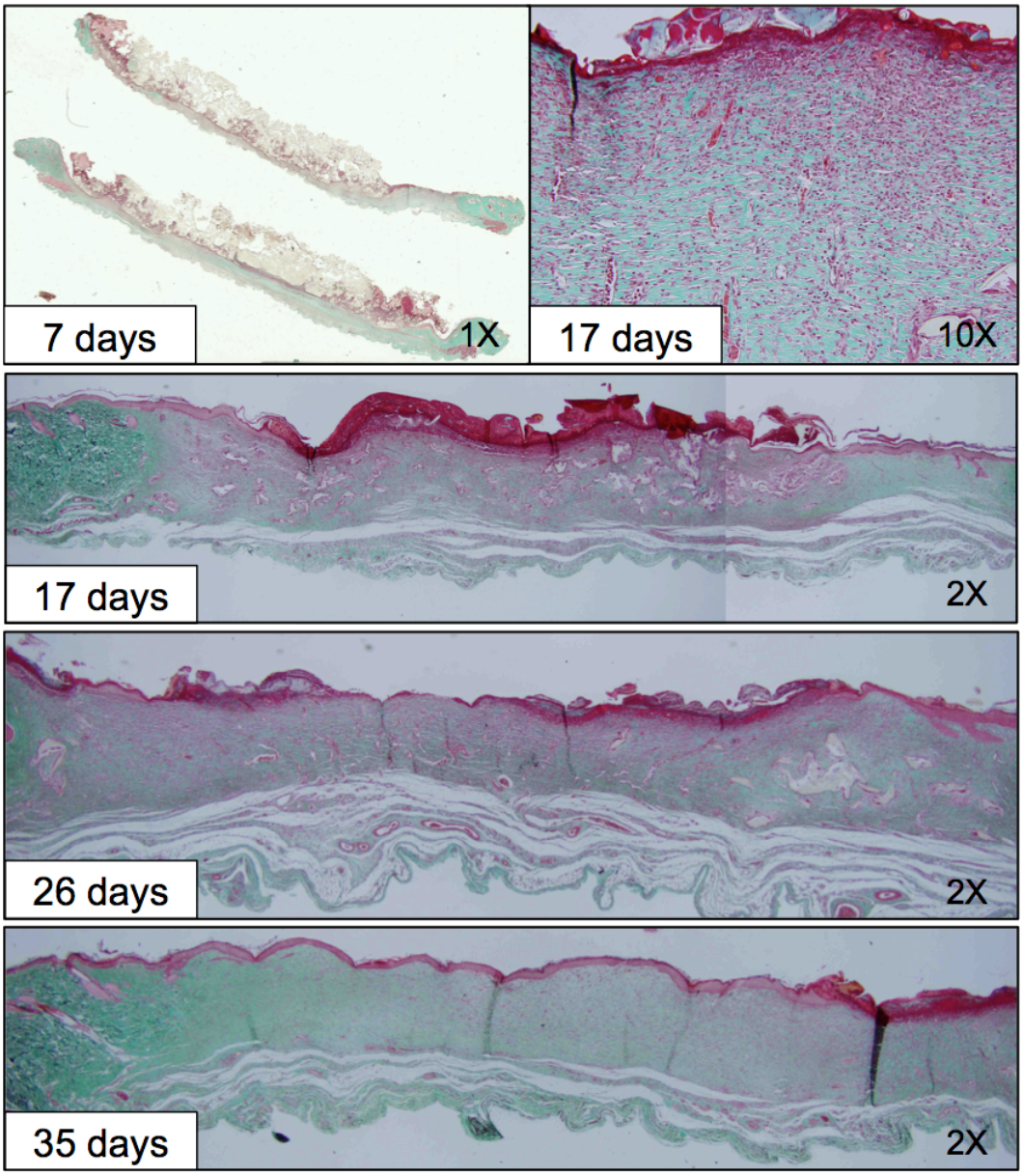

Figure 3.31. Trichrome histological sections of the large dermal wound healing show the PUR scaffold (25 wt-% CMC) in position at 7 days, but significantly degraded by 17 days. The 10X image at 17 days shows angiogenesis within the new matrix. The scaffold has almost completely degraded by day 35 with complete neoepidermal coverage.

In vivo bone formation within scaffolds. In bone defects, the liquid reactive mixture can fill any unoccupied space, ensuring thorough contact between the material and host bone. Figure 3.13 demonstrates the close apposition of polymer and native bone, even down to the scale of small, corrugated bone edges. This

hematoxylin and eosin (H & E) section was harvested just after surgery (day 0) to examine the initial state of the scaffold within the bone defect. Blood clots within the scaffold indicate that it is adequately perfused with blood and serum upon foaming, which may facilitate cell infiltration. This image also reveals some large and irregular pores, which are presumably the result of high moisture levels during foaming. SEM images of these same PUR scaffold samples *ex vivo* also display blood clots within the scaffold space, indicating rapid fluid uptake, and some undissolved HA (Figure 3.13).

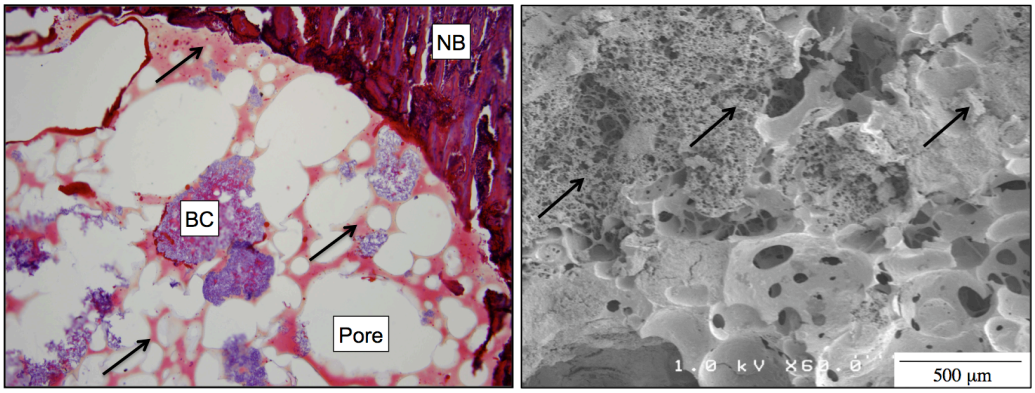

Figure 3.32. Histological section (left) and SEM image (right) at day 0 of injectable PUR scaffold (with 35 wt-% HA) in femoral plug defect. Material conforms to wound boundaries, as illustrated by close apposition between polymer (arrows) and native bone (NB) along corrugated bone edges. Blood clots (BC) indicate scaffold perfusion with blood. High moisture levels cause large and irregular pores. Undissolved HA and blood clots are evident in the SEM image (arrows).

At 2 weeks, µCT images show new bone starting to form at the edges of the defect and scaffold area (Figure 3.14). This new bone formation had increased by 4 weeks, although it had not yet grown through the entire defect. The scaffold itself does not demonstrate radio-opacity; thus only bone, not the material, is visible in µCT images. Decalcified histological sections stained with H & E supported the µCT findings, exhibiting cellular migration within the scaffold, as well as new bone

formation by osteoblasts near the defect edges (Figure 3.15). This histology shows new bone that is not yet mineralized, which does not manifest in μCT. At 4 weeks, the new bone is more mature and neoangiogenesis is apparent. PUR degradation is visible by week 2 and progressed by week 4; the size and shape of material remnants is altered from the original scaffold morphology (compared to Figure 3.13). Interestingly, cells do not seem to line the material fragments in the same way as in dermal wounds, which may indicate that macrophages are less prevalent within the bone microenvironment than in skin. The lower magnification images reveal that the injected scaffold protrudes slightly above the native bone surface. This may be due to over-foaming of the scaffold, or also as part of the normal callus formation during bone fracture repair.

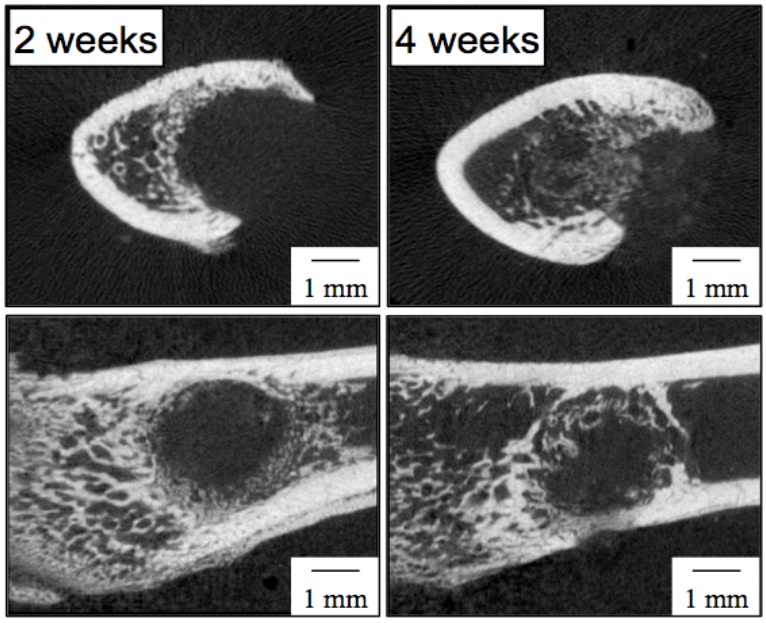

Figure 3.33. Coronal (top) and saggital (bottom) μCT images of injected PUR scaffold in femoral plug defect at 2 weeks (left) and 4 weeks (right) reveal bone ingrowth. The PUR scaffold itself is not radio-opaque.

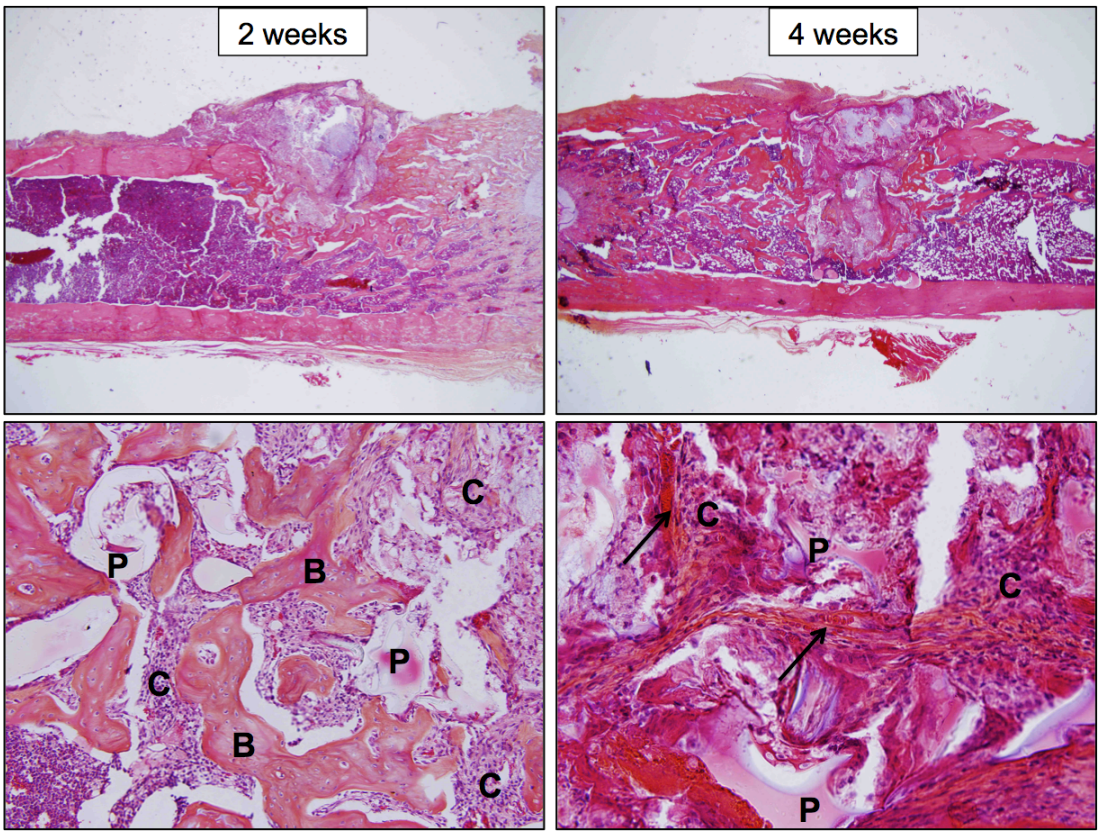

Figure 3.34. Decalcified histological bone sections with H & E staining at 4X (top) and 20X (bottom) magnification. Images at 2 weeks (left panels) demonstrate cellular infiltration (C) and new bone formation (B) within the scaffolds, alongside polymer remnants (P) that indicate ongoing PUR degradation. Integration proceeds at 4 weeks, with evidence of angiogenesis (arrows) within the healing bone defect.

Discussion

In this study, the potential of these biodegradable polyurethane scaffolds to be utilized as an injectable therapy was evaluated. The biocompatibility, elastomeric mechanical properties, and non-cytotoxic degradation products were established in Chapter II (Table 2.5). The attributes that allow these materials to be injected and cure *in situ* were subsequently demonstrated in these experiments. The LTI-PEG prepolymer was formulated to reduce possible isocyanate monomer toxicity, and the reaction produces a minimal exotherm. *In vivo* studies show no

evidence of acute toxicity from the polyurethane reaction. Beneficially, they adhered to the wound bed when injected, which is not the case with the implants.

However, challenges arise with the injectable indication, particularly with quality control amid site-specific variability. The most significant condition that arose was the substantially higher moisture level, from blood and serum, at the wound site than in a controlled laboratory setting. Excess water distorts the balance between the gelling and blowing reaction during PUR scaffold synthesis because it is necessary for the blowing reaction. In these situations, the blowing reaction outpaced the gelling reaction, which resulted in large and irregular pores, and an incomplete gelling reaction. The materials are formulated with an intended target index (NCO:OH ratio) of 115, so the excess water effectively increases the OH group availability and causes the foam to be under-indexed. The polymer was also prone to over-expansion, which caused difficulty in estimating the amount of material needed to expand and fill a given size wound. This problem was largely solved by incorporating solid hygroscopic fillers into the reactive PUR mixture to absorb the excess moisture, and dissolve into a quickly degrading gel.

An interesting, unforeseen phenomenon arose with the injectable materials. These foams form a nonporous film at any immiscible interface, such as air and the polystyrene mixing cups, during rising and curing. When synthesized in the lab, they are cut to the necessary size, such that all nonporous edges are trimmed away. However, this is clearly not an option when injected *in situ*. The first concern was that they might form this nonporous film against the wound bed surface, which would hinder cell migration into the scaffold. Fortunately the aqueous surface of the

wound bed allowed for a porous material-tissue interface. This still film forms on the exterior, air-facing surface of the scaffold in excisional dermal wounds. The film could be trimmed away to leave behind a porous facade, especially when the material foams beyond the epidermal surface, but this would be a tedious and prohibitive step in real-time surgery. Therefore attempts were made to estimate exactly the material needed for a given wound to avoid trimming. However, it was discovered that when the nonporous film remained atop the scaffold, healing was severely impeded. The eschar remained on the wound, limited granulation tissue, and did not reepithelialize. This suggests that fluid evaporation from the scaffold may be essential for stimulating fluid uptake, including nutrients essential for cells.

The search began for a topping that was miscible with the polymer to avoid the nonporous film formation, but that would not adhere to the scaffold permanently or alter the healing progression. That eliminated many commercially available synthetic, nondegradable wound dressings. The porous surface that resulted at the moist tissue-scaffold interface indicated that this film might not form at other (semi-) aqueous surfaces. An idea arose from this observation, which produced a feasible solution. A thin layer of a quickly degrading polysaccharide gel was applied to the foam surface during rising and curing. After the scaffold had cured and dried, the gel was then either wiped away or left to dissolve by natural wound exudate. The simplest candidates for this polysaccharide were those that were already included in the scaffold: hyaluronic acid and carboxymethylcellulose. CMC was chosen for cost purposes and was dissolved (15 mg/mL) in diH_2O, allowing it to be spread easily but also viscous enough to not flow. Like the

polyurethane reactants, this CMC gel was likewise sterilized by gamma irradiation prior to surgeries. The scaffold surfaces after applying (and drying) the gel did not have the same pore structure as the scaffold interior, but it was nevertheless porous in contrast to the untreated scaffold surface (Figure 3.16).

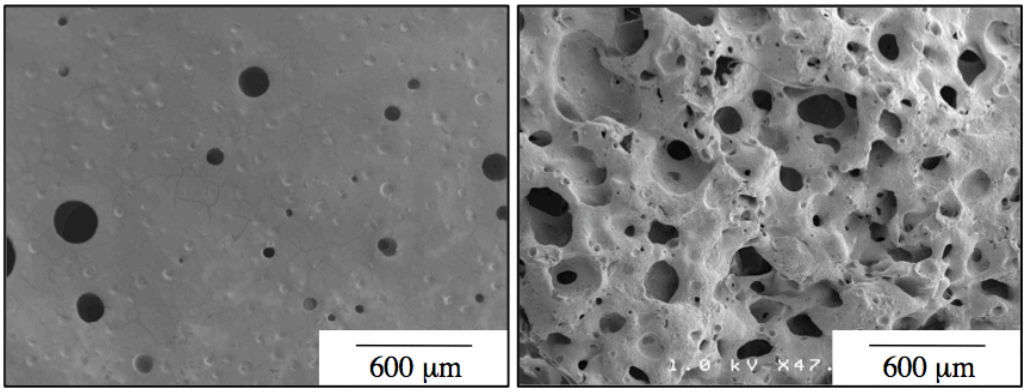

Figure 3.35. SEM images show low-porosity surface film of uncoated PUR scaffold (left) and higher porosity of CMC gel-coated surface (right). In this example, the gel has been wiped away and the foam was dried before imaging.

Hyaluronic acid was chosen as a filler because of its hygroscopic properties, but also its reported biological benefits [12-16]. Hyaluronan is present throughout the wound healing process. It reportedly upregulates type-III collagen and TGF-β3 expression, which may encourage a "fetal-like cell environment" for scarless healing. HA may play a role in controlling angiogenesis. Topically applied HA has been shown to accelerate skin wound healing in rats [12], which supports the incorporation of HA in the PUR scaffolds. The *in vivo* results of these studies qualitatively suggested that HA promoted slightly faster collagen deposition, angiogenesis, and material degradation. While the presence of either polysaccharide facilitated healing, the dosages used did not appear to have a large

effect. Furthermore, any benefit observed with HA would need to be weighed against the significant costs in comparison to CMC.

Conclusions

Injectable polyurethane scaffolds demonstrate potential as a template for wound repair and perhaps regeneration of bone, skin, and perhaps other soft tissues. These materials possess many benefits of an injectable application, namely ease of application, customizability, and complete filling of odd wound geometries. The elastomeric mechanical properties further ensure that the material will maintain contact with the native tissue. The *in situ* polymerization reaction does not exhibit any cytotoxic effects – chemical or thermal – on the surrounding tissue.

The injectable scaffolds appear to perform to the same standards as the implanted PUR materials. However, application-specific variables must always be considered, such as the moisture level at the wound site, which can cause variability in the scaffold pore structure and tissue adherence. The rate and quality of healing will likely be accelerated with the inclusion of chemokines within the scaffold, such as PDGF-BB, SDF, or BMP-2, to attract cells and stimulate new tissue matrix formation. While the presence of the PUR scaffold within a wound can prolong the total healing time for a wound that would otherwise close independently, the healed tissue seems to be of higher quality with reduced scar formation. The scaffolds would be especially beneficial in cases of critical size wounds that otherwise are too large to heal.

References

1. Praemer A, Furner S, Rice D. Musculoskeletal conditions in the united states. American academy of orthopaedic surgeons. Park Ridge, IL, 1992. p. 85-124.

2. Khan Y, Yaszemski MJ, Mikos AG, Laurencin CT. Tissue engineering of bone: Material and matrix considerations. *Journal of Bone & Joint Surgery: American Edition* 2008; 90(Supplement 1): 36-42.

3. Timmer MD, Ambrose CG, Mikos AG. Evaluation of thermal- and photo-crosslinked biodegradable poly(propylene fumarate)-based networks. *Journal of Biomedical Materials Research Part A* 2003; 66A(4): 811-818.

4. Kim CW, Talac R, Lu L, Moore MJ, Currier BL, Yaszemski MJ. Characterization of porous injectable poly(propylene fumarate)-based bone graft substitute. *Journal of Biomedical Materials Research Part A* 2008; 85(4): 1114-1119.

5. Adhikari R, Gunatillake PA, inventors. Biodegradable polyurethane/urea compositions Patent No. WO 2004/009227 A2, 2004.

6. Guelcher S, Srinivasan A, Hafeman A, Gallagher K, Doctor J, Khetan S, et al. Synthesis, in vitro degradation, and mechanical properties of two-component poly(ester urethane)urea scaffolds: Effects of water and polyol composition. *Tissue Engineering* 2007; 13(9): 2321-2333.

7. Dumas JE, Zienkiewicz K, Tanner SA, Prieto EM, Bhattacharyya S, Guelcher S. Synthesis and characterization of an injectable allograft bone/polymer composite bone void filler with tunable mechanical properties. *Tissue Engineering Part A* 2010.

8. Jiang D, Liang J, Noble PW. Hyaluronan in tissue injury and repair. *Annual Review of Cell and Developmental Biology* 2007; 23(1): 435-461.

9. ASTM-International. D3574-05. Standard test methods for flexible cellular materials - slab, bonded, and molded urethane foams. 2007; p. 360-368.

10. Hafeman AE, Li B, Yoshii T, Zienkiewicz K, Davidson JM, Guelcher SA. Injectable biodegradable polyurethane scaffolds with release of platelet-derived growth factor for tissue repair and regeneration. *Pharmaceutical Research* 2008; *25*(10): 2387-2399.

11. Torigoe I, Sotome S, Tsuchiya A, Yoshii T, Maehara H, Sugata Y, et al. Bone regeneration with autologous plasma, bone marrow stromal cells, and porous beta-tricalcium phosphate in nonhuman primates. *Tissue Eng Part A* 2009.

12. David-Raoudi M, Tranchepain F, Deschrevel B, Vincent J-C, Bogdanowicz P, Boumediene K, et al. Differential effects of hyaluronan and its fragments on

fibroblasts: Relation to wound healing. *Wound Repair and Regeneration* 2008; 16(2): 274-287.

13. Li L, Asteriou T, Bernert B, Heldin C-H, Heldin P. Growth factor regulation of hyaluronan synthesis and degradation in human dermal fibroblasts: Importance of hyaluronan for the mitogenic response of pdgf-bb. *Biochem J* 2007; 404(2): 327-336.

14. Poulsom R. Cd44 and hyaluronan help mesenchymal stem cells move to a neighborhood in need of regeneration. *Kidney International* 2007; 72(4): 389-390.

15. Price RD, Berry MG, Navsaria HA. Hyaluronic acid: The scientific and clinical evidence. *Journal of Plastic, Reconstructive & Aesthetic Surgery* 2007; 60(10): 1110-1119.

16. Zou L, Zou X, Chen L, Li H, Mygind T, Kassem M, et al. Effect of hyaluronan on osteogenic differentiation of porcine bone marrow stromal cells in vitro. *Journal of Orthopaedic Research* 2008; 26(5): 713-720.

CHAPTER IV

CHARACTERIZATION OF SCAFFOLD BIODEGRADATION MECHANISMS

Introduction

Biodegradable polyurethanes hold much promise for application in several areas of wound healing and tissue engineering. They have demonstrated biocompatibility and support of new tissue formation in bone [1-4], skin [5, 6], nerve [7], and cardiovascular regeneration [8], resorbed upon cell infiltration and deposition of new tissue. However, understanding the mode of degradation and nature of the degradation products, as well as the cellular response and mechanisms of local inflammation resulting from the implanted materials, is pivotal to the success of these biomaterials *in vivo*. The study of polyurethane biodegradation originated from observations of the premature degradation and failure of poly(ester urethane) Meme breast implants [9], which led to the use of more hydrolytically stable poly(ether urethane)s and poly(carbonate urethane)s for biomedical implants. Investigations continued to better understand the mechanisms of polyurethane biodegradation to then improve their stability and longevity *in vivo*.

In recent years, poly(ester urethane)s that are designed to undergo controlled degradation have been investigated as scaffolds for tissue regeneration. Poly(ester urethane)s (PUR) degrade by hydrolysis of the ester linkages [10, 11], but in many cases they have been observed to undergo significantly accelerated degradation *in vivo* compared to *in vitro*, suggesting cellular-mediated effects [5, 12].

Interestingly, the differential degradation rates between various polyurethane formulations are consistent *in vitro* and *in vivo*, implying that some chemical structures are inherently more susceptible to such mechanisms. Biodegradation of polyurethanes intended for long-term implants has been extensively investigated, contributing valuable insight into the mechanisms of degradation and possible strategies for extending polyurethane biostability *in vivo* after implantation [13-17]. While some studies have looked into cellular-mediated degradation of other biomaterials [18-20], to our knowledge, little has been reported regarding degradative mechanisms of biodegradable polyurethanes. For potential clinical use, it is especially important to understand how cells interact with these materials and the accompanying degradation characteristics and products of these materials. These materials ideally should be degraded and cleared from the body by natural processes, with a limited inflammatory response [21]. Such examples of complete degradation and resorption, via natural metabolic pathways, of synthetic materials derived from non-natural precursors are rare.

Biomaterial implantation immediately triggers an acute inflammatory response characterized predominantly by neutrophils and typically lasts several days, depending on the extent of injury [21]. A chronic inflammatory response follows with recruitment of mononuclear lymphocytes and circulating monocytes, which differentiate into macrophages at the wound site, spurred by local chemoattractants such as platelet-derived growth factor (PDGF), interleukin-1 (IL-1), and CXCL4. Serum and extracellular matrix (ECM) proteins including albumin, fibrinogen, and vitronectin, adsorb to the material surface and facilitate

macrophage-material adhesion via interactions with cell surface integrin receptors. Macrophages can phagocytose small material particles (10-100 μm), but fuse into multinucleated foreign body giant cells when larger surfaces that cannot be internalized and upon stimulation by IL-4 and IL-13 [21, 22]. Presence of these giant cells denotes an elevated degree of "cellular activation" and secretion of degradative enzymes [21].

For biocompatible materials, chronic inflammation is generally limited to the wound or implant site and lasts for no more than two weeks [21, 23]. Macrophages remain during the following period of matrix remodeling and/or material degradation, termed the foreign body reaction. Their continued presence and activity indicates a principal role in contributing to the accelerated degradation observed *in vivo* [23]. In addition to producing degradative substances, macrophages also secrete cytokines and chemokines that can recruit and stimulate cells, including fibroblasts and osteoblasts, to produce new tissue matrix, as well as stimulate angiogenesis [24]. Because of the macrophage-material adherence, the degradative activity depends on the material surface chemistry, and it follows that the surface-to-volume ratio, especially for our highly porous polyurethane scaffolds, can have a significant impact on degradation rate.

Labow and Santerre have conducted significant research of polyurethane degradation by macrophage-associated enzymes. They cultured model biostable polyurethanes, primarily polycarbonate- and polyether-urethanes, with neutrophils and monocyte-derived macrophages (MDM) and found the most active enzymes involved in hydrolytic polyurethane degradation to be cholesterol esterase, carboxyl

esterase and other serine proteases [16]. Cholesterol esterase expression in particular increases significantly as monocytes recruited to the implantation site differentiate into macrophages [25].

Anderson and colleagues have provided comprehensive studies for a parallel approach to studying *in vivo* degradation, focusing on a different aspect of macrophage-secreted substances: reactive oxygen intermediates (ROI). They demonstrated evidence of oxidative chain scission and crosslinking of specifically poly(ether-) and poly(carbonate urethane)s. *In vitro* incubation of these materials in media containing hydroxyl radicals produced similar ATR-FTIR spectra as when explanted materials had undergone degradation *in vivo* [26, 27].

Kohn and colleagues synthesized model compounds to mimic the repeat units of tyrosine-derived polycarbonates, in order to characterize the possible degradation pathway and products. Like polyurethanes, these materials degrade hydrolytically, and so identifying those bonds most susceptible to hydrolytic cleavage might allow the subsequent design of materials with tailored degradation properties. For example, they found that the backbone carbonate bond was hydrolyzed more readily than the ester bond on the pendent side chain, and that longer side chains lead to slower hydrolysis rates.

Previous *in vitro* and *in vivo* studies demonstrated that these biodegradable, porous poly(ester urethane) scaffolds are biocompatible in skin and bone wound healing. This study aims to utilize the insight from these previous studies to elucidate the degradation mechanism and products of our biodegradable poly(ester urethane)s. The cellular response to these materials was further investigated –

specifically the role of the inflammatory response in materials degradation. We evaluated the determinants of degradation, including soft and hard segment contributions, as well as the degradation products produced by cellular effects *in vivo*. Lastly, we assessed the scaffold physical and mechanical properties over the course of degradation, which are important for clinical performance.

Methods

Materials. Monobasic sodium phosphate buffer, sodium azide, hydrogen peroxide, and cobalt chloride were purchased from Fisher Scientific (Pittsburgh, PA), while all other reagents were purchased from Sigma-Aldrich (St. Louis, MO) or as indicated in Chapter II (p. 16).

PUR scaffold synthesis. Trifunctional polyester polyols (900-Da) were prepared according to the protocol in Chapter II (p. 16). PUR scaffolds were synthesized by one-shot reactive liquid molding of (A) hexamethylene diisocyanate trimer (HDIt; Desmodur N3300A) or lysine triisocyanate (LTI) and (B) a hardener component comprising the polyol, 1.5 parts per hundred parts polyol (pphp) water, 4.5 pphp (1.5 pphp for LTI foams) TEGOAMIN33 tertiary amine catalyst, 1.5 pphp sulfated castor oil stabilizer, and 4.0 pphp calcium stearate pore opener. The isocyanate was added to the hardener and mixed for 15 seconds in a Hauschild SpeedMixer™ DAC 150 FVZ-K vortex mixer (FlackTek, Inc., Landrum, SC). This reactive liquid mixture then rose freely for 10 – 20 minutes [5, 28]. The targeted index (the ratio of NCO to OH equivalents times 100) was 115. To examine the effects of a hydrophilic polyether segment on the material properties, some

materials were synthesized with poly(ethylene glycol) (PEG, 600 Da), such that the total polyol content consisted of 50 mol-% PEG and 50 mol-% of the polyester polyol.

In vitro degradation. Scaffold degradation rates *in vitro* were evaluated by measuring the mass loss at various time points up to 36 weeks. Triplicate 10-mg samples were incubated in 1 ml phosphate buffered saline (PBS) (pH 7.4) on a shaker at 37 °C, as described previously. The samples were not removed from the buffer until each specific time point, when they were rinsed in deionized water, dried under vacuum for 48 hours at room temperature, and weighed. These samples and buffer were used for the analysis of PUR scaffold degradation products, specifically a-hydroxy acids, lysine, and ethanolamine.

Degradation-dependent mechanical properties. Long-term *in vitro* degradation of scaffolds was measured with the periodic mass loss of triplicate samples through 36 weeks of incubation in phosphate buffered saline (pH 7.4) at 37 °C. Also at 4, 8, and 12 weeks, core densities were determined from mass and volume measurements of triplicate cylindrical foam cores (see Equation 2.4). The pore size distribution was assessed by scanning electron microscopy (Hitachi S-4200 SEM, Finchampstead, UK).

Dynamic mechanical properties of the scaffolds were measured using the dynamic mechanical analysis (DMA) in compression and tension modes after 4, 8, and 12 weeks degradation time. Cylindrical 7 x 6 mm samples were compressed along the axis of foam rise. Stress-strain curves were generated by controlled-force compression of the cylindrical foam cores at 37 °C. With an initial force of 0.1 N,

each sample was deformed at 0.1 N/min until it reached 50% strain (i.e. 50% of its initial height). The Young's modulus was determined from the slope of the initial linear region of each stress-strain curve [29]. Due to their highly elastic properties, the scaffolds could not be compressed to failure. Therefore, as a measure of compressive strength, the compressive stress of triplicate cylindrical samples after one minute at 50% strain was measured using the DMA stress relaxation mode at 37 °C [30]. Calculated from the measured force and cross-sectional sample area, the compressive stress indicates material compliance such that more compliant materials require lower stress to induce a particular strain.

Tensile testing was performed on thin, rectangular scaffold samples (10 mm long x 5 mm wide x 1.7 mm thick). Stress-strain curves were generated by elongating the samples at 1% strain per minute at 37 °C until failure. The Young's modulus was calculated as described above, and the tensile strength was determined as the stress (kPa) at failure.

In vitro degradation with assessment of enzymatic and oxidative effects. Scaffold degradation rates *in vitro* were evaluated by measuring the weekly mass loss up to 8 weeks of incubation in 0.5 M monobasic sodium phosphate buffer (pH 7.0) with 0.2% w/w sodium azide at 37 °C. Polyurethane degradation *in vivo* is documented to occur at a significantly faster rate than under *in vitro* conditions, suggesting that enzymatic or oxidative mechanisms contribute to the observed faster degradation *in vivo* [16, 18, 21]. To identify the mechanisms by which PUR scaffolds degrade *in vivo*, materials were incubated in the presence of each of the following: cholesterol esterase, carboxyl esterase, lipase, and hydrogen peroxide, as

well as with buffer alone, in order to study the roles of enzymatic and oxidative degradation mechanisms for biodegradable polyurethanes.

Triplicate 25-mg samples were each incubated in 1 mL of the respective enzyme- or peroxide-containing media, and the media was refreshed every 3-4 days to maintain enzyme activity. The enzyme concentrations, determined from previous literature as well as by the solubility limits of the enzymes in the media, were as follows: 1 U/mL cholesterol esterase (CE), 1 U/mL carboxyl esterase (CXE), 10 U/mL lipase (L), and 20 wt-% hydrogen peroxide (H_2O_2) in 0.1 M cobalt chloride ($CoCl_2$) [31, 32]. The cobalt ion and hydrogen peroxide react to form hydroxyl radicals, which simulate the oxidative radicals at the material-macrophage interface. Enzyme activity was verified with a nonspecific enzymatic activity assay based on the enzymatic conversion of *p*-nitrophenyl butyrate into *p*-nitrophenyl [17, 33].

Analysis of PUR scaffold degradation products. Lactic (from D,L-lactide), glycolic (from glycolide), 6-hydroxycaproic (from ε-caprolactone), and isocyanuric (from HDIt) acids were separated by isocratic elution in a Transgenomic ion exchange column (ICSep ICE-ION-300 Column 7.8 x 300 mm). They were passed through a guard column at 80 ˚C using 0.001 N sulfuric acid as eluent and analyzed at 210 nm (UV). With a flow rate of 0.5 mL/min, the standard peaks for isocyanuric, glycolic, lactic, and 6-hydroxycaproic acid eluted at 14.3, 15.4, 16.1, and 30.2 min, respectively. The samples were analyzed by an external standard curve in the range from 2.5 μg/mL to 100 μg/mL of each acid using the Waters Breeze system.

The lysine content in the scaffold degradation products was analyzed spectrophotometrically based on a colorimetric ninhydrin assay [34]. The

ninhydrin reagent was prepared by dissolving 3 g ninhydrin and 38 mg stannous chloride in 100 mL solvent (2:1:1, DMSO : H_2O : 4M acetic acid-acetate buffer). Degradation media samples from each of the scaffolds, diluted in sodium phosphate buffer as needed, was combined with 0.4 mL ninhydrin reagent in separate vials for a total volume of 1.5 mL each. These vials were then incubated in a heating block at 110 °C for 30 min, followed by immediate cooling in an ice water bath to stop the reaction. The solutions were then transferred to a 96-well plate at 150 μL per well for absorbance at 580 nm and compared to lysine standard curve of 0.5 – 50 μg/mL.

The released ethanolamine was derivatized with 5-(Dimethylamino)naphthalene-1-sulfonyl chloride (dansyl chloride, DNS-Cl) and quantified by HPLC. 50 μL of each sample was added to 225 μL dansyl chloride (40 mM in acetonitrile) and 225 μL borate buffer (pH 9.5). The mixtures were vortexed for 10 seconds and incubated at 55 °C for 30 minutes. After cooling to room temperature, the samples were syringe-filtered and injected into the column. Separation was performed in a Waters HPLC 1525 binary pump with an XTerra reverse-phase column (C18 5 μm 4.6 x 250 mm) and XTerra guard column (RP C8 5 μm 3.9 x 20 mm), followed by UV analysis at 230 nm. The samples were eluted with the following gradient program with two mobile phases at a 1 mL/min flow rate: (A) 0.1% (v/v) trifluoroacetic acid in water, and (B) 90% (v/v) acetonitrile with 0.1% trifluoroacetic acid. The samples were analyzed by an external standard curve in the range from 0.1 μg/mL to 5 μg/mL, and the ethanolamine-DNS-Cl peak eluted at approximately 6.1 min.

Table 4.13. HPLC solvent protocol for EthAm analysis.

Time (min)	% B		Time (min)	% B
0-2	20		12-13	43 → 95
2-6	20 → 29		13-15	95
6-7	29 → 42		15-17	95 → 20
7-12	42 → 43		17-20	20

In vivo wound healing. The materials were cut into 10 x 2 mm discs for *in vivo* implantation to assess degradation properties. The discs were sterilized by gamma irradiation prior to implantation into full-thickness excisional dorsal wounds in adult male Sprague-Dawley rats. The wounds were splinted with stainless steel washers and stay sutures for 7 days to prevent wound contraction. Semi-occlusive Tegaderm dressing (3M, St. Paul, MN) held the scaffolds in place and protected the wound. The wounds were harvested at 7, 14, and 21 days to evaluate the comparative rates of polymer degradation and new tissue formation within each of the scaffolds. The wounds were fixed in formalin for 24 hours followed by 70% ethanol for 48 hours. They were then paraffin-embedded and sectioned for histology with Gomori's trichrome and hematoxylin & eosin staining. Select paraffin-embedded tissue sections were submitted to proteinase K digestion and anti-PGP9.5 staining to detect the presence of macrophages around material remnants.

In vitro cell culture with macrophages. The PUR scaffolds were cut into thin 20 x 1-mm discs, sterilized by gamma irradiation, and placed in 24-well plates. RAW 264.7 murine macrophages were cultured with the materials in α-MEM with 10% FBS, added at 5 x 10^4 cells/well [19]. Each well contained 1 mL culture media,

which was replaced every 3 days. At two weeks, the media was removed and the scaffolds with seeded cells were fixed in 4% glutaraldehyde for 2 hours followed by tetroxide for another 2 hours. The materials were then dried under vacuum before observation with SEM.

Results

In vitro PUR degradation and mechanical properties. During the first 8 weeks of *in vitro* incubation, all the PUR materials retained at least 80% of their original mass, but showed differential rates thereafter (Figure 4.1). Overall, the scaffolds synthesized with LTI degraded to a greater extent, resulting in a clear solution of soluble degradation products. The LTI material with the T6C3G1L900 (6C) polyol clearly degraded more quickly than that with the T7C2G1L900 (7C) polyol, which is consistent with the previously reported half-lives of these polyesters (20 and 225 days, respectively) [35]. The 6C/HDIt material with 50% PEG initially lost mass more rapidly than the 6C/HDIt scaffold without PEG, probably facilitated by greater swelling due to the hydrophilic PEG segments. However, the 6C/HDIt + 50% PEG material showed less long-term mass loss, likely due to the less readily hydrolysable polyether PEG segments.

Compressive and tensile properties of the scaffolds were assessed with DMA stress-strain tests after 0, 4, 8, and 12 weeks of *in vitro* degradation. These scaffolds exhibited plastic mechanical properties and did not become brittle with time, as indicated by the compressive stress-strain curves did not yield or collapse. The Young's modulus, determined from the initial linear slope of the stress-strain

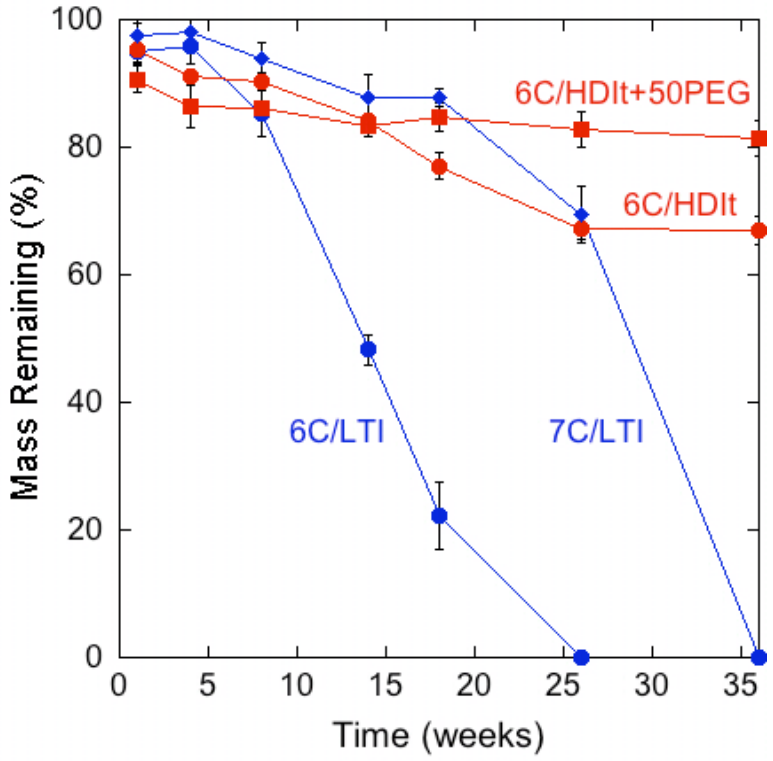

Figure 4.36. Long-term *in vitro* degradation in PBS shows that LTI scaffolds degraded at a faster rate than HDIt scaffolds. Selected data from Figure 2.6 (n = 3).

curves, under compression decreased consistently with time for all materials, which is consistent with the mass loss data (Figure 4.2). The 6C/LTI material was not structurally robust enough for measurement at 12 weeks. The compressive strength values (stress at 50% strain) followed a parallel trend. The Young's modulus and ultimate stress values measured in tension mode similarly decreased with degradation time, although the ultimate strain remained relatively constant (Figure 4.3). While these studies were informative in understanding how the PUR scaffold mechanical properties changed during degradation, under *in vivo* conditions infiltration of cells and ingrowth of new tissue within the scaffold interstices would anticipated to increase the mechanical properties.

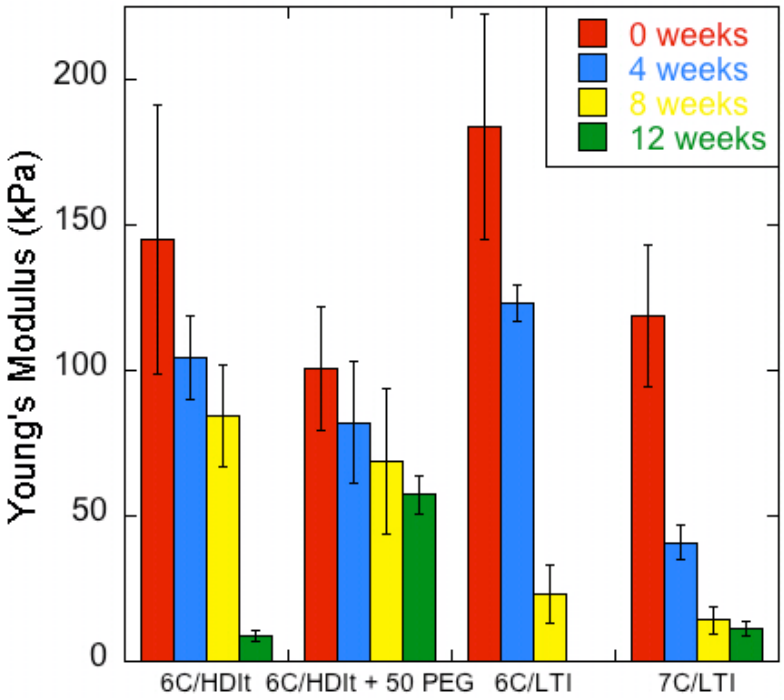

Figure 4.37. Compressive Young's modulus values decreased with extended *in vitro* degradation time (n = 3).

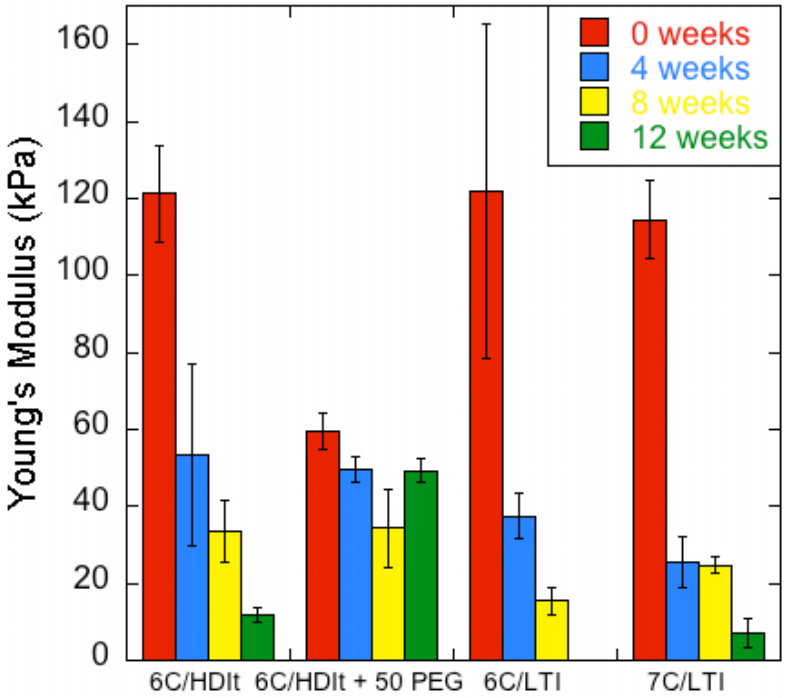

Figure 4.38. Tensile Young's modulus values decreased with *in vitro* degradation time (n = 3).

Scanning electron micrograph (SEM) images of the scaffolds after 0, 4, 8, and 12 weeks of degradation show thinning and pitting of the pore walls over time (Figure 4.4). Evidence of pitting is visible at 12 weeks, with some surface erosion discernible by 4 and 8 weeks. It has been suggested that the surface pitting of poly(ether urethanes) is associated with degradation of the polyether component due to chain scission, which can lead to removal of the low molecular weight degradation products [36], and that pitting becomes detectable at approximately 10-15% soft segment mass loss [37].

Table 4.2 provides the corresponding density and porosity measurements for the scaffolds at 0, 4, 8, and 12 weeks. Despite loss of mass and mechanical properties as shown in Figures 4.1, 4.2, & 4.3, the porosity values did not change significantly with time. These data suggest a thinning of pore walls without total breakdown of the scaffold structural integrity via a uniform, bulk degradation mechanism. The SEM images in Figure 4.4 support this conclusion, as they reveal thinning pore walls with time and eventual breakage of struts between pores, which contribute to the decreased mechanical properties but do not result in significant changes to pore size or morphology.

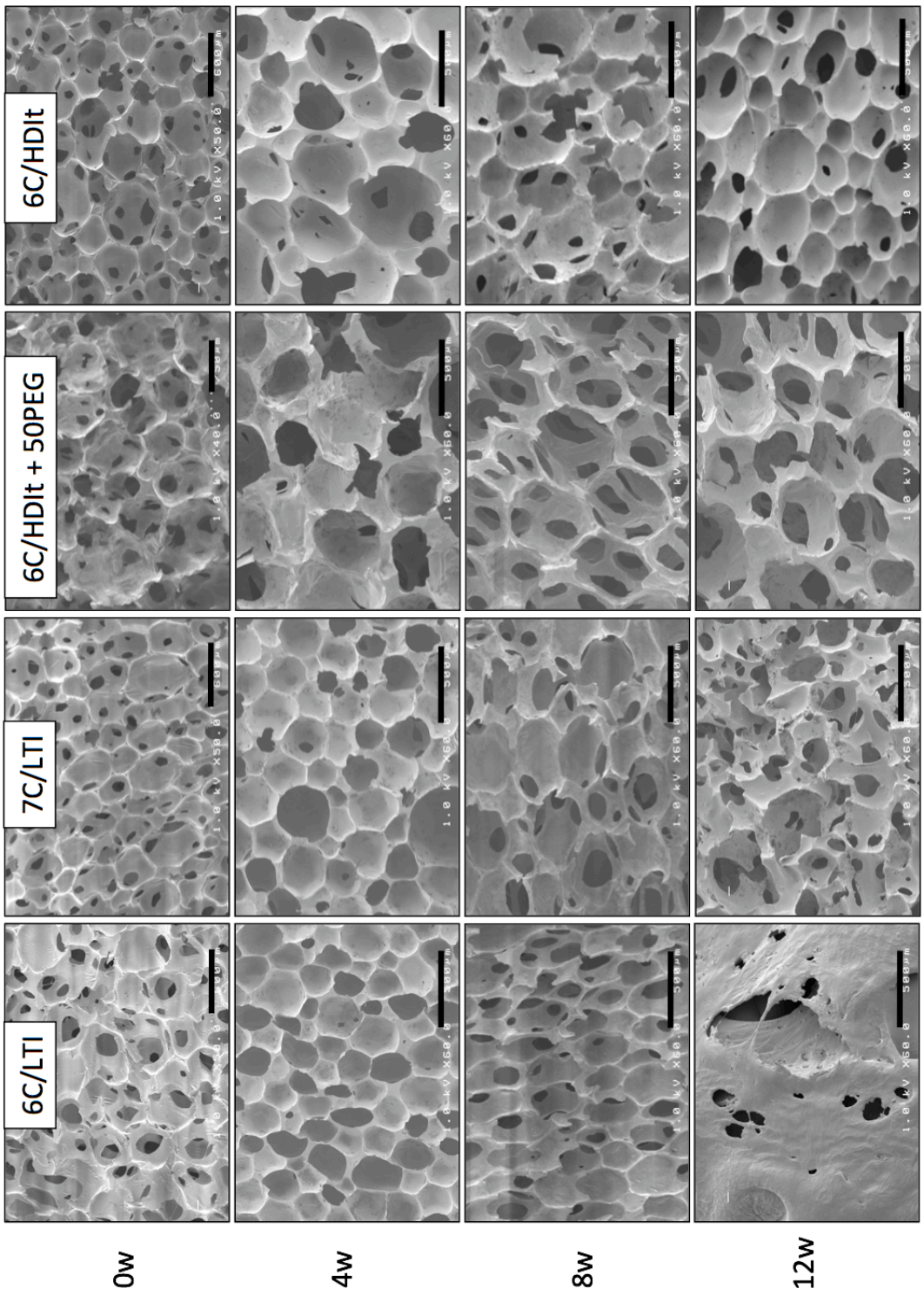

Figure 4.39. Representative SEM images of scaffolds after 0, 4, 8, and 12 weeks of *in vitro* degradation in buffer. Scale bar is 500 μm.

Table 4.14. Bulk scaffold density (mg/cm^3, in shaded squares) & porosity (vol-%, italicized, in white squares) at various stages of degradation (n = 3).

	0 weeks	4 weeks	8 weeks	12 weeks
6C/HDIt	98 ± 13	98 ± 6	101 ± 5	110 ± 7
	92 ± 1%	*93 ± 0.5%*	*92 ± 0.4%*	*91 ± 0.6%*
6C/HDIt + 50 PEG	94 ± 11	84 ± 5	91 ± 17	116 ± 6
	92 ± 1%	*93 ± 0.4%*	*93 ± 1%*	*91 ± 0.5%*
6C/LTI	88 ± 5	96 ± 6	199 ± 30	N/A
	93 ± 0.4%	*92 ± 0.5%*	*84 ± 3%*	*N/A*
7C/LTI	85 ± 14	66 ± 4	78 ± 0.6	184 ± 47
	93 ± 1%	*95 ± 0.3%*	*94 ± 0.1%*	*85 ± 4%*

In vitro enzymatic and oxidative PUR degradation. PUR scaffolds were incubated with the hydrolytic enzymes cholesterol esterase, carboxyl esterase, and lipase. These enzymes were chosen based on their previously reported effects of these enzymes on poly(ether urethane) and poly(carbonate urethane) degradation, as they exhibited higher degradative activity than other esterases secreted from adherent macrophages [15, 31]. Figure 4.5 shows that incubation with these enzymes accelerated degradation slightly, but few points were statistically significant ($p<0.05$). Surprisingly, there was little difference between the three candidate enzymes, in contrast with previous studies showing that cholesterol esterase has to have a greater effect than other enzymes [15].

In contrast, incubation with hydrogen peroxide, at approximately the concentration found in the pocket of macrophage-material attachment [26], had a more significant effect on the PUR degradation rate, especially for the LTI-based materials (Figure 4.5). The differences in mass loss between the buffer control and

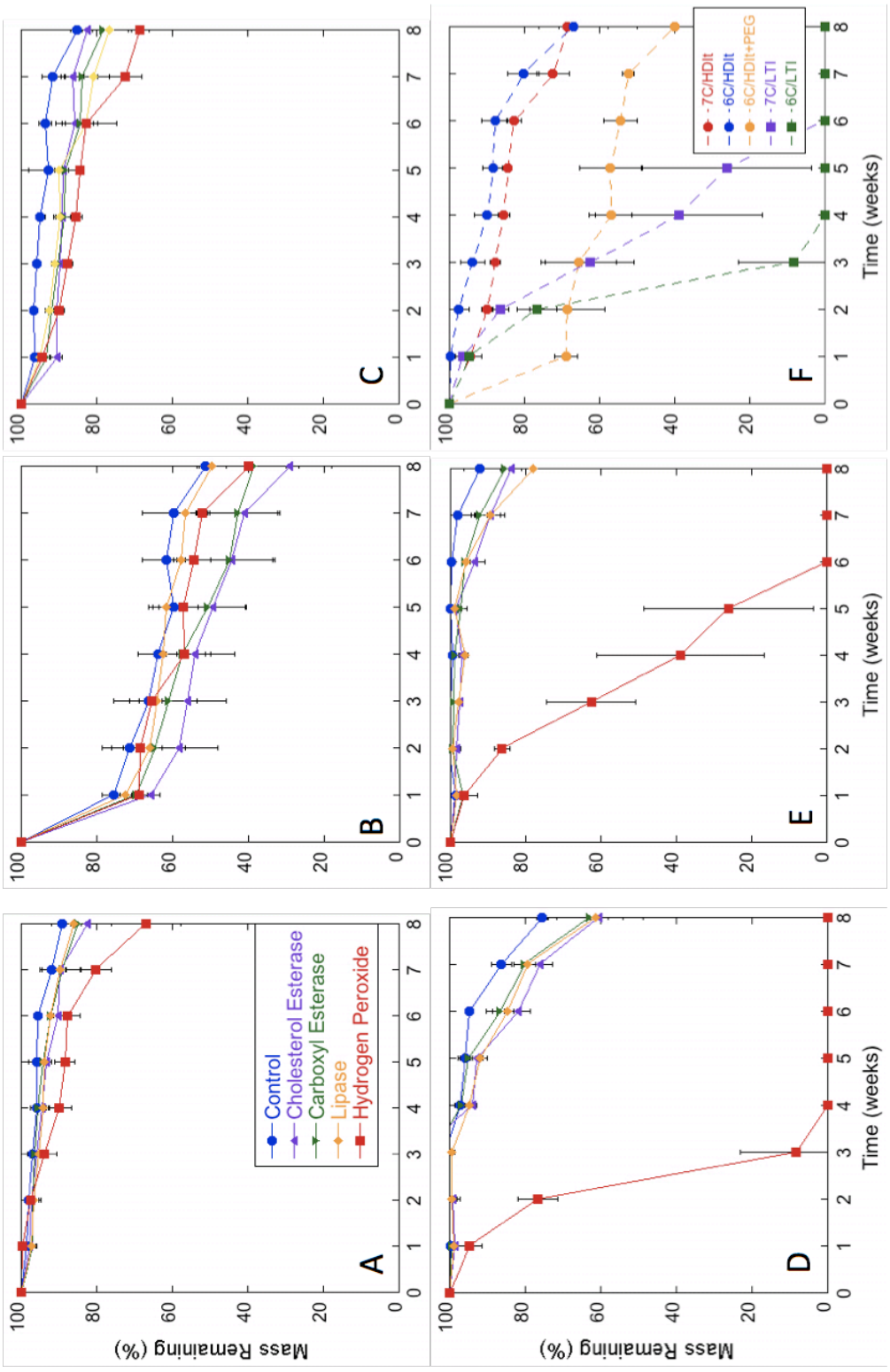

Figure 4.40. I*n vitro* degradation of PUR scaffolds in enzymatic or oxidative media, vs. buffer controls: (A) 6C/HDIt, (B) 6C/HDIt + 50 PEG, (C) 7C/HDIt, (D) 6C/LTI, (E) 7C/LTI. (F) LTI scaffolds exhibit faster degradation than HDIt scaffolds in hydrogen peroxide media (n = 3).

hydrogen peroxide degradation samples were statistically significant ($p<0.05$) after 2 weeks for all materials except the 6C/HDIt + PEG, which degraded faster in the presence of cholesterol and carboxyl esterase than with hydrogen peroxide due to the additional polyether segments. The hydrogen peroxide treatment group particularly highlighted the differential degradation rates between the LTI- and HDIt-based scaffolds compared to the controls. The 6C/LTI scaffold had completely dissolved by 4 weeks, and the 7C/LTI scaffold by 6 weeks, while ≥ 50% of the mass of HDIt scaffolds remained.

Peroxide solutions are acidic, with pH values down to 4 – 5. To investigate whether this could be contributing to the phenomenon of faster degradation in oxidative media, the 6C/LTI materials were incubated in buffer of pH 4 in comparison to pH buffer. As before, triplicate samples were incubated at 37 °C. In addition, the 6C/LTI scaffolds were incubated in varying concentrations of the $H_2O_2/CoCl_2$ media. Degradation in pH 4 buffer did not accelerate *in vitro* degradation, which suggests that the oxidative effects on degradation rates are independent of pH (Figure 4.6). The dose-dependent effect of the $H_2O_2/CoCl_2$ media on degradation rate supports the hypothesis that polymer chain oxidation may be the governing degradation mechanism in the presence of reactive oxygen species.

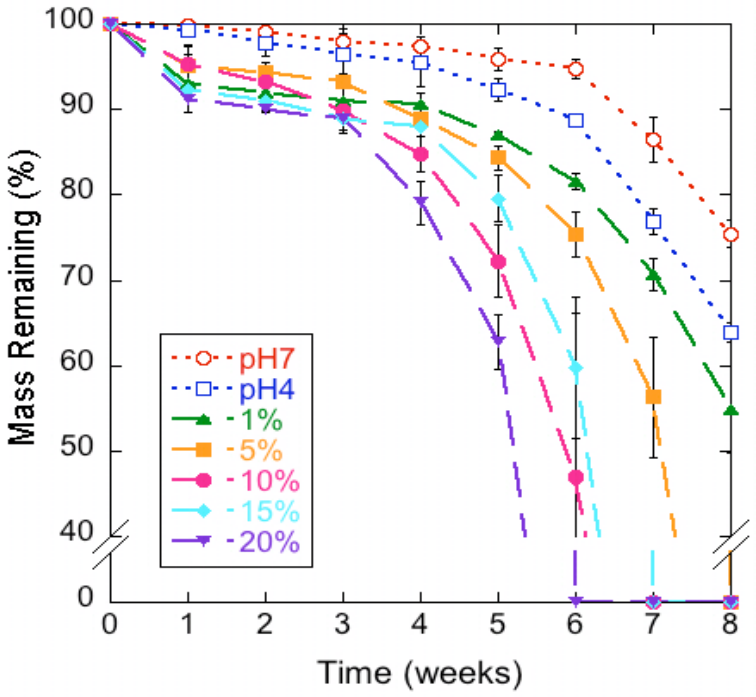

Figure 4.41. *In vitro* degradation of PUR scaffolds in buffer of pH 7 and pH 4 suggests that the oxidative effect is independent of pH. Varying H_2O_2 concentrations produces a dose-dependent effect on degradation rate (n = 3).

Analysis of α-hydroxy acid degradation products. Degradation of the PUR scaffolds *in vitro* yielded water-soluble degradation products, which enables them to diffuse away from the defect site and be eliminated from the body rather than accumulate near the wound. Structures of possible degradation products and mechanisms are shown in Figure 4.7, based on likely sites of hydrolysis and oxidation. Several unidentified peaks appeared in the HPLC spectra during analysis, which are conjectured to be various urethane adducts. HPLC analysis of the PUR degradation media showed time- and composition-dependent release of α-hydroxy acid monomers, which is indicative of ester hydrolysis within the polymer backbone (Figure 4.8 & 4.9). Isocyanuric acid, a potential degradation product resulting from hydrolysis of urethane and urea bonds in the HDIt materials, was not detected. The

LTI scaffolds produced more α-hydroxy acids for a given polyol (e.g.: 6C3G1L) than did the HDIt scaffolds at any given time point. Similarly, the 7C/LTI formulation, which degrades more slowly due to the longer polyol half-life, yielded less α-hydroxy acid products than did 6C/LTI formulation. Inclusion of PEG in the 6C/HDIt scaffold reduced the amount of α-hydroxy acids in the degradation medium, just as it slowed the degradation rate at longer time points.

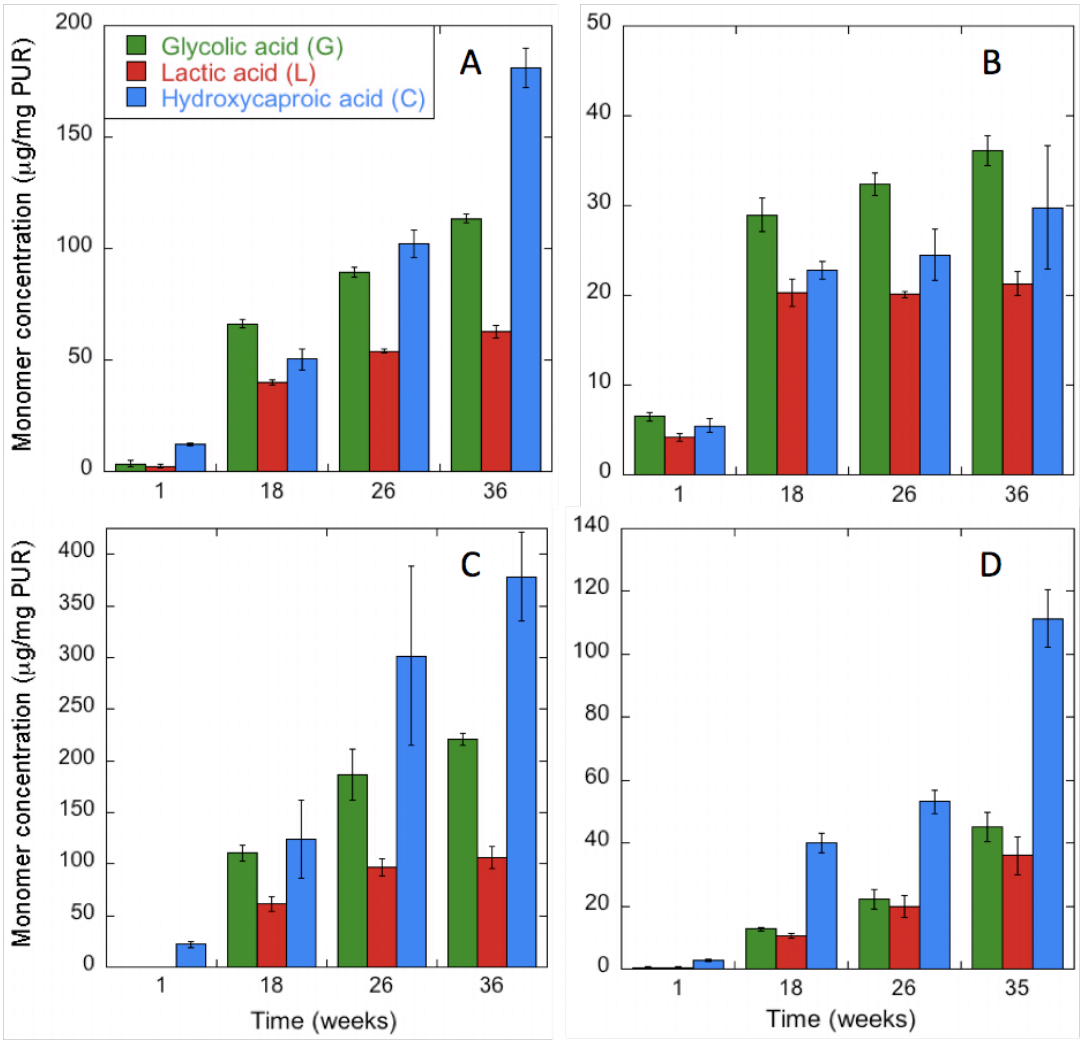

Figure 4.42. Recovery of α-hydroxy acids from soluble degradation products of PUR scaffolds *in vitro* in buffer: (A) 6C/HDIt, (B) 6C/HDIt + 50 PEG, (C) 6C/LTI, (E) 7C/LTI. Note the varying y-axis scales (n = 3).

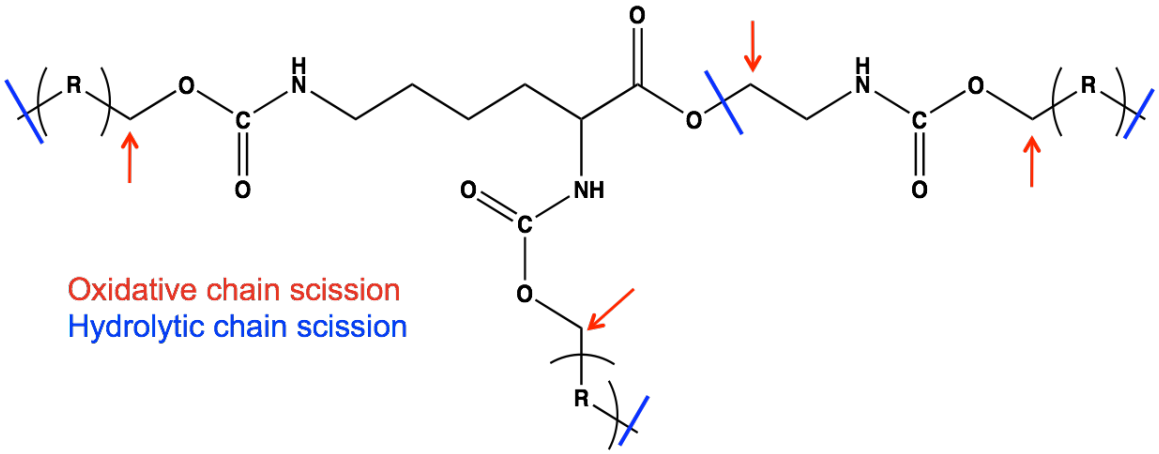

Figure 4.43. Possible degradation sites within the LTI-based PUR network. The soft polyol segments ("R") contain sites of ester hydrolysis that can liberate the α-hydroxy acids.

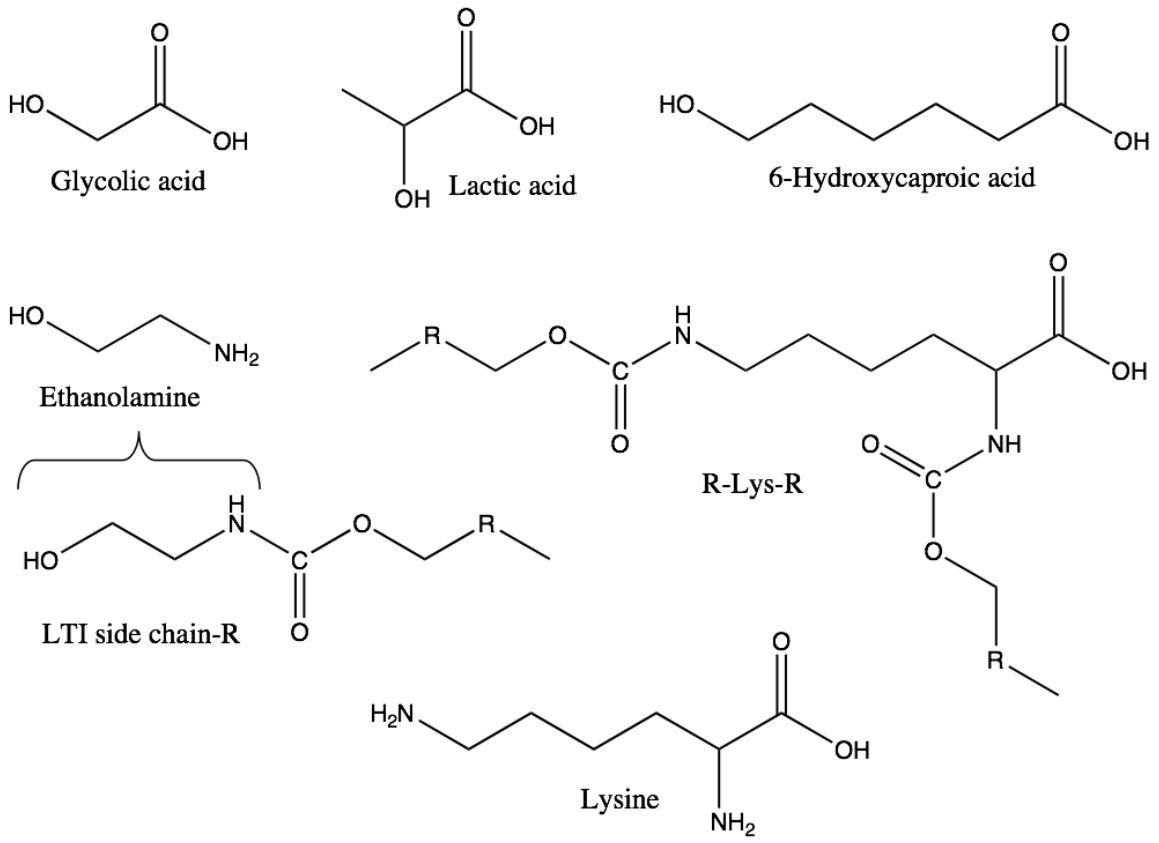

Figure 4.44. Possible degradation products from the LTI-based PUR network.

Analysis of lysine fragments. As shown in Figure 4.10, the amount of lysine (μg/mg PUR) recovered from the T6C3G1L/LTI scaffold degradation in buffer was significantly greater than that from the T7C2G1L/LTI scaffold after 14 weeks, which is consistent with the *in vitro* degradation rates (Figure 4.1). The percent recovery was calculated based on the mass fraction of lysine contained in the LTI used for PUR synthesis. After 36 weeks, 18% of the lysine in the 6C/LTI scaffolds was recovered, while 100% of the original mass had degraded to soluble degradation products. This suggests that the majority of the lysine is incorporated in soluble urethane and urea adducts, as hypothesized in Figure 4.7. *In vitro* cytotoxicity studies demonstrate that these soluble degradation products are nontoxic [5].

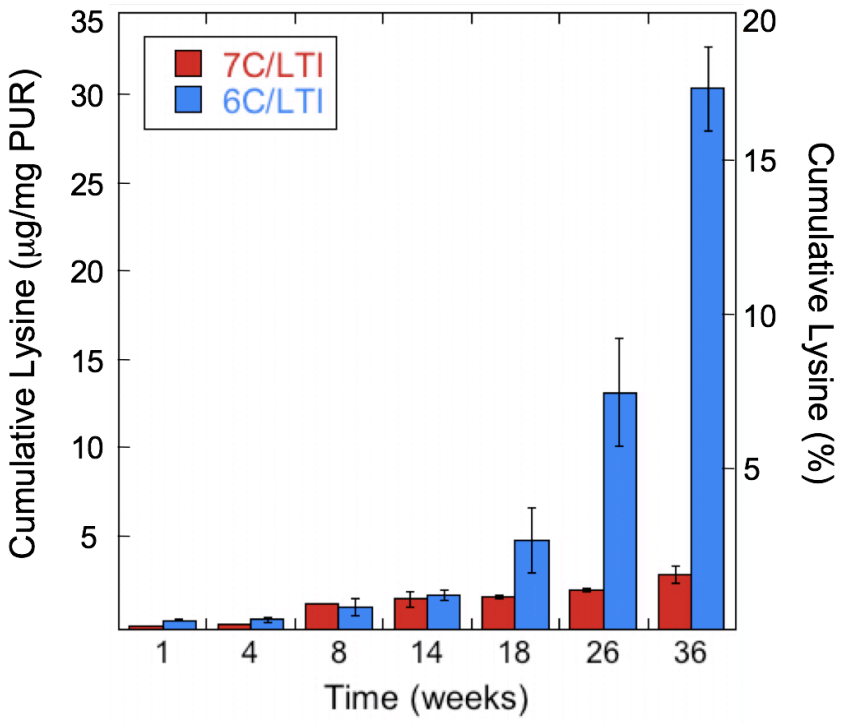

Figure 4.45. Lysine recovery from soluble degradation products of LTI scaffolds *in vitro* in buffer, which were all soluble, measured in absolute levels and percent of theoretical total lysine content if all lysine residues were to be liberated from the polymer. The faster-degrading 6C/LTI scaffolds yielded more lysine than corresponding 7C/LTI scaffolds (n = 3).

Analysis of ethanolamine. The recovery of ethanolamine was analyzed from the degradation media of the LTI scaffolds (Figure 4.11). Ethanolamine is released to the medium through hydrolysis of the ester group in LTI and a urethane (or urea) bond resulting from the reaction of LTI and the polyester triol (or water). The percent recovery was calculated in a similar manner to lysine in the previous paragraph, but taking into account that an ethanolamine molecule is 22.7% by mass of LTI. Ethanolamine was not detected (< 0.001 μg/mg PUR) in the degradation media until 14 weeks. Consistent with the lysine analysis, the 6C/LTI materials produced more ethanolamine at each time point, with up to 9% recovery upon complete scaffold dissolution at 36 weeks.

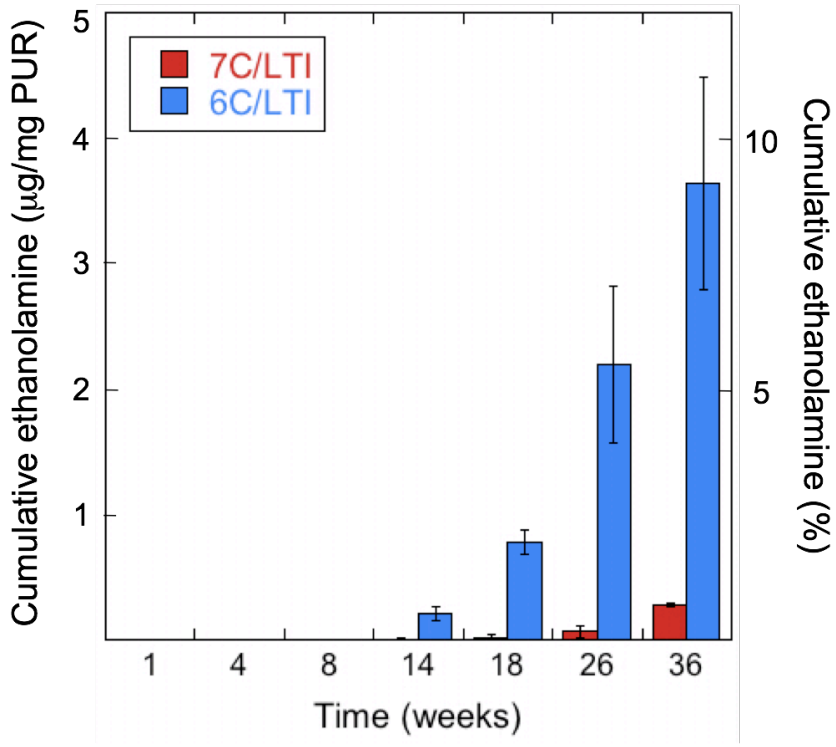

Figure 4.46. Ethanolamine recovery from LTI scaffold degradation *in vitro* in buffer, measured in absolute levels and percent of all possible EthAm fragments that could be liberated from the polymer. These quantities would remain sufficiently lower than toxic *in vivo* levels for clinical applications (n = 3).

The lysine and ethanolamine recovery depicted in Figures 4.10 and 4.11 are the cumulative, not weekly, amounts released at each time point. In the degradation experiment, the medium was collected at the specific time point without periodic refreshing due to difficulties associated with removing the medium and handling the wet scaffolds at longer time points. By removing the medium and recovering the scaffold only once (that is, at the specified time point), errors associated with solid-liquid phase separation were minimized. Thus the measured degradation product concentrations are likely higher than under the constant sink conditions associated with the wound site *in vivo*, where degradation products are cleared through the processes of convection and diffusion.

In vivo wound healing. Dermal wound healing was evaluated by implantation of 2 x 10 mm discs of each formulation into dorsal excisional wounds for up to 21 days. Early plasma permeation into the scaffold preceded cellular infiltration and formation of dense granulation tissue (Figure 4.12). Extracellular matrix with dense collagen fibers progressively replaced the characteristic, early cellular response. None of the implants engendered an overt inflammatory response or cytotoxicity.

Fibroplasia and angiogenesis appeared to be equivalent among the different formulations, despite the different degradation rates. The LTI scaffolds exhibited a greater extent of degradation at 21 days than the HDIt scaffolds with the T6C3G1L/LTI materials slightly accelerated with respect to the T7C2G1L/LTI, presumably due to the shorter half-life of T6C3G1L. The incorporation of PEG into the HDIt scaffold, however, accelerated its degradation significantly. These *in vivo* degradation rates are clearly faster than *in vitro* rates, although *in vitro* incubation

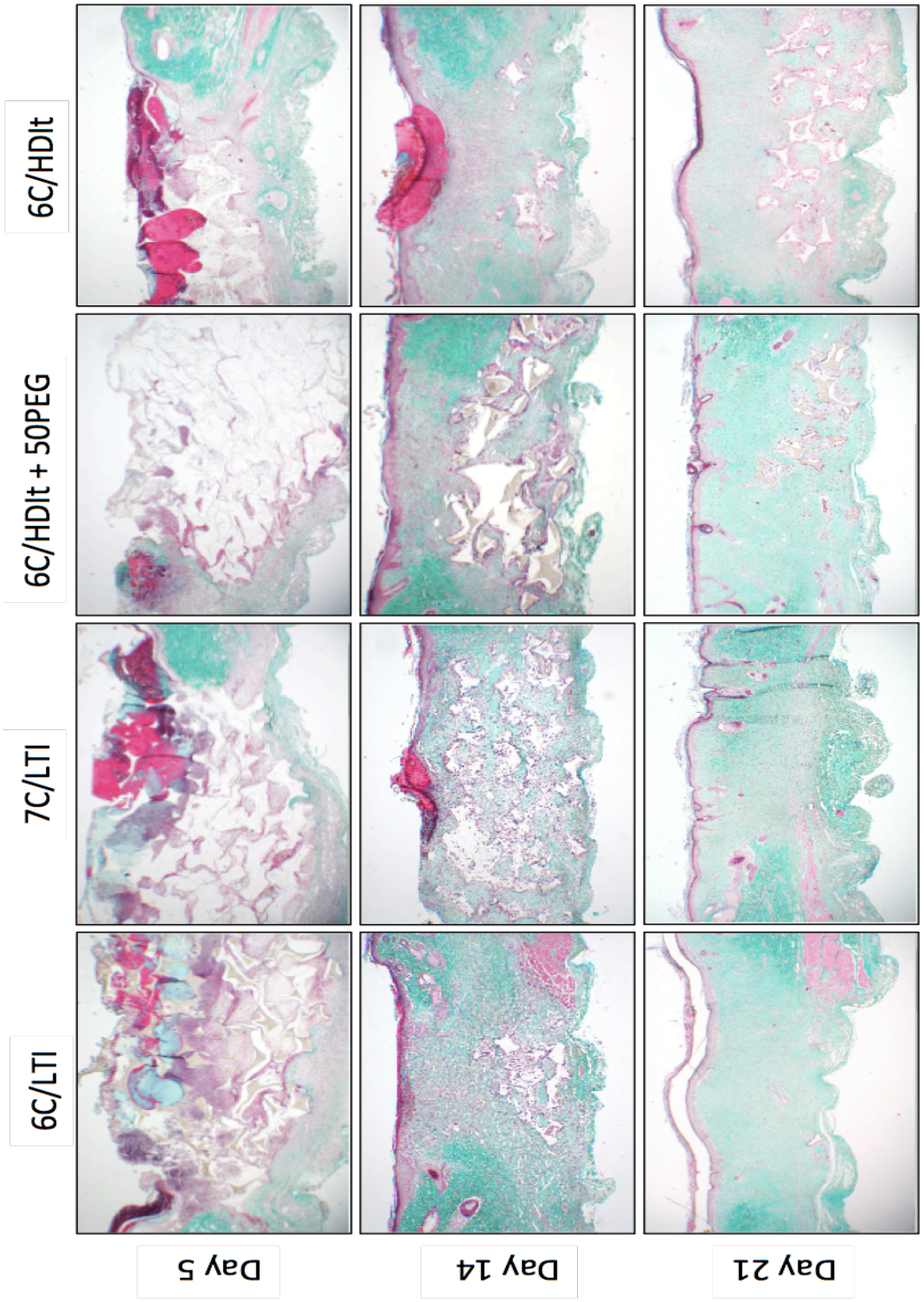

Figure 4.47. Representative histological images (trichrome) of dermal excisional implants at 5, 14, & 21 days show cellular infiltration and new matrix deposition with simultaneous scaffold degradation. The degradation rates vary depending on polymer formulation, from 6C/LTI (fastest) to 6C/HDIt (slowest).

with hydrogen peroxide nearly approximated these *in vivo* rates. With time, each of the materials showed signs of fragmentation and engulfment by a transient, giant cell, foreign body response. After the remnant material was completely resorbed, giant cells were no longer evident. Anti-PGP9.5 staining of the histological sections highlighted the presence of macrophages and foreign body giant cells surrounding the material remnants, with noticeably fewer in areas with new collagen and granulation tissue where the material had already degraded (Figure 4.13). Together with the *in vitro* culture with RAW264.7 cells, this strongly suggests the dominant role of cell-mediated degradation of LTI scaffolds *in vivo*.

In vitro cell culture with macrophages. Murine monocyte-derived macrophages (RAW 264.7 cells) were cultured *in vitro* on the porous PUR scaffolds. After 2 weeks, SEM images of the fixed cells on the material surfaces revealed active individual macrophages (5-10 μm diameter) and foreign body (FBGC) or multinucleated (MNGC) giant cells (20-30 μm diameter) fused from multiple macrophages (Figure 4.13). The images also displayed groups of aggregated cells that may have been in the process of fusing into giant cells, or larger aggregates that may be close to an apoptotic state. Interestingly, the material surface clearly shows evidence of pitting (as large as 20 μm), which implies focused degradation within the compartment enclosed between the macrophage and the material surface.

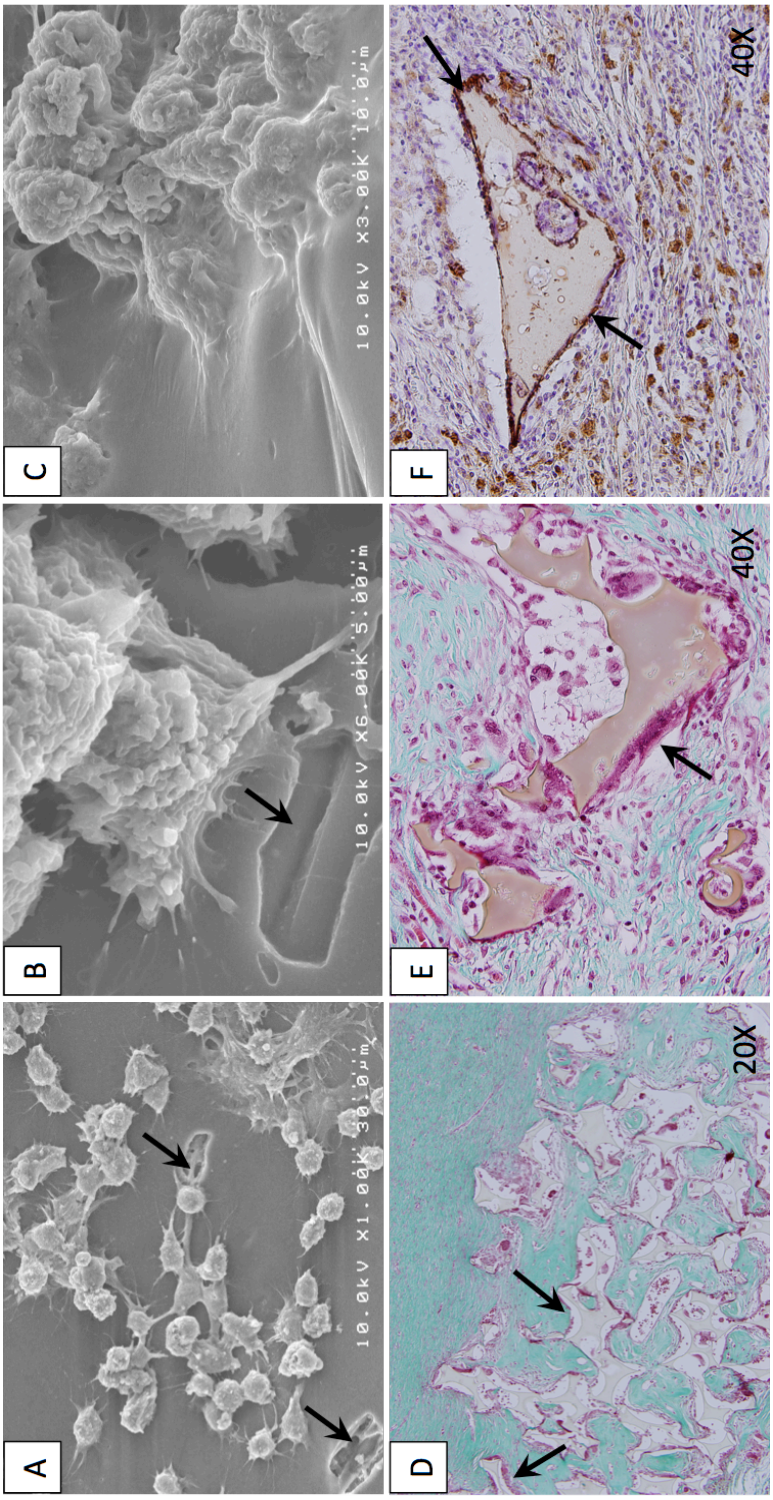

Figure 4.48. Interactions between macrophages and PUR scaffolds provide evidence of cell-mediated degradation. In SEM images of RAW 264.7 cells cultured on scaffolds *in vitro* for 2 weeks, degradation is evident by pitting on the material surface (A & B), as well as possible giant cell formation (C). Macrophages (magenta) line the edges of scaffold remnants as shown in histology of a 7C/LTI implant *in vivo* after 30 days (D & E). PGP9.5 staining verifies macrophage presence (brown) at the material surface (F).

Discussion

In order to be clinically useful, the biomaterial as well as its degradation products must be biocompatible. It is also important that the degradation rate matches the rate of new tissue formation, such that residual material remnants do not activate an inflammatory response that hinders healing, or, conversely, that the scaffold leaves a void by degrading too quickly. Thus understanding the mechanisms and products of biomaterial degradation is essential. While the degradation mechanisms of biostable polyurethane implants have been investigated extensively, the degradation mechanisms associated with lysine-derived poly(ester urethane)s are not as well characterized. In this study, we investigated the biodegradation of porous biodegradable polyurethane scaffolds synthesized from polyester triols and aliphatic and lysine-derived triisocyanates. Specifically, we aimed to study the hydrolytic and cellular-mediated degradation of these materials *in vitro* and *in vivo*.

The *in vivo* environment consistently accelerates PUR scaffold degradation. For example, the 6C/LTI formulation degrades entirely *in vivo* within 2-4 weeks (depending on its size and location), but up to 26 weeks *in vitro* to achieve complete mass loss. Our data support other published studies that this is a cell-mediated phenomenon, particularly driven by monocyte-derived macrophages, which maintain a central role in the foreign body reaction to biomaterials [15, 21, 22, 33, 38, 39]. Figure 4.13 (D & E) shows histology of an excisional dermal wound in which macrophages congregate at the material edges and, visible at high magnification, some have fused into multinucleated foreign body giant cells.

Meanwhile, few visible macrophages remain in areas with new collagen and granulation tissue but no scaffold remnants, illustrating the transient foreign body response. Figure 4.13 affirms these observations with anti-PGP9.5 staining of macrophages, with stained cells similarly concentrated around the material fragments. Macrophages recruited to the surface of the biomaterial not only accelerate degradation, but also contribute to new matrix deposition, as they secrete growth factors and cytokines that can promote the wound healing process [24]. These effects were reported in an earlier study, where PDGF delivered locally from the scaffold increased the rate of both new tissue ingrowth and material degradation, such that the overall rate of healing was accelerated [6]. While macrophages remain at the wound site for the material lifetime, neutrophils involved in the initial, acute inflammatory response likely expel a respiratory burst that catalyzes material degradation.

Macrophages attach to biomaterial surfaces, via adsorbed extracellular matrix proteins and integrin receptors, and often fuse into multinucleated foreign body giant cells (FBGC) [21, 22]. They form an enclosed compartment at the cell-material interface, within which they can produce high local concentrations of secreted factors such as reactive oxygen intermediates (ROI), acids and enzymes [19, 37, 40]. These pockets greatly accelerate degradation and cause pitting of the material surface, as shown in the SEM images. These pits manifested after 8 to 12 weeks in buffer (Figure 4.4), while incubation with RAW264.7 macrophages caused these pits to appear within just 2 weeks (Figures 4.13 A and B). Pitting of poly(ether urethane)s has been attributed to extraction of low molecular weight degradation

products resulting from polymer chain scission [36]. Thus the macrophage-induced pitting observed for the poly(ester urethane)s of the present study is conjectured to result from diffusion of α-hydroxy acid degradation products away from the scaffold. Recently, a time- and spatially-dependent peroxide gradient at the wound site following injury has been reported, which may also contribute to oxidative attack on biomaterials [41]. We can deduce that these cell-secreted substances are responsible for the accelerated polymer degradation, although the relative contributions of these substances and their mechanisms of attack are still under question. The enzymatic and oxidative pressures on a given urethane most likely depend on its particular composition and distribution. Local low pH and high acid concentrations likely increase polymer chain hydrolysis, further autocatalyzed by acidic degradation products. Several groups have also provided evidence of hydrolysis by esterolytic enzymes [16] and oxidative chain scission by ROIs [26, 32] of poly(ether-), poly(carbonate-), and poly(ester urethane)ureas. These studies provided a decent starting point for our own experiments to determine the dominant mechanisms of degradation for biodegradable polyester urethanes, especially those with lysine-derived isocyanates.

Santerre, Labow, and colleagues have contributed greatly to understanding polyurethane degradation by showing that physiological enzymes associated with monocyte-derived macrophages affect PUR degradation [16]. They focused on esterases with hydrolytic activity, which would have a noticeable impact on urethanes, but interestingly observed that oxidative enzymes (e.g. xanthine oxidase, horseradish peroxidase) did not produce a significant effect, even though these

enzymes can produce oxygen free radicals [13, 42]. Cholesterol esterase preferably degraded ester linkages adjacent to hard segment, more so than the urethane in hard segment, which may decrease incidence of toxic diamine degradation products [31]. This agrees with our observation that scaffolds with the 6C3G1L polyester polyol—which is more hydrolytically labile (shorter half life)—than with the 7C2G1L polyol. The group also demonstrated that these esterases could hydrolyze the urethane bond, albeit at a much lower rate than soft segment esters, releasing hard segment components. Following this evidence, we found that cholesterol esterase, carboxyl esterase, and lipase had some effects on our PUR degradation, although the mass differences between samples incubated with and without enzymes were not significant until weeks 7 and 8 of incubation. The degradation rates with enzymatic media did not approach *in vivo* rates, suggesting that these enzymes may not be primarily responsible for degrading these biodegradable PURs *in vivo*.

Incubation in media containing hydroxyl radicals had a remarkable effect on PUR degradation with respect to buffer controls (Figure 4.5). Except for the scaffold formulated with PEG, the $H_2O_2/CoCl_2$ media accelerated degradation more than did the various enzymatic media. This was somewhat unexpected for these poly(ester urethane)s because they are generally more susceptible to hydrolytic degradation. The inclusion of PEG in the HDIt scaffold soft segments increased the oxidative degradation rate (Figure 4.5), which is reasonable since ethers tend to be more prone to oxidation than esters. Most notably, the LTI scaffolds especially responded to the $H_2O_2/CoCl_2$ media, such that the oxidative degradation rates *in vitro*

approximated *in vivo* rates. The materials became tacky after 2 weeks in this media, implying marked chain scission and decreased polymer molecular weight. Hydrogen peroxide solutions, particularly at such a high concentration, have low pH values (pH 5), which might raise the question of whether the observed effect is really due to the polymer chain oxidation, or simply accelerated acid hydrolysis autocatalyzed by the low pH. Figure 4.6 shows that the 6C/LTI scaffolds do not degrade significantly faster in pH 4 buffer, so the effect of oxidation is independent of the low pH of these oxidative solutions.

Aliphatic poly(ester urethane)s traditionally degrade by hydrolysis of the ester bonds within the soft segments, with limited hydrolysis of the urethane bonds, such that increased hard segment concentration leads to greater hydrolytic resistance [10, 16, 28]. This is verified by the recovery of α-hydroxy acids from the PUR degradation media, which was proportional to both the polyol compositions and degradation rates (Figure 4.8). However, the data indicate that the isocyanate composition dramatically affects the degradation of these materials (Figures 4.1 and 4.5). LTI scaffolds degrade faster than HDIt scaffolds synthesized with the same polyol because of the hydrolysable ester linkage within the lysine residue, further autocatalyzed by the resulting release of a carboxylic acid group [5]. Urethane and urea linkage hydrolysis for lysine-derived polyisocyanates has been questioned, with some reports that they can only be degraded enzymatically [43, 44]. While enzymes likely hydrolyze these linkages *in vivo*, our data reveals that lysine is prevalent, after sufficient time, in the degradation products of LTI scaffolds incubated in buffer (Figure 4.10), which could occur only with urethane hydrolysis.

Similarly, ethanolamine (EthAm) could only occur with hydrolyzed urethane and urea linkages, although it most likely results from further hydrolysis of an LTI side chain (Figure 4.7), since it does not appear significantly until week 14 (Figure 4.11). Analysis of the degradation media verifies the release of α-hydroxy acids and lysine by chain scission. However, these quantities do not complete an expected mass balance of polymer reactants and degradation products. Furthermore, unidentified peaks in HPLC spectra of the degradation media implicate the presence of other nonspecific urethane adducts.

It has not been demonstrated previously that oxidation can be a significant mode of degradation for biodegradable poly(ester urethane)s, and specifically those made with lysine-derived polyisocyanates. Anderson and colleagues have focused their oxidation studies on poly(ester urethane)s (PEU) and poly(carbonate urethane)s (PCU) because of their greater resistance to degradation than poly(ester urethane)s and therefore more prevalent use in long-term urethane implants. These biostable implants generally contain aromatic isocyanates with hydrogen-bonded crystalline hard segments, in contrast to the aliphatic polyisocyanates that we employ in our studies. *In vitro* treatment of PEU and PCU with the $H_2O_2/CoCl_2$ media resulted in similar ATR-FTIR spectra of the materials as when they were explanted from *in vivo* settings [26, 27]. They highlighted soft segment oxidation, crosslinking, and chain scission, especially in PEU. Furthermore, they demonstrated evidence of hard segment degradation, which had not been as well known, and its inverse correlation with the degree of hard segment hydrogen bonding. Oxidation of hard segments occurs more readily when they are isolated within soft segments

or in an interphase region. In our materials, the micro-phase mixing and lack of hydrogen bonding allows these hard segments to be more susceptible to oxidation. The stark differences between LTI and HDIt scaffold degradation times in the $H_2O_2/CoCl_2$ media (Fig 4.5F) indicate that oxidation probably affects the hard segments more heavily than the polyester soft segments, especially for the lysine-derived isocyanate, since polyesters do not typically oxidize as readily. Nevertheless, this phenomenon in our lysine-derived poly(ester urethane)s is novel because aromatic isocyanates are traditionally more susceptible to oxidative attack than aliphatic isocyanates like LTI [45]. Oxidation of the lysine residue itself may occur, as suggested by Stadtman, which would further accelerate LTI scaffold degradation [42]. Unfortunately, the degradation products that resulted from PUR incubation in the oxidative or enzymatic media could not be evaluated directly due to assay limitations with the high enzyme and hydrogen peroxide concentrations. However, we can conjecture that the hard segment oxidation occurs by abstraction by the hydroxyl radical of the α-methylene hydrogen adjacent to the urethane linkage [26]. This produces a methyl radical within the polymer chain, which reacts with another free hydroxyl radical, and the resulting carbonyl-hemiacetal is then hydrolyzed to complete chain scission. As mentioned above, the terminal carboxylic and carbamic acid groups on the new fragments can autocatalyze further hydrolysis and polymer chain scission.

Important for clinical applications, these biodegradable polyurethane scaffolds yield completely soluble degradation products, suggesting that material fragments may be naturally metabolized and cleared from the wound site once

healed. It is relatively unusual for synthetic materials to fully degrade on such a wound healing timescale and to be naturally metabolized. The LTI scaffolds degrade entirely to yield a clear solution at 26 to 36 weeks in control buffer and at 4 to 6 weeks in radical hydroxyl-containing media. The HDIt scaffolds would likely do the same, given long enough degradation times, as demonstrated by past *in vivo* results. Several structural characteristics allow these materials to degrade completely on a wound healing timescale and differentiate them, in a complementary manner, from biostable polyurethanes. The ester within the LTI backbone provides another hydrolytic cleavage point to generate lower molecular weight fragments. The pendant carboxylic acid groups formed as a result of ester hydrolysis, both in the lysine and α-hydroxy acid segments, increase the solubility of the fragments [46]. Previous studies have indicated that these particular PURs are micro-phase mixed with a lack of hydrogen bonding between hard segments [5, 28], which makes the ester, urethane, and urea linkages more accessible and susceptible to hydrolysis (and oxidation) – especially within the hard segment [16]. The solubility of the PUR scaffold degradation products likely promotes clearance by natural pathways, such as removal by macrophage phagocytosis and the lymphatic system. In addition, the soluble products could perhaps freely diffuse from the scaffold area, allowing the local concentrations of degradation products to remain minimal.

The prevalence of lysine among the degradation products may promote the scaffold biocompatibility, since it is a natural amino acid residue that the body would recognize [5, 44]. Meanwhile, the occurrence of ethanolamine in the degradation media could raise concern, although the cumulative amount was

detected only after 14 weeks of uninterrupted incubation. However, upon further investigation, the EthAm amounts released per gram of PUR scaffold would not reach toxic levels *in vivo*, even considering the scale up required for clinical applications. Ethanolamine oleate (EO) is used clinically as a sclerosing agent for the treatment of vascular lesions and cysts, and has been injected at up to 15 g per injection (in a 5% EO solution) without significant side effects [47]. Given the EthAm fragment recovery in Figure 4.11, the local concentration of EthAm at the PUR implant site would not reach this level, especially with continual phagocytosis and lymphatic clearance of the degradation products.

Conclusions

Monocyte-derived macrophages attach to the PUR scaffold *in vivo* and form an enclosed compartment between the cell and material containing high local concentrations of secreted enzymes and reactive oxygen intermediates. This causes material pitting due to polymer chain scission and loss of low molecular weight fragments, which ultimately leads to material degradation. Analysis of the degradation media yielded α-hydroxy acids, lysine, ethanolamine, and other unspecified urethane adducts, indicating chain scission within both the polyol soft segments and isocyanate hard segments. Incubation of poly(ester urethane)s, made from an aliphatic lysine-derived polyisocyanate, in oxidative $H_2O_2/CoCl_2$ solution and enzymatic media accelerated material degradation beyond normal hydrolysis rates observed in buffer. The esterases catalyze hydrolysis of soft segment ester bonds, and less so, urethane linkages, but the changes were not significant in all

cases. Meanwhile, hydroxyl radicals caused significant mass loss, especially among the lysine-derived scaffolds, suggesting oxidative attack in both the soft and hard segments, which had not been shown before for these formulations. The lack of hydrogen bonding in these biodegradable poly(ester urethane)s makes them particularly susceptible to hard segment hydrolysis and oxidation.

Utilizing knowledge gained from these studies, we can customize biodegradable polyurethane implants with specific chemical structures and extent of hydrogen bonding, to control the *in vivo* degradation rate and ensure non-cytotoxic degradation products. While long-term biostable implants benefit from suppressing the macrophage-material interactions that can otherwise lead to device failure, biodegradable materials require macrophages for degradation, resorption, and ultimately new tissue regeneration. These porous, biodegradable polyurethane scaffolds hold much promise for wound healing and tissue regeneration, especially with further understanding of their hydrolytic, enzymatic, and oxidative degradation mechanisms yielding soluble, non-toxic degradation products.

References

1. Gogolewski S, Gorna K. Biodegradable polyurethane cancellous bone graft substitutes in the treatment of iliac crest defects. *Journal of Biomedical Materials Research Part A* 2007; 80A(1): 94-101.

2. Li B, Yoshii T, Hafeman AE, Nyman JS, Wenke JC, Guelcher SA. The effects of controlled release of bmp-2 from biodegradable polyurethane/microsphere composite scaffolds on new bone formation in rat femoral plug model. *Biomaterials* 2009; *30*(35): 6768-6779.

3. Guelcher SA. Biodegradable polyurethanes: Synthesis and applications in regenerative medicine. *Tissue Eng Part B Rev* 2008; 14(1): 3-17.

4. Bonzani IC, Adhikari R, Houshyar S, Mayadunne R, Gunatillake P, Stevens MM. Synthesis of two-component injectable polyurethanes for bone tissue engineering. *Biomaterials* 2007; 28(3): 423-433.

5. Hafeman AE, Li B, Yoshii T, Zienkiewicz K, Davidson JM, Guelcher SA. Injectable biodegradable polyurethane scaffolds with release of platelet-derived growth factor for tissue repair and regeneration. *Pharmaceutical Research* 2008; *25*(10): 2387-2399.

6. Li B, Davidson JM, Guelcher SA. The effect of the local delivery of platelet-derived growth factor from reactive two-component polyurethane scaffolds on the healing in rat skin excisional wounds. *Biomaterials* 2009; 30(20): 3486-3494.

7. Borkenhagen M, Stoll RC, Neuenschwander P, Suter UW, Aebischer P. In vivo performance of a new biodegradable polyester urethane system used as a nerve guidance channel. *Biomaterials* 1998; 19(23): 2155-2165.

8. Fujimoto KL, Tobita K, Merryman WD, Guan J, Momoi N, Stolz DB, et al. An elastic, biodegradable cardiac patch induces contractile smooth muscle and improves cardiac remodeling and function in subacute myocardial infarction. *Journal of the American College of Cardiology* 2007; 49(23): 2292-2300.

9. Benoit FM. Degradation of polyurethane foams used in the mícme breast implant. *Journal of Biomedical Materials Research* 1993; 27(10): 1341-1348.

10. Stokes K, McVenes R, Anderson JM. Polyurethane elastomer biostability. *Journal of Biomaterials Applications* 1995; 9(4): 321-354.

11. Oertel G. Polyurethane handbook. 2 ed. Berlin: H. Gardner Publications, 1994.

12. Zhang J-Y, Beckman EJ, Piesco NP, Agarwal S. A new peptide-based urethane polymer: Synthesis, biodegradation, and potential to support cell growth in vitro. *Biomaterials* 2000; 21: 1247-1258.

13. Wang GB, Labow RS, Santerre JP. Biodegradation of a poly(ester)urea-urethane by cholesterol esterase: Isolation and identification of principal biodegradation products. *Journal of Biomedical Materials Research* 1997; 36(3): 407-417.

14. Tang YW, Labow RS, Santerre JP. Enzyme-induced biodegradation of polycarbonate polyurethanes: Dependence on hard-segment concentration. *Journal of Biomedical Materials Research* 2001; 56(4): 516-528.

15. Labow RS, Meek E, Matheson LA, Santerre JP. Human macrophage-mediated biodegradation of polyurethanes: Assessment of candidate enzyme activities. *Biomaterials* 2002; 23(19): 3969-3975.

16. Santerre JP, Woodhouse K, Laroche G, Labow RS. Understanding the biodegradation of polyurethanes: From classical implants to tissue engineering materials. *Biomaterials* 2005; 26(35): 7457-7470.

17. McBane JE, Santerre JP, Labow RS. The interaction between hydrolytic and oxidative pathways in macrophage-mediated polyurethane degradation. *Journal of Biomedical Materials Research Part A* 2007; 82A(4): 984-994.

18. Lu L, Peter SJ, D. Lyman M, Lai H-L, Leite SM, Tamada JA, et al. In vitro and in vivo degradation of porous poly(d,l-lactic-co-glycolic acid) foams. *Biomaterials* 2000; 21(18): 1837-1845.

19. Xia Z, Huang Y, Adamopoulos IE, Walpole A, Triffitt JT, Cui Z. Macrophage-mediated biodegradation of poly(dl-lactide-co-glycolide) *in vitro*. *Journal of Biomedical Materials Research Part A* 2006; 79A(3): 582-590.

20. Chapanian R, Tse MY, Pang SC, Amsden BG. The role of oxidation and enzymatic hydrolysis on the in vivo degradation of trimethylene carbonate based photocrosslinkable elastomers. *Biomaterials* 2009; 30(3): 295-306.

21. Anderson JM, Rodriguez A, Chang DT. Foreign body reaction to biomaterials. *Seminars in Immunology* 2008; 20(2): 86-100.

22. Xia Z, Triffitt JT. A review on macrophage responses to biomaterials. *Biomedical Materials* 2006; 1(1): R1-R9.

23. Anderson JM. Mechanisms of inflammation and infection with implanted devices. *Cardiovascular Pathology* 1993; 2(3).

24. Martin P, Leibovich SJ. Inflammatory cells during wound repair: The good, the bad and the ugly. *Trends in Cell Biology* 2005; 15(11): 599-607.

25. Williams DF. Some observations on the role of cellar. In: Syrett A, editor. Corrosion and degradation of implant materials: ASTM STP, 1979. p. 61-75.

26. Christenson EM, Anderson JM, Hiltner A. Oxidative mechanisms of poly(carbonate urethane) and poly(ether urethane) biodegradation: *In vivo* and *in vitro* correlations. *Journal of Biomedical Materials Research Part A* 2004; 70A(2): 245-255.

27. Zhao Q, Topham N, Anderson JM, Hiltner A, Lodoen G, Payet CR. Foreign-body giant cells and polyurethane biostability: *In vivo* correlation of cell adhesion and surface cracking. *Journal of Biomedical Materials Research* 1991; 25(2): 177-183.

28. Guelcher S, Srinivasan A, Hafeman A, Gallagher K, Doctor J, Khetan S, et al. Synthesis, in vitro degradation, and mechanical properties of two-component poly(ester urethane)urea scaffolds: Effects of water and polyol composition. *Tissue Engineering* 2007; 13(9): 2321-2333.

29. ASTM-International. D695-02a. Standard test method for compressive properties of rigid plastics. 2007.

30. ASTM-International. D3574-05. Standard test methods for flexible cellular materials - slab, bonded, and molded urethane foams. 2007; p. 360-368.

31. Labow RS, Meek E, Santerre JP. The biodegradation of poly(urethane)s by the esterolytic activity of serine proteases and oxidative enzyme systems. *Journal of Biomaterials Science Polymer Edition* 1999; 10(7): 699-713.

32. Schubert MA, Wiggins MJ, Anderson JM, Hiltner A. Role of oxygen in biodegradation of poly(etherurethane urea) elastomers. *Journal of Biomedical Materials Research* 1997; 34(4): 519-530.

33. Labow RS, Meek E, Santerre JP. Model systems to assess the destructive potential of human neutrophils and monocyte-derived macrophages during the acute and chronic phases of inflammation. *Journal of Biomedical Materials Research* 2001; 54(2): 189-197.

34. Beckwith AC, Paulis JW, Wall JS. Direct estimation of lysine in corn meals by the ninhydrin color reaction. *Journal of Agriculture and Food Chemistry* 1975; 23(2): 194-196.

35. Sawhney AS, Hubbell JA. Rapidly degraded terpolymers of d,l-lactide, glycolide, and ε-caprolactone with increased hydrophilicity by copolymerization with polyethers. *Journal of Biomedical Materials Research* 1990; 24: 1397-1411.

36. Renier M, Wu YK, Anderson JM, Hiltner A, Lodoen GA, Payet CR. Characterization of extractable species from poly(etherurethane urea) (peuu) elastomers *Journal of Biomaterials Science Polymer Edition* 1994; 5(6): 511-529.

37. Christenson EM, Patel S, Anderson JM, Hiltner A. Enzymatic degradation of poly(ether urethane) and poly(carbonate urethane) by cholesterol esterase. *Biomaterials* 2006; 27(21): 3920-3926.

38. Matheson LA, Labow RS, Santerre JP. Biodegradation of polycarbonate-based polyurethanes by the human monocyte-derived macrophage and u937 cell systems. *Journal of Biomedical Materials Research* 2002; 61(4): 505-513.

39. Valentin JE, Stewart-Akers AM, Gilbert TW, Badylak SF. Macrophage participation in the degradation and remodeling of extracellular matrix scaffolds. *Tissue Engineering, Part A* 2009; 15(7): 1687-1694.

40. Heiple JM, Wright SD, Allen NS, Silverstein SC. Macrophages form circular zones of very close apposition to lgg-coated surfaces. *Cell Motility and the Cytoskeleton* 1990; 15(4): 260-270.

41. Niethammer P, Grabher C, Look AT, Mitchison TJ. A tissue-scale gradient of hydrogen peroxide mediates rapid wound detection in zebrafish. *Nature* 2009; 459(7249): 996-999.

42. Stadtman ER. Oxidation of free amino acids and amino acid residues in proteins by radiolysis and by metal-catalyzed reactions. *Annual Review of Biochemistry* 1993; 62(1): 797-821.

43. Elliott SL, Fromstein JD, Santerre JP, Woodhouse KA. Identification of biodegradation products formed by l-phenylalanine based segmented polyurethaneureas. *Journal of Biomaterials Science Polymer Edition* 2002; 13(6): 691-711.

44. Zhang J-Y, Beckman EJ, Hu J, Yang G-g, Agarwal S, Hollinger JO. Synthesis, biodegradability, and biocompatibility of lysine diisocyanate-glucose polymers. *Tissue Engineering* 2002; 8(5): 771-785.

45. Lambda NMK, Woodhouse KA, Cooper SL. Polyurethanes in biomedical applications: CRC Press, 1997.

46. Tangpasuthadol V, Pendharkar SM, Kohn J. Hydrolytic degradation of tyrosine-derived polycarbonates, a class of new biomaterials. Part i: Study of model compounds. *Biomaterials* 2000; 21(23): 2371-2379.

47. Yamamoto K, Sakaguchi H, Anai H, Tanaka T, Morimoto K, Kichikawa K, et al. Sclerotherapy for simple cysts with use of ethanolamine oleate: Preliminary experience. *Cardiovascular and Interventional Radiology* 2005; 28: 751-755.

CHAPTER V

CONTROLLED RELEASE OF ANTIBIOTICS FROM SCAFFOLDS FOR LOCAL DELIVERY

Background

Open fractures resulting from orthopaedic trauma often allow bacteria into the wound, which can cause osteomyelitis—persistent bone infections—and thereby compromise fracture healing [1-5]. Contamination must be treated immediately to allow proper healing. Local delivery of antibiotics is advantageous by achieving high local concentrations while systemic levels remain low. This approach is a common clinical practice and has been demonstrated in animal studies to be safe and effective for treating osteomyelitis [6-12].

Local delivery of tobramycin from implanted poly(methyl methacrylate) (PMMA) cement beads is an established therapy for treating infected fractures, but only a small amount (< 10%) of the drug is released [10, 13-16]. The PMMA beads are not resorbable and must be surgically removed after two to six weeks, at which time a bone graft can be implanted to aid healing [14]. PMMA can be conducive to biofilm-forming bacteria, can reach unfavorably high temperatures during polymerization, and unreacted monomer can be cytotoxic [17]. Biodegradable calcium sulfate pellets impregnated with antibiotic (Osteoset T, Wright Medical) offer a tobramycin burst release of 58%, with little more after 2 – 3 days. They have been shown to be effective in treating osteomyelitis in animals and humans, but

they can be associated with seromas and drainage problems [6, 17-19]. Sustained release of tobramycin encapsulated in poly(DL-lactic-co-glycolic acid) (PLGA) biodegradable microspheres has also been reported over a period of up to four weeks, and the released tobramycin is biologically active *in vivo* [20]. While these materials may be clinically effective for infection control, they do not provide structural integrity for setting the fractures.

Tissue engineered scaffolds potentially offer advantages for controlled release of antibiotics by providing both sustained release of the bioactive component as well as a template for infiltration of new cells and tissue. Biodegradable polyurethanes (PUR) have been investigated extensively as scaffolds for tissue regeneration due to their potential for controlling the degradation rate and mechanical properties [21-27]. Scaffolds prepared from segmented PUR elastomers based on hexamethylene diisocyanate (HDI) have been shown to support ingrowth of cells and new bone formation and to degrade to non-cytotoxic decomposition products when implanted in the iliac crest of sheep [28, 29]. Other *in vivo* studies have demonstrated the potential of segmented PUR elastomers for regeneration of cardiovascular tissue [30-32].

In an alternative approach, PUR networks have been synthesized by two-component reactive liquid molding [24, 26, 33-35]. An advantage of reactive two-component systems is the potential to develop injectable scaffolds that can be combined with a biological, such as antibiotics or growth factors, prior to injection. Two-component foams with porosities > 90% prepared from HDI and polyester triols supported mineralization *in vitro* [26]. However, these materials were cured

at 60 °C and are therefore not suitable for injection. In another study, a reactive putty comprising a lysine diisocyanate (LDI) prepolymer and calcium phosphate exhibited good integration with host tissue, fibrovascular penetration, and ingrowth of vascular buds when implanted in rats [35]. However, the porosity and pore size of these materials was not reported, and scaffolds fabricated from LDI have been reported to have poor resilience [36].

PUR biomaterials have also been investigated as delivery systems. Biodegradable polyurethane scaffolds prepared from linear segmented elastomers were shown to support controlled release of bFGF, suggesting the potential utility of polyurethane scaffolds for drug delivery applications [37]. In another study, release of PDGF-BB from a reactive two-component PUR network was shown [36]. However, the bioactivity of the PDGF-BB released from the reactive PUR network was not investigated.

In this study, we report the release of biologically active tobramycin from reactive two-component polyurethane scaffolds. This presents a novel method of incorporating antibiotics into a reactive tissue engineered scaffold. This system may also be utilized for local delivery of other water-soluble antibiotics, proteins, or small molecule drugs.

Methods

Materials. Tobramycin was purchased from X-Gen Pharmaceuticals (Big Flats, NY). Simplex P cement beads with Tobramycin were obtained from Stryker

(Mahwah, NJ). All other reagents were purchased from Sigma-Aldrich (St. Louis, MO) or as outlined in the Materials section of Chapter II (p. 16).

Polyurethane (PUR) scaffold synthesis. The 900-Da trifunctional polyester polyols were prepared as described in Chapter II (p. 16) from ε-caprolactone, glycolide, and D,L-lactide monomers at a ratio of 60/30/10 (T6C3G1L) or 70/20/10 (T7C2G1L). As shown in previous studies, the half-life of the polyester triol regulates the degradation rate of the PUR network in which they are incorporated [36, 38]. The 7C2G1L polyol has a longer half-life (225 days) than 6C3G1L (20 days). Therefore, the two different polyol compositions were used to evaluate the effects of scaffold degradation times on the tobramycin release characteristics.

The PUR scaffolds were synthesized by reactive liquid molding of the aliphatic hexamethylene diisocyanate trimer (HDIt) and hardener, as explained in Chapter II (p. 18). Some materials were synthesized with poly(ethylene glycol) (PEG, 600 Da), such that the total polyol content consisted of 50 or 70 mol-% polyester polyol with 50 or 30 mol-% PEG. Core densities and porosities were determined from mass and volume measurements of triplicate cylindrical foam cores (Equation 2.4). Pore size distribution and interconnectivity also assessed by scanning electron microscopy (Hitachi S-4200 SEM, Finchampstead, UK).

Strategies for tobramycin incorporation into the PUR scaffolds. A few different strategies were evaluated to achieve controlled release of tobramycin from the PUR scaffolds. First, tobramycin was incorporated into a polyester polymer that was used to coat tricalcium phosphate (TCP) granules (Vitoss; Orthovita, Malvern, PA), which were subsequently added to the scaffolds during PUR synthesis [44, 45].

Tricalcium phosphate was utilized because as an osteoconductive material, it has been shown to facilitate new bone growth [39]. The polymers used for coating were synthesized in the same manner as described above for polyol synthesis, although poly(ethylene glycol) (PEG) was used as a starter instead of glycerol, and the final polyester polyol molecular weights was MW 9800 (instead of 900, as used in PUR scaffold synthesis). The PEG used to start the polyol reaction was either MW 600, 1450, or 3350, and the ratio of ε-caprolactone, glycolide, and D,L-lactide monomers was 60/30/10 (T6C3G1L). Tobramycin was dissolved to 50 mg/mL in 0.01 N HCl; 200 μL of this solution was added to 200 mg polymer and 500 mg TCP granules, all in 3 mL distilled acetone. This mixture was incubated on a plate shaker at room temperature for 30 min, followed by removal of the acetone by centrifugal evaporation. These coated granules were stored at -20 °C until use to prevent unintended tobramycin redistribution or diffusion from the polymer coating.

The second approach involved encapsulating tobramycin inside microspheres, which were again subsequently added at 25 wt-% to PUR scaffolds containing 30% PEG. The microspheres consisted of 50:50 poly(D,L-lactic-*co*-glycolic) acid (PLGA, 0.39 dL/g PLGA) and 0 or 5% poly(ethylene glycol) (PEG, MW 600 Da) via a double emulsion method in 0.5 wt% poly(vinyl alcohol) (PVA) [20, 40]. First the PVA solution was prepared by dissolving 2.75 g solid PVA into 550 mL deionized water and mixing at 50 °C, covered, overnight with a magnetic stirrer. A total of 250 mg of PLGA and PEG (with either 0 or 5% PEG) was dissolved in 5 mL dichloromethane (DCM). 50 mg tobramycin was added to this solution, after which it was sonicated for 30 minutes to create a homogeneous emulsion. The PVA and

PLGA solutions were then transferred into two separate syringes and mounted into syringe pumps. These solutions were pumped through two concentric tubes into a receiving beaker filled with excess PVA – PLGA through the inner metal tube at 12.5 mL/hr and PVA through the outer glass tube at 50 mL/hr. The ends of the tubes were submerged in the beaker of excess PVA such that the PLGA/PEG/tobramycin would precipitate immediately upon encountering the PVA, when the DCM is extracted into the aqueous phase. The beaker with PVA and PLGA microspheres was stirred magnetically for 3 hours at room temperature. The microspheres were then vacuum-filtered from the PVA solution and washed with deionized water to remove any residual PVA. Finally, the microspheres were lyophilized overnight.

The encapsulation efficiency of tobramycin inside the microspheres was determined by solvent extraction. Because tobramycin prefers the aqueous PVA phase to the organic DCM phase, tobramycin cannot be encapsulated at 100% efficiency, as some is lost into the external PVA phase. Knowledge of this efficiency allows for the estimation of tobramycin loading during microsphere synthesis to reach a target release level, as well as the calculation of the percentage of tobramycin released from the microspheres. Triplicate batches of microspheres (20 mg) were each dissolved in 1 mL dichloromethane and shaken on an end-over-end mixer at room temperature for 6 hours. The samples were then vortexed for 30 seconds after adding 1 mL PBS and centrifuged for 5 min at 9,000 rpm. The aqueous PBS phase containing tobramycin was removed, and the process was repeated three more times for a total of 24 hours. At the end of the 24 hours, the aqueous samples removed at each 6-hour time point were assayed, and the results summed to

determine the total encapsulated tobramycin. The released tobramycin was quantified using a CBQCA Protein Quantitation assay (Invitrogen Molecular Probes, Carlsbad, CA).

As the simplest approach, tobramycin was added as a powder to the hardener prior to reaction with the triisocyanate resin in order to minimize its reactivity with the reactive two-component polyurethane. This was uncertain because tobramycin's five primary amino groups otherwise cause it to react rapidly with isocyanates when in solution [41]. Tobramycin is insoluble in polyester polyol, the primary component in the hardener; consequently the tobramycin remains in the solid phase during the chemical reaction. A loading of 8 wt-% (20 pphp) was chosen to approximate the level of tobramycin delivered from the equivalent volume of PMMA cement beads, but higher loading can be achieved if necessary. Because this straightforward approach was successful, it is the primary method for tobramycin incorporation into the scaffolds for the remaining studies included here, unless stated otherwise.

PMMA bead synthesis. The PMMA cement beads were made according to the manufacturer's instructions. Briefly, the liquid monomer was added to the bone cement powder and hand mixed. The resulting paste was rolled into individual 50-mg beads, approximately 5 mm in diameter. Tobramycin release from these beads was compared to that from the PUR scaffolds.

In vitro tobramycin release. Triplicate 500-mg samples of the scaffolds each in 1 mL phosphate buffered saline (PBS, pH 7.4) were mixed end-over-end while incubating at 37 °C. At designated time points from 0.5 to 30 days, the buffer was

removed from each vial and replaced. All release samples were frozen until analysis at the end of the 30 days. The released tobramycin was derivatized with *o*-phthaldialdehyde (PHT) and quantified with a Waters Breeze HPLC and UV detector, using a previously published method [42]. 250 μL of each sample was added to 100 μL PHT (100 mg/mL in methanol) and 150 μL isopropanol. This mixture was vortexed for 30 seconds and incubated at room temperature for 45 minutes before injection. The injected sample (50 μL) was separated in an XTerra reverse-phase guard column (C8 5-μm 3.9 x 20 mm) and XTerra reverse-phase column (C18 5-μm 4.6 x 250 mm) and analyzed at 333 nm. The mobile phases were as follows: (A) 0.1% acetic acid in water, and (B) 88.5% acetonitrile in water with 0.1% acetic acid. Both were filtered through a 0.2 μm filter and degassed under vacuum. The buffer ratio was 80/20 A/B (A/B) for the first 2 min, with a gradual gradient to 77/23 (A/B) from 2 to 6 min. The samples were calibrated by an external standard curve from 0.05 μg/mL to 30 μg/mL. With a 1.0-mL/min flow rate, the tobramycin peak eluted at approximately 6.5 minutes.

Bioactivity of released tobramycin. The tobramycin activity was evaluated by Kirby-Bauer, or diffusion, assays. Colonies of methicillin-susceptible *Staphylococcus aureus* (*S. aureus*) from the American Type Culture Collection (ATCC 25923) were suspended in trypticase soy broth and the turbidity was matched to a 0.5 MacFarland standard. The bacteria were then streaked onto Mueller-Hinton agar plates (lower limit of detection was 20 CFU/mL). Tobramycin scaffold samples were cut into discs (6 x 2 mm, 400 – 600 μg tobramycin per disc) and placed on the agar plates. Zones of inhibition (ZI) were measured in comparison with 10-μg

tobramycin BBL SensiDiscs (BD, Franklin Lakes, NJ) and individual PMMA beads, with 3 – 4 mg tobramycin per bead, after incubation at 37 °C for 24 hours. The 10-μg tobramycin BBL SensiDiscs were chosen as a positive laboratory control, since this is a standard control used in pathology laboratories. Additionally, the bioactivity of the tobramycin after sustained release was evaluated. 0.5-μg tobramycin aliquots from release samples at 8, 20, and 30 days, as well as 0.5 μg pure tobramycin, were pipetted onto blank SensiDiscs. These discs were again placed onto *S. aureus*-streaked agar plates and the ZI were measured after 24 hours.

Mechanical properties. Dynamic mechanical properties of a representative selection of scaffolds, both with and without tobramycin, were measured in compression mode. Cylindrical 7 x 6 mm samples were compressed along the axis of foam rise. The temperature-dependent storage modulus and glass transition temperature (T_g) of each material were evaluated under a temperature sweep of -80 °C to 100 °C, at a compression frequency of 1 Hz, 20-μm amplitude, 0.3% strain, and 0.2-N static force. The stress relaxation modulus was evaluated as a function of time under 2% strain and 0.2-N static force. The frequency-dependent storage modulus was also evaluated by a frequency sweep of 0.1 to 10 Hz at a constant temperature of 37 °C, with 0.3% strain and 0.2-N static force. Stress-strain curves were generated by controlled-force compression of the cylindrical foam cores at 37 °C. With an initial force of 0.1 N, each sample was deformed at 0.1 N/min until it reached 50% strain (i.e. 50% of its initial height). The Young's (elastic) modulus was determined from the slope of the initial linear region of each stress-strain curve [43]. The scaffolds could not be compressed to failure due to their elasticity, so the

compressive stress was measured at 37 °C after one minute at 50% strain in the DMA stress relaxation mode, as a measure of compressive strength [44]. Calculated from the measured force and cross-sectional sample area, the compressive stress indicates material compliance such that more compliant materials require lower stress to induce a particular strain.

Statistical Analysis. Statistical analysis of the results was performed using single factor analysis of variance (ANOVA). In cases where statistical significance is cited, the sample size is greater than or equal to three replicates per material.

Results

PUR scaffold characterization. The density and porosity of the PUR scaffolds with and without tobramycin are shown in Table 5.1. Incorporation of 8 wt-% tobramycin in the PUR scaffolds increased the density (and therefore decreased the porosity), although not with statistical significance ($0.05 > p > 0.005$). In most cases, the addition of PEG had an insignificant effect on PUR density and porosity. However, the T6C3G1L-PEG50 scaffold with tobramycin exhibited a significantly higher density than any of the other materials. The porosity and pore structure was not significantly affected by the incorporation of tobramycin.

Table 5.15. Density and porosity of PUR/tobramycin scaffolds (with T6C3G1L polyol) (n = 3).

Material	Tobramycin	Density (kg m^{-3})	Porosity (vol-%)
PEG 0	+	140 ± 6	89 ± 0.5
	-	98 ± 13	92 ± 1
PEG 10	+	134 ± 21	89 ± 2
PEG 20	+	107 ± 12	91 ± 1
PEG 30	+	119 ± 9	90 ± 9
	-	90 ± 3	93 ± 0.2
PEG 50	+	177 ± 4	85 ± 0.3
	-	94 ± 11	92 ± 1

In vitro tobramycin release. Tobramycin release profiles from the PUR scaffolds and PMMA beads are presented in Figure 5.1. The burst release increased from 45% to 95% as the PEG content in the polyol component was increased from 0 to 50%. Interestingly, there was a significant increase in the burst release of tobramycin when the PEG content was elevated from 20% to 30%. As the PEG content increased, the amount of tobramycin released at later time points (after the initial burst) decreased from 35% of the total release to < 5%. Therefore, at the highest PEG content (50%), almost no additional antibiotic was released after the first 24 hours. After 30 days, the total release of tobramycin ranged from 70 to 95%, with 30 and 50% PEG scaffolds demonstrating the highest cumulative release. In contrast, the total release of tobramycin from the PMMA cement beads after 30 days was 20%, with little additional release after 7 days. Tobramycin release is likely independent of material degradation, as the 6C3G1L-PEG0 and 7C2G1L-PEG0 scaffolds demonstrate similar tobramycin release profiles yet different degradation

rates. Conversely, while the release profiles of the scaffolds containing 0, 30, and 50% PEG differed considerably, the *in vitro* degradation rates of these scaffolds demonstrated no statistically significant differences ($p > 0.05$) during the 4-week time period corresponding to the release experiments (Figure 2.6) [36].

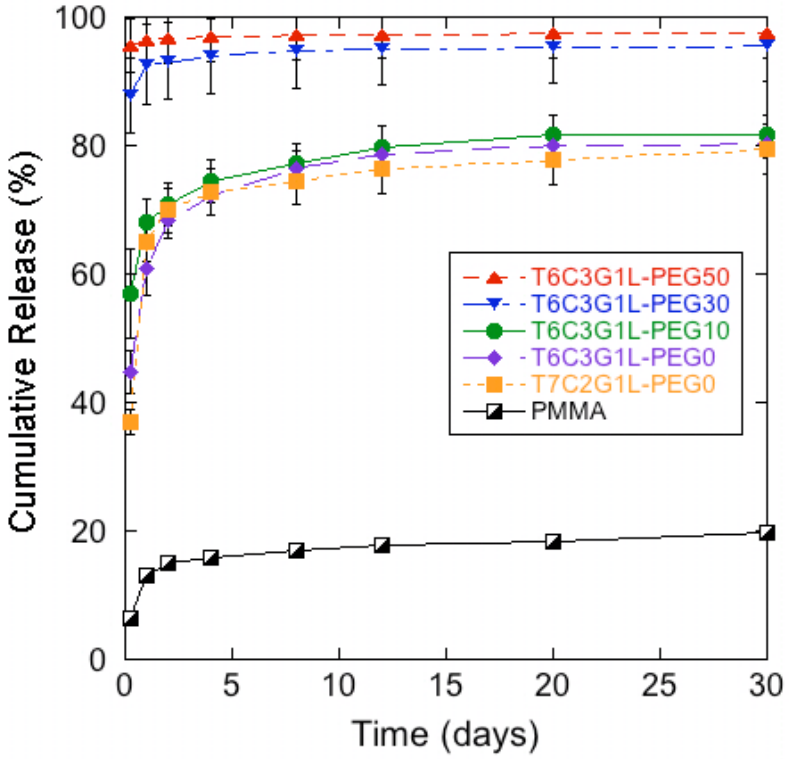

Figure 5.49. *In vitro* tobramycin release from PUR scaffolds and PMMA beads. Materials were incubated at 37 °C in PBS, which was completely removed and refreshed at each time point. Tobramycin concentration in the releasate was measured by HPLC (n = 3).

The encapsulation efficiency of tobramycin inside the PLGA/PEG microspheres averaged 41% of that added to the emulsion. The microsphere diameter ranged from 150 – 300 μm. The high water solubility of tobramycin causes it to preferably partition to the aqueous PVA phase, instead of the polymer phase. Release from the PUR scaffolds with PLGA/PEG microspheres is shown in

Figure 5.2, in comparison to the release of powdered tobramycin from the equivalent 30% PEG scaffold. Incorporation into microspheres within the scaffolds clearly decelerated the release rate, due to the additional diffusion paths through hydrophobic PLGA. Tobramycin release from the coated TCP granules is presented in Figure 5.3.

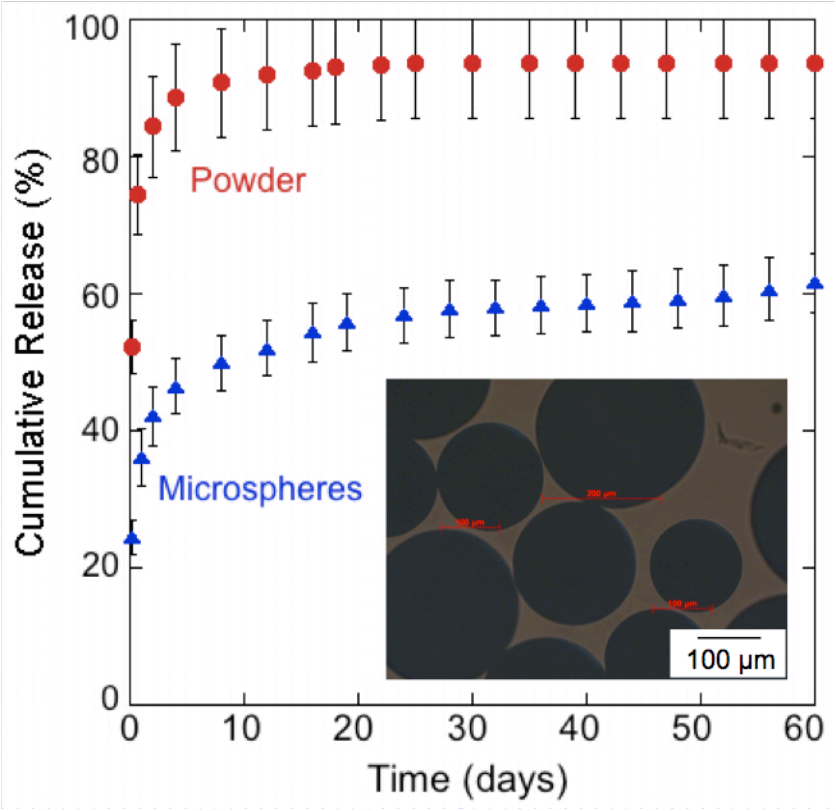

Figure 5.50. Tobramycin release, when encapsulated in microspheres vs. as a powder, from the PUR scaffolds. Inset image depicts microspheres as captured by a light microscope (n = 3).

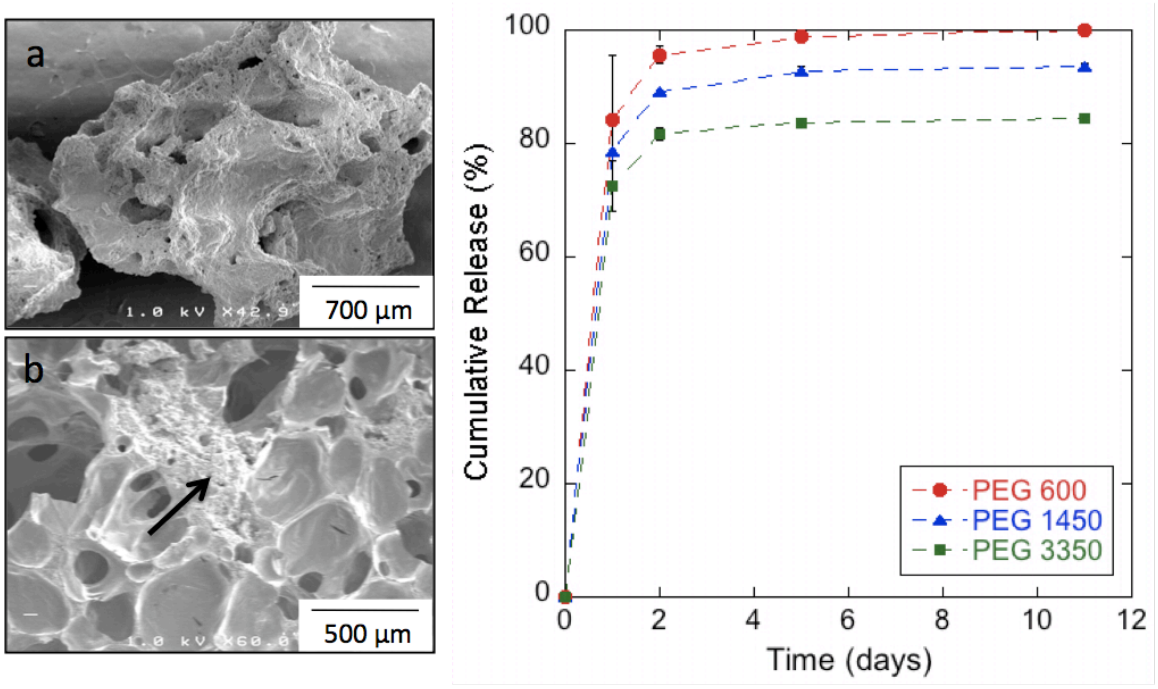

Figure 5.51. TCP granule coated with tobramycin-containing polyol (a). Coated TCP granule (arrow) embedded within a PUR scaffold (b). Short-term tobramycin release (right).

Bioactivity of released tobramycin. While the data in Figure 3 demonstrate that tobramycin is released from the PUR scaffolds, they do not address the question of whether the tobramycin is biologically active. Therefore, the bioactivity of the tobramycin released from the PUR scaffolds and PMMA cement beads over 24 hours was assessed by the standard Kirby-Bauer assay (Figure 5.4). In the Kirby-Bauer assay, the drug is loaded in a disc that is then placed on an agar plate that has been swabbed with a microorganism (e.g., *S. aureus*). As the drug diffuses from the disc into the agar, the local concentration of tobramcyin in the zone near the disc exceeds the MIC, thereby creating a zone of inhibition (ZI) in which there are no bacteria. Thus the objective of the Kirby-Bauer assay is to assess antimicrobial efficacy through cumulative deposition of antibiotic in the agar to exceed local MIC

values. While the cumulative deposition release conditions in the Kirby-Bauer assay differ from the semi-infinite sink conditions in the release study, the advantage of the Kirby-Bauer assay is that it provides an established test to assess antimicrobial efficacy. The zones of inhibition (ZI) generated by the PUR samples (400 – 600 μg tobramycin each) were consistently greater than both the positive laboratory control (10 mg each) and the PMMA beads (3 – 4 mg each). As might be expected from the release curves (Figure 5.1), the PEG scaffolds produced larger ZI, with statistically significant differences from the positive control and PMMA beads (p < 0.005). Furthermore, blank PUR scaffolds with no tobramycin generated no ZI.

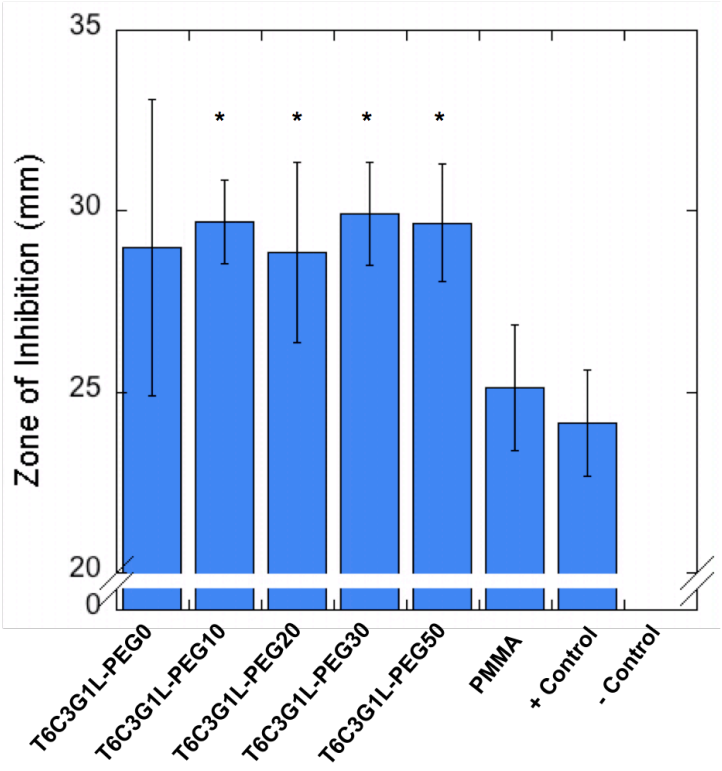

Figure 5.52. ZI measured after 24 hours for PUR scaffolds using the Kirby-Bauer test. Positive control: 10-μg tobramycin BBL SensiDiscs. Negative control: PUR scaffolds with no tobramycin. (* = p < 0.005 by ANOVA test with respect to the positive control and PMMA, n=6).

These data indicate that the tobramycin released from the PUR scaffolds in the first 24 hours is biologically active, as demonstrated by the observed inhibition of *S. aureus* growth.

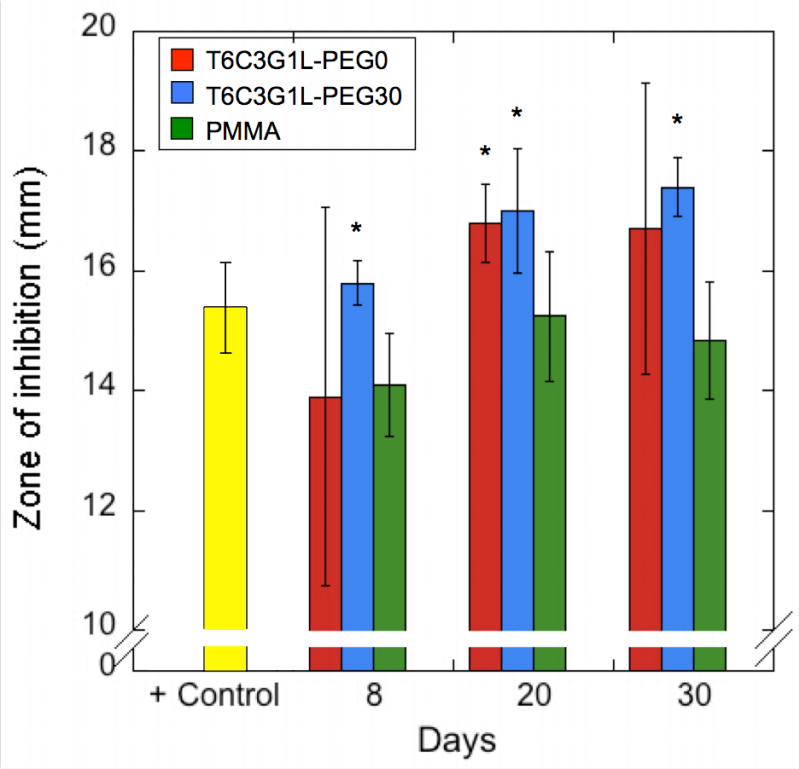

Figure 5.53. Bioactivityx of tobramycin did not diminish when released from PUR scaffolds and PMMA cement beads after 8, 20, and 30 days of incubation in PBS, evaluated by Kirby-Bauer tests. Blank BBL SensiDiscs were loaded with 0.5 mg tobramycin (in 10 mL) PBS) from each releasate (as determined by HPLC), as well as 0.5 mg exogenous tobramycin for the positive control. (* = $p < 0.005$ by ANOVA tes with respect to the positive control, n = 6).

While the Kirby-Bauer data in Figure 5.4 suggest that the released tobramycin is biologically active in the initial release period, they do not answer the question of whether the drug is active when released at later time periods. Therefore, the bioactivity of the tobramycin released after 8, 20, and 30 days was analyzed in order to investigate the tobramycin stability and activity over time. The

appropriate volumes of releasate containing 0.5 mg tobramycin per sample (as calculated from the release data in Figure 5.1) were lyophilized, reconstituted in 10 mL PBS, and deposited on blank BBL SensiDiscs for Kirby Bauer tests. Figure 5.5 shows the ZI for releasates from the PMMA beads, T6C3G1L-PEG0 scaffold, and T6C3G1L-PEG30 scaffold. These data indicate that the bioactivity of the tobramycin released from PUR scaffolds is comparable to that of the PMMA and exogenous tobramycin controls for up to 30 days.

Mechanical properties. Glass transition temperatures (T_g) of the PUR scaffolds were measured by DMA temperature sweeps in compression mode (Table 5.2). The T_g values ranged from 3 – 41 °C. With exception of the non-PEG materials, tobramycin depressed the T_g with a variable effect on the scaffold mechanical properties. In previous studies, we observed a reduction in storage modulus at 37 °C coinciding with a decrease in T_g, but this trend seems to be confounded by the presence of tobramycin [36]. The compressive stress (at 50% strain) and storage modulus at 37 °C consistently increased with addition of tobramycin, while the Young's modulus values showed no regular trend.

The frequency-dependent storage and loss moduli at 37 °C for some of the materials, both with and without tobramycin, are illustrated in Figure 5.6. These representative materials were selected to illustrate the overall trends observed in response to the presence of PEG and/or tobramycin. The left panel depicts moduli of the T6C3G1L scaffolds without PEG. These materials have glass transition temperatures near 40 °C, and their properties at 37 °C are representative of leathery materials in the glassy transition zone [45]. The storage modulus (E') and

Table 5.16. Mechanical properties of PUR/tobramycin scaffolds (with T6C3G1L polyol) measured by DMA (n = 3).

Material	Tobramycin	T_g (°C)	Storage Modulus at 37°C (kPa)	Young's Modulus (kPa)	Compressive Stress (kPa)
PEG 0	+	41.3	1268	106 ± 16	68 ± 19
	-	40.3	723	115 ± 30	11 ± 1
PEG 10	+	16.5	1059	99 ± 19	48 ± 7
PEG 20	+	2.8	43	43 ± 5	12 ± 1
PEG 30	+	7.5	152	41 ± 8	22 ± 7
	-	24.3	14	58 ± 15	7 ± 0.5
PEG 50	+	8.8	28	48 ± 17	38 ± 10
	-	18.5	18	15 ± 3	7 ± 0.6

loss modulus (E''), which characterize the energy stored elastically and energy lost through viscous dissipation, respectively, were comparable and both rose by an order of magnitude with increasing frequency. As the PEG content of the materials is increased, the glass transition temperature is reduced to temperatures well below 37 °C. The scaffolds therefore behaved more like ideal elastomers in the rubbery plateau zone, with moduli approximately an order of magnitude lower than the non-PEG materials. The storage modulus consistently remained well above the loss modulus, thus exhibiting less damping than the materials without PEG. The storage modulus was relatively constant over the frequency range, while the loss modulus increased by less than an order of magnitude. As shown in Figure 6, the incorporation of tobramycin did not affect the viscoelastic properties of the scaffolds, as evidenced by the similar shape of the frequency sweeps in both the presence and absence of tobramycin. Stress relaxation experiments at 2% strain are generally consistent with the frequency sweeps (data not shown), with PEG

scaffolds exhibiting a purely elastic response and non-PEG scaffolds a more viscoelastic response.

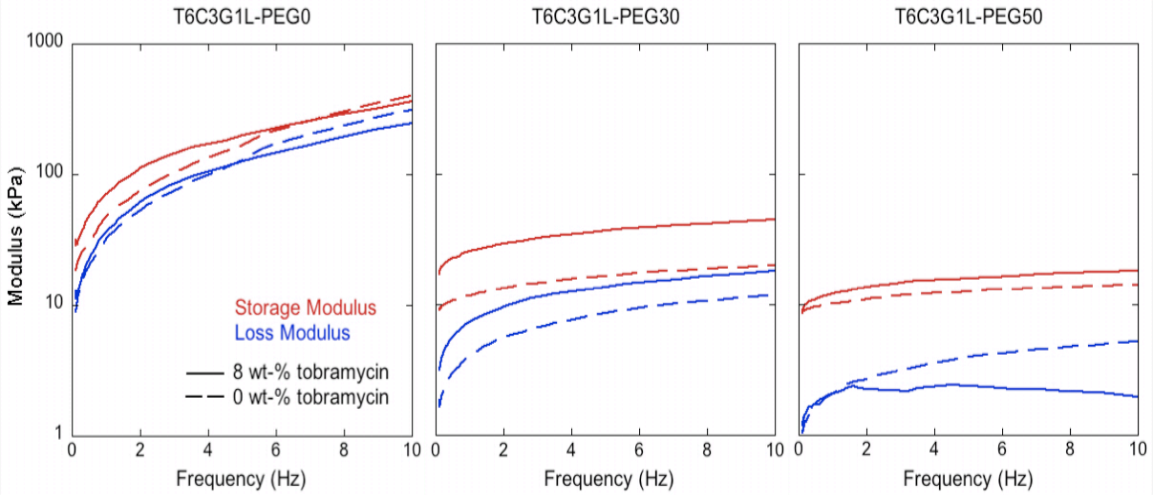

Figure 5.54. Storage (bold) and loss moduli as a function of shear rate in compression mode during DMA frequency sweeps from 0.1 to 10 Hz. Illustrated are the results from T6C3G1L scaffolds with 0%, 30%, and 50% PEG, each with (solid line) and without (dotted line) tobramycin.

While tobramycin augmented the mechanical strength of the dry scaffolds, this effect was reversed after the scaffolds were immersed in buffer *in vitro* due to polymer swelling and release of tobramycin. This occurred for scaffolds both with and without tobramycin. For example, while the scaffolds retained their elastomeric properties (no failure at compressive strains up to 50%), the compressive stress at 50% strain decreased by 25-30%, and the storage modulus by as much as 50%, after one week of *in vitro* release. Therefore, the compressive strength and modulus of the scaffolds decreases due to diffusion of tobramycin from the scaffold. However, it is important to note that the scaffolds retain their elasticity. Furthermore, previous *in vivo* studies suggested that cells and granulation tissue are

present by that time, which is conjectured to the strengthen the implant since the processes of tobramycin release and ingrowth of new tissue are occurring at the same time scale [36].

Discussion

Two-component polyurethane scaffolds demonstrate promise as tissue engineered scaffolds because they provide both porous structural supports for cell migration and new tissue formation, as well as local delivery of antibiotics to treat and prevent fracture-related osteomyelitis. Starting from a reactive liquid mixture, they potentially can be injected to cure *in situ* by a gas foaming process, allowing them to expand and fill irregularly shaped wounds [36]. In our unpublished experiments, PUR scaffolds injected into femoral plug defects in the femurs of Sprague-Dawley rats have been shown to adhere to the host bone, and mCT analysis suggests the formation of new bone after 6 weeks post-injection[46]. PUR scaffolds have been shown to biodegrade to non-cytotoxic degradation products and facilitate cell proliferation and new tissue formation, both *in vitro* and *in vivo* [33, 36, 47]. As shown here and in previous work, the dynamic mechanical properties and hydrophilicity can be adjusted by varying the level of poly(ethylene glycol) [36]. These effects primarily seem to result from glass transition temperature changes, causing the mechanical properties of the scaffolds to vary from glassy to elastomeric, although all materials demonstrate low permanent deformation and high resilience.

These PUR scaffolds exhibit tobramycin release comparable to the release kinetics reported for PMMA and calcium sulfate bone cements. We observed a burst release of 45%, 90%, and 95% with 0, 30, and 50% PEG, respectively, followed by a sustained release for up to 30 days. To determine whether the release at later time points exceeded the minimum inhibitory concentration (MIC, 4 – 8 μg/mL) and minimum bactericidal concentration (MBC, 16 μg/mL) for tobramycin with *S. aureus*, the daily release (mg/mL implant) was calculated from logarithmic fits of the cumulative release profiles as shown in Figure 5.7 [48]. While the semi-infinite sink conditions utilized in this study do not perfectly mimic the *in vivo* microenvironment, it is noteworthy that at each time point the concentration of tobramycin released from the PUR scaffolds exceeded that released from the PMMA beads, an established clinical therapy for elimination of osteomyelitis. These are clinically effective, but they exhibit low release efficiency and must be removed during a second surgery because they are not biodegradable. Furthermore, PMMA can be conducive to biofilm-forming bacteria, can reach unfavorably high temperatures during polymerization, and unreacted monomer can be cytotoxic [17]. Biodegradable calcium sulfate pellets with 10 wt-% tobramycin, approved for clinical use in countries outside the United States, have also successfully treated intramedullary infections and facilitated new bone growth in both animals and humans [6, 17-19]. These pellets offer a tobramycin burst release of 58%, with little more after 2 – 3 days; a more sustained release might be desired to avoid antibiotic resistance developed from subtherapeutic antibiotic levels. There also have been drainage and seroma formation issues associated with this material.

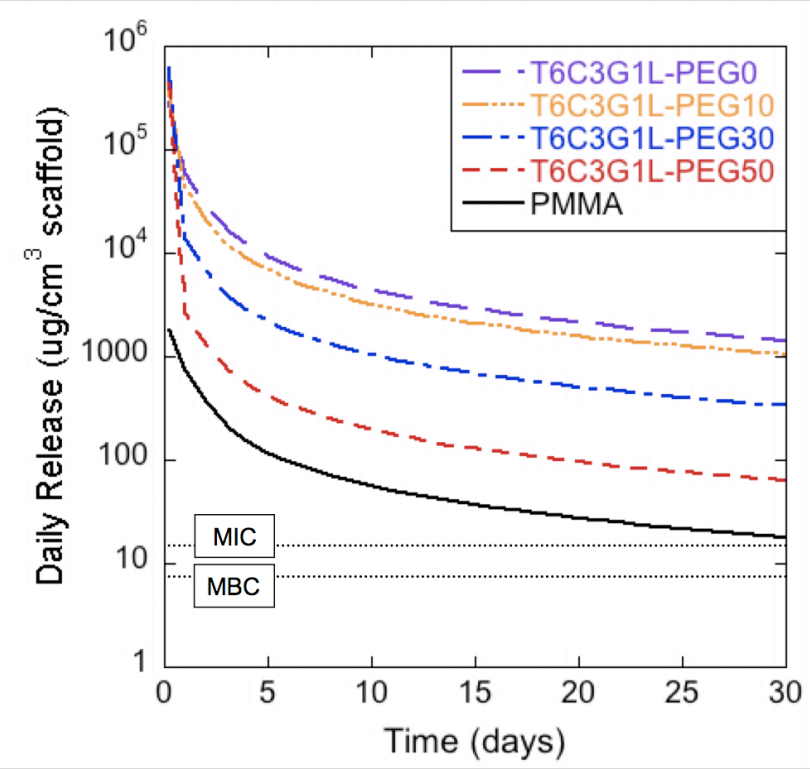

Figure 5.55. Average daily release profiles calculated from exponential fits of the cumulative release profiles, shown in comparison to the MIC and MBC for tobramycin against *S. aureus*.

Alternatively, biodegradable PLGA microspheres provide sustained tobramycin release over one month, with relatively high encapsulation efficiencies of 40 – 60% [20]. Control of the release profile can be achieved by varying the microsphere ratio of PLGA and PEG. Microspheres with 4.5-wt% tobramycin were implanted into a rabbit radial defect model infected with *S. aureus,* and after 4 weeks, the infection was eliminated and bone healing was observed [48]. While these PLGA microspheres have been shown to be efficient antibiotic delivery vehicles, they must be pre-made, which precludes customization at the time of implantation or injection, and they do not possess the structural integrity typically associated with a scaffold.

Tobramycin release from the PUR scaffolds, as well as from the other referenced materials, may be diffusion-controlled. Thus release is independent of — and occurs on a shorter time scale than — the polyurethane degradation. When immersed in buffer (or serum), the scaffold swells with water, which dissolves any accessible tobramycin, allowing it to diffuse out of the scaffold into the surrounding media. The burst release may result from the immediate dissolution of any tobramycin located on or near the scaffold surfaces, with extended release resulting from eventual dissolution and diffusion of tobramycin embedded within the pore walls. The increased burst release of tobramycin from PUR scaffolds incorporating PEG may result from the more hydrophilic nature of the polymer through two possible mechanisms predicted by the Higuchi equation [49]. First, due to increased swelling of the PUR scaffolds incorporating PEG, the diffusivity of tobramycin in the scaffold may increase. Furthermore, the presence of PEG likely increases the solubility of the drug within the scaffold. The burst and overall rate of release directly depend on the drug solubility, as observed experimentally. Drugs with lower water solubility than tobramycin tend to exhibit a lower burst release and more linear, longer-term release profiles [50]. At high porogen loadings (e.g., > 30%), channels can form in the scaffold due to dissolution of the porogen, thereby increasing the diffusivity of the drug and the release rate [49]. While under certain conditions PEG functions as a porogen, it is important to note that in the PUR scaffolds, the PEG is covalently bound to the polymer network and thus cannot dissolve.

The five primary amino groups in tobramycin potentially could be very reactive with the polyurethane, which reacts with free amines and hydroxyl groups during synthesis (the material is no longer reactive after synthesis is complete) [41]. Thus the tobramycin, as well as any added drug or growth factor, is added as a lyophilized powder to the hardener component of the polyurethane to limit reactivity. This approach differs from a previously published method of incorporating ascorbic acid, which can stimulate osteoblast differentiation, in the polymer by reaction in the liquid phase with a prepolymer of lysine diisocyanate (LDI) and glycerol [51]. The ascorbic acid was dissolved in glycerol prior to the reaction and, due to its four hydroxyl groups, reacted with the LDI to form urethane linkages and covalently bind to the polymer. Ascorbic acid release from the gas-foamed scaffold consequently was coupled to the material degradation rate.

We have verified the bioactivity of tobramycin released from the PUR scaffolds with Kirby-Bauer assays, suggesting negligible reaction between the lyophilized tobramycin and polyurethane during synthesis. Furthermore, due to the heat stability of aminoglycosides, activity seems to be unaffected by the slightly exothermic (up to 40 °C) polyurethane reaction [25]. The Kirby-Bauer assays show that these scaffolds release sufficient tobramycin to exceed the MIC and MBC for *S. aureus* [48]. PUR scaffolds containing colistin and tigecycline achieved similar Kirby-Bauer results (data not shown), demonstrating that this system can be used with other antibiotics besides tobramycin. The release and Kirby-Bauer assays were repeated with identical PUR scaffolds that had been sterilized by ethylene oxide treatment, to verify that future *in vivo* experiments would not be affected by

the sterilization method. No differences were detected, both for tobramycin release rates as well as bioactivity of the tobramycin releasate. While the Kirby-Bauer assay is an established *in vitro* model for measuring antimicrobial efficacy, the release kinetics of tobramycin *in vivo* are anticipated to differ substantially from those in saline or agar due to differences in diffusivity and hydrodynamics in the bone microenvironment. Furthermore, it is not possible to model the *in vivo* biochemical environment *in vitro*. Therefore, although the *in vitro* data reported in this study suggest that PUR scaffolds incorporating antibiotics have potential for treating infected fractures, the results must be validated in an established animal model of infection, such as an infected segmental femoral defect [52]. These experiments are ongoing in our laboratory.

The mechanical and biological properties of these PUR scaffolds can be adjusted to benefit a variety of wounds and applications. We have shown previously their potential utility in dermal wounds, such as burns and diabetic lesions. That study included the local delivery of platelet-derived growth factor, suggesting that the scaffolds can also carry growth factors or small molecule therapeutics to enhance healing [36]. Similar materials were successfully used for cardiac regeneration, so the PUR scaffolds may benefit soft tissue wounds as well [37, 53].

Modeling of release kinetics

The understanding of release kinetics is important for predicting and designing systems of controlled drug delivery. By understanding the release mechanisms and contribution of physical properties of the polymer and drug

system, certain parameters can be adjusted to achieve desired release profiles. Numerous studies have been published, beyond those discussed here, about mathematical models to describe these release systems [54-60]. These differ in their approach to the drug-polymer system, primarily based on either empirical or mechanistic models, as well as the polymer geometries and degradation characteristics considered. Some studies simulate polymer degradation and drug dissolution as random events using Monte Carlo techniques [55]. These studies, as well as this discussion, consider only systems where the drug is physically immobilized within polymer matrix; cases where the drug is covalently bound to the polymer would be entirely degradation-dependent. In addition, most models assume that the initial drug concentration is higher than the solubility of the drug within the polymer matrix.

The general scheme of drug release involves water permeation into the polymer, which dissolves the drug, followed by diffusion of the drug through the polymer or aqueous pores out of the system and into surrounding media due to a concentration gradient. The release kinetics behavior depends principally on the physical and chemical characteristics of the released drug and polymer matrix, including mass transport and chemical reaction considerations:

1) water uptake in polymer (swelling)
2) polymer glass transition from a glassy to rubbery state
3) polymer degradation
    a. autocatalysis
    b. local pH changes

4) crystallization of polymer degradation products within matrix
5) creation of aqueous pores or channels in polymer
6) polymer matrix geometry
7) drug dissolution
8) drug solubility limit within polymer
9) drug solubility limit within surrounding media
10) drug diffusion within polymer
11) drug diffusion through aqueous pores.

Mathematical models would become far too complex if they accommodated all of these influences, so these parameters must be prioritized and consolidated to model a given polymer-drug system. Empirical or semi-empirical models often address this issue by combining several physical and chemical characteristics into one or two constants.

Initial release studies and models did not account for matrix degradation [56], but the onset and importance of biodegradable drug carriers has subsequently brought polymer degradation into most models. The primary focus is on the spatial constraints of erosion, distinguishing bulk and surface eroding polymers. The mechanism for a given polymer system is determined by the ratio of water diffusion into the polymer compared to the degradation rate of the polymer backbone [61].

Bulk erosion: (rate of water uptake) > (rate of polymer cleavage)

Surface erosion: (rate of water uptake) < (rate of polymer cleavage)

Most systems considered contain high initial drug loadings with homogeneous dispersion, where the initial concentration (c_0) is higher than the drug solubility

within the polymer (c_s). The drug must dissolve, either within the polymer or in the aqueous media, before diffusing out of the polymer matrix, thereby implicating the drug solubility limit as a rate-limiting step. Furthermore, as the drug diffuses out of the scaffold, it creates aqueous pores within the polymer matrix, which can accelerate subsequent drug diffusion [62].

Clearly the diffusion coefficient (D) of the drug in the polymer is another rate-limiting step in the overall release rate. This parameter depends on the polymer molecular weight and degree of crosslinking, as well as the glassy or rubbery state of the polymer. Glassy polymer matrices yield lower diffusion coefficients, but even in these cases, water that permeates the polymer acts as a plasticizer and effectively lowers the glass transition temperature [63]. Thus the diffusion coefficient can be dependent on time and spatial coordinates, as water uptake can cause the polymer to transition from a glassy to rubbery state. The *in vitro* drug release experiments, both in the literature and in this study, attempt to approximate infinite sink conditions such that a boundary diffusion layer can be considered negligible. However, the *in vitro* release kinetics likely differs from the *in vivo* release kinetics because of the accelerated, cell-mediated scaffold degradation *in vivo* due (as discussed in Chapter IV). Polymer degradation likely influences the release rates *in vivo* because of a possibly closer correlation between the rates of degradation and release.

While many mechanistic models based on Fick's second law of diffusion are quite convincing and robust, empirical models were chosen for this system because of their practicality and adequate fit. These models were fit to the experimental

data using MATLAB, and mostly derive from the classic Higuchi equation. The Higuchi model considers purely diffusion-controlled release from a one-dimensional, non-degradable slab with no swelling [56]. Assuming pseudo-steady state and perfect sink conditions, it outlines a zone of diffusion, or diffusion front, with a linear concentration gradient derived from Fick's second law of diffusion (Equation 5.1).

$$\frac{\partial c}{\partial t} = \nabla \cdot \left(D \nabla c \right) \tag{5.1}$$

With an assumed constant diffusion coefficient, this becomes:

$$\frac{\partial c}{\partial t} = D \cdot \nabla^2 c \tag{5.2}$$

The Higuchi model simplifies to the following equation under short-time behavior,

$$\frac{M_t}{M_\infty} = \sqrt{Dt\left(2c_0 - c_s\right)c_s} \qquad \text{for} \qquad c_0 > c_s \tag{5.3}$$

where D is the diffusion coefficient of the drug in the polymer matrix, c_0 is the initial drug loading, and c_s is the saturation concentration of the drug within the polymer. In other words, the cumulative fraction of drug released at a given time (t) scales with the square root of time. This can also be written

$$\frac{M_t}{M_\infty} = k\sqrt{t} \qquad \text{where} \qquad k = \sqrt{D\left(2c_0 - c_s\right)c_s} \tag{5.4}$$

The Higuchi model, which is typically valid only for $\frac{M_t}{M_\infty} \leq 0.6$, fit the tobramycin release data poorly and is not shown.

In order to make a more comprehensive, but still semi-empirical, model of drug release based on Fickian diffusion, Ritger and Peppas expanded the Higuchi

equation [63-65]. They introduced a second non-Fickian term to address another limiting case of zero-order release kinetics, independent of time.

$$\frac{M_t}{M_\infty} = k't \tag{5.5}$$

The heuristic combination of Equation 5.5 with the Higuchi equation becomes:

$$\frac{M_t}{M_\infty} = k_1\sqrt{t} + k_2 t = kt^n \tag{5.6}$$

otherwise known as the power law model. The constant k accounts for the characteristics of the polymer system, and n (> 0) is the diffusional exponent, which indicates the diffusion mechanism(s) responsible for the given release profile. This model thus describes both Fickian and Case-II transport mechanisms, or the combination thereof. Case II transport pertains to polymer relaxation, especially in the conditions of glassy polymers and dynamic swelling [66]. When n = 0.5, this equation is equivalent to the original Higuchi equation, denoting purely Fickian diffusion. However, this critical value of n is specific to the slab geometry used in the development of the Higuchi model. Ritger and Peppas derived their power law model for cylindrical and spherical geometry as well, where purely Fickian diffusion has the following values of n: slab (n = 0.5), cylinder (n = 0.45), sphere (n = 0.43). The diffusion mechanisms can be approximately extrapolated from the value of n in that gives the best fit to the experimental data, as expressed in Table 5.3.

Table 5.17. Diffusion mechanism for drug from a polymer system with slab geometry.

Exponent *n*	Diffusion mechanism
n > 1	Supercase II
n = 1	Case II transport
½ < n < 1	Anomalous
n = ½	Fickian
n < ½	Pseudo-Fickian

The fits of the power law model to the PUR-tobramycin release data are shown in Figure 5.8, and the associated parameters are given in Table 5.4. Table 5.4. Overall, the models reasonably fit the data, including at release fractions above 60%, even though the models only stipulate accuracy $\frac{M_t}{M_\infty} \leq 0.6$.

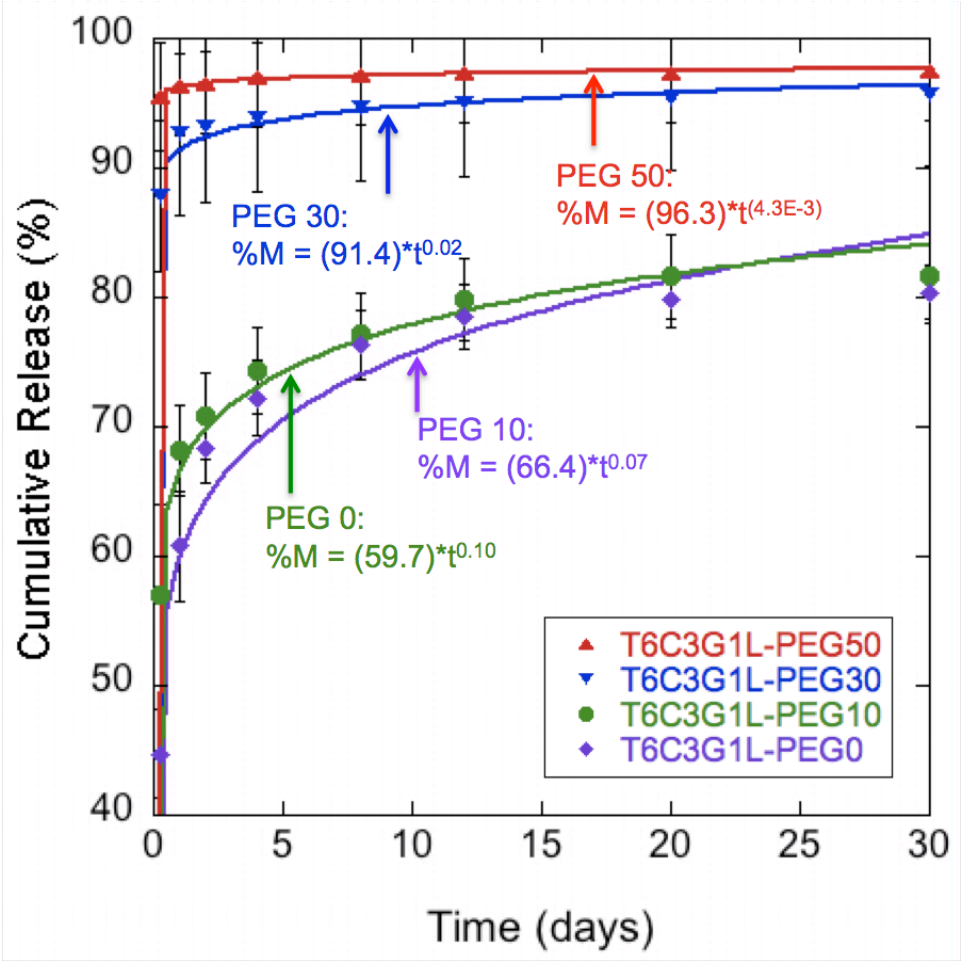

Figure 5.56. Fit of tobramycin release data (individual data points) to the power law model (solid lines). With rising PEG concentrations, the constant values (k) increase but the exponent values (n) decrease.

Table 5.18. Parameters obtained by fitting tobramycin release data to the power law model, $\frac{M_t}{M_\infty} = kt^n$. The exponent n approaches zero as the wt-% PEG increases.

Data	R^2	k	n
PEG 0	0.895	59.7	0.10
PEG 10	0.950	66.4	0.07
PEG 30	0.874	91.4	0.016
PEG 50	0.957	96.3	4.3 E -3
Microspheres	0.956	36.7	0.13

Peppas and Sahlin subsequently developed a model to more explicitly express the different contributions of diffusion (Fickian term) and relaxation (Case II transport) to the overall release profile, valid for any geometry [63, 67].

$$\frac{M_t}{M_\infty} = k_1 t^n + k_2 t^{2n} \tag{5.7}$$

The first term, with constant k_1, represents the contribution of Fickian diffusion (F), while the second term with constant k_2 denotes the case II relaxational contribution (R). The relative influences can be expressed by the ratio in Equation 5.8.

$$\frac{R}{F} = \frac{k_2 t^n}{k_1} \tag{5.8}$$

As shown in Figure 5.9 and Table 5.5, this model again fits the PUR-tobramycin release kinetics quite well. These two models strongly implicate pseudo-Fickian diffusion as the primary mechanism of tobramycin release from the polyurethane scaffolds. The low values of the exponent n fall within the realm of pseudo-Fickian diffusion ($n < ½$) in Table 5.3. Surprisingly, the R^2, k_1, and n values are almost identical for the power law and two-term power model. Moreover, the k_2 values in the two-term model approach zero, which provides very small values of the relaxational contribution R. Together, these outcomes suggest that the Fickian term (F) influences the release kinetics far more than the relaxational contribution. This is reasonable because these scaffolds behave as rubbery elastomers at 37 °C, the temperature at which the release studies are conducted (see Chapter II). The T_g values are below 37 °C for all the materials according to DSC, and for the PEG-containing foams according to DMA (Figure 2.7).

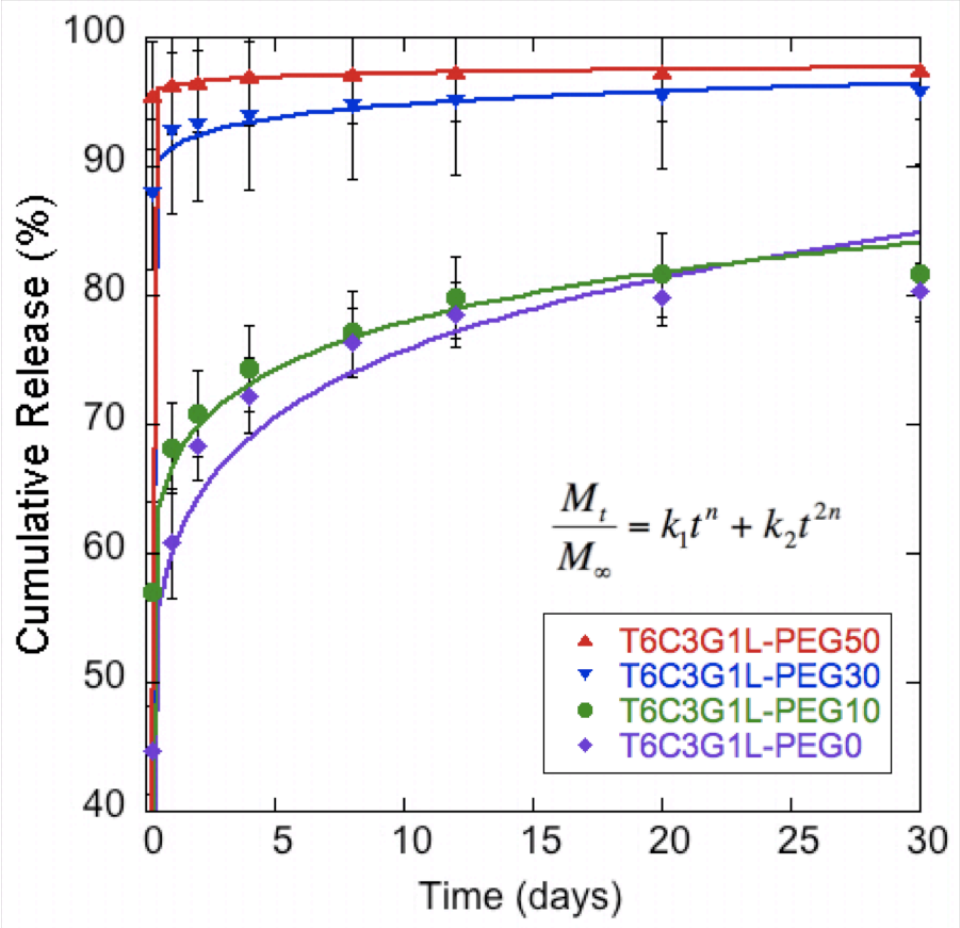

Figure 5.57. Fit of tobramycin release data (individual data points) to the coupled, two-term power law model (solid lines). The respective equations for these fits are very similar to those for the single-term power law models because of the small values of n and k_2 nearly approximates zero.

Table 5.19. Parameters obtained by fitting tobramycin release data to the coupled, two-term power law model, $\frac{M_t}{M_\infty} = k_1 t^n + k_2 t^{2n}$. These values are nearly identical to those obtained from the single-term power law model, shown in Table 5.4.

Data	R^2	k_1	k_2	n
PEG 0	0.895	59.7	~ 0	0.10
PEG 10	0.950	66.4	~ 0	0.07
PEG 30	0.874	91.4	4.5E-04	0.02
PEG 50	0.957	96.3	5.9E-05	4.3E-3
Microspheres	0.956	36.7	~ 0	0.10

While the trends and relative values of the parameters k and n are very informative, the exact values cannot be explicitly interpreted. This model is designed for slab geometry (also for cylindrical or spherical geometries with slightly modified versions of the equation), but the porous PUR scaffolds have a complex geometry that is not well defined by any specific geometry. Nevertheless, the fitted models illustrate an evident trend for increasing k and decreasing n values as the percentage of PEG within the foam increases. The parameter k incorporates many macromolecular aspects of the polymer matrix, some of which are stated in Equation 5.4. This includes a direct relationship with the diffusion coefficient, which very likely increases with the PEG content because the hydrophilic PEG soft segments swell more with water than the hydrophobic polyester soft segments and isocyanate hard segments. Greater swelling, with a higher volume fraction of water, leads to additional free volume within the polymer matrix and higher mobility of the polymer chains, facilitating diffusion of small molecules out of the matrix [59]. A higher swelling ratio also depresses the T_g and pushes the polymer further into the rubbery plateau.

Polymer degradation by chain scission produces higher mobility of the shortened polymer chains, thereby increasing the diffusion coefficient [60].

$$D = D_0 - A \ln M_n \tag{5.9}$$

D_0 is the initial diffusion coefficient at t = 0, and A is a nonspecific constant. Therefore the diffusion coefficient becomes time-dependent on the timescale of polymer degradation. If polymer chain scission follows first-order kinetics (as an

example, although actual degradation is probably more complicated with autocatalytic and biological effects), the diffusion coefficient would increase exponentially with time, where D_0 is again the initial diffusion coefficient at t = 0, and k is the polymer degradation rate constant [68].

$$D(t) = D_0 \cdot \exp(kt) \tag{5.10}$$

A constant diffusion coefficient can be assumed in these systems because *in vitro* release of tobramycin from the PUR scaffolds occurs on a much faster timescale (days to weeks) than polymer degradation (months). However, PUR degradation is greatly accelerated *in vivo* due to cellular-mediated effects, so degradation is anticipated to influence the drug release rates at the release timescale in this case via increased diffusion coefficient and decreased diffusion path lengths.

As mentioned in the Discussion section above, high drug loadings likely lead to the formation of aqueous pores within the polymer due to drug diffusing out of the polymer matrix. These aqueous pores facilitate diffusion of subsequent molecules, and can explain why a higher cumulative percent of release is observed for higher drug loading concentrations of a given drug. A modified Higuchi equation adeptly takes this development of porosity (ε) and pore tortuosity (τ) of the polymer [62].

$$\frac{M_t}{M_\infty} = c_0 \sqrt{\frac{D_{media}}{\tau} c_s t \left(2c_0 - \varepsilon c_{s,media}\right)} \tag{5.12}$$

However, this model was not included in the release analysis of the PUR-tobramycin system because it maintains the same order of dependence on time for the fractional release ($f(t) \sim t^{1/2}$).

Conclusions

Injectable, biodegradable polyurethane scaffolds provide both structural templates and antibiotic delivery vehicles for enhanced healing of infected fractures. Local tobramycin release from these reactive scaffolds potentially achieves higher local concentrations with lower systemic levels. The release profiles, characterized by a burst within the first 2 days followed by extended release for 30 days, can be tuned by the relative amount of PEG included in the scaffolds. While PEG was found to increase the cumulative release of tobramycin, it also substantially increased the burst release, thus incorporation of PEG may only be desirable in applications that require a higher burst of hydrophobic compounds. The tobramycin remains biologically active after sustained release, which is remarkable because this type of delivery strategy had not been demonstrated before in a reactive system. Previously, biological molecules were incorporated by coating, immersion, adsorption, or covalent binding. The versatility of this system enhances its potential for other uses, either with other antibiotics or for healing of tissues other than bone, such as infected soft tissue or dermal wounds.

References

1. Gustilo RB, Anderson JT. Prevention of infection in the treatment of one thousand and twenty-five open fractures of long bones: Retrospective and prospective analyses. *Journal of Bone & Joint Surgery, American volume* 2002; 84(4): 682.

2. Gustilo RB, Merkow RL, Templeman D. The management of open fractures. *Journal of Bone & Joint Surgery* 1990; 72(2): 299-304.

3. Kelly CM, Wilkins RM, Gitelis S, Hartjen C, Watson JT, Kim PT. The use of a surgical grade calcium sulfate as a bone graft substitute. *Clinical Orthopaedics & Related Research* 2001; 382: 42-50.

4. Rittmann WW, Perren SM. Cortical bone healing after internal fixation and infection. New York: Springer, 1974.

5. Worlock P, Slack R, Harvey L, Mawhinney R. The prevention of infection in open fractures: An experimental study of the effect of fracture stability. *Injury* 1994; 25: 31-38.

6. Beardmore AA, Brooks DE, Wenke JC, Thomas DB. Effectiveness of local antibiotic delivery with an osteoinductive and osteoconductive bone-graft substitute. *Journal of Bone & Joint Surgery* 2005; 87A: 107-112.

7. Calhoun J, Mader J. Treatment of osteomyelitis with a biodegradable antibiotic implant. *Clinical Orthopaedics & Related Research* 1997; 341: 206-214.

8. Dahners L, Funderburk C. Gentamicin-loaded plaster of paris as a treatment of experimental osteomyelitis in rabbits. *Clinical Orthopaedics & Related Research* 1987; 219: 278-282.

9. Humphrey J, Mehta S, Seaber A, Vail T. Pharmacokinetics of a degradable drug delivery system in bone. *Clinical Orthopaedics & Related Research* 1998; 349: 218-224.

10. Kanellakopoulou K, Giamarellos-Bourboulis EJ. Carrier systems for the local delivery of antibiotics in bone infections. *Drugs* 2000; 59(6): 1223-1232.

11. Mader JT, Calhoun J, Cobos J. In vitro evaluation of antibiotic diffusion from antibiotic-impregnated biodegradable beads and polymethylmethacrylate beads. *Antimicrobial Agents and Chemotherapy* 1997; 41(2): 415-418.

12. Rogers-Foy J, Powers D, Brosnan D, Barefoot S, Friedman R, LaBerge M. Hydroxyapatite composites designed for antibiotic drug delivery and bone reconstruction: A caprine model. *Journal of Investigative Surgery* 1999; 12: 263-275.

13. Buchholz H, Elson R, Heinert K. Antibiotic-loaded acrylic cement: Current concepts. *Clinical Orthopaedics & Related Research* 1984; 190: 96-108.

14. Osterman P, Seligson D, Henry S. Local antibiotic therapy for severe open fractures: A review of 1085 consecutive cases. *Journal of Bone & Joint Surgery, British volume* 1995; 77: 93-97.

15. Seeley SK, Seeley JV, Telehowski P, Martin S, Tavakoli M, Colton SL, et al. Volume and surface area study of tobramycin-polymethylmethacrylate beads. *Clinical Orthopaedics & Related Research* 2004; 420: 298-303.

16. Stevens CM, Tetsworth KD, Calhoun JH, Mader JT. An articulated antibiotic spacer used for infected total knee arthroplasty: A comparative in vitro elution study of simplexæ and palacosæ bone cements. *Journal of Orthopaedic Research* 2005; 23(1): 27-33.

17. McLaren AC. Alternative materials to acrylic bone cement for delivery of depot antibiotics in orthopaedic infections. *Clinical Orthopaedics & Related Research* 2004; 427: 101-106.

18. Gitelis S, Brebach G. The treatment of chronic osteomyelitis with a biodegradable antibiotic-impregnated implant. *Journal of Orthopaedic Surgery (Hong Kong)* 2002; 10: 53-60.

19. McKee M, Wild L, Schemitsch E, Waddell J. The use of an antibiotic impregnated, osteoconductive, bioabsorbable bone substitute in the treatment of infected long bone defects: Early results of a prospective trial. *Journal of Orthopaedic Trauma* 2002; 16: 622-627.

20. Ambrose CG, Gogola GR, Clyburn TA, Raymond KA, Peng AS, Mikos AG. Antibiotic microspheres: Preliminary testing for potential treatment of osteomyelitis. *Clinical Orthopaedics & Related Research* 2003; 415: 279-285.

21. Santerre JP, Woodhouse KA, Laroche G, Labow RS. Understanding the biodegradation of polyurethanes: From classical implants to tissue engineering materials. *Biomaterials* 2005; 26: 7457-7470.

22. Fromstein JD, Woodhouse KA. Elastomeric biodegradable polyurethane blends for soft tissue applications. *Journal of Biomaterials Science Polymer Edition* 2002; 13(4): 391-406.

23. Guelcher SA. Biodegradable polyurethanes: Synthesis and applications in regenerative medicine. *Tissue Eng B: Reviews* 2008; 14(1): 3 - 17.

24. Bonzani IC, Adhikari R, Houshyar S, Mayadunne RTA, Gunatillake PA, Stevens MM. Synthesis of two-component injectable polyurethanes for bone tissue engineering. *Biomaterials* 2007; 28: 423-433.

25. Tataia L, Moore TG, Adhikari R, Malherbe F, Jayasekara R, Griffiths I, et al. Thermoplastic biodegradable polyurethanes: The effect of chain extender structure on properties and in-vitro degradation. *Biomaterials* 2007; 28: 5407-5417.

26. Gorna K, Gogolewski S. Preparation, degradation, and calcification of biodegradable polyurethane foams for bone graft substitutes. *J Biomed Mater Res* 2003; 67A: 813-827.

27. Guan J, Sacks MS, Beckman EJ, Wagner WR. Biodegradable poly(ether ester urethane)urea elastomers based on poly(ether ester) triblock copolymers and putrescine: Synthesis, characterization and cytocompatibility. *Biomaterials* 2004; 25: 85-96.

28. Gogolewski S, Gorna K. Biodegradable polyurethane cancellous bone graft substitutes in the treatment of iliac crest defects. *J Biomed Mater Res* 2007; 80A: 94-101.

29. Gogolewski S, Gorna K, Turner AS. Regeneration of bicortical defects in the iliac crest of estrogen-deficient sheep, using new biodegradable polyurethane bone graft substitutes. *J Biomed Mater Res* 2006; 77A: 802-810.

30. Fujimoto KL, Guan J, Oshima H, Sakai T, Wagner WR. In vivo evaluation of a porous, elastic, biodegradable patch for reconstructive cardiac procedures. *Ann Thorac Surg* 2007; 83 (2): 648-654.

31. Fujimoto KL, Tobita K, Merryman WD, Guan J, Momoi N, Stolz DB, et al. An elastic, biodegradable cardiac patch induces contractile smooth muscle and improves cardiac remodeling and function in subacute myocardial infarction *J Am Coll Cardiol* 2007; 49(23): 2292-2300.

32. Alperin C, Zandstra PW, Woodhouse KA. Polyurethane films seeded with embryonic stem cell-derived cardiomyocytes for use in cardiac tissue engineering applications. *Biomaterials* 2005; 26: 7377-7386.

33. Guelcher S, Srinivasan A, Hafeman A, Gallagher K, Doctor J, Khetan S, et al. Synthesis, in vitro degradation, and mechanical properties of two-component poly(ester urethane)urea scaffolds: Effects of water and polyol composition. *Tissue Engineering* 2007; 13(9): 2321-2333.

34. Zhang J-Y, Beckman EJ, Piesco NJ, Agarwal S. A new peptide-based urethane polymer: Synthesis, biodegradation, and potential to support cell growth in vitro. *Biomaterials* 2000; 21: 1247-1258.

35. Bennett S, Connolly K, Lee DR, Jiang Y, Buck D, Hollinger JO, et al. Initial biocompatibility studies of a novel degradable polymeric bone substitute that hardens in situ. *Bone* 1996; 19(1, Supplement): 101S-107S.

36. Hafeman AE, Li B, Yoshii T, Zienkiewicz K, Davidson JM, Guelcher SA. Injectable biodegradable polyurethane scaffolds with release of platelet-derived growth factor for tissue repair and regeneration. *Pharmaceutical Research* 2008; *25*(10): 2387-2399.

37. Guan J, Stankus JJ, Wagner WR. Biodegradable elastomeric scaffolds with basic fibroblast growth factor release. *Journal of Controlled Release* 2007; 120(1-2): 70-78.

38. Guelcher SA, Srinivasan A, Hafeman AE, Gallagher KM, Doctor JS, Khetan S, et al. Synthesis, *in vitro* degradation, and mechanical properties of two-component poly(ester urethane)urea scaffolds: Effects of water and polyol composition. *Tissue Eng* 2007; 13(9): 2321-2333.

39. Yuan H, Yang Z, Li Y, Zhang X, De Bruijn JD, De Groot K. Osteoinduction by calcium phosphate biomaterials. *Journal of Materials Science: Materials in Medicine* 1998; 9(12): 723-726.

40. Cleek RL, Ting KC, Eskin SG, Mikos AG. Microparticles of poly(d,l-lactic-co-glycolic acid)/poly(ethylene glycol) blends for controlled drug delivery. *Journal of Controlled Release* 1997; 48(2-3): 259-268.

41. Oertel G. Polyurethane handbook. 2 ed. Berlin: Hanser Gardner Publications, 1994.

42. Caturla MC, Cusido E, Westerlund D. High-performance liquid chromatography method for the determination of aminoglycosides based on automated pre-column derivatization with o-phthalaldehyde. *Journal of Chromatography A* 1992; 593(1-2): 69-72.

43. ASTM-International. D695-02a. Standard test method for compressive properties of rigid plastics. 2007.

44. ASTM-International. D3574-05. Standard test methods for flexible cellular materials - slab, bonded, and molded urethane foams. 2007; p. 360-368.

45. Mark JE, Erman E, Eirich FR, editors. Science and technology of rubber. 2nd ed. San Diego, CA: Academic Press, Inc., 1994.

46. Hafeman AE, Zienkiewicz KJ, Yoshii Y, Davidson JM, Guelcher SA. Injectable, biodegradable, porous polyurethane scaffolds for tissue regeneration. Society for Biomaterials Annual Meeting; 2009; San Antonio, TX; 2009.

47. Guelcher SA, Patel V, Gallagher KM, Connolly S, Didier JE, Doctor JS, et al. Synthesis and in vitro biocompatibility of injectable polyurethane foam scaffolds. *Tissue Engineering* 2006; 12(5): 1247-1259.

48. Ambrose CG, Clyburn TA, Louden K, Joseph J, Wright J, Gulati P, et al. Effective treatment of osteomyelitis with biodegradable microspheres in a rabbit model. *Clinical Orthopaedics & Related Research* 2004; 421: 293-299.

49. Loo Y, Leong KW. Biomaterials for drug and gene delivery. In: Guelcher SA, Hollinger JO, editors. An introduction to biomaterials. Boca Raton: CRC Press, 2006.

50. Hombreiro-Pérez M, Siepmann J, Zinutti C, Lamprecht A, Ubrich N, Hoffman M, et al. Non-degradable microparticles containing a hydrophilic and/or a lipophilic drug: Preparation, characterization and drug release modeling. *Journal of Controlled Release* 2003; 88(3): 413-428.

51. Zhang J-Y, Doll BA, Beckman EJ, Hollinger JO. Three-dimensional biocompatible ascorbic acid-containing scaffold for bone tissue engineering. *Tissue Engineering* 2003; 9(6): 1143-1157.

52. Chen XQ, Tsukayama DT, Kidder LS, Bourgeault CA, Schmidt AH, Lew WD. Characterization of a chronic infection in an internally-stabilized segmental defect in the rat femur. *J Orthopaedic Res* 2005; 23: 816-823.

53. Guan J, Fujimoto KL, Sacks MS, Wagner WR. Preparation and characterization of highly porous, biodegradable polyurethane scaffolds for soft tissue applications. *Biomaterials* 2005; 26(18): 3961-3971.

54. Arifin DY, Lee LY, Wang C-H. Mathematical modeling and simulation of drug release from microspheres: Implications to drug delivery systems. *Advanced Drug Delivery Reviews* 2006; 58(12-13): 1274-1325.

55. Gopferich A, Langer R. Modeling monomer release from bioerodible polymers. *Journal of Controlled Release* 1995; 33(1): 55-69.

56. Higuchi T. Rate of release of medicaments from ointment bases containing drugs in suspension. *Journal of Pharmaceutical Sciences* 1961; 50(10): 874-875.

57. Joshi A, Himmelstein KJ. Dynamics of controlled release from bioerodible matrices. *Journal of Controlled Release* 1991; 15(2): 95-104.

58. Rothstein SN, Federspiel WJ, Little SR. A simple model framework for the prediction of controlled release from bulk eroding polymer matrices. *Journal of Materials Chemistry* 2008; 18(16): 1873-1880.

59. Siepmann J, Gopferich A. Mathematical modeling of bioerodible, polymeric drug delivery systems. *Advanced Drug Delivery Reviews* 2001; 48(2-3): 229-247.

60. Wada R, Hyon S-H, Ikada Y. Kinetics of diffusion-mediated drug release enhanced by matrix degradation. *Journal of Controlled Release* 1995; 37(1-2): 151-160.

61. Burkersroda Fv, Schedl L, Gopferich A. Why degradable polymers undergo surface erosion or bulk erosion. *Biomaterials* 2002; 23(21): 4221-4231.

62. Park K. Controlled drug delivery: Challenges and strategies. Washington, D.C.: American Chemical Society, 1997.

63. Siepmann J, Peppas NA. Modeling of drug release from delivery systems based on hydroxypropyl methylcellulose (hpmc). *Advanced Drug Delivery Reviews* 2001; 48(2-3): 139-157.

64. Ritger PL, Peppas NA. A simple equation for description of solute release ii. Fickian and anomalous release from swellable devices. *Journal of Controlled Release* 1987; 5(1): 37-42.

65. Ritger PL, Peppas NA. A simple equation for description of solute release i. Fickian and non-fickian release from non-swellable devices in the form of slabs, spheres, cylinders or discs. *Journal of Controlled Release* 1987; 5(1): 23-36.

66. Sperling LH. Introduction to physical polymer science. 4th ed. Hoboken, NJ: John Wiley & Sons, Inc., 2005.

67. Peppas NA, Sahlin JJ. A simple equation for the description of solute release. Iii. Coupling of diffusion and relaxation. *International Journal of Pharmaceutics* 1989; 57(2): 169-172.

68. Charlier A, Leclerc B, Couarraze G. Release of mifepristone from biodegradable matrices: Experimental and theoretical evaluations. *International Journal of Pharmaceutics* 2000; 200(1): 115-120.

69. Papadopoulou V, Kosmidis K, Vlachou M, Macheras P. On the use of the weibull function for the discernment of drug release mechanisms. *International Journal of Pharmaceutics* 2006; 309(1-2): 44-50.

CHAPTER VI

SUSTAINED RELEASE OF LOVASTATIN FROM SCAFFOLDS FOR LOCAL DELIVERY

Introduction

Bone morphogenetic protein-2 (BMP-2) has been shown to stimulate the differentiation of mesenchymal stem cells into osteoblasts and chondrocytes and enhance bone formation and healing [1-3]. However, BMP-2 may not be an ideal therapeutic because it is expensive to manufacture, involving recombination and purification, and there have been some problems reported with finding appropriate carriers for local BMP-2 delivery [4]. For example, a typical injection of the FDA-approved INFUSE spinal fusion therapeutic can cost up to $7,000. In addition, there may be issues with maintaining BMP-2 stability and bioactivity for a necessary shelf life or period of extended release. Thus we have a clinical need for anabolic, small-molecule drugs to substitute such growth factors for enhancing bone formation, particularly in patients with osteoporosis, osteolytic tumors, and traumatic bone injuries.

In a screen of over 30,000 compounds, statins were determined to be the only natural compounds that stimulated BMP-2 activity, and lovastatin was the most active [5]. Statins, both natural and synthetic, are a class of drugs most commonly prescribed to reduce serum cholesterol. They inhibit the enzyme 3-hydroxy-3-methylglutaryl coenzyme A (HMG Co-A) reductase, which mediates a pivotal step in

hepatic cholesterol biosynthesis, thereby lowering the total serum cholesterol in the body. They have also been reported to exhibit pleiotropic effects on other systems, including the musculoskeletal, nervous, immune, cardiovascular systems [6-8]. Specifically in bone, statins stimulate BMP-2 activity and bone formation, both *in vitro* and *in vivo*, by upregulating expression of BMP-2 mRNA and increasing BMP-2 gene transcription in osteoblasts [5, 9-11]. Statins require a much lower cost of synthesis as compared to BMP-2, and they have already been used clinically for many years in the treatment of hypercholesterolemia [5, 12, 13]. Therefore, the use of statins for treating bone injuries has generated increasing research and clinical interest over the past decade [9-12].

The effect of statins on bone growth seems to result from a similar mechanism as its inhibition of HMG Co-A reductase and lowering of cholesterol, because when the downstream metabolite (mevalonate) was added to the site of delivery, bone growth was no longer enhanced. Interestingly, statins do not upregulate gene expression of other factors, including other BMP's. Lovastatin, simvastatin, fluvastatin, and mevastatin all increased the amount of new bone formed by two- to threefold, which approximates bone growth enhancement seen with application of BMP-2 and FGF-1 [5].

Local application of statins directly to the injury site is highly preferable for drug efficacy. Statins are ineffective when administered orally because they are eliminated in first-pass metabolism in the liver, which prevents transport of sufficient concentrations to bone fracture sites [13]. However, local injection is not ideal because high local concentrations of statins can induce an adverse

inflammatory response, and they have short half-lives once dissolved [9, 10]. Therefore, a local, controlled delivery system is optimal for the therapeutic use of statins.

Numerous *in vitro, in vivo,* and clinical studies have been performed to assess the efficacy of statins, including some with controlled release mechanisms. Whang et al. demonstrated sustained release kinetics of simvastatin *in vitro* by grafting the statin to poly(lactide-*co*-glycolide), such that the simvastatin was released upon hydrolytic degradation of the polymer [14]. Benoit et al. synthesized a poly(ethylene glycol) (PEG) hydrogel-derived delivery system for fluvastatin and showed that the released fluvastatin induced osteogenic differentiation *in vitro* [15]. Garrett et al. showed that locally delivered lovastatin from poly(D,L-lactide) nanoparticles (mean particle size ~ 200 nm) enhanced fracture repair [16]. Jeon et al. reported that control-release of simvastatin hydroxyacid from microspheres composed of a blend of cellulose acetatephthalate and a poly(ethylene oxide) and poly(propyleneoxide) block copolymer enhanced bone formation in calvarial onlay model in rats [17].

Based on these previous studies, biodegradable PUR scaffolds containing lovastatin incorporated within the polymer matrix for controlled statin release could produce an optimal therapy for bone injuries at a lower cost than with BMP-2. Lovastatin (LV) was chosen for these studies because it is readily available and displays the one of the highest osteogenic potentials of the statins. While lovastatin has been utilized in previous controlled release study, it has never been incorporated in a reactive polymer system, so the bioactivity of released lovastatin

had to be verified. Lovastatin presented a unique challenge as compared to other molecules delivered from the PUR scaffolds, such as antibiotics and growth factors, because it has very low water solubility and therefore undetermined release kinetics. Lovastatin is typically administered as a non-water soluble prodrug. *In vivo*, the closed lactone ring is readily hydrolyzed to its active acid form, which is more water soluble and readily taken up by cells. In this study, the release profile of lovastatin, the biocompatibility of PUR scaffolds containing lovastatin, and the osteogenic potential of lovastatin released from PUR scaffolds were investigated. The effects of locally delivered lovastatin from PUR scaffolds on *in vivo* bone formation were subsequently investigated in a rat femoral plug model.

Methods

Materials. Lovastatin was obtained from Stason Pharmaceuticals Incorporated (Irvine, CA), and α-minimal essential medium (a-MEM) for cell culture was purchased from Fisher Scientific (Pittsburgh, PA). Reagents for cell culture were purchased from HyClone (Logan, UT). All other reagents were purchased from Sigma-Aldrich (St. Louis, MO), or as outlined in Chapter II.

Synthesis of polyurethane scaffolds. Trifunctional polyester polyols of 900-Da molecular weight were prepared with from a glycerol starter and the α-hydroxy acid cyclic ester monomers ε-caprolactone, glycolide, and D,L-lactide (60/30/10), and stannous octoate catalyst [18, 19]. The procedure followed that described in Chapter II (p. 16).

PUR scaffolds were synthesized by reactive liquid molding of lysine triisocyanate (LTI) and a hardener comprising the polyol (70%), PEG (30%), 1.5 parts per hundred parts polyol (pphp) water, 1.5 pphp TEGOAMIN33 tertiary amine catalyst, 1.5 pphp sulfated castor oil stabilizer, and 4.0 pphp calcium stearate pore opener. The isocyanate was added to the hardener and mixed for 30 sec in a Hauschild SpeedMixer™ DAC 150 FVZ-K vortex mixer (FlackTek, Inc., Landrum, SC). The resulting reactive liquid mixture rose freely for 10–20 minutes [18, 19]. The targeted index (the ratio of NCO to OH equivalents times 100) was 115.

In order to incorporate lovastatin (LV) into PUR scaffolds (PUR/LV scaffolds), lovastatin particles were added to the hardener component before mixing with the isocyanate. Powdered lovastatin was mixed thoroughly with the hardener at 20 μg (low dose) and 200 μg (high dose) per gram of foam. The biologically active open-ring form of lovastatin (lovastatin acid, LVA) is much more soluble in water than the closed-ring lactone form (LV), so release kinetics of the might differ between the two forms. Lovastatin acid was hydrolyzed from the lactone form by treatment with sodium hydroxide in 50/50 AcN/H_2O and lyophilized, after which it was incorporated into the PUR scaffolds as described above.

In vitro lovastatin release. Triplicate 500-mg samples of the scaffolds each in 5 mL phosphate buffered saline (PBS, pH 7.4) were mixed end-over-end while incubating at 37 °C. The buffer was removed from each vial and replaced daily to approximate sink conditions and to avoid the lovastatin solubility limit. The release samples were evaporated and re-dissolved in acetonitrile to extract the lovastatin, which was then quantified with a Waters Breeze HPLC and UV detector. Releasates

were passed through an XTerra reverse-phase guard column (C8 5-μm 3.9 x 20 mm) and XTerra reverse-phase column (C18 5-μm 4.6 x 250 mm) at a flow rate of 1.0 mL/min and analyzed at 237 nm. The mobile phase was a 18/82 (A/B) ratio of the following: (A) 10 mM NH_4 formate (pH 4.0)/isopropyl alcohol (95:5), and (B) 10 mM NH_4 formate (pH 4.0)/acetonitrile (5:95). Both mobile phases were filtered through a 0.2 μm filter and degassed under vacuum. The concentration of lovastatin was calculated from peak area by injecting samples of known concentration and preparation of a standard curve correlating concentration with peak area. The release levels of lovastatin and lovastatin acid were analyzed independently.

In vitro biocompatibility of PUR/LV scaffolds. The biocompatibility of the PUR scaffolds alone was previously shown in Chapter II. Using similar methods, the biocompatibility of the PUR/LV scaffolds was assessed to verify that the presence of lovastatin did not negatively affect cell viability or motility. MC3T3-E1 mouse osteoblast precursor cells were statically seeded onto thin foam discs (25 x 1 mm) at 5 x 10^4 cells per well in 24-well tissue-culture polystyrene plates. The cells were cultured with 1 mL α-minimum essential medium (α-MEM) per well, containing 10% fetal bovine serum (FBS), 1% penicillin (100 units/mL) and streptomycin (100 μg/mL). The plates were maintained in a humidified incubator with 5% CO_2 for 5 days, with the medium refreshed after 2 days. The cell-seeded scaffolds were then removed from culture, washed with PBS, and transferred to a new 24-well plate to verify cell adherence to the materials. 4 μM Calcein AM from the Live/Dead Viability/Cytotoxicity Kit for mammalian cells (Invitrogen, Eugene, OR) was added to the samples to identify live cells, which then emit green fluorescence

(excitation/emission: 485/515 nm). Cell viability was assessed qualitatively by fluorescent images acquired with an Olympus DP71 camera attached to a fluorescent microscope (Olympus CKX41, U-RFLT50, Center Valley, PA). Cell viability was assessed qualitatively by fluorescent images acquired with an Olympus DP71 camera attached to a fluorescent microscope (Olympus CKX41, U-RFLT50).

In addition, cell attachment, viability, and proliferation were quantified using the MTT (3-[4,5-dimethylthiazol-2-yl]-2, 5-diphenyltetrazolium bromide) assay from Sigma-Aldrich [20, 21]. To evaluate cell attachment, 5 x 10^4 cells were again statically seeded on each scaffold disc, as well as directly onto the polystyrene surface as a control, in 24-well tissue-culture plates. The samples were incubated for 4 hours at 37 °C with 5% CO_2 to allow the cells attach to the scaffold after cell seeding. To evaluate cell viability and proliferation, the same number of cells per scaffold was cultured for 2 and 5 days after seeding, with the medium refreshed after 2 days. The scaffolds were subsequently washed with PBS and transferred to a new 24-well plate. MTT solution was added to each well and incubated at 37 °C for 4 hours as indicated by the assay manual. The insoluble formazan crystals were dissolved in dimethyl sulfoxide (DMSO) and absorbance was measured at 590 nm in a microplate reader (ELX 800, Bio-Tek) with a reference wavelength at 620 nm.

Effect of lovastatin delivery on osteogenic differentiation in vitro. The effects of lovastatin released from PUR scaffolds (r-LV) on osteogenic differentiation were evaluated *in vitro* using murine osteoblast precursor (MC3T3-E1) cells, using assays to measure BMP-2 expression, alkaline phosphatase (ALP) activity, and mineralization in the MC3T3 cells. Samples of released lovastatin were obtained

from the buffer in which the PUR/LV materials were incubated for the *in vitro* lovastatin release assay; the concentration was adjusted as needed by dilution in cell culture medium. MC3T3-E1 cells were treated with r-LV (1 μM) and fresh LV (1 μM) was used as a positive control. In general, the concentrations of lovastatin in the release samples were several orders of magnitude greater than the concentration needed for *in vitro* studies. Thus only a small volume of release media was added to the cells, so the media composition was not altered significantly. Osteogenic medium containing 2.5% FBS, 5 mM β-glycerophosphate (Sigma-Aldrich), and 100 μg/mL ascorbic acid phosphate (Wako, Osaka, Japan) was used for mineralization assays.

BMP-2 expression. Cells were plated at 2×10^5 cells/well in 6-well plates and treated with either r-LV or exogenous LV for 24 hours (n=4), at d 1 μM, concentration. To assess BMP-2 mRNA expression, total RNA was isolated using TriZOL reagent (Invitrogen), followed by transcription to cDNA using Superscript II (Invitrogen). Quantitative real time PCR of mouse BMP-2 mRNA was performed using the cDNA template and mouse BMP-2 TaqMan primers/probe (Mm01340178_m1, Applied Biosystems) on the 7300 real-time PCR system (Applied Biosystems). Eukaryotic 18S rRNA detected using a VIC-MGB probe (4319413E; Applied Biosystems) served as an endogenous control [22].

ALP activity. Cells were plated at 2.5×10^4 cells/well in a 48-well plate with osteogenic-conditioned medium (5 mM β-glycerophosphate and 100 μg/mL ascorbic acid phosphate). After 24 hours, the cells were treated with either r-LV or exogenous LV for 3 and 7 days, 1 μM, along with 50 ng/mL exogenous BMP-2 as a

positive control. Cells were washed with PBS and lysed with 0.1% Triton X-100. The plates were then subjected to three freeze/thaw cycles. The lysates (20 μL) were added to 100 μL of substrate buffer (2 mg/mL disodium p-nitrophenylphosphate hexahydrate and 0.75 M 2-amino-2-methyl-1-propanol) in a 96-well plate. After incubation of the mixtures at 37 °C for 30 min, absorbance at 405 nm was measured. ALP activity, which is a marker of osteoblast differentiation and osteogenesis, was quantified from a standard curve generated by employing the reaction of a p-nitrophenyl solution. The ALP activity was normalized by the total protein content, as determined using the BCA assay (Pierce).

Mineralization assay. Cells were plated at 5×10^4 cells/well in a 24-well plate and treated with either r-LV or exogenous LV in the osteogenic medium for 25 days. After the cells were washed with PBS and fixed with 10% phosphate-buffered formalin, mineralized nodule formation was evaluated by Von Kossa staining, wherein 5% silver nitrate solution was added to the well under incandescent light for 20–45 min. After granules developed, the silver nitrate was removed and wells were washed with water to stop the reaction. Mineralized nodule formation was assessed by capture of digital images (4x) with an Olympus DP71 camera. The fractional area determined as mineralized in the digital images of four regions per sample was evaluated using ImageJ software (NIH) and the average data was used for analysis (n=4).

*Bone formation with PUR/LV scaffolds in vivo***.** The behavior of PUR scaffolds with local delivery of lovastatin on *in vivo* bone formation was evaluated using a rat femoral plug defect model [23]. A monocortical plug bone defect (3 mm) was

created in the distal region of the femur diaphysis in male Sprague-Dawley rats, and cylindrical PUR scaffolds (3×5 mm) were implanted into the defect. Treatment groups are outlined in Table 6.1, and included PUR (without LV as a control), PUR/LV containing 25 μg of LV (LV-L), and PUR/LV containing 100 μg of LV (LV-H). Each animal had bilateral femoral defects and treatments, producing n = 6 for each treatment group. After 2 and 4 weeks post-implantation, the femurs were harvested and fixed in 10% phosphate-buffered formalin

Table 6.1. Study design for evaluation of bone defect healing capacity of PUR-lovastatin scaffolds *in vivo*.

Treatment group	LV dose	2 weeks	4 weeks
Control PUR	Blank	3	3
PUR + low LV	25 μg LV	3	3
PUR + high LV	100 μg LV	3	3

Quantitative 3D analysis of mineralized bone formation in the scaffolds was performed using a μCT40 (SCANCO Medical, Bassersdorf, Switzerland) at a voxel size of 24 μm (isotropic). Utilizing the Scanco evaluation software, the amount of bone formation in the scaffold was quantified as the ratio of bone volume per total volume, in which total volume was generated by measuring the contour of the defect site. Because the μCT40 is calibrated to known densities of hydroxyapatite (phantom), the mineral density (mg HA/cm^3) of each voxel was automatically provided for segmented bone. Meanwhile, the PUR scaffold itself is not radio-opaque, so it does not appear in the μCT images. The mean volumetric bone density of the mineralized tissue was evaluated.

The rat femur samples were then decalcified with 10% ethylenediaminetetraacetic acid (EDTA, Invitrogen), dehydrated, embedded in paraffin, and sectioned into 5-μm thick slices. The coronal slice sections were stained with hematoxylin and eosin (H&E). Specimens were examined under light microscopy. For histomorphometric examination, the amount of new bone formation in the scaffolds and the residual scaffolds were quantified at the center sections of the samples [24]. The newly formed bone and polymer scaffold remnants at the defect site were highlighted using image-editing software (Photoshop, Adobe Systems Incorporated) and measured using image-analysis software (Scion Image, Scion Corporation), and the ratio of new bone formation and implant per whole scaffold area was evaluated.

Statistical analysis. Statistical analysis of the results was performed using single factor analysis of variance (ANOVA). In cases where statistical significance is cited, the sample size is greater than or equal to three replicates per material.

Results

In vitro lovastatin release. The cumulative % release of lovastatin measured by HPLC shows a nearly linear release profile and constant daily elution (Figures 6.1 & 6.2). By 30 days, 10% of the low dose and 20% of the high dose lovastatin had released from each of the respective scaffolds. The lovastatin release profiles differ dramatically from the tobramycin elution profiles shown in Chapter V, which are characterized by an initial burst release. Both molecules have similar molecular weights (lovastatin MW 404.5, tobramycin MW 467.5), so particle size is not a likely

factor. The disparate release profiles are due to the significant difference in water solubilities between tobramycin (>300 mg/mL) and lovastatin (0.4 μg/mL).

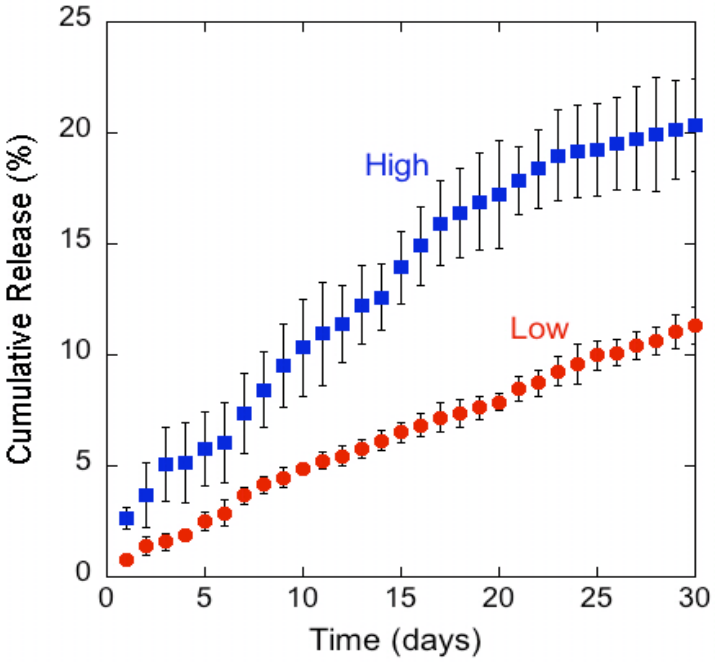

Figure 6.1. *In vitro* lovastatin release from PUR scaffolds in PBS at 37 °C measured by HPLC reveals a linear and constant elution profile (n = 3).

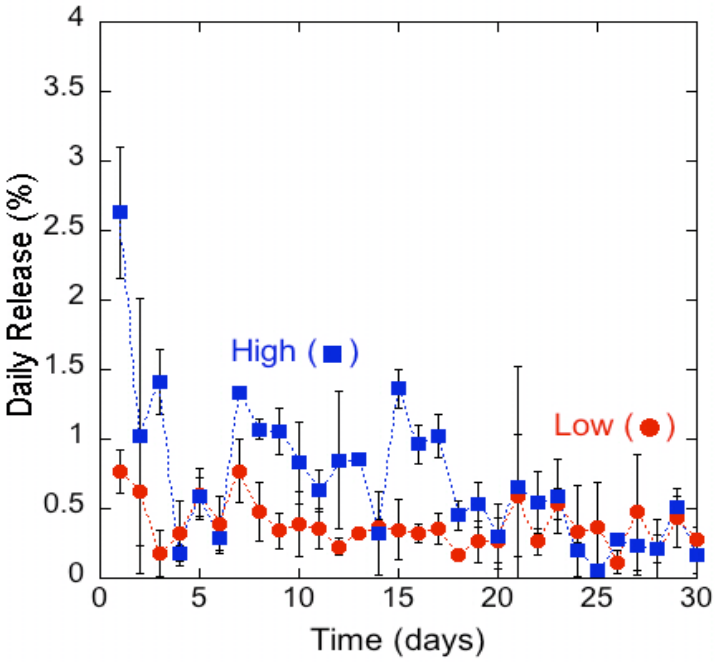

Figure 6.2. Nearly constant daily release of lovastatin from PUR scaffolds (n = 3).

Release profiles of lovastatin acid from the scaffolds surprisingly demonstrated no significant difference from those of pure lovastatin. Perhaps spontaneous interconversion between the two forms produces the similar release profiles. Consequently, scaffolds for the remaining experiments were synthesized directly with the closed-ring, lactone form of lovastatin.

In vitro biocompatibility of PUR/LV scaffolds. The MC3T3-E1 osteoblastic cells infiltrated and adhered to the PUR/LV scaffolds, just as they did in blank PUR scaffolds (Figure 2.12). Figure 6.3 illustrates viable cells in green, contrasted against the autofluorescent red PUR/LV scaffold, showing that the incorporation of lovastatin did not affect cellular viability.

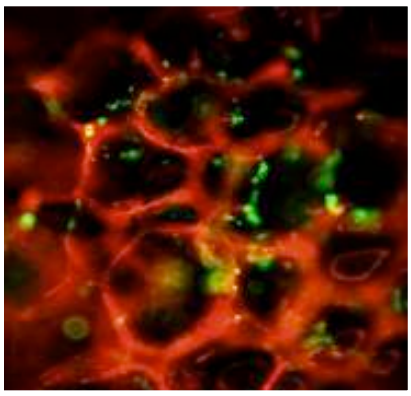

Figure 6.3. Fluorescent micrograph showing viable osteoblast cells (bright spots) stained with Calcein on PUR-LV scaffold.

MC3T3 cell attachment, viability, and proliferation on the scaffolds were quantified by an MTT assay. There were no significant differences in cell attachment or viability between scaffolds with and without lovastatin after 4 hours of incubation (Figure 6.4). These results suggest that PUR scaffolds are

biocompatible and the incorporation of lovastatin did not affect cell viability or proliferation on the scaffolds in osteoblastic cell culture.

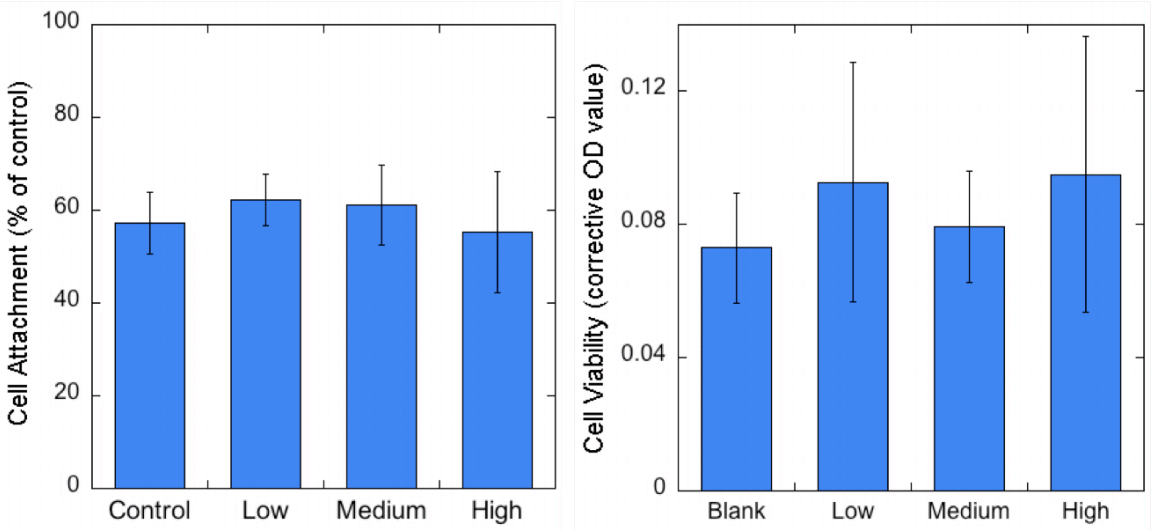

Figure 6.4. Osteoblast cell attachment and viability on PUR scaffolds as measured by MTT assay. Cell outcomes are not significantly affected by addition of LV to scaffolds at various doses (20, 200, & 800 μg/g PUR) (n = 3).

Effect of lovastatin delivery on osteogenic differentiation in vitro. BMP-2 gene expression and osteogenic differentiation of MC3T3 cells were evaluated to verify the bioactivity of lovastatin released from the PUR scaffolds. Released lovastatin (r-LV) from the release media was added to the cell cultures, rather than the cells being cultured directly on the PUR/LV scaffolds, because lovastatin release rates *in vitro* were not sufficiently high on this experimental timescale to initiate the biological effect of lovastatin. As shown in Figure 6.5, BMP-2 expression in the osteoblastic cells treated by r-LV was 2-fold higher than that in the control without lovastatin. Lovastatin released from PUR scaffolds enhanced osteogenic differentiation as evidenced by increased ALP activity, especially at day 7 (Figure

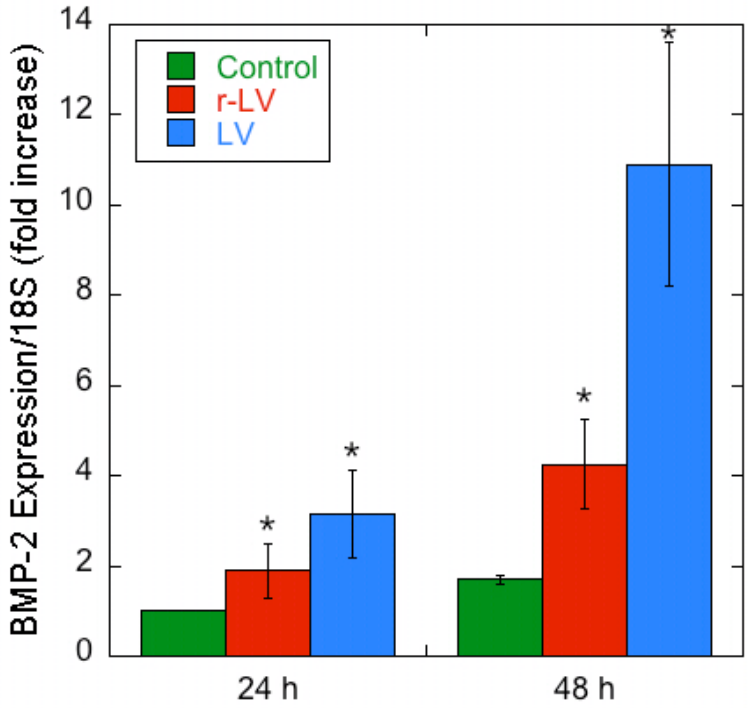

Figure 6.5. Lovastatin released from PUR scaffolds (r-LV) and fresh lovastatin (LV) at 1 μM stimulated BMP-2 expression in MC3T3 osteoblast cells. (*: $p < 0.05$ vs. control, n = 3).

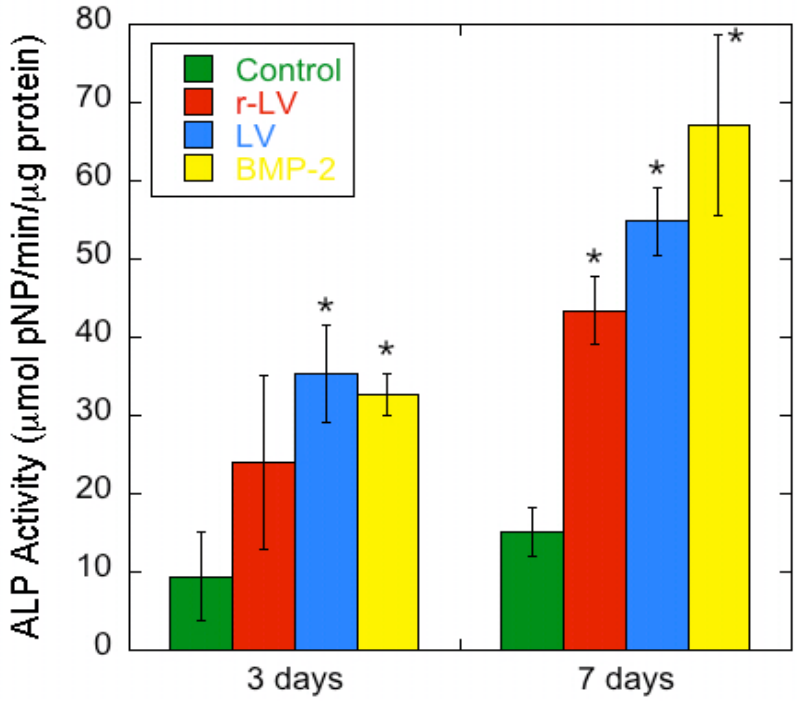

Figure 6.6. Lovastatin released from PUR scaffolds (r-LV) and fresh lovastatin (LV) at 1 μM stimulated ALP activity in MC3T3 osteoblast cells. Differences between effects of LV and BMP-2 (1 μM) were not significant. (*: $p < 0.05$ vs. control, n = 3).

6.6). Bone nodule formation in the cells treated with lovastatin releasates for 25 days was also significantly enhanced when compared to the control (Figure 6.7). While BMP-2 gene expression, ALP expression, and bone nodule formation were higher for fresh lovastatin (positive control) compared to released lovastatin, but the released lovastatin also demonstrated statistically significant effects with respect to the control. This suggests that the stimulatory effect of lovastatin on osteogenic differentiation was preserved during the polyurethane reaction of scaffold synthesis.

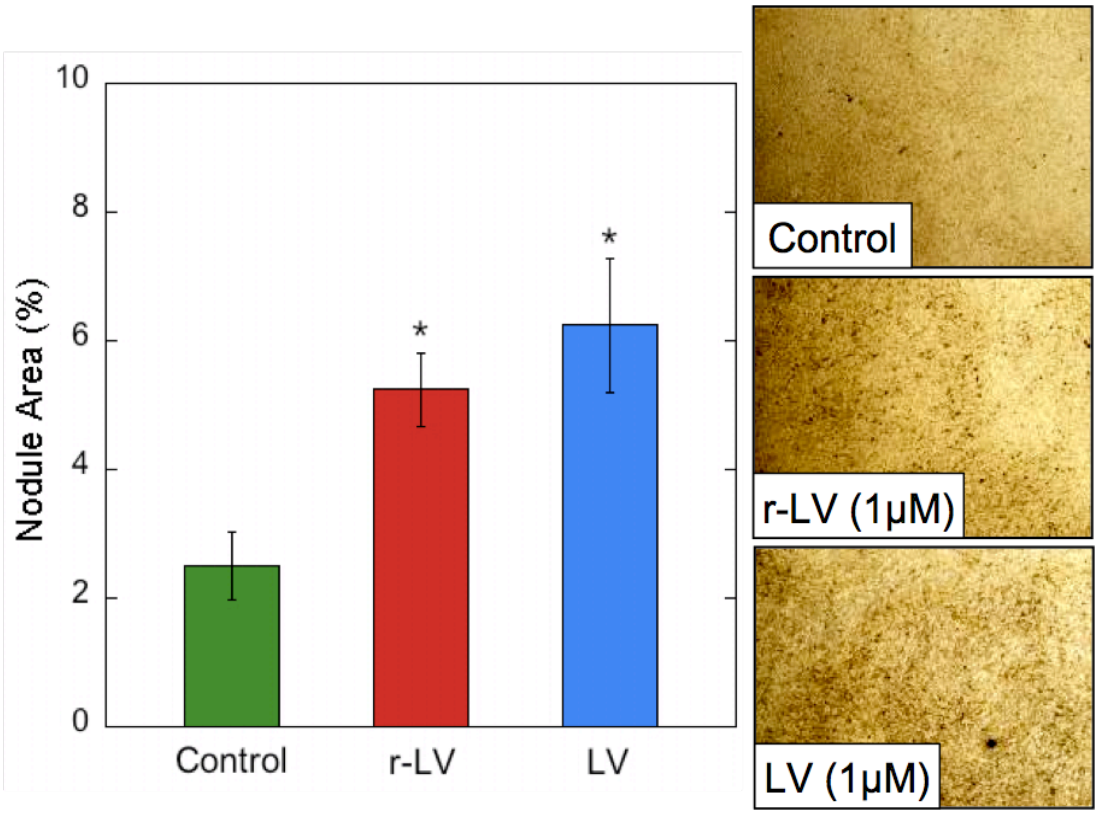

Figure 6.7. Lovastatin released from PUR scaffolds (r-LV) and fresh lovastatin (LV), both at 1 μM concentration, stimulated bone nodule formation, quantified from Von Kossa staining. (*: $p < 0.05$ vs. control, n = 3).

Bone formation with PUR/LV scaffolds in vivo. Cylindrical PUR scaffolds with and without lovastatin were implanted into rat femoral plug defects to evaluate the promotion of *in vivo* bone formation. At week 2, μCT analysis showed that new bone started forming mainly at the peripheral area in the materials (Figure 6.8), and at week 4, μCT images showed that increased bone formation was visible throughout the implants in all treatment groups, and to the greatest degree in the LV-H group (Figure 6.9). There were no significant differences among the groups in the amount of new bone volume and bone density. Quantitative μCT analysis at week 4 revealed that the volume of new bone formed per total scaffold volume was higher in LV-H samples, although the differences were not significant ($p=0.068$) (Figure 6.10). Meanwhile, the density of newly formed bone in LV-H samples was significantly higher than that observed in the control PUR scaffolds at 4 weeks (Figure 6.10).

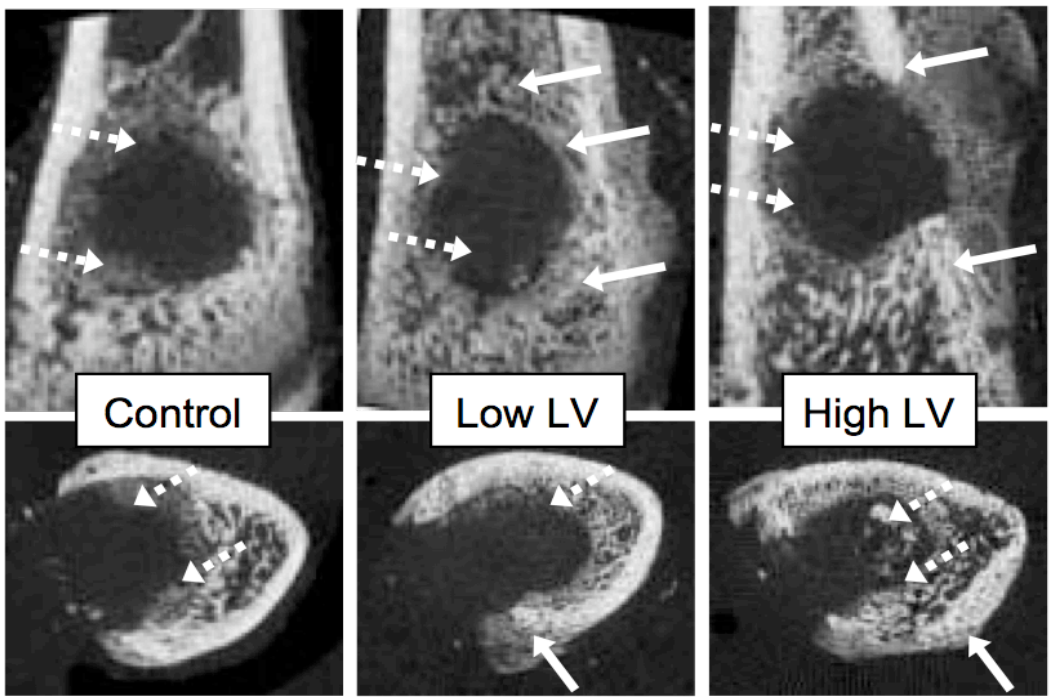

Figure 6.8. Representative saggital (top) and coronal (bottom) μCT images of 3-mm rat femoral plug defects filled with PUR-LV scaffolds after 2 weeks. Mineralized bone formation is visible around the defect edges (solid arrows), but not as much within the scaffolds (dashed arrows). Low dose (25 μg LV per implant) and high dose (100 μg LV per implant).

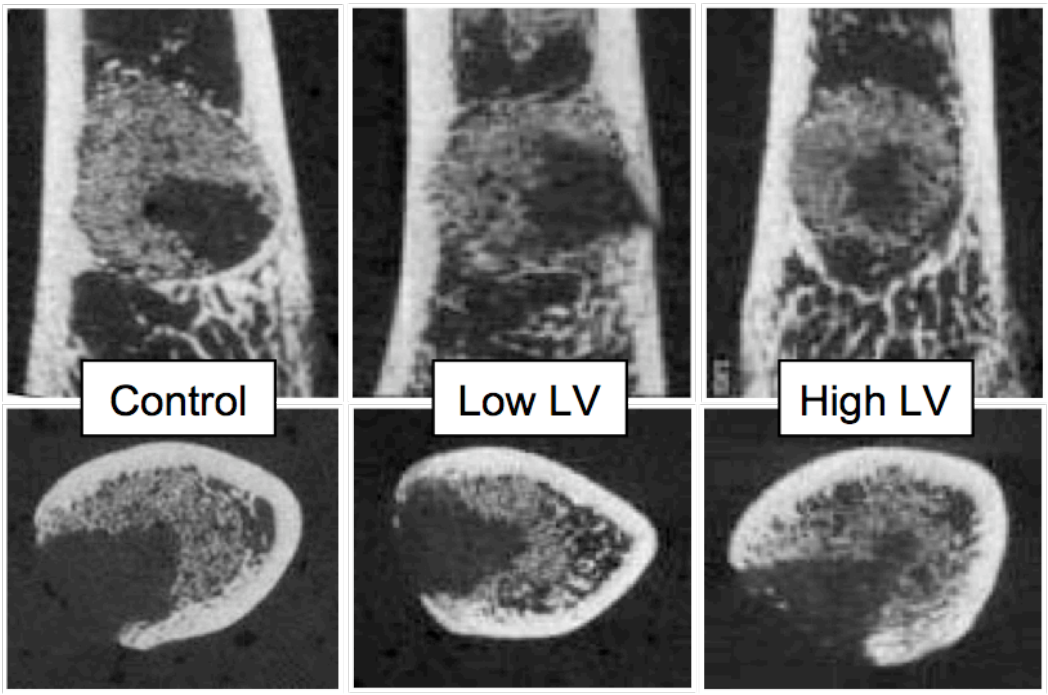

Figure 6.9. Representative saggital (top) and coronal (bottom) μCT images of femoral plug defects filled with PUR-LV scaffolds after 4 weeks. Mineralized bone formation was slightly, but not significantly, enhanced with the high LV treatment.

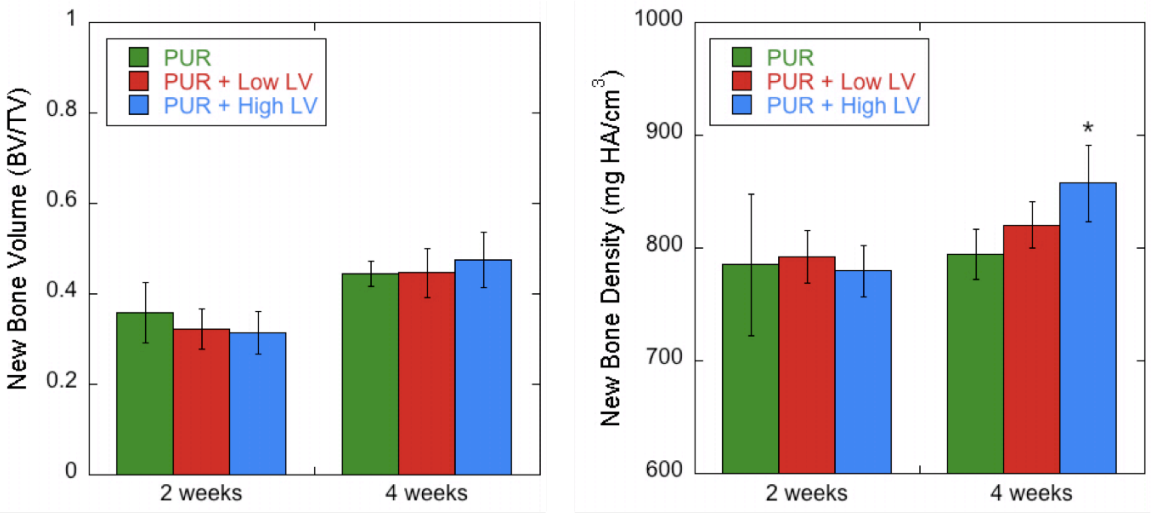

Figure 6.10. New mineralized bone volume, quantified from μCT images, was greater in the high LV group at 4 weeks, but not significantly. Bone volume is expressed per total implant volume. However, the mean density of newly formed bone was significantly higher for this group. (*: $p < 0.05$ vs. control, n = 6).

In the histological analysis, substantial cell infiltration was observed in all groups at week 2, and new bone formation had started at the implant edges (Figure 6.11). At week 4, an increased amount of mature bone had formed throughout the entire area of the implants, again with the greatest amounts in the LV-H samples. The PUR implants showed more extensive degradation at week 4 than at week 2 for all treatment groups. While histomorphometrical analysis showed no significant differences between groups at week 2 in new bone formation, by week 4 the LV-H samples showed significantly greater bone formation than the control group (Figure 6.12). This difference was statistically significant when evaluated by histomorphometry, which measures both mineralized and non-mineralized new bone, but not by μCT, which only quantifies mineralized bone. In all groups, the residual polymer area at week 4 was nearly half that of the samples at week 2; there

were no significant differences among treatment groups both at week 2 and week 4 (Figure 6.12).

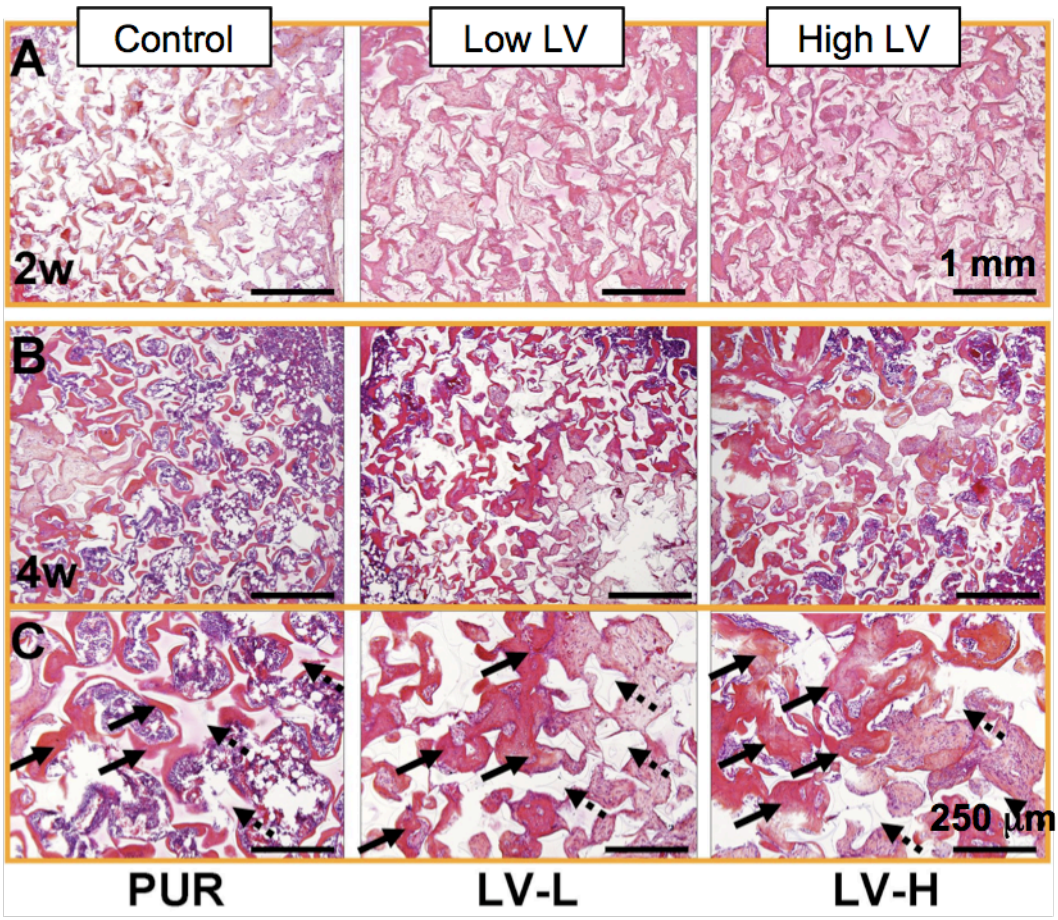

Figure 6.11. Decalcified histological sections at 2 (row A) & 4 (row B) weeks, stained with H & E. Row C contains higher-magnification views of the 4-week samples. Substantial cell infiltration at 2 weeks is followed by mater bone formation at 4 weeks. Solid arrows indicate new bone, while dotted arrows point to polymer remnants.

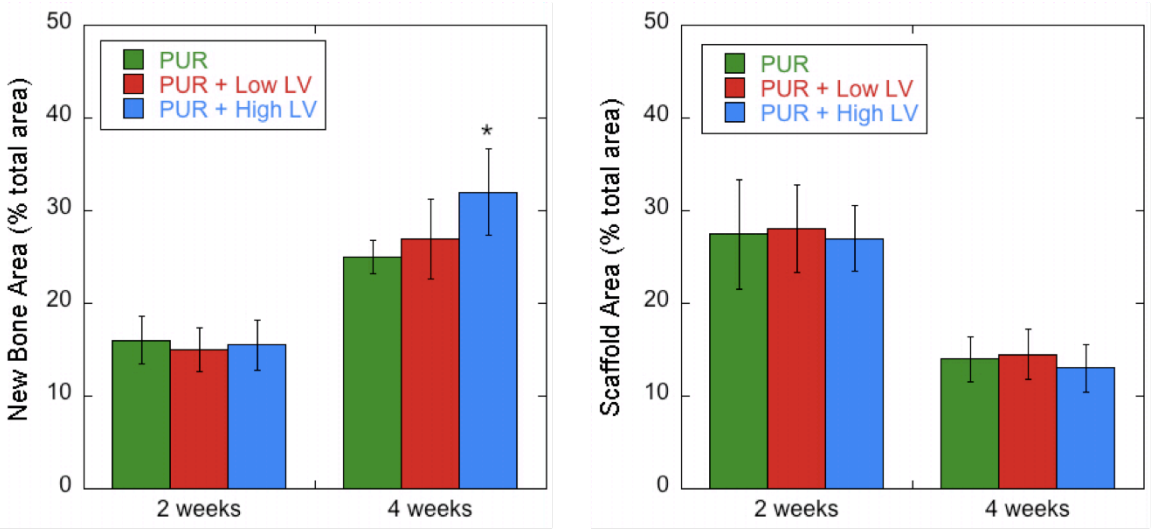

Figure 6.12. New bone formation and remaining scaffold fragments as determined by histomorphometry of the histological sections proceed at corresponding but inverse rates. (*: $p < 0.05$ vs. control, n = 6).

Discussion

MC3T3 cells have been observed to migrate through the PUR scaffolds used in this study, both in Chapter II and in previously published work, suggesting that the scaffold pores are interconnected [25]. In the present *in vivo* study, cellular infiltration and ingrowth of new bone into the scaffolds were observed as early as 2 weeks, with increased new bone formation at 4 weeks. These results suggest that the LTI-based two-component PUR scaffolds demonstrate osteoconductive properties.

Incorporation of biologically active molecules in a scaffold is an established and effective approach to regenerating tissue [26, 27]. The PUR scaffolds have been shown to deliver tobramycin [28], platelet-derived growth factor-BB (PDGF-BB) [29] and recombinant human bone morphogenetic protein-2 (rhBMP-2) [30], and other PUR materials have delivered basic fibroblast growth factor (bFGF) [31].

Since statins are rapidly absorbed after oral administration and their systemic bioavailability is low [13], administering statins locally to defect sites was anticipated to be a more effective strategy for bone regeneration than systemic delivery. In this study, lovastatin was incorporated into the PUR scaffolds as a powder – in a similar manner to tobramycin (Chapter V) and the growth factors mentioned above. Like tobramycin and PDGF, lovastatin maintained its biological activity and was not adversely affected by the polyurethane reaction when it was added as a solid powder [28, 29]. These molecules have active hydrogen (e.g., hydroxyl and amine) groups that can covalently bond to the polyurethane when they are added as an aqueous solution instead of in solid form. This results in almost negligible release of the molecule on the experimental timescale *in vitro*, since the release is then degradation-controlled instead of diffusion-controlled [28]. The incorporation of these solid particles does not affect the overall porosity or pore structure of the scaffolds, except when the particles are larger than the pore wall thickness (~ 10 μm) or added at a high enough loading such that the scaffold density changes significantly.

In order to deliver statins safely and effectively to the wound site, a sustained local delivery system is preferred to systemic delivery. An adverse inflammatory response has been reported following local injections of high statins doses *in vivo* [32, 33]. Locally high statin concentrations may dramatically reduce production of cholesterol, a molecule required for membrane integrity, and result in cytotoxicity. In this study, lovastatin release from PUR scaffolds followed a sustained and linear profile, thus minimizing the potentially negative side effects of locally high statin

concentrations. The burst release was < 3%, and after the 30 days the cumulative release varied from 12% (low dose) to 22% (high dose). These data agree with an earlier study with simvastatin—which also has very low water solubility—released from PLGA scaffolds, where the burst release was 5% and the cumulative release after 30 days was 32% [34].

In vitro release kinetics of tobramycin and lovastatin, as well as with water-soluble growth factors in ongoing studies, suggest that particle release from PUR scaffolds is diffusion-controlled. As long as the time scale of polymer degradation is significantly longer than that of release, the particle release rate is independent of polymer degradation. As described in more detail in Chapter V, water uptake into the polymer leads to dissolution of available particles, followed by diffusion out of the scaffold. Thus lovastatin releases slowly due to its very low water solubility, in contrast to the high burst release (> 30%) of readily soluble tobramycin [28].

The higher cumulative release of lovastatin that was released at the high dose relative to the low dose (Figure 6.1) likely results from the formation of aqueous channels within the polymer created by lovastatin that has already diffused away from the interior of the scaffold. A higher lovastatin loading might create more channels for lovastatin diffusion from the polymer, resulting in accelerated release kinetics (Equation 5.12). The lovastatin release rate can also be accelerated slightly by incorporating poly(ethylene glycol) (PEG), which increases the hydrophilicity and swelling of the PUR scaffold [28]. Faster release rates of statins have been achieved through other approaches, such as encapsulation of lovastatin in nanospheres 50 – 350 nm in diameter, which exhibited a minimal burst release and

25% release after 10 days, presumably due to the relatively short diffusion path [16]. In another study, fluvastatin (substantially more water soluble than lovastatin) tethered to a PEG hydrogel by a degradable lactic acid spacer exhibited tunable release kinetics, with 100% cumulative release after a period of 7 – 40 days *in vitro* [15]. The faster statin release kinetics observed for the fluvastatin hydrogel delivery system is attributed to its degradation-controlled release mechanism in contrast to the diffusion-controlled mechanism associated with the PUR scaffolds.

The scaffolds both with and without lovastatin exhibited biocompatibility when cultured with osteoblastic cells *in vitro*. As a result, PUR/LV scaffolds demonstrated equal potential for osteoblastic cell attachment and proliferation *in vitro* as PUR scaffolds without lovastatin. PUR/LV and PUR scaffolds also showed similar abilities to allow cell infiltration to the scaffolds *in vivo* at 2 weeks post-implantation. Histological analysis demonstrated substantial degradation of PUR scaffolds at week 4 *in vivo*, which is in agreement with the studies in Chapters I and II. None of the histological sections showed severe inflammation, suggesting that neither the PUR degradation products nor the released lovastatin induced an adverse inflammatory response for the lovastatin doses used in this study. These facts suggest that the PUR/LV sustained delivery system can be used safely for bone tissue repair by delivering lovastatin doses that are high enough to promote new bone formation but below the threshold for inflammation.

Based on the fact that lovastatin needs to be converted to the hydrophilic acid form to become biologically active [35], the biological activity of lovastatin released from the scaffolds was assessed by its effect on osteogenesis *in vitro*. These

experiments were designed to determine whether the biological activity of lovastatin was adversely affected by the polyurethane reaction. Induction of osteogenic differentiation and mineralization, as evaluated by ALP activity and mineralized nodule formation, resulted when MC3T3-E1 osteoblastic cells were cultured with lovastatin releasates. It has been reported that osteogenic differentiation in MC3T3-E1 osteoblastic cells is promoted by simvastatin through increased BMP-2 expression [36, 37]. Similarly, the enhanced ALP activity and mineralized nodule formation in this study is attributed to increased expression of BMP-2 caused by lovastatin releasates, suggesting that lovastatin is released from PUR scaffolds in an active form and the stimulatory osteogenic effect by promoting BMP-2 production is thus preserved. Since the osteogenic potential of BMP-2 is well known to be beneficial for fracture repair and regenerating bone defects [38-40], delivery of bioactive lovastatin with PUR scaffolds can be useful for bone regeneration.

In clinical settings, defects in long bones caused by pathological or traumatic conditions (e.g. bone tumors, infections, major trauma) often require reconstruction using bone substitutes [41]. To evaluate the anabolic effect of lovastatin in long bone defects and investigate its utility as a bone void filler, the PUR/LV scaffolds were evaluated in a rat femoral defect model, which is highly reproducible and useful for investigating the efficacy of new materials and drugs. While published reports have demonstrated the efficacy of statins for healing of defects in craniofacial bone, the effects of local delivery of lovastatin on healing of orthopaedic long bone defects are not known. The *in vivo* study demonstrated that new bone

formation was enhanced to some extent by local delivery of lovastatin from PUR scaffolds, which is consistent with several previous studies for bone defect repair using statins [33, 42, 43]. The biological activity of statins *in vivo* is attributed to increased production of endogenous BMP-2 [44]. Interestingly, there were no differences in the amount of bone formation at week 2, but bone matrix formation in histological sections was significantly promoted by local delivery of lovastatin at week 4. Although the difference in mineralized bone volume evaluated by μCT was not statistically significant at week 4, it is possible that the effects of lovastatin on mineralized bone formation may extend beyond week 4 as previously reported [33]. It is known that progenitor cells require time to infiltrate substantially the defect and scaffold [45]. Therefore, the effect of lovastatin in enhancing endogenous BMP-2 production may be delayed until these cells are present, at which point subsequent osteogenic differentiation and mineralization can occur. For this reason, an optimal delivery strategy might first involve the release of a chemotactic agent, such as PDGF-BB, to attract cells into the scaffold, followed by sustained release of lovastatin. In a previous fracture healing study using lovastatin, delayed percutaneous injection of lovastatin (1 week after surgery) into the fracture site resulted in enhanced fracture repair relative to injection within one day in a rat model [46]. The improvement in repair associated with delayed injection was considered to result from a larger number of cells at the fracture site. This observation further suggests that sustained release of lovastatin from scaffolds is important for effective bone formation.

In the non-critical-sized plug defect model used in this study, a faster release profile of an anabolic drug would likely perform better than a slower release profile for the necessarily short observation periods due to the fast healing of the defect [30]. Therefore, a larger defect model, such as a critical sized segmental defect model [47, 48], could be more suitable for longer observation periods and thus should be investigated to further examine the effects of sustained release of lovastatin on bone formation.

Modeling of release kinetics

Apropos of the mathematical modeling discussion in Chapter V, the lovastatin release curves provide an interesting comparison to the tobramycin release data. Lovastatin release from the PUR scaffolds is linear, with a near constant daily release (Figures 6.1 & 6.2), in contrast to the burst release of tobramycin. These two molecules have similar molecular weights; the markedly different water solubility levels provide the basis for their dissimilar release profiles. Tobramycin is very readily soluble in water, so the rate-limiting step in its release from the scaffolds is diffusion from the polymer matrix. Conversely, lovastatin is minimally soluble in water, so the rate-limiting step is dissolution in the aqueous pores before diffusing from the polymer.

The lovastatin release studies described earlier were conducted for 30 days, which is shorter than the polymer degradation timescale. However, only 10% (low dose) and 20% (high dose) of the total incorporated lovastatin was released by 30 days. If the experiments had been carried out longer – for multiple weeks to

months, on the timescale of polymer degradation – a biphasic release profile would have been expected, where the release rate would accelerate at the onset of significant polymer degradation, until 100% cumulative release.

Similar to the investigation of tobramycin release mechanisms, the lovastatin data was fit to multiple mathematical models using MATLAB. The fits (as indicated by the R^2 values) were consistently better than the corresponding fits of the tobramycin release curves, as illustrated in Figure 6.13. Table 6.2 lists the fitted parameters for each of the models. The PUR scaffolds from which lovastatin release was measured contained no PEG. Therefore, the lovastatin release curves can be contrasted with the PUR-tobramycin scaffolds with 0 PEG. The parameters for these tobramycin scaffolds in the two power law models are also listed in Table 6.2 for direct comparison. These scaffolds are synthesized from the same polyol and isocyanate compositions, so the scaffold swelling and degradation behaviors are consistent across samples. Thus the identity of the additive, lovastatin or tobramycin, is the only variable changed between these *in vitro* release studies. However, the aqueous pore formation may be more extensive in the tobramycin scaffolds because of the higher initial level of diffusion and burst release.

The lovastatin release curves essentially demonstrate a linear dependence on time. This system exhibits zero order release kinetics, where the rate constant (the parameter b in Table 6.2), determined by the lovastatin solubility and rate of dissolution, does not change with time. The experimental arrangement for measuring lovastatin release *in vitro* must approximate a constant sink as closely as possible (i.e. with frequent media changes and sample agitation), in order to prevent

the formation of a boundary layer of relatively high lovastatin that could act as a diffusion barrier.

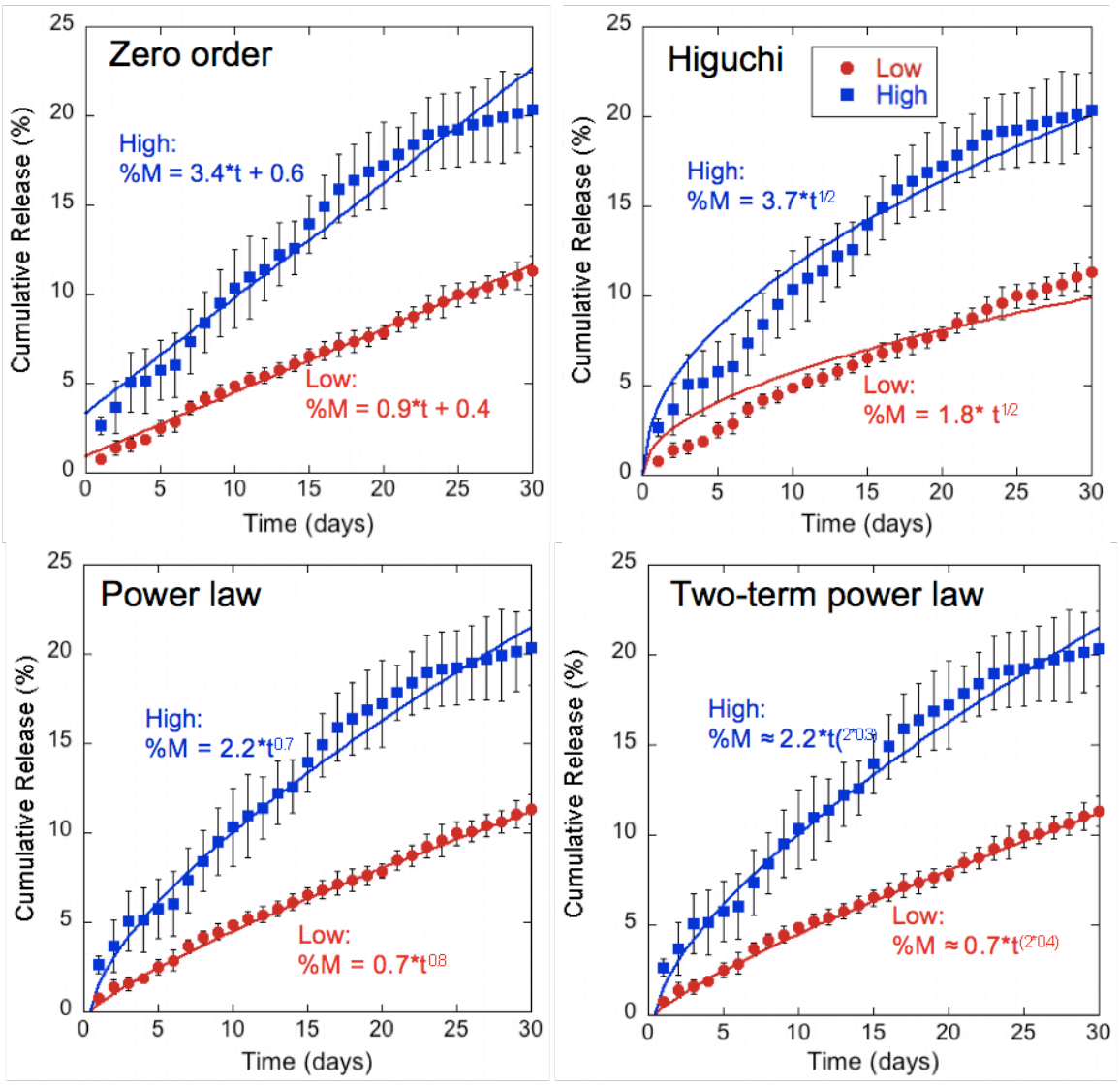

Figure 6.13. Mathematical model fits (solid lines) of experimental in vitro lovastatin release data (individual data points) in MATLAB.

Table 6.2. Parameters obtained by fitting lovastatin release data, for both the low and high doses, to various models. The power law model parameters for tobramycin released from 0 PEG scaffolds are included for comparison.

ZERO ORDER			**f(t) = a + bt**	
	R^2	a	b	
LV-low	0.993	0.91	0.36	
LV-high	0.967	3.35	0.64	
HIGUCHI			**$f(t) = kt^{1/2}$**	
	R^2	k		
LV-low	0.904	1.80		
LV-high	0.943	3.66		
POWER LAW			**$f(t) = kt^n$**	
	R^2	k	n	
LV-low	0.998	0.73	0.81	
LV-high	0.985	2.21	0.67	
Tobramycin	*0.895*	*59.7*	*0.10*	
TWO-TERM POWER LAW			**$f(t) = k_1t^n + k_2t^{2n}$**	
	R^2	k_1	k_2	n
LV-low	0.998	2.6E-06	0.73	0.40
LV-high	0.985	5.1E-11	2.21	0.34
Tobramycin	*0.895*	*59.7*	*~ 0*	*0.10*

The parameter values of the empirical power law fits favor the relaxational mechanism of drug release over Fickian diffusion. The n values in the power law model ($0.5 < n < 1.0$) indicate "anomalous" transport, between Fickian and Case-II transport (see Table 5.3 for significance of n values). Meanwhile, in the two-term modified power law model, k_2 is much greater than k_1, which suggests the relative importance of Case-II transport. As shown in Table 6.2, these trends are opposite of

the tobramycin scaffold parameters. A possible hypothesis is that lovastatin release portrays Case-II transport because it depends more on the swelling of the polymer, leading to (very slow) dissolution, than on pure diffusion. As stated earlier, the rate-limiting step seems to be lovastatin dissolution into the aqueous pores in the scaffold. The lovastatin concentration gradient between the polymer interstices and the external aqueous media is possibly quite minimal. Since the solute concentration gradient is fundamental for Fick's law of diffusion, a diminutive gradient may consequently lessen the extent of Fickian diffusion.

Conclusions

In this study, the effects of locally delivered lovastatin, released from PUR scaffolds, on osteoblastic differentiation *in vitro* and new bone formation *in vivo* were investigated. At a dose of 200 μg per implant, the lovastatin concentration was sufficiently high to enhance new bone formation in a rat femoral plug model, but below the threshold at which adverse inflammation occurs. Further studies are required to investigate the effects of local delivery of lovastatin on healing of more challenging wounds, such as critical-size defects. However, this study showed the potential of using statins to enhance healing of bony defects through local delivery from polymeric scaffolds.

References

1. Govender S, Csimma C, Genant HK, Valentin-Opran A, Amit Y, Arbel R, et al. Recombinant human bone morphogenetic protein-2 for treatment of open tibial fractures: A prospective, controlled, randomized study of four hundred and fifty patients. *Journal of Bone & Joint Surgery, American Volume* 2002; 84(12): 2123-2134.

2. Urist MR. Bone morphogenetic protein: The molecularization of skeletal system development. *Journal of Bone and Mineral Research* 1997; 12(3): 343-346.

3. Einhorn TA, Majeska RJ, Mohaideen A, Kagel EM, Bouxsein ML, Turek TJ, et al. A single percutaneous injection of recombinant human bone morphogenetic protein-2 accelerates fracture repair. *Journal of Bone & Joint Surgery* 2003; 85(8): 1425-1435.

4. Einhorn TA. Clinical applications of recombinant human bmps: Early experience and future development. *Journal of Bone & Joint Surgery, American Volume* 2003; 85(S3): 82-88.

5. Mundy G, Garrett R, Harris S, Chan J, Chen D, Rossini G, et al. Stimulation of bone formation in vitro and in rodents by statins. *Science* 1999; 286(5446): 1946-1949.

6. Liao JK, Laufs U. Pleiotropic effects of statins. *Annu Rev Pharmacol Toxicol* 2005; 45: 89-118.

7. Almuti K, Rimawi R, Spevack D, Ostfeld RJ. Effects of statins beyond lipid lowering: Potential for clinical benefits. *Int J Cardiol* 2006; 109(1): 7-15.

8. Weber MS, Youssef S, Dunn SE, Prod'homme T, Neuhaus O, Stuve O, et al. Statins in the treatment of central nervous system autoimmune disease. *J Neuroimmunol* 2006; 178(1-2): 140-148.

9. Mundy GR. Statins and their potential for osteoporosis. *Bone* 2001; 29(6): 495-497.

10. Gonyeau MJ. Statins and osteoporosis: A clinical review. *Pharmacotherapy* 2005; 25(2): 228-243.

11. Gutierrez GE, Lalka D, Garrett IR, Rossini G, Mundy GR. Transdermal application of lovastatin to rats causes profound increases in bone formation and plasma concentrations. *Osteoporos Int* 2006; 17(7): 1033-1042.

12. Toh S, Hernandez-Diaz S. Statins and fracture risk. A systematic review. *Pharmacoepidemiol Drug Saf* 2007; 16(6): 627-640.

13. Schachter M. Chemical, pharmacokinetic and pharmacodynamic properties of statins: An update. *Fundam Clin Pharmacol* 2005; 19(1): 117-125.

14. Whang K, McDonald J, Khan A, Satsangi N. A novel osteotropic biomaterial og-plg: Synthesis and in vitro release. *J Biomed Mater Res A* 2005; 74(2): 237-246.

15. Benoit DS, Nuttelman CR, Collins SD, Anseth KS. Synthesis and characterization of a fluvastatin-releasing hydrogel delivery system to modulate hmsc differentiation and function for bone regeneration. *Biomaterials* 2006; 27(36): 6102-6110.

16. Garrett IR, Gutierrez GE, Rossini G, Nyman J, McCluskey B, Flores A, et al. Locally delivered lovastatin nanoparticles enhance fracture healing in rats. *J Orthop Res* 2007; 25(10): 1351-1357.

17. Jeon JH, Piepgrass WT, Lin YL, Thomas MV, Puleo DA. Localized intermittent delivery of simvastatin hydroxyacid stimulates bone formation in rats. *J Periodontol* 2008; 79(8): 1457-1464.

18. Guelcher SA, Patel V, Gallagher KM, Connolly S, Didier JE, Doctor JS, et al. Synthesis and in vitro biocompatibility of injectable polyurethane foam scaffolds. *Tissue Eng* 2006; 12(5): 1247-1259.

19. Guelcher S, Srinivasan A, Hafeman A, Gallagher K, Doctor J, Khetan S, et al. Synthesis, in vitro degradation, and mechanical properties of two-component poly(ester urethane)urea scaffolds: Effects of water and polyol composition. *Tissue Eng* 2007; 13(9): 2321-2333.

20. Wutticharoenmongkol P, Pavasant P, Supaphol P. Osteoblastic phenotype expression of mc3t3-e1 cultured on electrospun polycaprolactone fiber mats filled with hydroxyapatite nanoparticles. *Biomacromolecules* 2007; 8(8): 2602-2610.

21. Zhang LF, Yang de J, Chen HC, Sun R, Xu L, Xiong ZC, et al. An ionically crosslinked hydrogel containing vancomycin coating on a porous scaffold for drug delivery and cell culture. *Int J Pharm* 2008; 353(1-2): 74-87.

22. Zhao M, Ko SY, Liu JH, Chen D, Zhang J, Wang B, et al. Inhibition of microtubule assembly in osteoblasts stimulates bone morphogenetic protein 2 expression and bone formation through transcription factor gli2. *Mol Cell Biol* 2009; 29(5): 1291-1305.

23. Karp JM, Rzeszutek K, Shoichet MS, Davies JE. Fabrication of precise cylindrical three-dimensional tissue engineering scaffolds for in vitro and in vivo bone engineering applications. *J Craniofac Surg* 2003; 14(3): 317-323.

24. Torigoe I, Sotome S, Tsuchiya A, Yoshii T, Maehara H, Sugata Y, et al. Bone regeneration with autologous plasma, bone marrow stromal cells, and porous beta-tricalcium phosphate in nonhuman primates. *Tissue Eng Part A* 2009.

25. Guelcher S, Srinivasan A, Hafeman A, Gallagher K, Doctor J, Khetan S, et al. Synthesis, in vitro degradation, and mechanical properties of two-component poly(ester urethane)urea scaffolds: Effects of water and polyol composition. *Tissue Engineering* 2007; 13(9): 2321-2333.

26. Rose FR, Hou Q, Oreffo RO. Delivery systems for bone growth factors - the new players in skeletal regeneration. *J Pharm Pharmacol* 2004; 56(4): 415-427.

27. Drosse I, Volkmer E, Capanna R, De Biase P, Mutschler W, Schieker M. Tissue engineering for bone defect healing: An update on a multi-component approach. *Injury* 2008; 39 Suppl 2: S9-20.

28. Hafeman AE, Zienkiewicz K, Carney E, Litzner B, Stratton C, Wenke J, et al. Local delivery of tobramycin from injectable biodegradable polyurethane scaffolds. *Journal of Biomaterials Science: Polymer Edition* 2010; 21(1).

29. Li B, Davidson JM, Guelcher SA. The effect of the local delivery of platelet-derived growth factor from reactive two-component polyurethane scaffolds on the healing in rat skin excisional wounds. *Biomaterials* 2009; 30(20): 3486-3494.

30. Goldstrohm GL, Mears DC, Swartz WM. The results of 39 fractures complicated by major segmental bone loss and/or leg length discrepancy. *J Trauma* 1984; 24(1): 50-58.

31. Guan J, Stankus JJ, Wagner WR. Biodegradable elastomeric scaffolds with basic fibroblast growth factor release. *J Control Release* 2007; 120(1-2): 70-78.

32. Stein D, Lee Y, Schmid MJ, Killpack B, Genrich MA, Narayana N, et al. Local simvastatin effects on mandibular bone growth and inflammation. *J Periodontol* 2005; 76(11): 1861-1870.

33. Nyan M, Sato D, Oda M, Machida T, Kobayashi H, Nakamura T, et al. Bone formation with the combination of simvastatin and calcium sulfate in critical-sized rat calvarial defect. *J Pharmacol Sci* 2007; 104(4): 384-386.

34. Whang K, McDonald J, Khan A, Satsangi N. A novel osteotropic biomaterial og-plg: Synthesis and in vitro release. *J Biomed Mater Res Part A* 2005; 74A: 237-246.

35. Garrett IR, Gutierrez G, Mundy GR. Statins and bone formation. *Current Pharmaceutical Design* 2001; 7: 715-736.

36. Maeda T, Matsunuma A, Kawane T, Horiuchi N. Simvastatin promotes osteoblast differentiation and mineralization in mc3t3-e1 cells. *Biochem Biophys Res Commun* 2001; 280(3): 874-877.

37. Maeda T, Matsunuma A, Kurahashi I, Yanagawa T, Yoshida H, Horiuchi N. Induction of osteoblast differentiation indices by statins in mc3t3-e1 cells. *J Cell Biochem* 2004; 92(3): 458-471.

38. Mont MA, Ragland PS, Biggins B, Friedlaender G, Patel T, Cook S, et al. Use of bone morphogenetic proteins for musculoskeletal applications. An overview. *J Bone Joint Surg Am* 2004; 86-A Suppl 2: 41-55.

39. Wozney JM, Rosen V. Bone morphogenetic protein and bone morphogenetic protein gene family in bone formation and repair. *Clin Orthop Relat Res* 1998(346): 26-37.

40. Termaat MF, Den Boer FC, Bakker FC, Patka P, Haarman HJ. Bone morphogenetic proteins. Development and clinical efficacy in the treatment of fractures and bone defects. *J Bone Joint Surg Am* 2005; 87(6): 1367-1378.

41. Paderni S, Terzi S, Amendola L. Major bone defect treatment with an osteoconductive bone substitute. *Chir Organi Mov* 2009; 93(2): 89-96.

42. Wong RW, Rabie AB. Statin collagen grafts used to repair defects in the parietal bone of rabbits. *Br J Oral Maxillofac Surg* 2003; 41(4): 244-248.

43. Wong RW, Rabie AB. Histologic and ultrastructural study on statin graft in rabbit skulls. *J Oral Maxillofac Surg* 2005; 63(10): 1515-1521.

44. Alam S, Ueki K, Nakagawa K, Marukawa K, Hashiba Y, Yamamoto E, et al. Statin-induced bone morphogenetic protein (bmp) 2 expression during bone regeneration: An immunohistochemical study. *Oral Surg Oral Med Oral Pathol Oral Radiol Endod* 2009; 107(1): 22-29.

45. Seeherman H, Li R, Bouxsein M, Kim H, Li XJ, Smith-Adaline EA, et al. Rhbmp-2/calcium phosphate matrix accelerates osteotomy-site healing in a nonhuman primate model at multiple treatment times and concentrations. *J Bone Joint Surg Am* 2006; 88(1): 144-160.

46. Oshina H, Sotome S, Yoshii T, Torigoe I, Sugata Y, Maehara H, et al. Effects of continuous dexamethasone treatment on differentiation capabilities of bone marrow-derived mesenchymal cells. *Bone* 2007; 41(4): 575-583.

47. Moore DC, Pedrozo HA, Crisco JJ, 3rd, Ehrlich MG. Preformed grafts of porcine small intestine submucosa (sis) for bridging segmental bone defects. *J Biomed Mater Res A* 2004; 69(2): 259-266.

48. Chu TM, Warden SJ, Turner CH, Stewart RL. Segmental bone regeneration using a load-bearing biodegradable carrier of bone morphogenetic protein-2. *Biomaterials* 2007; 28(3): 459-467.

CHAPTER VII

CONCLUSION

As a result of the developments underscored in this work, the biodegradable polyurethane scaffolds hold the potential to greatly impact the treatment of wounds that cost billions of dollars per year in the United States alone. The intended application is for injuries that cannot heal independently. Highlights of the material's benefits and novelty include the improvement of elastomeric mechanical properties, introduction of an injectable application, and a delivery strategy for small molecules. These small molecules, such as growth factors, antibiotics, analgesics, and anabolic drugs are pivotal to enhancing and directing the natural repair and regeneration process.

In bone wounds, critical sized defects are too large to heal, and require a scaffold to bridge the gap and allow new cells to infiltrate the void. However, many clinically available bone substitutes and void fillers fall on either end of the mechanical properties spectrum Materials like hydrogels might be advantageous for delivering therapeutics, but cannot withstand the stresses and strains of the bone setting. Conversely, stiff calcium phosphate and hydroxyapatite materials can bear weight, but are often too brittle to maintain integrity in the dynamic bone setting. In contrast, the polyurethane scaffolds' resilience and elastomeric mechanical properties are especially unique among synthetic bone void fillers as they can maintain their shape amidst local movement and strain.

In skin wound repair, the primary and most costly concern is in non-healing wounds, such as diabetic ulcers. In this case, current dermal substitutes are generally thin sheets of synthetic or natural substances that are intended for temporary protection before placement of a full dermal autograft. The elastomeric and highly porous structure of the scaffolds is a great advantage for these wounds as well. They can fill three-dimensional voids and promote new tissue formation, as well as sustain the torques and stresses typical in skin. This project also featured the development of any injectable application for these materials, which is desired and anticipated by clinicians. Dermal wounds especially can be prone to irregular boundaries.

Porous, biodegradable polyurethane scaffolds demonstrate promise as templates for tissue repair and regeneration. The studies and conclusions outlined in the preceding chapters involve the design and development of the synthetic biomaterials into potential regenerative therapies, particularly for bone void and skin wound healing. Until recently, polyurethanes use in biomedical applications had mostly been for non-degrading implants, but they were often synthesized from toxic isocyanate monomers and degraded to toxic products.

Preceding this work, poly(ester urethane)urea scaffolds were formulated with polyester triols and aliphatic diisocyanates that had low vapor pressures and degraded to non-cytotoxic products, but lacked the robust mechanical properties typical of other urethane scaffolds. The chemical structures reduced the hydrogen bonding between hard segments traditionally observed in segmented polyurethanes. Therefore the first milestone of these studies entailed the

improvement of the scaffolds resilience and elastomeric mechanical properties. This was accomplished with trifunctional aliphatic isocyanates, specifically hexamethylene diisocyanate trimer and lysine triisocyanate, which produce scaffolds with greatly improved compression set characteristics over the diisocyanate foams. The lysine-derived isocyanates contain a lysine residue within the polymer backbone that might contribute to the scaffold biocompatibility and degradation characteristics.

The structure-property relationships of these scaffolds were investigated, resulting in an array of methods to tune the mechanical properties and degradation rates. The isocyanate, as well as the polyol composition and molecular weight, alter the material hard-to-soft segment ratios, the thermal properties, and rate of hydrolytic chain cleavage, all of which influence the resultant mechanical properties. These studies focused on scaffolds without fillers or additives, which can otherwise modify the mechanical strength and stiffness. Preliminary *in vivo* studies established that these novel scaffolds supported cellular infiltration, new tissue formation in skin and bone, degraded to non-cytotoxic products, and elicited minimal inflammation at the wound site. Current engineered skin substitutes are generally fragile and lack sufficient mechanical properties to be stand-alone therapies, so a resilient dermal scaffold would be advantageous.

Several synthetic biomaterials have demonstrated success in promoting bone fracture healing and dermal wound repair, but few can cure *in situ*. Thus a distinct advantage of these polyurethane scaffolds is their capability to be injectable in a one-shot process. Initially in the form of a reactive liquid mixture, the materials can

flow to fill the wound contours, regardless of geometric complexity, and foam to completely fill the wound volume within 10 minutes by a minimally exothermic reaction. Together with the elastomeric mechanical properties, the injectability can promote close apposition with the surrounding tissue. The injectable application also enables a minimally invasive and customizable procedure in surgery.

The scaffolds were reformulated slightly for the injectable application. Although LTI has a much lower contact and inhalant toxicity with a low vapor pressure, the most reactive –NCO groups of LTI were partially reacted with MW-200 poly(ethylene glycol) to form an LTI-PEG prepolymer in order to further reduce possibilities of monomeric isocyanate toxicity.

The *in vivo* studies revealed much faster degradation than observed *in vitro*, suggesting a cellular-mediated mechanism for PUR scaffold biodegradation. Monocyte-derived macrophages were determined to play a critical role in PUR degradation, as they attach to the material surface and secrete enzymes and reactive oxygen intermediates that degrade the polymer at an accelerated rate compared to basic hydrolysis in buffer. *In vitro* experiments indicate that the reactive oxygen intermediates, approximated experimentally by a $H_2O_2/CoCl_2$ solution, likely have a greater degradative effect on these materials than the secreted hydrolytic enzymes. Based on the polyurethane structure, the primary degradation products were determined, and quantified, to be α-hydroxy acids (lactic, glycolic, and 6-hydroxycaproic acid), lysine, ethanolamine, and other unspecified urethane adducts. Based on evidence from recent literature and studies described here, hydroxyl radicals likely cause significant mass loss, especially among the lysine-derived

scaffolds, due to oxidative attack in both the soft and hard segments, which had not been shown before for these biodegradable polyurethane scaffolds. The lack of hydrogen bonding between hard segments allow these materials to degrade to completely soluble degradation products, which did not produce any signs of toxicity.

In addition to providing a template for cellular ingrowth and tissue regeneration, biologically active small molecules can be incorporated into the scaffolds for controlled delivery localized to the wound site. It was remarkable that these molecules retained their activity not only during the reactive system polyurethane foaming, but also for extended periods of time within the scaffold and after release. Molecules of interest currently include growth factors (BMP-2, PDGF, SDF-1), antibiotics (tobramycin, vancomycin), and drugs (lovastatin, analgesics). Such biologicals might serve to prevent infection, stimulate cell infiltration, or influence morphogenesis into bone-producing or skin matrix-producing cells, all of which would enhance and/or accelerate the wound healing response. Targeted delivery of these biologicals allows for higher local concentrations with lower systemic levels, which is more effective and safer in terms of avoiding systemic toxicities.

The antibiotic tobramycin was the first molecule to be successfully delivered from the scaffolds, demonstrating bioactivity and successfully inhibiting bacteria *in vitro* and *in vivo*. The release rate, characterized by a burst release and plateau, could be somewhat dictated by the concentration, encapsulation in microspheres, and the addition of hydrophilic PEG to the scaffolds. The release rate is governed by

diffusion of the molecule through the polymer and aqueous pores out of the scaffold, so the release profile depended almost entirely on the molecule type and solubility.

Lovastatin is a commonly used drug to lower serum cholesterol, but it also has anabolic effects on bone, as it stimulates BMP-2 activity. Thus lovastatin was incorporated into the scaffolds as well. However, its highly hydrophobic nature and minimal water solubility produced a very different release profile than the highly water soluble tobramycin. *In vitro* LV release experiments reveal a constant, linear elution profile from the scaffolds. LV released from the polyurethane scaffolds enhances BMP-2 expression *in vitro*, and does not negatively affect cell attachment and viability. *In vivo*, the lovastatin concentration was sufficiently high to enhance new bone formation in a rat femoral plug model, but below the threshold at which adverse inflammation occurs. A subsequent model was carried out successfully, where a suspension of PEG microspheres containing lovastatin was injected directly into the scaffold, which bridged a rat femoral segmental defect. New bone infiltration and healing was enhanced by local lovastatin release, demonstrating the potential therapeutic application of PUR scaffold with lovastatin delivery for bone reconstruction.

This work has laid the foundation for many promising studies to follow. The regenerative potential could be further enhanced by the incorporation of dual growth factors, adenoviral vectors, and perhaps even encapsulated autologous cells. The resilient and three-dimensional porous structure will ideally promote its application in other areas of the body besides skin and bone – perhaps endothelial lining, tendons, and cartilage.

APPENDIX I

CHEMICAL STRUCTURES

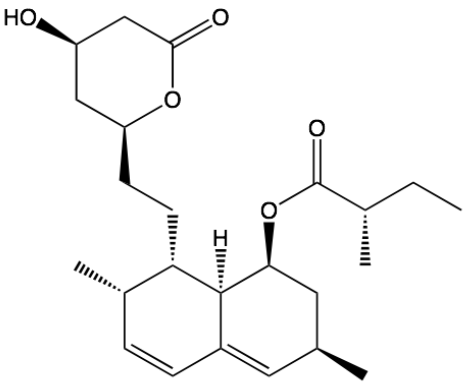

Lovastatin

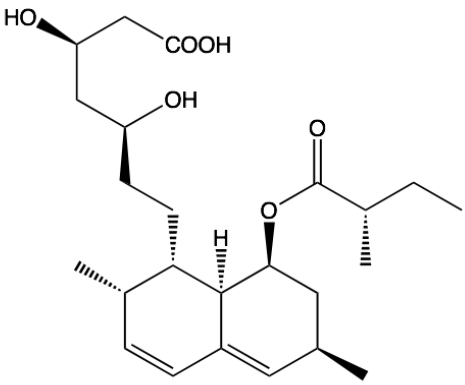

Lovastatin Acid

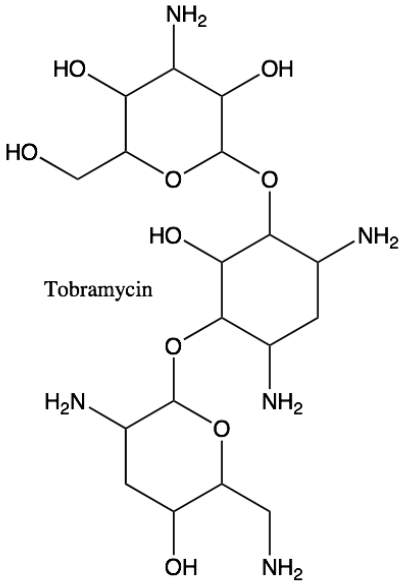

Tobramycin

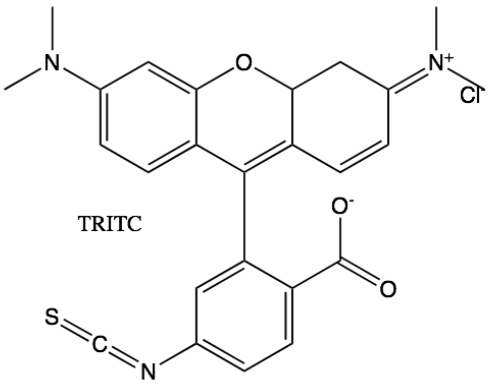

TRITC

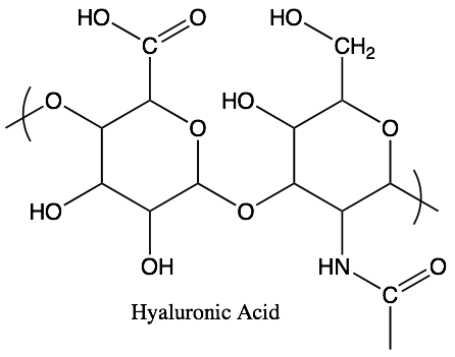

Hyaluronic Acid

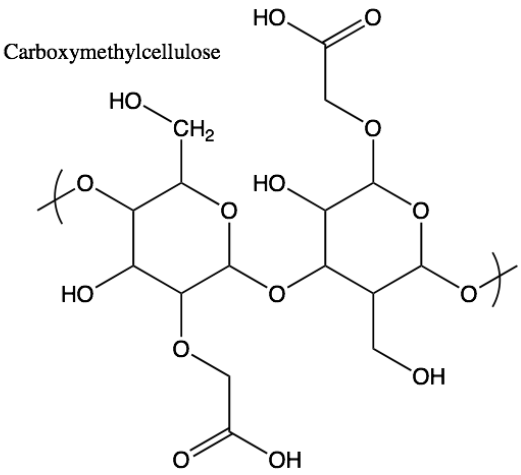

Carboxymethylcellulose

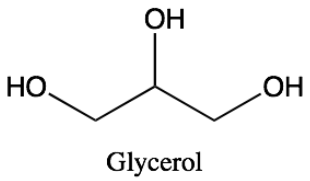

Glycerol

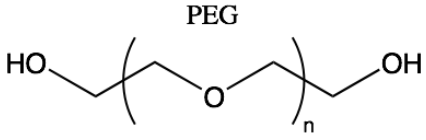

PEG

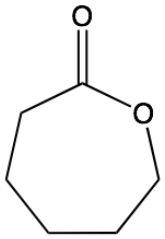

ε-Caprolactone

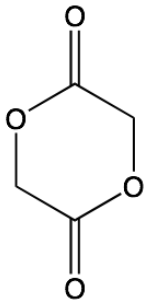

Glycolide

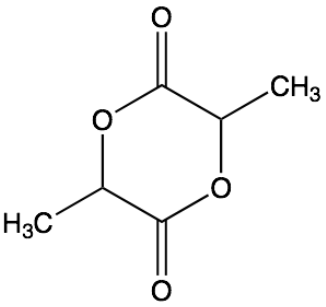

Lactide

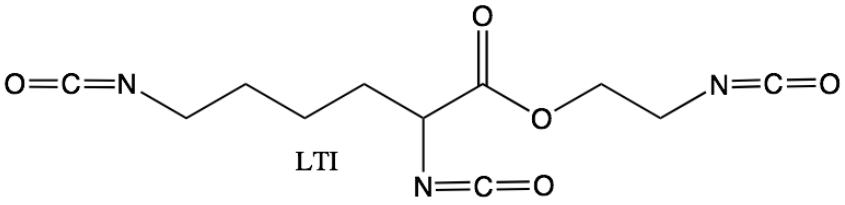

LTI

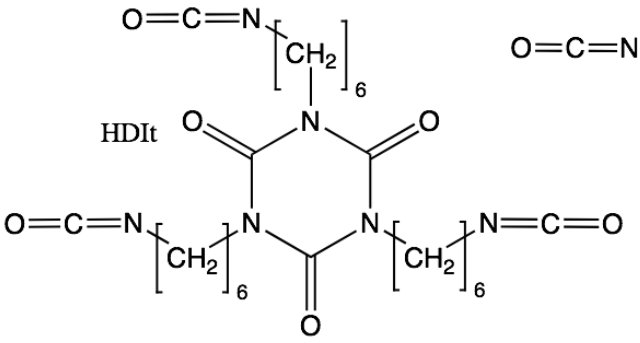

HDIt

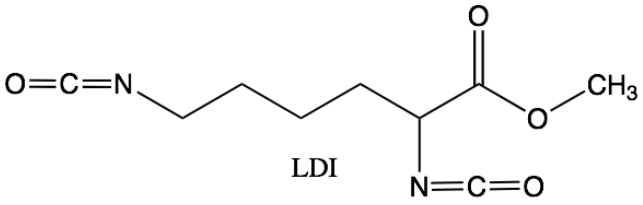

LDI

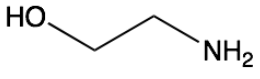

Ethanolamine

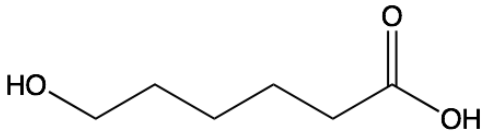

6-Hydroxycaproic acid

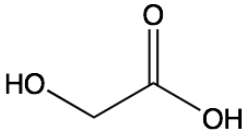

Glycolic acid

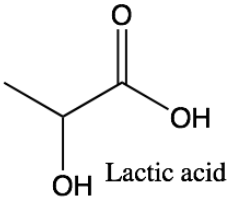

Lactic acid

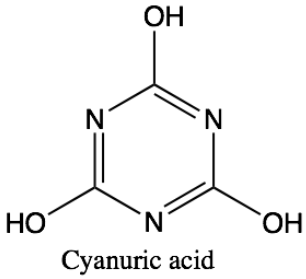

Cyanuric acid

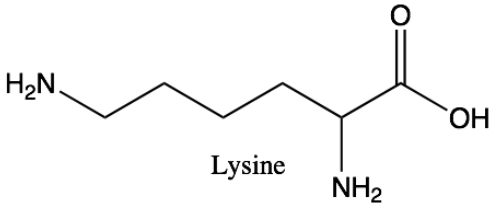

Lysine

APPENDIX II

CHEMICAL REACTIONS

LTI-PEG Prepolymer Synthesis

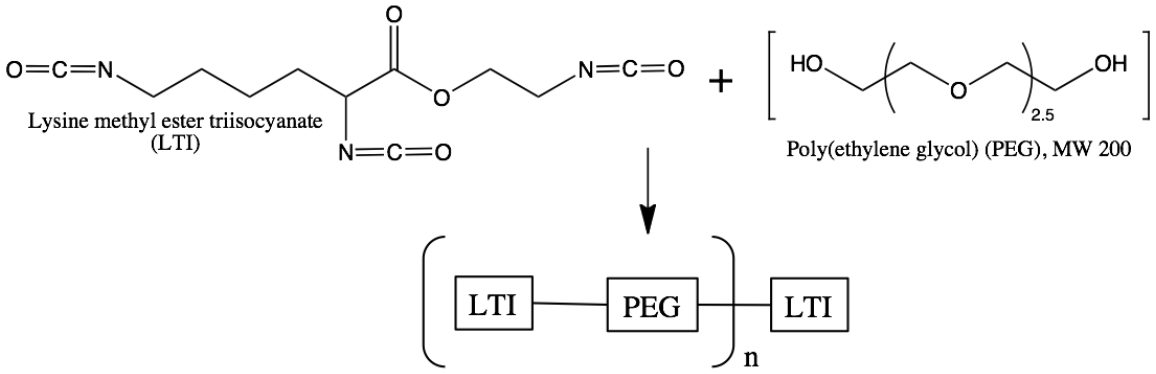

LTI-PEG prepolymer

Polyol Synthesis

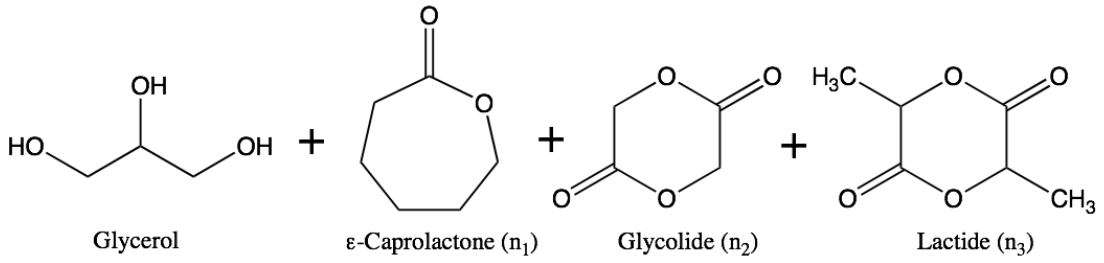

Glycerol | ε-Caprolactone (n_1) | Glycolide (n_2) | Lactide (n_3)

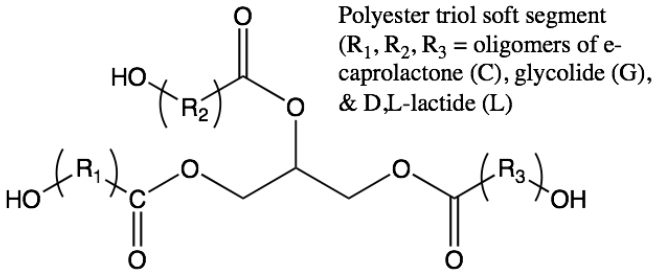

Polyester triol soft segment
(R_1, R_2, R_3 = oligomers of e-caprolactone (C), glycolide (G), & D,L-lactide (L)

PUR Synthesis - gelling reaction

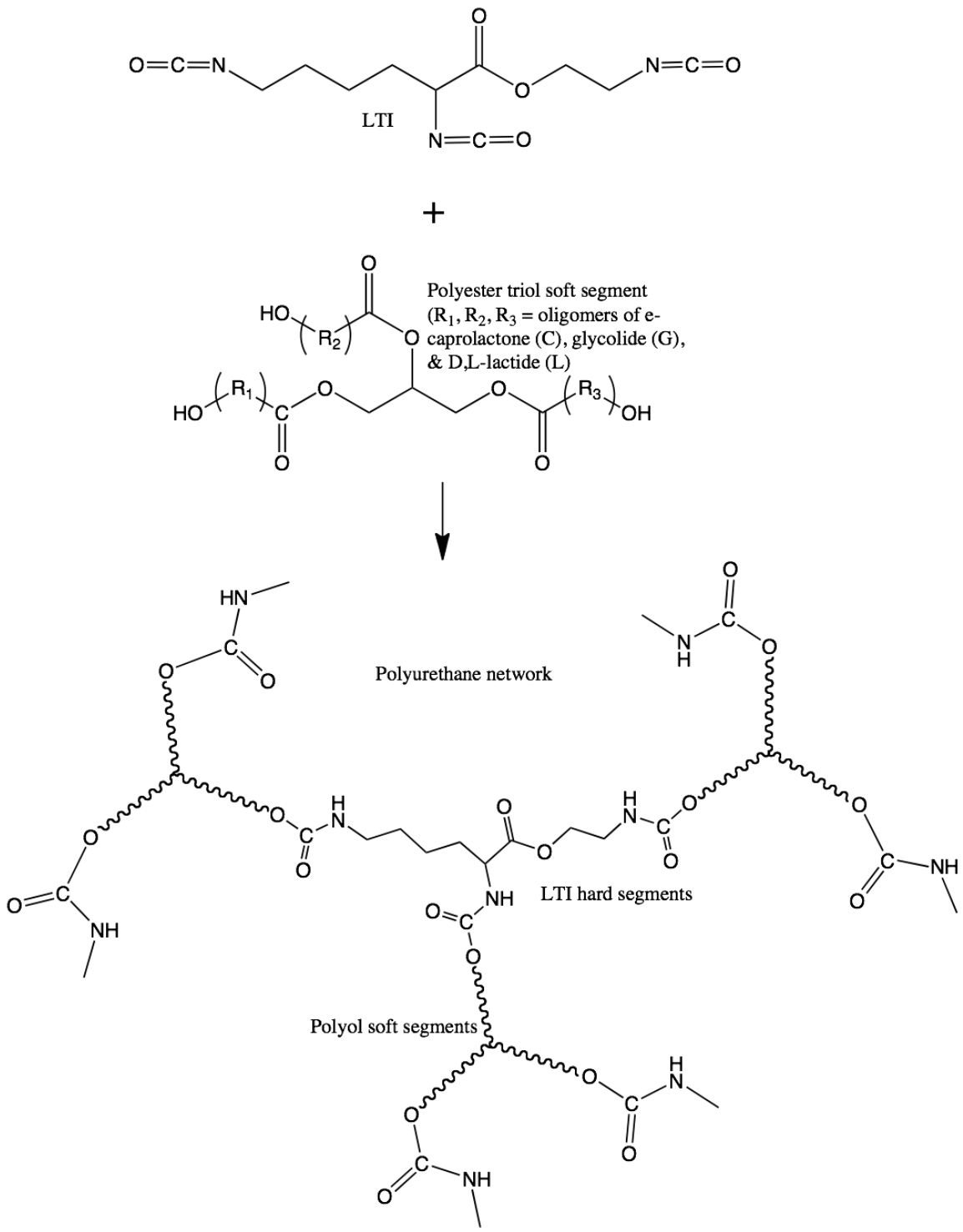

PUR Synthesis - foaming reaction

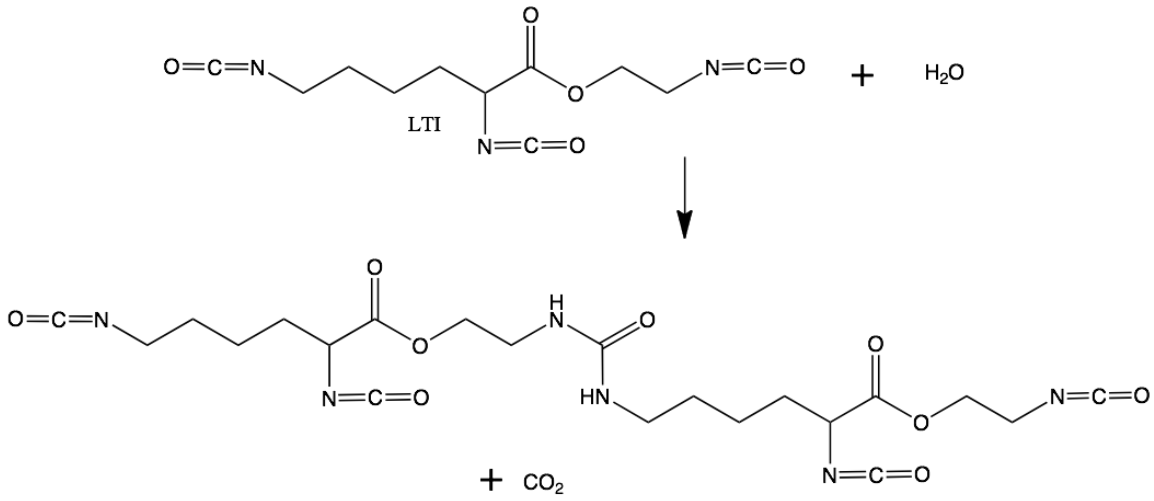

Possible hard segment oxidative degradation